DETERMINATION OF EARTHQUAKE SOURCE PARAMETERS FROM INVERSION OF BODY WAVES

by

John L. Nábělek

B.S., Massachusetts Institute of Technology (1974)

M.S., Massachusetts Institute of Technology (1975)

SUBMITTED IN PARTIAL FULFILLMENT
OF THE REQUIREMENTS FOR THE DEGREE OF
DOCTOR OF PHILOSOPHY

at the

January, 1984

Signature of Author . . . . . .
Department of Earth, Atmospheric, and Planetary Sciences
January, 1984

Certified by. . . . . .
Thesis Supervisor

Accepted by . . . . . .
Chairman, Departmental Committee on Graduate Students

DETERMINATION OF EARTHQUAKE SOURCE PARAMETERS FROM INVERSION OF BODY WAVES

by

John L. Nábělek

Submitted to the Department of Earth, Atmospheric, and Planetary Sciences
Massachusetts Institute of Technology
on January 24, 1984
in partial fulfillment of the requirements
for the degree of Doctor of Philosophy.

ABSTRACT

Earthquakes provide us with important information about ongoing tectonic processes. In the past, only the arrival time data and rough measurements of the amplitudes of the recorded seismograms were used in the analysis of large numbers of earthquakes using formal inversion techniques. Detailed studies utilizing the information contained in the full seismograms were limited in number because of the time consuming trial-and-error techniques involved; only recently have comparable automatic techniques begun to emerge. An increase in the global coverage by digital networks has certainly provided an impetus for such endeavors.

This thesis develops a technique for extracting average (point source) earthquake properties from the teleseismic body wave data. The technique enables us to obtain precise estimates of the source strength and mechanism and its depth and time history for earthquakes of magnitude 4.5 and higher. For larger events, it also provides an estimate of the location of the source centroid relative to the source nucleation point, giving a minimum measure of the fault dimensions and the direction of rupture. Parameterization in terms of a line source is also presented. For complex events, multiple sets of parameters can be estimated.

Numerical tests indicate that for simple events and typical station coverage the accuracy of the depth determination using long-period data is approximately 1 km. The source orientation can be determined to within 2-3° and the seismic moment to within a few percent. For small events, the accuracy in depth determination can be further improved by using short-period data. Numerical tests also show that inversions using source parameterizations which ignore the effects of source duration give biased depth estimates.

The technique was applied to four earthquakes of different size and complexity: the 1975, Lice, Turkey earthquake; the 1982, New Brunswick, Canada earthquake and its main aftershock; and the 1981 El Asnam, Algeria earthquake. Two of these events, Lice and El Asnam, broke the surface of the earth and were studied extensively in the field. Parameters such as fault length, displacement and slip direction (at least on the surface), are therefore well established. The results of the inversions are consistent with these observations.

The New Brunswick earthquake was studied in detail using both long-and short-period data. It was found to be associated with a stress drop of approximately 960 bars. In this study attenuation of P waves at ~1 Hz for paths from New Brunswick was also investigated The strongest attenuation (t^* = 1 2-1.3s) was observed for paths to the western U.S.; the smallest attenuation (t^* = 0.6-0.8s) was observed for South American stations.

The inversion techniques were also applied to two underground nuclear explosions: the August 18, 1979 Kazakhstan, U.S.S.R. event and the March 26, 1970 (Handley), N.T.S., event. It was shown that the teleseismic body waves can resolve the isotropic component of the moment tensor. Deconvolution of the instrument response from the short-period records also helped greatly in stabilizing the inversion. In general, the P-wave travel paths from Kazakhstan are characterized by very low attenuation with values of t^* as low as 0.3s for paths to stations CHTO (Thailand), BCAO (Central Africa), and ANTO (Turkey). The largest t^* value (1 s) was observed for station ANMO (New Mexico).

Thesis Advisor: M. Nafi Toksoz

Professor of Geophysics

ACKNOWLEDGEMENTS

I would like to express my appreciation to Prof. Nafi Toksoz, my thesis advisor, for advise and encouragement throughout the course of this work. I also thank Profs. Keiiti Aki, Ted Madden, Peter Molnar and George Sutton (University of Hawaii) who greatly contributed to my graduate education.

I am particularly grateful to Michel Bouchon for introducing me to the body-wave synthesis and for countless hours of discussions of the source problems. The former Lincoln Lab crew, Tom Fitch introduced me to the virtues of the waveform inversion and Bob North made his SRO data-handling programs accessible to me. Allen Olson kindly gave me his inversion routines with positivity constraints. I had many useful discussions concerning the El Asnam earthquake with Geoff King, Raul Madariaga and Barbara Romanowicz.

Over the years I have enjoyed and profited from cooperation with Eric Bergman, Rob McCaffrey, Wang-Ping Chen and Gerardo Suarez.

Most of all, my profound thanks are extended to Anne Trehu who has always offered the most constructive critique of my work. She read the whole thesis and provided countless scientific and editorial comments.

The nicest figures in this thesis were drafted by Sim Wissler. She also performed the inversion for the Handley explosion. A special thank-you to Dorothy Frank who spent many hours of her free time typing this manuscript. A big thank-you to Debby Roecker and Sara Brydges whose administrative prowess managed to keep me out of trouble (most of the time).

My stay at MIT would not be the same were it not for friedship of Rob Stewart, Brian Tucker, Steve Roecker and Rob McCaffrey. And there is, of course, a long list of others who contributed to my well-being: Danielle and Bernard Chouet, Dave McTigue, John Crowe, Helene Lyon-Caen, Cliff Thurber,

Steve Taylor, Silvie LeDouaran, Jean Baranowski, Colleen Barton, Paul Huang, Roger Morin, Ken Tubman, Dave Olgaard, Arthur Cheng, Kaye Shedlock, Bob Nowack, Jay Pulli, Roger Buck, Scott Phillips, Rob Comer, ...

This research was supported by the Advanced Research Projects Agency of the Department of Defence, monitored by the Air Force Office of Scientific Research under grant F 49620-82-K-0004.

TABLE OF CONTENTS

CHAPTER I

INTRODUCTION

Earthquake epicenter and origin time are the most quoted basic parameters of earthquakes. Although clearly of value, they are not the only, and perhaps not even the most important, parameters that can be used for geological interpretation. The reason for their popularity is simply the fact that they can be estimated using fast, essentially fully automated procedures. Earthquake epicenter estimation from travel time data was the first successful inverse problem in geophysics.

Because of recent advances in digital seismometry, the estimation of other fundamental earthquake parameters from information contained in the full waveforms is now feasible. Of interest for general studies are, in particular, the average source parameters such as the average source mechanism, depth, epicenter, seismic moment and some rough measure of the fault dimensions.

In first applications of automated inversion schemes surface waves were used to determine the source mechanism [Dziewonski and Gilbert, 1974; Patton and Aki, 1979; Kafka and Weidner, 1979; Trehu et al., 1981; Romanowicz, 1981]. The source time history and depth were usually assumed or determined by a grid search. Burdick and Mellman [1976], Stump and Johnson [1977], Strelitz [1978], Fitch et al. [1980] and Ward [1980a] made first attempts in applying inverse methods to body waves. Their efforts concentrated mainly on the determination of the source mechanism. Advances in source time function parameterization suitable for inverse methods were made by Langston [1981] and Kikuchi and Kanamori [1982]. Dziewonski et al. [1981] applied the concepts of Backus and Mulcahy [1976a] to the inversion of very long-period body waves and estimated the zero'th and the first

order terms of the Taylor series expansion of the moment tensor density distribution, which describe the average source mechanism, the centroid location (epicenter and depth) and the centroid time (mid-point of the source time function). Ward [1983] used the same concepts but used a grid search to determine the source depth. Doornbos [1982] and Silver and Jordan [1983], on the other hand, assumed the centroidal parameters and estimated the zero'th and second order terms of the expansion, i.e., the average source mechanism, approximate source duration, dimensions and rupture velocity.

This thesis develops an inversion technique applicable to teleseismic P and S waves from earthquakes with a wide range of magnitude and complexity. The main features of the technique are 1) direct inversion for the centroid depth, 2) improved parameterizations of the source time function, 3) determination of the centroid location with respect to the source nucleation point, 4) determination of the source mechanism and moment (either moment tensor or double couple), 5) inclusion of source finiteness effects using a generalized Haskell model and 6) extension to multiple events. If instabilities occur, a variety of built-in constraints allows control of the inversion. Formal uncertainties (standard errors) of all estimated parameters aid in evaluation of the results.

Chapter II contains most of the theoretical development for the forward and the inverse problem. Additional details are presented in the appendices. Although the source parameterization used here is not strictly a Taylor series expansion of the moment tensor density distribution, a major part of the theoretical discussion is in terms of Taylor series, because it provides most straightforward means of evaluating the importance of spacial and temporal characteristics of the source.

The discussion in Chapter III is geared towards the limitations of the technique, in part due to the particular choice of the source parameterization and in part due to the fact that the observations are made at teleseismic distances in a limited frequency range. Numerical tests simulating real earth situations are conducted in order to help evaluate the results in standard applications. Effects of different source parameterizations are compared.

Chapter IV presents the application of the technique to four earthquakes. Two of the earthquakes produced extensive surface faulting. The geological mapping and the aftershock studies of these events give strong constraints on the source parameters. These events provide an additional test of the accuracy of the estimated source parameters. Inversions using short-period data are also presented.

In Chapter V the inversion technique is applied to two underground nuclear explosions. The ability to resolve the isotropic moment tensor component is thus tested. Due to the extreme shallowness of the source, the resolution of the isotropic component is a difficult task. These events, therefore, provide a particular challenge.

Because their goal is to investigate the limits of resolution of various earthquake parameters, the analyses and discussions presented in Chapters IV and V are very detailed. A more routine application of the technique to a large number of events can be found in Bergman, Nabelek and Solomon [1984]. Two additional studies in which the body wave analyses were performed by the author are presented in Appendices F and G.

Chapter VI gives a summary of the major results.

CHAPTER II

THEORETICAL DEVELOPMENT

2.1 INTRODUCTION

This chapter discusses general properties of earthquakes. It presents commonly used kinematic and dynamic earthquake models and their mathematical representations. It also presents a general discussion of resolvability of details of the seismic source process from the far-field. Based on these considerations a particular model parameterization is given and a procedure for calculating synthetic seismograms is outlined. This defines the "forward problem" for this study. Inversion techniques which can be used for estimating the parameter values of this model from recorded seismograms are then discussed.

2.2 FORWARD PROBLEM

2.2.1 MATHEMATICAL REPRESENTATION OF SEISMIC SOURCES

This thesis is concerned with subterranean sources, mainly earthquakes (a few examples of analysis of nuclear explosions are presented in Chapter V). The generally accepted model for an earthquake in the earth's crust is brittle failure of the rock along a planar surface (a good review of the subject can be found in Aki [1979a]). Except at very shallow depths, the Earth is under compression and consequently shear fracture is the expected mode of failure. Tensile fracturing, which sometimes occurs near the free surface, is not sufficiently energetic to be recorded teleseismically. Models of earthquakes involving voluminal collapse under preexisting stresses, abrupt phase changes or movement of magma through underground channels have also been put forward [Honda, 1932; Ishimoto, 1935; Evinson, 1963; Knopoff and Randall, 1970].

This section will first introduce the equivalent body force and moment tensor densities, which can be used to describe the most general seismic source. It will be shown that the usefulness of these quantities is limited to forward problems and to inverse problems for which a point source is an adequate representation. A large part of this discussion is based on the work by Backus and Mulcahy [1976a,b], Backus [1977a,b], Stump and Johnson [1977, 1982] and Doornbos [1981, 1982]. The representation and properties of finite crack and dislocation models will then be discussed in more detail.

Mathematically, a seismic source represents a temporary failure of the equations of motion in a certain part of the earth, and the source is a correction that is needed to make the equations work again. This correction can be introduced, depending on what is more convenient or

physically more descriptive for a particular problem, either by boundary or initial conditions or by virtual body forces in certain parts of the earth. Since all boundary or initial conditions can also be expressed by equivalent body forces, body forces provide a basis (although not necessarily a physically descriptive one) for describing a general seismic source [Morse and Feshbach, 1953; Burridge and Knopoff, 1964; Backus and Mulcahy, 1976a]. The representation theorem expresses the motion due to a distribution of equivalent body force density

$$u_k(\underline{x},t) = \int_{-\infty}^{t} \int_{V} g_{ki}(\underline{x},t;\underline{\xi},\tau) F_i(\underline{\xi},\tau) dV_\xi d\tau \qquad (2.2.1)$$

where $u_k(x,t)$ is the displacement in the k-direction at the point $\underline{x}$ and time t; $g_{ki}(\underline{x},t;\underline{\xi},\tau)$ is the Green function, i.e., the displacement in the k-direction at $(\underline{x},t)$ due to a unit impulse force in the i-direction at $(\underline{\xi},\tau)$; and F_i is the equivalent body force density. The integration is over a volume V containing the non-zero equivalent body forces.

For a dislocation-type source the equivalent body force density can be expressed as

$$F_i(\underline{\xi},\tau) = -\frac{\partial}{\partial \xi_j}\{c_{pqij} n_q \bar{u}_p \delta(S)\} \qquad (2.2.2)$$

[Burridge and Knopoff, 1964] where $\bar{u}_p$ is the discontinuity in displacement on the fault surface S, n_q is the normal to this surface, c_{pqij} are the Lame constants; and $\delta(S)$ is the surface delta function. The equivalent body force density for volume-type sources is

$$F_i(\underline{\xi},\tau) = -\frac{\partial}{\partial \xi_j} c_{ijpq} \epsilon_{pq}(\underline{\xi},\tau) = -\frac{\partial}{\partial \xi_j} \Gamma_{ij}(\underline{\xi},\tau) \qquad (2.2.3)$$

where ϵ_{pq} is the stress free strain [Eshelby, 1957] and Γ_{ij} is the stress

glut [Backus and Mulcahy, 1976a]. Being a virtual quantity, the body force density is usually difficult to interpret in terms of physical models. Moreover, although the body force density is uniquely determined by the knowledge of the motion everywhere in the earth [Backus and Mulcahy, 1976], its interpretation in terms of physical models is nonunique, i.e., a given body force density distribution can result from many different physical models [Backus and Mulcahy, 1974]. A quantity which better reflects the physics of an internal source is the seismic moment tensor density [Gilbert, 1971; Backus and Mulcahy, 1976a,b; Backus, 1977a,b]. Because the net force and the net torque on the earth must vanish any internal source can be described by a symmetric tensor quantity. The moment tensor density is related to the body force density by

$$F_i = -\frac{\partial}{\partial \xi_j} m_{ij} \tag{2.2.4}$$

The more direct link of the moment tensor density to the physical models is readily apparent after substitution of (2.2.4) into (2.2.2) and (2.2.3). For a dislocation, the moment tensor density is

$$m_{ij} = c_{pqij} n_q \bar{u}_p \delta(S) \tag{2.2.5}$$

and for a volume source

$$m_{ij} = c_{ijpq} \epsilon_{pq} = \Gamma_{ij} \tag{2.2.6}$$

Displacement due to a moment tensor density distribution is obtained by inserting (2.2.4) into (2.2.1) and integrating by parts.

$$u_k(\underline{x},t) = \int_V m_{ij}(\underline{\xi},t) * g_{ki,j}(\underline{x},t;\underline{\xi},0) dV \ . \tag{2.2.7}$$

Here the time integration was also replaced by the convolution.

It should be emphasized that the moment tensor density, like the body force density, is a general mathematical description and not a physical explanation of the source. Furthermore, from (2.2.4) we see that if the moment tensor density is known, the body forces are uniquely specified, but not vice versa. Therefore, the earth motion, which uniquely specifies the body forces, does not uniquely specify the moment tensor density. This limits the usefulness of the moment tensor density in a general inverse problem.

When the wavelengths under consideration are much longer than the dimensions of the source, it is sufficient to expand the Green function about a convenient point $\underline{\xi}^\circ$ in V and keep only the first few terms of the expansion

$$g_{ki}(\underline{x},t;\underline{\xi},\tau) = g_{ki}(\underline{x},t;\underline{\xi}^\circ,\tau) + (\xi_\ell-\xi_\ell^\circ)g_{ki,\ell}(\underline{x},t;\underline{\xi}^\circ,\tau) + \ldots \quad (2.2.8)$$

Substitution into (2.2.7) gives

$$\begin{aligned} u_k(\underline{x},t) = & \int_V m_{ij}(\underline{\xi},t)*g_{ki,j}(\underline{x},t;\underline{\xi}^\circ,0)dV \\ & + \int_V m_{ij}(\underline{\xi},t)*(\xi_\ell-\xi_\ell^\circ)g_{ki,j\ell}(\underline{x},t;\underline{\xi}^\circ,0)dV \\ & + \ldots \end{aligned} \quad (2.2.9)$$

It is therefore useful to define

$$\begin{aligned} M_{ij}(t) &= \int_V m_{ij}(\underline{\xi},t)dV \\ M_{ij\ell}(t) &= \int_V (\xi_\ell-\xi_\ell^\circ)m_{ij}(\underline{\xi},t)dV \\ M_{ij\ell\ldots m}(t) &= \int_V (\xi_\ell-\xi_\ell^\circ)\ldots(\xi_m-\xi_m^\circ)m_{ij}(\underline{\xi},t)dV \quad . \end{aligned} \quad (2.2.10)$$

Equation (2.2.9) can then be rewritten as

$$u_k(\underline{x},t) = g_{ki,j}(\underline{x},t;\underline{\xi}^\circ,0)*M_{ij}(t) + g_{ki,j\ell}(\underline{x},t;\underline{\xi}^\circ,0)*M_{ij\ell}(t) + \ldots \quad (2.2.11)$$

$M_{ij}(t)$ is called the seismic moment tensor or the seismic moment tensor of degree 0 and $M_{ij\ell\ldots}(t)$ are called the higher order seismic moment tensors (degree 1, 2, etc.). Backus and Mulcahy [1976a] showed that the symmetry requirements which the moment tensor must satisfy are sufficient to make moment tensors of degree zero and one unique. The moment tensors of degree two and higher, however, are nonunique and thus, in an inverse problem, one is forced to impose a priori constraints on the source model. Note also that the number of independent parameters grows rapidly with each additional moment. For example, keeping only the first term of the expansion, we have 6 independent parameters, with the first two terms we have 24, and with the three terms we have 60 independent parameters. Even from a practical standpoint, some a priori constraints on the source model are, therefore, desirable in an inverse problem.

Next we shall evaluate the importance of the source time history on the observed displacements. Although a general treatment is possible [Backus, 1977a,b], in view of future needs, I shall gear the following development toward teleseismic body waves. In the epicentral distance range of 30 to 90°, teleseismic body waves are well decribed by a single ray parameter and the Green function takes on a particularly simple form (a more detailed discussion of the body-wave Green function will follow)

$$g_{ki} = g_{ki}^{P\downarrow} + g_{ki}^{P\uparrow} + g_{ki}^{S\downarrow} + g_{ki}^{S\uparrow} = \sum_n g_{ki}^n \quad (2.2.12)$$

where $g_{ki}^{P\downarrow}$, $g_{ki}^{P\uparrow}$, $g_{ki}^{S\downarrow}$ and $g_{ki}^{S\uparrow}$ are the contributions to the Green's function

from the rays which depart from the source downward and upward as P and S waves. The spacial derivatives of this Green function can be expressed as [Aki and Richards, 1980; Doornbos, 1982]

$$\begin{aligned} g_{ki,j} &= \sum_n \frac{\gamma_j^n}{c^n} \dot{g}_{ki}^n \equiv \dot{g}_{ki;j} \\ g_{ki,j\ell} &= \sum_n \frac{\gamma_j^n \gamma_\ell^n}{c^n c^n} \ddot{g}_{ki}^n \equiv \ddot{g}_{ki;j\ell} \\ &\vdots \end{aligned} \tag{2.2.13}$$

where the dot denotes the time derivative, γ_j^n are the direction cosines of the departing rays and c^n, depending of the type of ray, is either the compressional or shear velocity in the source region. We can then rewrite (2.2.11) as

$$\begin{aligned} u_k(\underline{x},t) &= \dot{g}_{ki;j}(\underline{x},t;\underline{\xi}^\circ,0)*M_{ij}(t) + \ddot{g}_{ki;j\ell}(\underline{x},t;\underline{\xi}^\circ,0)*M_{ij\ell}(t) + .. \\ &= g_{ki;j}(\underline{x},t;\underline{\xi}^\circ,0)*\dot{M}_{ij}(t) + \dot{g}_{ki;j\ell}(\underline{x},t;\underline{\xi}^\circ,0)*\dot{M}_{ij\ell}(t) + .. \end{aligned} \tag{2.2.14}$$

Since the displacement in the far-field depends on the time derivative of the moment tensor, the observed displacement is pulse like.

If the periods of the motion are much longer than the source duration, τ^∞, we can expand (2.2.14) about a convenient time, τ°, in the time frame $0<\tau^\circ<\tau^\infty$,

$$\begin{aligned} u_k(\underline{x},t) = {} & g_{ki;j}M_{ij}^0 - \dot{g}_{ki;j}M_{ij}^1 + \dot{g}_{ki;j\ell}M_{ij\ell}^0 \\ & + \tfrac{1}{2}\ddot{g}_{ki;j}M_{ij}^2 - \ddot{g}_{ki;j\ell}M_{ij\ell}^1 + \tfrac{1}{2}\ddot{g}_{ki;j\ell m}M_{ij\ell m}^0 + \cdots \end{aligned} \tag{2.2.15}$$

where

$$g_{ki;j\ldots} \equiv g_{ki;j\ldots}(\underline{x},t;\underline{\xi}^\circ,\tau^\circ)$$

and

$$M^{n}_{ij\ldots} = \int_{o}^{\tau^{\infty}} (\tau-\tau^{o})^{n}\, \dot{M}_{ij\ldots}(\tau)d\tau. \qquad (2.2.16)$$

Thus, M^{n}_{ij} are combined spacial and temporal moments of the moment tensor density.

M^{0}_{ij}, ξ^{o} and τ^{o} are the fundamental point source quantities, which, at least in principle, can be uniquely determined. The tensor norm (first invariant) $M_{n} \equiv \|\underline{\underline{M}}^{0}\|$ defines the source strength and M^{0}_{ij}/M_{n} defines its polarization (i.e., source mechanism). ξ^{o} and τ^{o} can be chosen such that M^{1}_{ij} and $M^{0}_{ij\ell}$ vanish, in which case ξ^{o} and τ^{o} are the centroid location and the centroid time of the moment tensor density, respectively. The higher order moment tensors carry information about the time history and spacial extent of the moment tensor density around the centroidal points. The centroidal points are the optimum points for which the expansion converges fastest, giving the least residual. A least squares inversion of data for a source model specified by the truncated expansion should, therefore, give centroidal parameters as the solution. Dziewonski et al. [1981] used such a parameterization as the basis for their inversion scheme. Doornbos [1982] used a second order expansion with constraints and was thus able to estimate roughly the source duration, dimensions and rupture velocity. Equation (2.2.15) tells us that if we want to obtain an unbiased estimate of the centroid location we must also estimate the source time function, or at least its centroid time.

In the case of an axially-symmetric medium, the Green's functions are axially-symmetric and the problem separates into P-SV and SH components. The above equations can then be written in a more appropriate form for most long-period studies in the Earth. For example, the displacement due to

$M_{ij}(t)$ for the P-SV case becomes [Ward, 1980a]

$$\begin{aligned}\underline{u}^{PSV}(\phi,\Delta,t) = {} & \underline{I}^{PSV\,2}(\Delta,h,t)\left[\tfrac{1}{2}(M_{yy}+M_{xx}) - \tfrac{1}{2}(M_{yy}-M_{xx})\cos 2\phi + M_{xy}\sin 2\phi\right] \\ & + \underline{I}^{PSV\,1}(\Delta,h\ t)\left[M_{yz}\sin\phi + M_{xz}\cos\phi\right] \\ & + \underline{I}^{PSV\,0}(\Delta,h.t)M_{zz}.\end{aligned} \tag{2.2.17a}$$

and for the SH case

$$\begin{aligned}\underline{u}^{SH}(\phi,\Delta,t) = {} & \underline{I}^{SH\,2}(\Delta,h,t)\left[\tfrac{1}{2}(M_{yy}-M_{xx})\sin 2\phi + M_{xy}\cos 2\phi\right] \\ & + \underline{I}^{SH\,1}(\Delta,h,t)\left[M_{yz}\cos\phi - M_{xz}\sin\phi\right]\end{aligned} \tag{2.2.17b}$$

where ϕ and Δ are the azimuth and distance to the observation point and h is the source depth and $\underline{I}$'s are the excitation functions (for additional details see Appendix A).

In general, moment tensor formulations have many more degrees of freedom than necessary for describing most commonly occurring earthquakes. In the absence of phase changes, the moment tensor of most natural earthquakes should not contain a volume change (i.e., it is purely deviatoric); this decreases the number of free parameters. Furthermore, most earthquakes are caused by a shear fracture of the rock, and the moment tensor density takes on a particular form

$$m_{ij} = \mu(\bar{u}_i n_j + \bar{u}_j n_i)\delta(S) \tag{2.2.18}$$

which is equivalent to a double-couple distribution along the fault surface. The static seismic moment M_o [Aki, 1966] is given by

$$M_o = \frac{1}{\sqrt{2}} M_n \tag{2.2.19}$$

where M_n denotes the corresponding tensor norm.

When using the unconstrained moment tensor parameterization for estimating earthquake source mechanisms, it is a common practice to decompose the moment tensor into its isotropic and deviatoric components and then to further decompose the deviatoric components into either a double-couple and a linear-vector-dipole pair or a major and a minor double-couple pair. Unless one has a specific model in mind, these decompositions are not useful. Only the isotropic-deviatoric decomposition is unique. The others are non-unique. When one is certain that the double-couple mechanism is in fact the expected source mechanism it can be extracted from the moment tensor. Assuming that the isotropic part of the moment tensor was removed and the deviatoric part was diagonalized, the decomposition which maximizes the double-couple contribution is the following:

$$\underline{\underline{M}}' = \begin{bmatrix} \sigma_1 & & \\ & \sigma_2-\sigma_1 & \\ & & -\sigma_2 \end{bmatrix} = \begin{bmatrix} \frac{1}{2}(\sigma_1+\sigma_2) & & \\ & 0 & \\ & & -\frac{1}{2}(\sigma_1+\sigma_2) \end{bmatrix} + \begin{bmatrix} \frac{1}{2}(\sigma_1-\sigma_2) & & \\ & -(\sigma_1-\sigma_2) & \\ & & \frac{1}{2}(\sigma_1-\sigma_2) \end{bmatrix}$$

$\sigma_1, \sigma_2 \geq 0$.

The first term on the right side of the equation is the double-couple component (following Dziewonski et al. [1981] I will refer to it as the best double-couple estimate) and the second term on the right is the linear-vector-dipole component.

In summary, because all internal seismic sources can be represented by a moment tensor density, it is a useful quantity in forward problems where, in a manner analogous to the body force density, it provides a weighting factor for the excitation functions in the volume integration. Due to non-uniqueness, its use in the inverse problem is limited to situations where we are interested only in the point source, i.e. average properties

of the source. The spacial moment tensor of degree zero and its location can be uniquely determined, assuming good data coverage. Even when we expect the source to be a double-couple, it is sometimes useful to use the unconstrained moment tensor as the source model, in spite of overparameterization, because it enters linearly into the equations and simplifies the procedures. Because the double-couple constraint is non-linear, the inverse problem is somewhat more complicated.

2.2.2 DISLOCATION AND CRACK MODELS OF EARTHQUAKES

Dislocation and crack models are commonly used to describe the dynamics of earthquake faulting. Dislocation models are those in which the displacement on the fault is assigned in a kinematic fashion, without regard to actual physical plausibility. The use of kinematic dislocation models is widespread since for most purposes such a description can adequately describe the observed data. The best known of such models are those by Ben Menahem [1961], Haskell [1964], Savage [1966], Molnar et al. [1973], Sato and Hirasawa [1973], and Dahlen [1974]. The crack models employ the principles of fracture mechanics to prescribe the slip functions on the fault and are physically more realizable. These include models by Kostrov [1966], Burridge and Willis [1969], Ida [1972], Richards [1973], Madariaga [1976], and Das and Aki [1977].

At high frequencies the amplitude spectra for the crack models are dominated by the stopping phases which result in a ω^{-2} high-frequency asymptote [Madariaga, 1981]. Although some kinematic models predict other behavior at high frequencies, the ω^{-2} relationship is favored by the observations [Aki, 1967; Hanks, 1979].

The unrealizability of the dislocation models demonstrates itself as a singularity in the stress drop on the fault surface (Figure 2.1a). The stress drop for the crack models, however, is finite (Figure 2.1b). Because spacial resolution of the actual fault displacement at scales shorter than the wavelengths of the recorded data is physically impossible [Kostrov, 1975], the distinction between the crack and dislocation models may not be important for fitting the data and roughly estimating the fault size and the amount of slip. If, however, the purpose of the investigation is to determine the stress drop, the crack model must be applied [Madariaga, 1979]. This can be done in a posteriori fashion by interpreting the results of the kinematic analysis in terms of an appropriate crack model.

Usually the "average" stress drop is determined by assuming a constant stress drop crack model with the source geometry of the kinematic model. For a circular crack, the stress drop $\Delta\sigma$, is given by

$$\Delta\sigma = \frac{7}{16} \frac{M_o}{R^3} \qquad (2.2.20a)$$

[Eshelby, 1957; Keilis-Borok, 1959] where M_o is the seismic moment and R is the crack radius. For a rectangular fault the relation is

$$\Delta\sigma = C \frac{M_o}{w^2 L} \qquad (2.2.20b)$$

where w and L are the fault width and length, respectively, and C is $\frac{2}{\pi}$ for strike-slip faults [Star, 1928] and $\frac{8}{3\pi}$ for dip-slip faults [Knopoff; 1958].

The consequences of such assumptions are discussed in detail by Madariaga [1979] and Rudnicki and Kanamori [1981]. They show that the "average" stress drop determined in this fashion is weighted towards the

center of the fault. It provides a good estimate of the true average if the largest displacements occur near the center of the fault but can substantially underestimate the stress drop if the largest displacements occur near the fault edges.

Pulses from the circular Madariaga model are shown in Figure 2.2 and show directivity in the direction perpendicular to the plane of the crack. This type of model is usually satisfactory for describing small earthquakes.. The fact that many (especially large) earthquakes show directivity analogous to the unilateral kinematic Haskell-type model indicates that a simple crack model is inappropriate for large events. This observation, among others, led to the development of the barrier model [Das and Aki, 1977; Aki, 1979b].

In the barrier model the fault zone is initially subjected to a uniform tectonic stress field. As the rupture initiates it encounters barriers (strong patches) in its path which temporarily arrest its progress. The build up of the stresses at the barrier, however, triggers faulting on the other side of the barrier and rupture propagates further without actually breaking the barrier. The slip in an area between two barriers is well described by a simple crack-type model but, because different areas of slip do not communicate directly, the fault as a whole acts like the Haskell type model (Figure 2.3). With time, the unbroken barriers also break producing a sequence of aftershocks.

The barrier model as proposed by Das and Aki [1977] cannot, however, explain the occurrence of foreshocks. This led to the development of the asperity model [Kanamori, 1978]. In this model, the potential fault zone consists of both strong and weak patches, and the weak patches break as foreshocks. Prior to the mainshock, the fault zone consists of strong

highly stressed patches (asperities) and weak stressless patches. When the mainshock occurs, the asperities break, the stress is released and slip occurs on the entire fault plane. The weak parts do slip, but there is no stress drop associated with this motion. The asperity model produces a jerky motion but, because in the final stage the stress is uniform over the entire fault plane, the overall displacement can be well approximated by a simple crack-like model. In contrast to the barrier model, the asperity model does not explain the occurrence of aftershocks. In reality, large earthquakes should be modeled by a combination of the two models.

Temporal as well as spacial complexity is common for large events [Kanamori and Stewart, 1978; Rial, 1978; Philip and Meghraoui, 1983; this thesis]. Unless one is satisfied with a very long period approximation of the average properties, these events require a complicated source parameterization. Before presenting the specific source parameterization(s) I have chosen for the inverse problem, the procedures for determining the Green's function will be discussed.

2.2.3 GREEN'S FUNCTION FOR THE EARTH

In section 2.2.1 (also see Appendix A) it was shown that the theoretical seismogram from an arbitrary point stress drop source can be easily constructed if the Green's functions can be determined. This obviously is not a trivial task. One approach would be to measure the response of the earth from a controlled source acting at the same site as the source we want to investigate, hence considering the earth as a black box. The other approach, if we possessed a complete knowledge of the earth's structure and had the theoretical capability of calculating its exact response, would be to do just that. Of course, neither of these approaches is feasible for practical applications. Compromises, i.e.,

approximations to the Green's functions, are clearly needed, and these approximations will have a direct bearing on the resolution of the source parameters which we seek to estimate.

For an unbiased estimate of the source properties, it is necessary to work in a frequency range in which the Green's function is correct on average, with the discrepancies being small and randomly distributed; their effect can then be averaged out by making many observations. The usual approach is to separate the Green's function into distinct phases (arrivals within a given time window) and treat only those phases for which the path effects are understood.

The vertical stratification of the earth is reasonably well understood and can be accounted for computationally with a varying degree of efficiency depending on the phase studied. Lateral heterogeneities, on the other hand, are poorly understood and are the source of the largest uncertainties in the Green's functions. In general, the largest lateral heterogeneities in the earth occur in the crust and uppermost mantle. Phases which propagate laterally over large distances in these layers will therefore be significantly affected. Unless detailed analysis of these effects is made, we are restricted to using phases which either do not travel long distances laterally through this part of the earth or have wavelengths long enough to average out the effect of these heterogeneities.

In this thesis, body waves in the distance range of 30 to 90° are the primary data set. These waves propagate steeply (15-35° from the vertical) through the crust and uppermost mantle and therefore "feel" only the vertical structure below the source and receiver. Most of the lateral movement takes place in the deep mantle, which is remarkably homogeneous

[Burdick and Helmberger, 1978]. The body waves travel through it without significant dispersion. Using teleseismic body waves, details of the source can be usually determined from waveforms with periods as short as a few seconds. (In Chapter IV, I will show an application using data with periods of 0.5-1 s.)

Some use will also be made of long-period, fundamental mode surface waves. For shallow sources, the surface wave is the most energetic phase recorded on the long-period instruments at teleseismic distances and, consequently, it has been studied extensively. Unfortunately, because most of the surface wave energy propagates through the crust and upper mantle, these waves are subject to severe diffraction, scattering and other effects of lateral heterogeneities, which limit their usefulness for source studies. Although periods as short as 25 or 30s can be used for relatively short paths contained within simple geological provinces if careful calibration of the path effect is made [Patton, 1980; Trehu et al., 1981; Romanowicz, 1981], in general, only periods of 100s and longer can be considered with average earth models. This limits their application to very large events and severely degrades the resolution of the source parameters [Kanamori and Given, 1981; Silver and Jordan, 1983]. In this thesis surface waves are used mainly to obtain an independent estimate of the seismic moment.

2.2.4 COMPUTATION OF BODY WAVE SYNTHETIC SEISMOGRAMS

Teleseismic body waves are perhaps the easiest of all seismic phases to model with synthetic seismograms because, due to the homogeneity of the earth's mantle and the fact that the observations are made at a great distance from the source, these wave packets are approximately characterized by a single ray parameter (i.e., a constant apparent velocity

of propagation along the free surface). For a shallow source, the wave packet of a teleseismic P or S wave is usually composed of at least three energetic rays: the direct, and two reflections from the free surface (pP and sP for the P-wave packet and sS and pS for the S-wave packet) [Langston and Helmberger, 1975]. When there are large impedance contrasts in the crust (for example, at the rock-water interface in oceanic environments), reverberations within the crustal layers also must be considered [Ward, 1979; Trehu et al., 1981; Stewart and Helmberger, 1981; Appendix F].

The simplest way to calculate the teleseismic body wave Green's function is to split the calculation into three parts: the contributions from the crustal and free surface effects in the source and receiver regions and the contribution from the mantle (Figure 2.4). Because of the homogeneity of the mantle, this portion of the propagation path can be accounted for by considering only geometrical spreading [Bullen, 1963], anelastic attenuation [Futterman, 1962] and travel time.

The effect of the free surface and crustal structure in the receiver region on a plane wave impinging from below can be easily computed using propagator matrixes [Haskell, 1953]. Because most stations of the WWSSN, Canadian and GDSN networks used in this thesis are located on hard rock sites, no unusual site effects are expected. When a large number of stations is included in the analysis, it is usually sufficient to use only a single average crustal model common to all stations, since any differences should average out.

In contrast to the modest requirements for precise knowledge of the receiver crustal structure, it is important that the assumed source crustal structure be a good representation of the true structure at the wavelengths sampled by the dominant frequencies contained in the data. Errors in this

part of the Green's function will not be reduced by the inclusion of many stations because this part of the model is common to all of the seismograms. It is also important that the determination of the response for different source depths be efficiently computed because depth is one of the source parameters that we shall be interested in determining and in the inversion procedures used in this thesis many trial depths will be required.

The body-wave displacement in a half-space due to a force acting in a stack of overlaying crustal layers can be obtained in the time or frequency domain by various methods. These assume either that all the contributions come from waves with only one ray parameter (horizontal wave number) [Langston and Helmberger, 1975; Bouchon, 1976] or that they come from a small anulus around the dominant ray parameter [Chapman, 1978; Cormier and Choy, 1981]. In this thesis, the seismograms are calculated assuming one ray parameter. This approximation implies that out of all the rays of up- and down-going P and S waves which depart from the source only four contribute to the body wave seismogram at a given point in the half-space and that the Green's function can be written in the form of equation 2.2.12

$$g_{ki} = g_{ki}^{\downarrow P} + g_{ki}^{\uparrow P} + g_{ki}^{\downarrow S} + g_{ki}^{\uparrow S} \equiv \sum_{n} g_{ki}^{n}.$$

It also implies that for a horizontally layered structure, as long as the source remains within a given layer, the responses g_{ki}^{n} remain the same (except for the change in travel time to the first interface) regardless of the vertical position of the source (Figure 2.5). If g_{ki}^{n} are known for one depth h, the g_{ki}^{n} for a depth of $h+\Delta h$ are obtained simply by the appropriate

time shifts of the originals, i.e.,

$$g^n_{ki}(h+\Delta h) = g^n_{ki}(h)\ \delta(t-\eta^n \Delta h)$$
$$\underline{\eta} = (-\eta_\alpha, \eta_\alpha, -\eta_\beta, \eta_\beta) \qquad (2.2.21)$$

where δ is the delta function and $\eta_{\alpha(\beta)}$ is the vertical slowness, of the P(S) wave rays in the layer in which the source is located. This is a very useful property since the efficiency of iterative inverse procedures depends greatly on how quickly one can update the model after each iteration and depth is one of the parameters which we usually want to determine.

The response g^n_{ki} is simply a sum of rays entering the half-space which results from the crustal interaction of the parent ray. In the ray methods, the rays are traced through the crust and multiplied by the appropriate plane wave transmission and reflection coefficients. The resulting time series is then multiplied by the source radiation pattern and a ratio $\eta^{\text{half-space}}/\eta^n$ (an important, but often forgotten factor) which accounts for the fact that in the vicinity of the source the waves are spherical and experience a change in geometrical spreading due to differences in the wave velocity in the source layer and the wave velocity in the half-space. That this simple correction is the only one required to this otherwise strictly plane wave procedure was derived in a rather lengthy, complicated analysis by Langston and Helmberger [1975]. Gupta [1967] and Bouchon [1976] showed, however, that it can be obtained in an almost trivial fashion using the reciprocity theorem (see Appendix C). In this thesis, g^n_{ik} are calculated in the frequency domain using propagator matrices (Appendix D).

2.2.5 A SPECIFIC MODEL PARAMETERIZATION

Objective: The main objective of this study was to find a source parameterization which would adequately describe a large variety of earthquakes of different sizes and complexity, and yet be suitable for a routine analysis of the long-period WWSSN and GDSN data. In routine applications which deal with a great quantity of data the emphasis must be on the stability of the solution since an exhaustive analysis of non-uniqueness is not feasible. This usually necessitates a slight underparameterization of the source, i.e., using a model with the least number of parameters which can adequately describe the observed data. One must be cautious, however, not to introduce a bias into the solution by ignoring certain parameters. In section 2.2.1 it was shown that the simplest source description, a point source, requires a determination of the source strength, mechanism, centroid origin time, and centroid location (depth and epicenter). This parameterization is adequate only for long-period-long-wavelength data relative to the source duration and spacial extent [Dziewonski et al., 1981; Ward, 1983]. The data must be low-pass filtered if it does not conform to this requirement. Filtering, however, removes valuable information and degrades the resolution of the centroidal parameters. Clearly, if feasible, one should instead try to estimate the source duration and fault dimensions; even rough estimates of these parameters will improve the resolution of the centroidal parameters.

Some investigators [Backus, 1977a,b; Doornbos, 1982; Silver, 1983] advocate parameterizations in terms of moment expansions as discussed in section 2.2.1 and always keeping terms of the same order in space and time. Their considerations, however, are based mainly on models with smoothly propagating ruptures and uniform stress release from the entire fault. A

wealth of experience from the forward modeling of WWSSN records indicates the common occurrence of heterogeneous stress release and complex time histories [Burdick and Mellman, 1976; Kanamori and Stewart, 1978; Rial, 1978; Cipar, 1981; Stewart and Kanamori, 1982; this thesis]. Often earthquakes known to be of small dimensions can have energy released in small bursts spread over a relatively long time. In order to match the data, a relatively more detailed parameterization is required for the time history than for the spacial effects.

This thesis uses several types of source parameterizations. In the simplest one, the source is assumed to be well represented by an average source mechanism and the spacial location of its centroid. The time history is, however, allowed to be complicated.

Source mechanism parameterization: Unconstrained and constrained moment tensor representations are used. Usually pure deviatoric or pure double-couple mechanisms are assumed. The coordinate conventions are those of Aki and Richards [1980] (Figure E.1).

The centroid location parameters: The centroid depth is always included as a parameter in the inversion. Simplicity of the body wave Green's function calculations for different source depths was highlighted earlier. The procedures adopted there ignore the absolute travel time; therefore, the absolute epicentral location or the origin time of the centroid cannot be directly determined. The absolute travel time is the most variable part of the Green's function between different stations. The effect of these fluctuations must be removed (i.e. we must calibrate the paths) unless we want to sacrifice resolution of other parameters and consider only very long period data and average earth models. (It should be evident from the earlier discussion that the observed first motion does

not necessarily provide correct alignment for the seismograms of the average, centroid model. Because of the finiteness effects, which we ignored, the average, centroidal seismograms will begin earlier or later than the observed first motions at different stations.) In this study the calibration is done in two ways.

(1) Inversions are initially performed using the theoretical arrival time or the observed first motion as the t=0 of the synthesized waveform, then after convergence a solution of the observed and the synthesized waveforms are realigned, if a better cross-correlation could be found. The inversion is restarted again and the procedure repeated if large misalignments still exist. It was found that this two step procedure was more efficient in most cases than introducing "travel time" corrections explicitly into the inversion.

(2) A more enlightened approach, which works for P waves, is to determine the arrival time from the short-period records. Assuming that the earthquake nucleated at a point and the observed first motions at all stations represent energy from the same point in the source volume we have in fact calibrated the travel path. In a manner analogous to the relative hypocenter determination using the master event technique [Everden, 1969], we can locate the centroid with respect to the nucleation point. Thus in addition to correct alignments we also obtain a rough minimum estimate of the source dimension and the direction of rupture. The effect of a different location of the centroid with respect to the nucleation point can be expressed as a simple time shift of the whole synthetic seismogram with respect to the first motion by the amount

$$\bar{\eta}_1 \zeta + \rho\cos(\phi-\psi) \qquad (2.2.22)$$

where (ρ,ψ,ζ) are the relative coordinates of the source centroid with

respect to the nucleation point as defined in Figure E.3, ϕ is the station azimuth, $\bar{\eta}_1$ is the average vertical slowness of the direct P wave (S wave, in the SH problem) over the vertical distance ζ and p is the ray parameter.

Source time function parameterization: Two types of far-field source time function parameterizations are used. 1) In the earlier work in this thesis, following the idea of Langston [1981], the time function $\Omega(t)$ is discretized by a series of box-functions $B_{\Delta\tau}(t)$ of equal durations $\Delta\tau$ but of variable amplitude w_k (Figure 2.6):

$$\Omega(t) = \sum_k w_k \, B_{\Delta\tau}(t-\tau_k)$$
$$\tau_k = \Delta\tau(k-1). \qquad (2.2.23)$$

The problem with this parameterization is that unless sufficiently small time increments are chosen, the synthetic seismograms are usually too rich in high frequencies. It was mentioned earlier that earthquake spectra are characterized by ω^{-2} decay at high frequencies; the box-function decay is, however, only ω^{-1}. A more suitable choice is a triangle function, which has the proper decay. A time function parameterization using overlapping isosceles triangles was employed in later studies and has the form (Figure 2.6):

$$\Omega(t) = \sum_k w_k \, T_{\Delta\tau}(t-\tau_k)$$
$$T_{\Delta\tau}(t) = B_{\Delta\tau}(t) * B_{\Delta\tau}(t) \qquad (2.2.24)$$
$$\tau_k = \Delta\tau(k-1).$$

Compared to the box-function parameterization, fewer elements are needed for an adequate description of the source.

In both parameterizations, amplitudes w_k are determined by the inversion, but the number of the time function elements and their durations are chosen a priori. Inversions, usually begin with a few coarsely spaced

elements covering the expected total duration of the source. The model is then refined by introducing more, closer spaced elements until the data are matched to their expected accuracy or until no more significant improvement in the residual is observed. The number of elements of significant amplitude determines the total source duration. In the above parameterization we assume that the observed source time function is entirely due to the time history of the source. The consequences of this assumption will be discussed in the next chapter.

The forward problem: By virtue of the fact that the teleseismic body waves can be represented by a single ray parameter and a particular choice of the time function representation, the synthetic seismogram (i.e., the forward problem) can be written in the following computationally efficient form

$$s(t) = M_n \sum_{k=1}^{n} \sum_{i=1}^{m} w_k H_i[t-\tau_k-(\eta_i-\eta_1)d+\bar{\eta}_1\zeta+p\rho\cos(\phi-\psi)]r_i \qquad (2.2.25)$$

where

$$H_i(t) = h_i(t)*T_{\Delta\tau}(t)*M(t)*C^R(t)*R(t).$$

and

M_n - moment tensor norm

w_k - weight of the source time function element k

$H_i(t)$ - elementary seismograms

t - time

τ_k - time shift of a time function element

η_i - vertical slowness of the parent rays

$\bar{\eta}_1$ - average vertical slowness over vertical distance of the ray contributing to the first motion

d - centroid depth with respect to the layer interface above

ζ - centroid depth with respect to the nucleation point

p - ray parameter

ρ - radial distance from the epicenter of the nucleation point to the epicenter of the centroid

ψ - azimuth from the epicenter of the nucleation point to the epicenter of the centroid

ϕ - station azimuth

r_i - normalized source radiation pattern

n - number of time function elements

m - is 4 for P-SV waves and 2 for SH waves

$h_i(t)$ - response of the source crust to the parent rays from a point P, SV and SH source

$T_{\Delta\tau}(t)$ - normalized time function element

M(t) - mantle response function

$C^R(t)$ - receiver crustal response

R(t) - receiver (instrument) response

This expression is derived in detail in Appendices A and D. The coordinate conventions are shown in Figures E.1-E.4 (Appendix E). The whole seismogram is constructed by a weighted and time shifted sum of the elementary seismograms $H_i(t)$. These remain the same as long as the source stays within the same layer. The source crust response functions $h_i(t)$ are computationally the most time consuming part of the problem. A set for each layer must be computed in any application of the standard Thomson-Haskell propagator matrix procedure. These can then be stored, and, in the event that the source jumps to a new layer, the complete crustal response need not be recomputed.

Generalized Haskell model: For events of large spacial extent relative to the wavelengths of the data, a point source parameterization may not be appropriate. When one dimension of the fault is much larger than the other, the fault can be well approximated by a propagating line source. Using the Fraunhofer approximation, the effect of a unilateral rupture (bilateral rupture can be obtained by a superposition of two opposing unilaterally propagating sources) is easily introduced by varying the duration of one of the box-functions in (2.2.24) as a function of station azimuth and distance to the epicenter (ray parameter). For non-horizontally propagating sources, the time function of each of the elementary seismograms $H_i(t)$ will be affected differently. An element of the source time function of each $H_i(t)$ can be written as

$$T_{\Delta\tau_i}(t) = B_{\Delta\tau_i}(t) * B_{\Delta\tau^R}(t) \qquad (2.2.26)$$

$$\tau_k = (k-1)\Delta\tau_i$$

where

$$\Delta\tau_i = \Delta\tau^L\{1 - v^\theta p\cos(\phi-\theta) - v^\delta[-\eta_i \sin\delta + p\cos\delta\sin(\phi-\theta)]\}$$

and v^θ and v^δ are the components of the rupture velocity along the fault strike θ and dip δ, respectively. ϕ is the station azimuth. $\Delta\tau^L = \Delta L/|(v^\theta, v^\delta)|$ is the rupture duration over a fault segment ΔL. $\Delta\tau^L$ is analogous to the point source $\Delta\tau$ and is chosen using the same criteria. $\Delta\tau^R$ is the rise time which approximates the effect of the width of the fault. The weights of the time function elements represent relative moment release from the individual fault segments.

For horizontal rupture the effect is the same for all $H_i(t)$ at a given station and the above formula simplifies to

$$\Delta\tau_i = \Delta\tau' = \Delta\tau^L\{1 - v^\theta p\cos(\phi-\theta)\}.$$

$T_{\Delta\tau'}(t)$ are azimuthally dependent trapezoid functions (Figure 2.7).

This parameterization is similar to that by Kikuchi and Kanamori [1982] who parameterize the source time function as a series of trapezoids of variable duration and amplitude. The advantage of their parameterization is that it usually requires fewer time function elements for an adequate match to the data. It is, however, non-linear and requires an iterative procedure. The parameterization used here is linear; for a given depth and source mechanism, a one step solution is therefore possible. Because the source time function is the only source property which Kikuchi and Kanamori [1982] determine, slight non-linearity is not a serious drawback. The goal of the procedures presented here, however, is also to determine other pertinent source properties, some of which, especially the source depth, are strongly non-linear. It was felt that introducing additional non-linearities into the problem would not be appropriate.

Multiple events. Often earthquakes are generated by motion on several fault-planes in a complex sequence in time and space. In order to describe the observed data additional events must be introduced. The seismogram for a multiple event with n_e subevents delayed with respect to the origin time by a time Δt_e can be written as

$$s(t) = \sum_{e=1}^{n_e} s_e(t-\Delta t_e) \qquad (2.2.27)$$

where $s_e(t-\Delta t_e)$ is the seismogram due to a subevent e with the centroidal location referenced relative to the nucleation point of the first subevent.

2.3 INVERSE PROBLEM

2.3.1 INTRODUCTION

As in every inverse problem, we hope that the model is properly parameterized so that any unknowns in the assumed parameters are averaged out when we make many measurements. Because earthquakes vary in size and complexity but are recorded only in certain frequency bands, a parameterization appropriate for one earthquake may not be appropriate for another. The inversion is, therefore, necessarily a step-wise trial-and-error process. After determining a set of parameters, one must look and compare the model predictions with the observed data. If the predictions agree to within the accuracy of the data and the uncertainties in the model parameters are acceptable, one's job is finished. If, however, the data are not matched acceptably one must either filter the data or increase the number of model parameters if one suspects that the discrepancies are due to particular features of the earthquake source. If the uncertainties in the model parameters are so large that the estimates are not of much value, constraints must be applied to the model. This is usually the most difficult part of the inverse problem.

Soft or hard constraints can be applied in many ways, and it is up to researchers to decide which constraints are appropriate. Since most inversion schemes minimize the L2 or the L1 norm of the differences between the data and the predicted values, the basic principles are very similar. The differences come only in the details of how one weighs the data and how the model is filtered in case of instabilities. The most common remedies for instability are:

1) Increasing the grid spacing of the model,

2) Low-pass filtering the model by damping the small eigenvalues,

3) Applying firm bounds on parameters based on physical considerations (e.g., requiring that the parameters be positive),

4) Requiring firm relations between certain parameters (e.g., double-couple constraint on the moment-tensor),

5) Applying soft bounds on parameters in a statistical manner based on some previous knowledge about their expected values and the associated uncertainties,

6) Forcefully fixing unresolved parameters.

Except for (2), all of the above methods are used in this thesis. (2) is a popular method in inverse problems which involve a number of similar, spacially distributed variables (e.g., velocities at nodal points in a spacial grid) and results in a spacial smoothing of the model similar to that achieved by using (1). The low-pass filtering, however, is usually difficult to control when mixed variables are estimated, because it often results in unwanted trade-offs between certain variables. In particular, if the source time function is overparameterized and becomes unstable, one could smooth it by damping; this may result, however, in a complex interplay with other variables. By decreasing the number of time function elements and increasing their duration, the effect of smoothing is confined to interactions between the neighboring time function elements. Judicial control of the model grid spacing is an important part of any inverse problem because it saves computer time and simplifies the interpretation.

Applying positivity constraints to the source time function was found to be useful in studies of complex events (e.g., El Asnam, Chapter 4.4). It greatly stabilized the inversion and increased the speed of the iteration process. The positivity constraints were applied in the manner outlined by Lawson and Hanson [1974].

In the studies of the earthquakes in this thesis, the moment-tensor formulation was not found to be particularly useful. Usually, after confirming that the source could be well represented by a double-couple mechanism, the inversion solutions were refined using the double-couple constraint.

2.3.2 MAXIMUM LIKELIHOOD INVERSE

The principle of maximum likelihood provides an objective means of estimating a set of model parameters from data. The principle can be applied to both the data and the estimated model parameters if some *a priori* information about the model parameters is available. If the errors in the data and model parameters are Gaussian, the maximum likelihood inverse amounts to minimization of χ^2,

$$\chi^2 = [\underline{d}-\underline{m}(\underline{p})]^T \underline{C}_{d_o}^{-1} [\underline{d}-\underline{m}(\underline{p})] + [\underline{p}_o-\underline{p}]^T \underline{C}_{p_o}^{-1} [\underline{p}_o-\underline{p}] \qquad (2.3.1)$$

where $\underline{d}$ is an array of all observed digitized seismogram amplitudes, $\underline{m}(\underline{p})$ is an array of corresponding predicted values for the model parameters $\underline{p}$, p_o are the *a priori* model parameter estimates, and $\underline{C}_{d_o}$ and $\underline{C}_{p_o}$ are *a priori* estimates of the covariance of the data and parameters, respectively.

Becuase $\underline{m}(\underline{p})$ is non-linear, the minimum of (2.3.1) is found iteratively. The improvement to the solution from the k'th to k+1'th iteration can be expressed in a standard iterative least-squares form

$$\underline{p}_{k+1} = \underline{p}_k + (\underline{A}_k^T \underline{A}_k)^{-1} \{\underline{A}_k^T \underline{f}_k\} \qquad (2.3.2)$$

where

$$\underline{A}_k = \begin{bmatrix} \underline{C}_{d_o}^{-1/2} \underline{J}_k \\ \underline{C}_{p_o}^{-1/2} \end{bmatrix} \qquad \underline{f}_k = \begin{bmatrix} \underline{C}_{d_o}^{-1/2} [\underline{d}-\underline{m}(\underline{p}_k)] \\ \underline{C}_{p_o}^{-1/2} (\underline{p}_o-\underline{p}_k) \end{bmatrix}$$

and $\underline{\underline{J}}$ is the Jacobian of $\underline{m}(\underline{p})$, i.e. $J_{ij} = \partial m_i/\partial p_j$. The above expression is derived in detail in Appendix B. It is an alternate form of the expressions given by Jackson [1979] or Tarantola and Valette [1982]. The *a posteriori* parameter covariance is given by

$$\underline{\underline{C}}_p = (\underline{\underline{A}}_k^T \underline{\underline{A}}_k)^{-1} \tag{2.3.3}$$

Note, (2.3.2) differs from the commonly used prescription

$$\underline{p}_{k+1} = \underline{p}_k + (\underline{\underline{J}}^T \underline{\underline{C}}_{d_o}^{-1} \underline{\underline{J}} + \underline{\underline{C}}_{p_o})^{-1} \underline{\underline{J}}_k^T \underline{\underline{C}}_{d_o}^{-1} [\underline{d} - \underline{m}(p_k)] \tag{2.3.4}$$

in the explicit use of the *a priori* parameter estimates. It was found that when using (2.3.4) the solution was extremely difficult to control and produced very undesirable results. The performance of (2.3.4) is particularly poor for noisy data when some model parameters are reasonably well known but others are not and the initial guess for the unknown parameters is far from the actual solution. After a few iterations, the better known parameters usually drift outside of their *a priori* bounds, even when a departure from the *a priori* values is not truly demanded by the data. On the other hand, the solution is easily controllable using (2.3.2).

In practice it is useful to control the size of the iteration steps by introducing a damping parameter $\varepsilon \underline{\underline{D}}_o$, where $\underline{\underline{D}}_o$ is a diagonal matrix and ε is the Marquardt parameter [Marquardt, 1963]. ε is reduced to zero upon converging to a solution,

$$\underline{p}_{k+1} = \underline{p}_k + (\underline{\underline{A}}_k^T \underline{\underline{A}}_k + \varepsilon \underline{\underline{D}}_o)^{-1} \{\underline{\underline{A}}_k^T \underline{f}_k\} \tag{2.3.5}$$

This practice reduces numerical errors and wild initial iterations. The choice of the components of $\underline{\underline{D}}_o$ is not statistically motivated; it should be inversely proportional to the square of the singular values of $\underline{\underline{A}}$, but the

exact values are not critical. For simple source models, the ratio of the largest to the smallest singular value of $\underline{A}$ is seldom greater than 30. I usually take $\underline{D}_o$ to be composed of the inverse of the square of the vector norms of the columns of $\underline{A}_o$, i.e., the "a posteriori" parameter variance estimates at the zero'th iteration (see equation 2.3.3).

In most cases we have no specific a priori information about the source parameters. In that case the a priori parameter variance is set to $\underline{C}_{p_o} = \sigma_p^2 \underline{I}$ with $\sigma_p^2 \to \infty$. Except for large, complicated events, the centroidal parameters are usually unique and sufficiently well determined [this thesis; Bergman, Nabelek, and Solomon, 1984] and a priori constraints are seldom required.

2.3.3 ERROR ANALYSIS

Because we have introduced a priori information about the model directly into the estimation, the resolution error vanishes [Jackson, 1979; and Tarantola and Valette, 1982]. The solution will stay at the a priori values unless it is required to change by the data. The a posteriori model parameter variance is always less or equal to the a priori model parameter variance. Only if the a posteriori variance is smaller than the a priori variance, do we gain more information about the parameter. Since in most of the inversions in this thesis, the model a priori variance is infinite, theoretically, the increase in knowledge is assured.

When applying a priori parameter constraints, correct estimates of the data uncertainty must also be made. In the studies presented in this thesis, the error of each digitized amplitude d_i of the observed seismograms is estimated using a formula

$$\sigma_i = \sigma_a + \sigma_m d_i \qquad (2.3.6)$$

where σ_a is the rms power of the background noise and σ_m, which accounts for the multiplicative errors, is assumed to be zero except for the New Brunswick earthquake (Chapter 4.3) where it was assumed to be 0.15. An *a posteriori* estimate of the data error can be made using formula (B8) of Appendix B.

Further discussion of the errors is deferred to Chapter III, where controlled tests of the quality of the inversions and the relations between the calculated parameter variances and the actual errors are conducted.

2.3.4 CALCULATION OF PARTIAL DERIVATIVES

The inversion procedures discussed above (i.e., equation 2.3.2) require calculation of the partial derivatives of the predicted seismograms with respect to the unknown model parameters. The formulas for the partial derivatives of the forward problem of equation (2.2.25) are given explicitly in Appendix B. Their main feature is that they are all simple weighted and time shifted sums of the elementary seismograms $H_i(t)$. It is mainly because of this simple construction of the synthetic seismograms and their derivatives that the inversion is carried out in the time domain.

2.4 DATA AND DATA PREPARATION

The data set in this thesis consists of P and S waves recorded on either the analog long- and short-period WWSSN (World Wide Standard Seismograph Network) or GDSN (Global Digital Seismograph Network) instruments. The GDSN stations are a network of former digital SRO and ASRO stations and WWSSN stations converted to the digital format. The response of these instruments (except for magnification) is very similar, with the peak gain at T=28s for the long-period instruments and T=1s for the short-period instruments. The analog WWSSN long-period instruments

have the peak response at the period of approximately T=15s. The short-period response is similar to a GDSN short-period response. The response curves for the above instruments are displayed in Figure 2.8.

The digital long- and short-period data are digitized at 1s and 0.05s time intervals, respectively. The analog data are hand-digitized and interpolated to equal time intervals (usually, 0.25 or 0.5s for the long-periods and 0.05s for the short-periods). In order to remove long-period trends and D.C. bias, all data are high-pass filtered with a zero phase 3-pole Butterworth filter with the cut-off outside of the range of significant power in the data. Using instruments with different characteristics adds stability to the inversion.

The data from different stations are equalized to a common instrument magnification and corrected for the differences in geometrical spreading. In addition to the weights based on background noise considerations, weights compensating for uneven station distribution are also applied. The details of this procedure are discussed in connection with the Lice earthquake in Chapter 4.2.3.

In some situations the errors in the absolute amplitude of the data from different stations are too large to furnish reliable information about the source. The shapes of the seismograms, however, may still be useful. In that case it is probably more appropriate to normalize the data amplitudes with respect to the $\sqrt{\text{power}}$ of the observed seismogram at a given station. Naturally, we must perform identical procedures for the theoretical seismograms. Under these circumstances, the results of an inversion should be similar to those done by trial-and-error techniques which commonly rely only on the shapes of the recorded waves. Due to the

loss of information, the convergence of the inversion using data with absolute amplitudes removed is considerably slower than when the full amplitude information is utilized.

FIGURE CAPTIONS

2.1 Slip and stress distribution for the dislocation and crack models (adopted from Madariaga [1981]).

2.2 Far-field P and S wave pulses from a circular crack model. θ is measured from the normal of the fault-plane (adopted from Madariaga [1976]).

2.3 Far-field seismic pulses from the two-barrier model P-SV-2 of Das and Aki [1977]. The model produces a strong directivity in the direction of rupture (adopted from Das and Aki [1977]).

2.4 The problem configuration for the determination of the Green's function of the teleseismic body waves. $\underline{g}^S(t)$ represents the effect of the earth's crust in the source region. $\underline{C}^R(t)$ is the effect of the crust under the receiver and M(t) in the mantle response. G, $A(f,t^*)$ and $\delta(t-t_m)$ and $\delta(t-t_m)$ represent contributions due to geometrical spreading, anelastic attenuation and travel time in the mantle, respectively.

2.5 Examples of the elementary seismograms $H_i(t)$ for teleseismic P waves using an oceanic structure. For a source at different depths within the same crustal layer, only the parent ray (dashed lines) travel time will vary. $H_i(t)$ represent the response of the earth to the parent ray together with the effect of a recording instrument and a source time function element.

2.6 Illustration of the source time function parameterization in terms of a series of box-functions and overlapping isosceles triangle functions.

2.7 Illustration of the effect of the rupture propagation along a thin fault with variable displacements upon the far-field seismic pulses. The effect is easily accounted for by varying the duration of $\Delta\tau'$.

2.8 The amplitude response curve for the WWSSN and GDSN instruments.

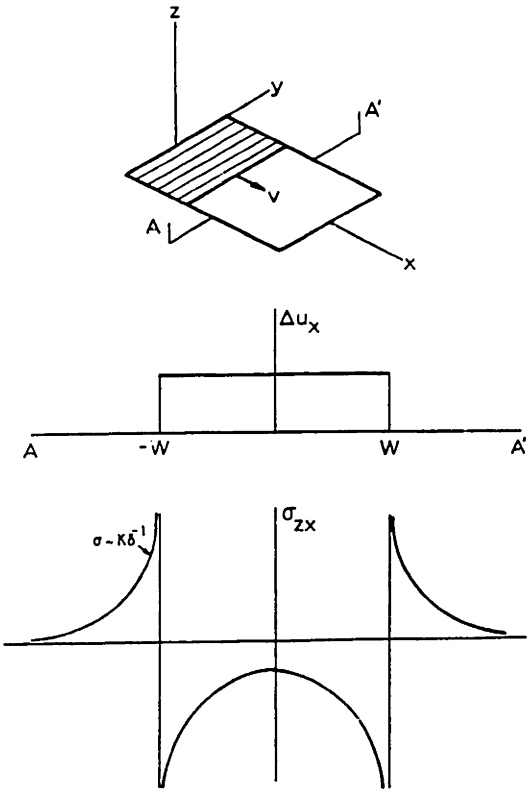

Haskell's rectangular dislocation model. At the top is shown the geometry of the rupture. At the center is the slip on the AA' cross-section. At the bottom is the stress change on the same section.

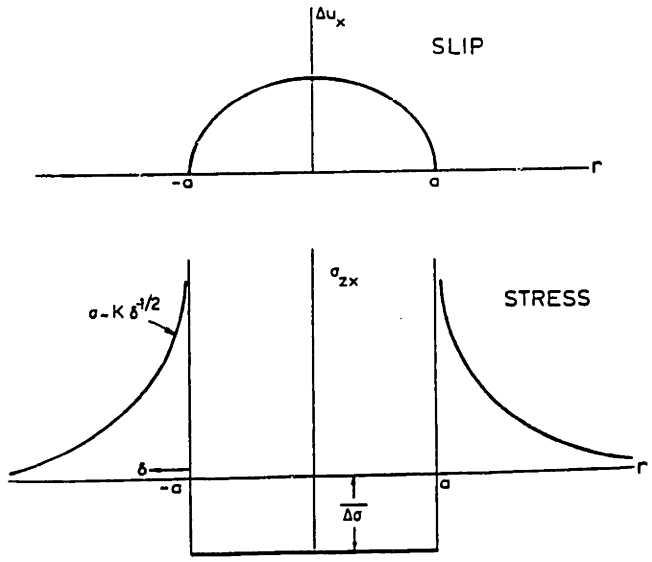

Slip and stress from a circular crack model of radius a. Stress drop inside the crack is uniform. Stress concentrations are seen outside the crack.

Figure 2.1

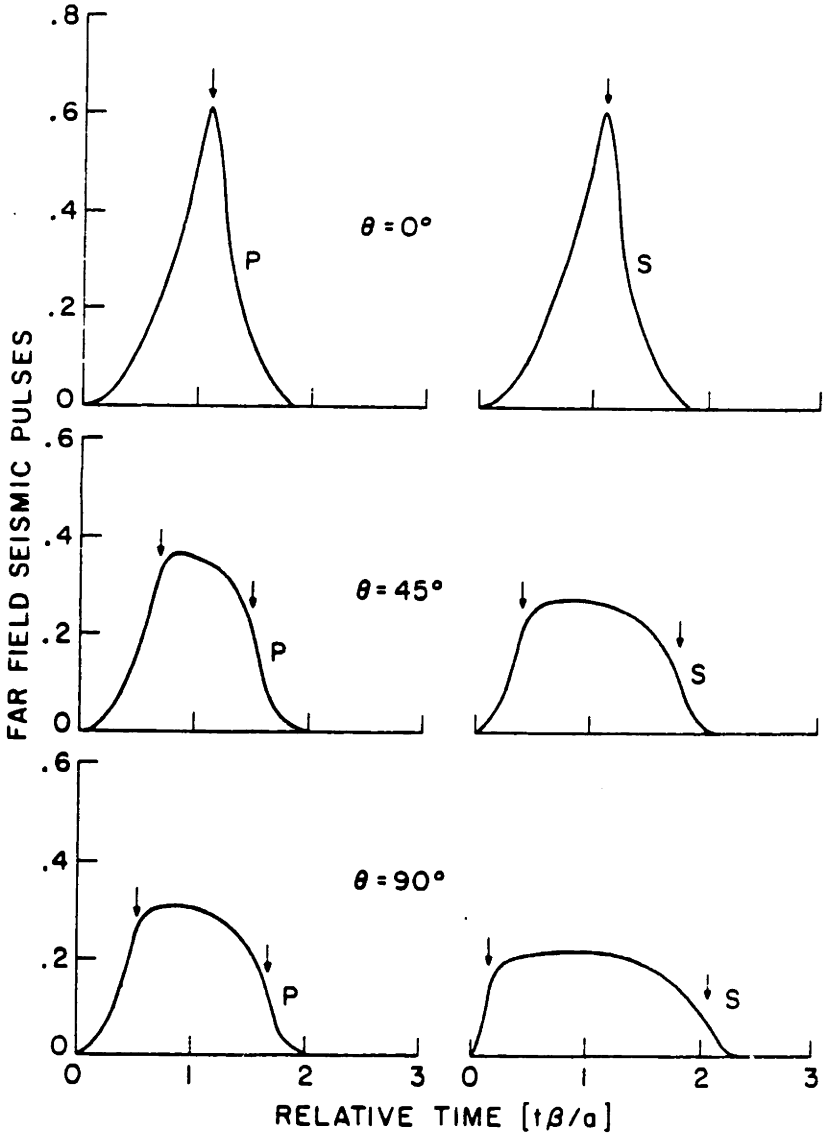
.8
.6
.4
.2
0
θ = 0°
P
S
.6
.4
.2
0
θ = 45°
P
S
.6
.4
.2
0
θ = 90°
P
S
FAR FIELD SEISMIC PULSES
0
1
2
3
0
1
2
3
RELATIVE TIME [tβ/a]

Figure 2.2

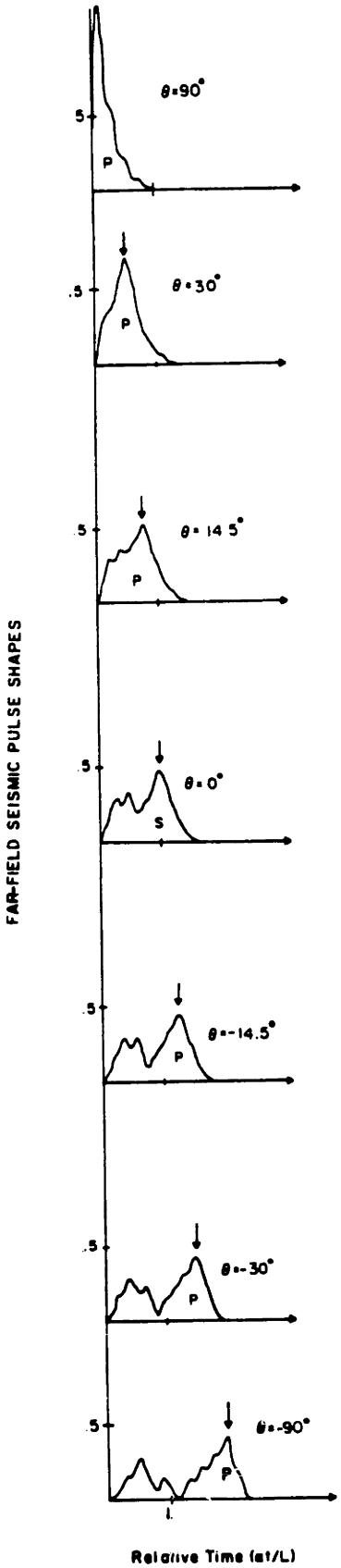
FAR-FIELD SEISMIC PULSE SHAPES
θ=90°
θ=30°
θ=14.5°
θ=0°
θ=-14.5°
θ=-30°
θ=-90°
P
S
.5
1.
Relative Time (at/L)

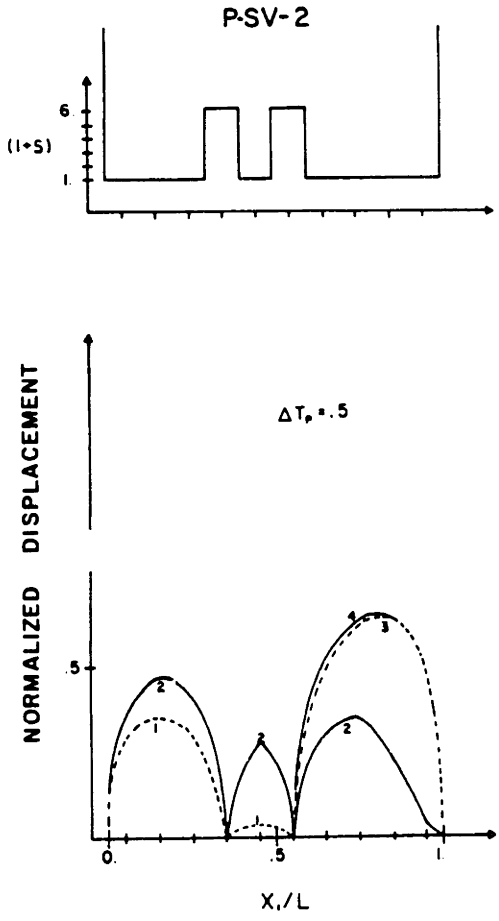
P-SV-2
6.
(1+S)
1.
NORMALIZED DISPLACEMENT
ΔTp=.5
.5
0.
.5
1.
X1/L

Figure 2.3

$$\underline{g}(t) = \underline{g}^{S}(t) * M(t) * \underline{C}^{R}(t)$$

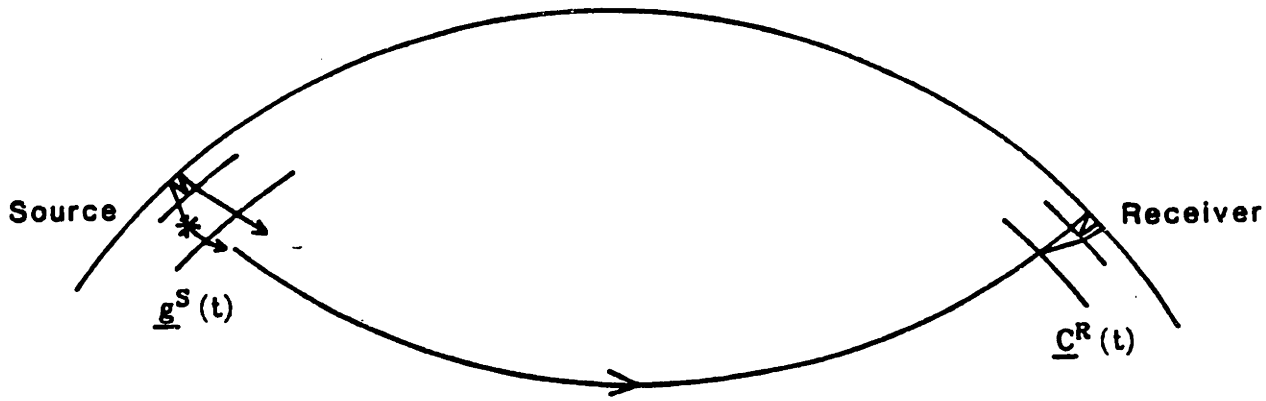

$$M(t) = G * A(t,t^{*}) * \delta(t-t_{m})$$

Figure 2.4

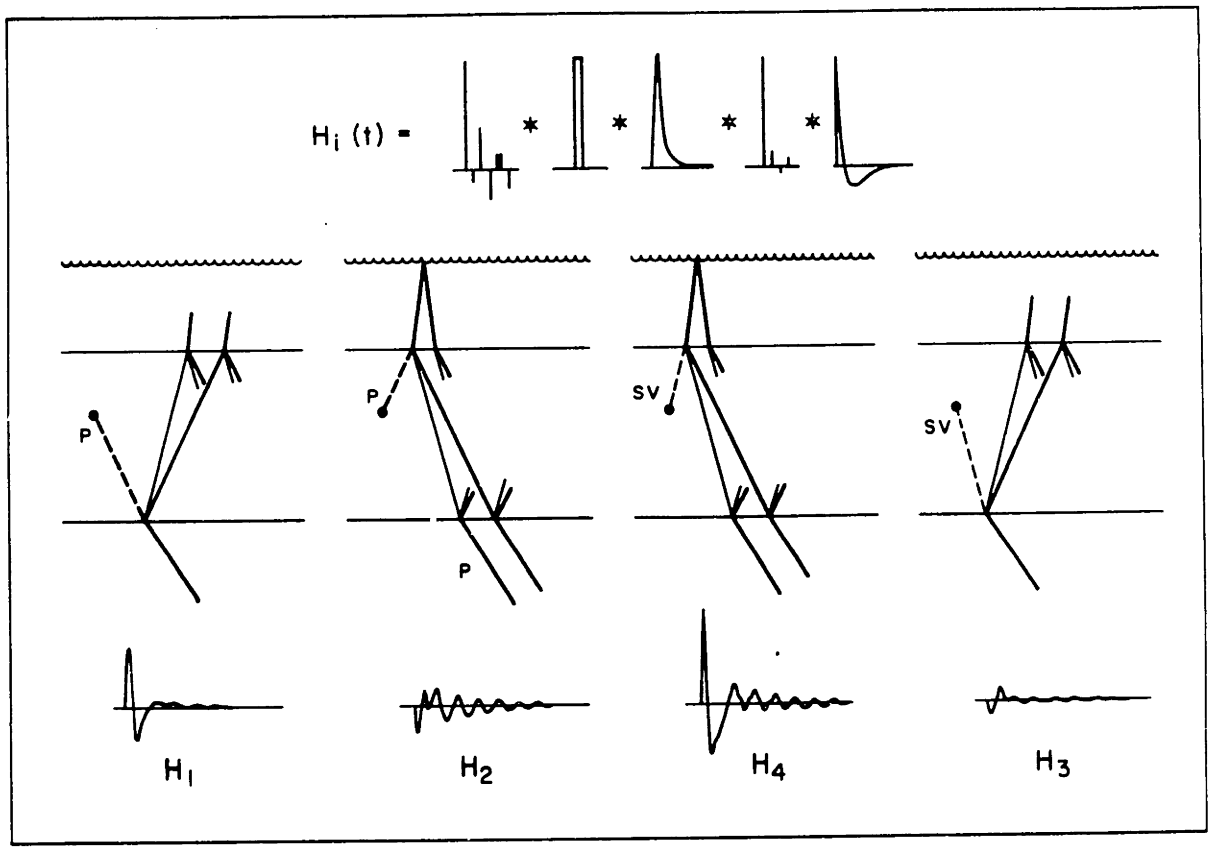

Figure 2.5

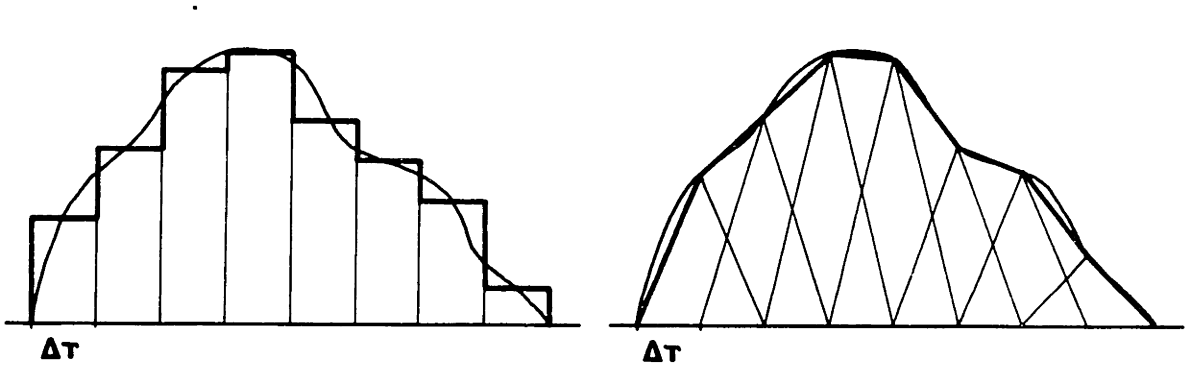

Figure 2.6

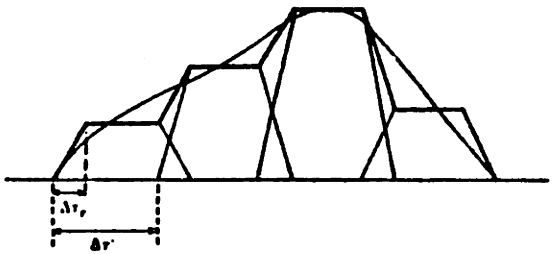

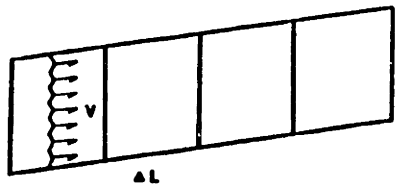

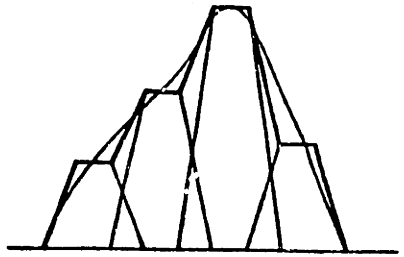

$$\Omega(t,\Theta) = \sum_k w_k T_{\Delta\tau'}(t-\tau_k)$$

$$T_{\Delta\tau'}(t) = B_{\Delta\tau'}(t) * B_{\Delta\tau_r}(t)$$

$$\Delta\tau' = \Delta\tau\,(1-vp\cos\Theta)$$

$$\Delta\tau = \Delta l / v$$

$$\tau_k = \Delta\tau'(k-1)$$

Figure 2.7

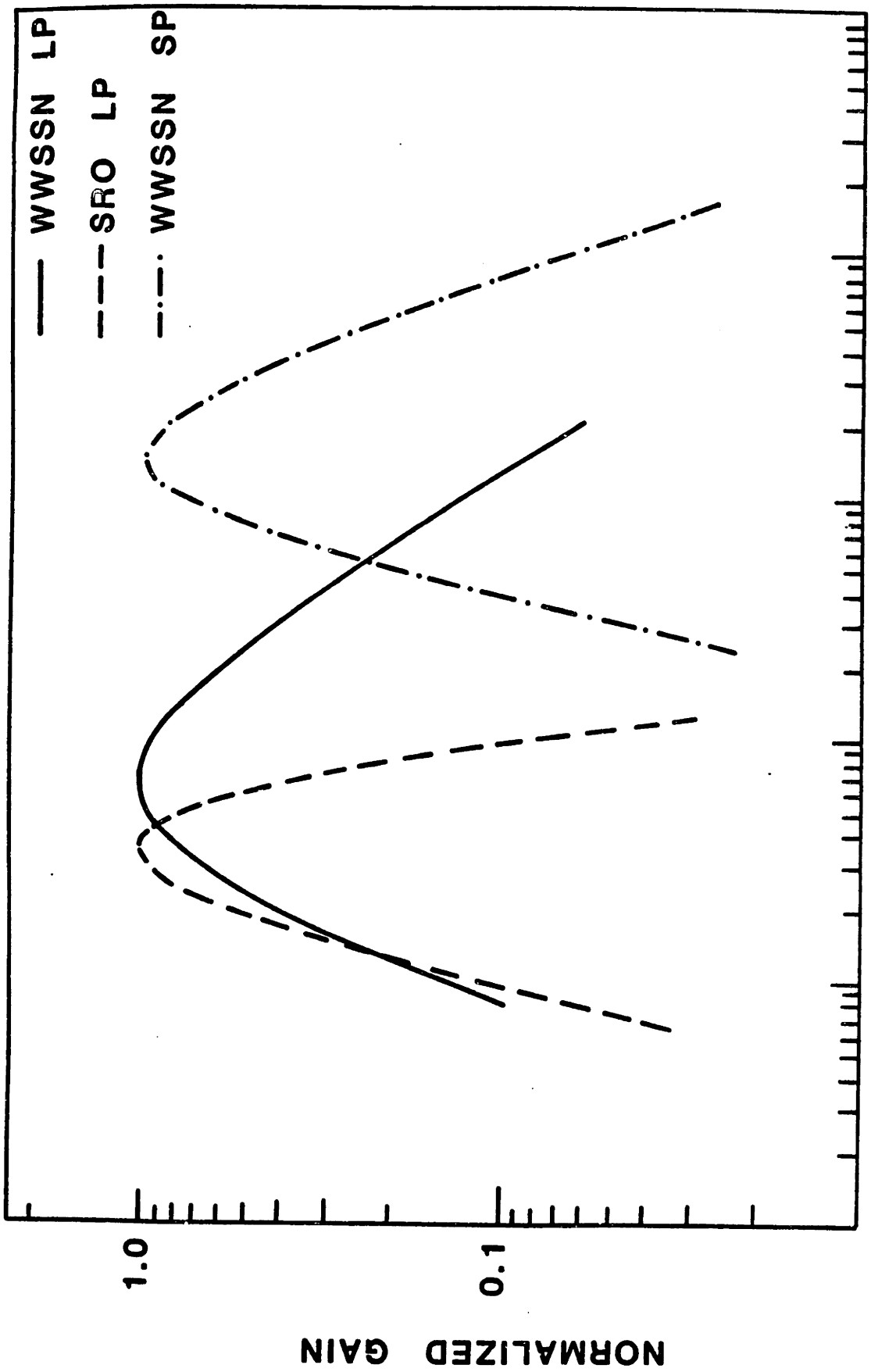
WWSSN LP
SRO LP
WWSSN SP
NORMALIZED GAIN
1.0
0.1
FREQUENCY (Hz)
0.01
0.1
1.0
10

Figure 2.8

CHAPTER III

RESOLUTION, ERRORS AND STABILITY - TESTS USING SYNTHETIC DATA

3.1 INTRODUCTION

This chapter discusses the practical limitations on resolving earthquake source parameters from body waves at teleseismic distances. Some of the theoretical limitations were discussed in Chapter II. The effects of non-Gaussian errors in the data on the least squares solution are also investigated. Numerical tests are conducted in order to investigate the biases introduced into the estimation of the centroidal source parameters by different source parameterizations in typical real-earth situations. These tests also give us an idea about the meaning of the formal errors when the conditions for their theoretical validity may not be strictly observed.

3.2 RESOLUTION OF THE SOURCE PARAMETERS

For most shallow earthquakes, the strongest effect which limits the resolution of the source mechanism, depth and the source time function is the interference between direct and surface reflected phases. If the source is deep and the direct and reflected phases are well separated in time, the resolution is mainly limited by the incomplete coverage of the focal sphere by teleseismic body waves. This limitation can be minimized by using both P and S waves in the analysis. Interference affects the resolution in a complicated manner.

A qualitative feel for different effects can be obtained by visual examination of the excitation functions $\underline{I}^0$, $\underline{I}^1$ and $\underline{I}^2$ (equation 2.2.17). The excitation functions for teleseismic P, SV and SH waves for two epicentral distance ranges and three different source depths are shown in

Figures 3.1a,b,c. The excitation functions were generated using a two layer Herrin crustal model [Herrin, 1968] in the source region and a half-space in the receiver region. An attenuation of t^* equal to 1 or 4s (typically observed values) was used for P waves and S waves, respectively. Due to higher attenuation, S waves lack the high-frequency resolution of P waves. The source time function is a step function. The major contributing phases to the teleseismic body wave response functions are P, pP and sP for the P wave packet, S, pS and sS for the SV wave packet, and S and sS for the SH wave packet. As the source depth increases, the phases become more separated in time.

Note the highly anomalous behavior of the SV wave at the epicentral distance of 35°. The large amplitude ringing is due to entrapment of the compressional wave energy in the crustal wave guide whose slow leakage as a converted SV wave is its only means of escape. These ringing SV waves are known as shear coupled PL waves or S_{PL} waves. Because of their strong dependence on crustal and upper mantle structure, their use in source studies is limited. Because of this same feature, however, their potential value for studies of crustal structure in the source region is great.

Since in most situations we deal with purely deviatoric sources, it is useful to enter this linear constraint directly into equation (2.2.17). The displacement of the P-SV coupled waves can then be expressed as

$$\begin{aligned} \underline{u}^{PSV}(\phi,\Delta,t) = \; & \underline{I}^{PSV2}[-\tfrac{1}{2}(M_{yy}-M_{xx})\cos 2\phi + M_{xy}\sin 2\phi] \\ & + \underline{I}^{PSV1}[M_{yz}\sin\phi + M_{xz}\cos\phi] \\ & + (\underline{I}^{PSV0} - \tfrac{1}{2}\underline{I}^{PSV2})M_{zz}. \end{aligned} \qquad (3.2.1)$$

The expression for the SH waves remains unchanged. The excitation function ($\underline{I}^{PSV0} - \frac{1}{2}\underline{I}^{PSV2}$) is also displayed in Figure 3.1.

From Figure 3.1 it is evident that the resolution of a certain source parameter depends to a large extent on the behavior of the other parameters. The following few paragraphs summarize the most important trade-offs between source parameters.

Resolution of Source Mechanism: The resolution of the M_{xx}, M_{yy} and M_{xy} moment tensor components depends on the behavior of the excitation function $\underline{I}^2$. $M_{yy}-M_{xx}$ and M_{xy} determine the strike-slip component of the source mechanism ($M_{yy}+M_{xx}$ is important in determining the isotropic component and will be discussed later). When only P waves are used in the analysis, the strike-slip source mechanism is the most difficult to resolve. The reason for this is two-fold: 1) Except for very shallow depths, the P-wave excitation function $\underline{I}^2$ is about three times smaller in amplitude than the $\underline{I}^1$, $\underline{I}^0$ or $\underline{I}^0 - \frac{1}{2}\underline{I}^2$, and 2) the radiation from $M_{yy}-M_{xx}$ and M_{xy} is π-periodic in azimuth, this is a higher periodicity than the azimuthal periodicity of M_{xz} and M_{yz} (2π) or M_{zz} (isotropic); the higher the azimuthal periodicity of a component, the more difficult it is to resolve with a sparse station distribution. The resolution of M_{xx}, M_{yy} and M_{xy} can be improved by using SH or surface waves (especially Love waves, Figure 3.2).

Resolution of M_{xz} and M_{yz}, i.e., the horizontal thrust or vertical dip-slip mechanism, depends on the behavior of $\underline{I}^1$. This excitation function vanishes at the earth's surface due to the stress free boundary condition. Consequently, resolution of M_{xz} and M_{yz} is difficult from very long period data. The M_{xz} and M_{yz} are usually the least resolved moment-tensor components in surface wave analyses. Because teleseismic body waves contain more high frequencies, resolution of M_{xz} and M_{yz} does

not usually pose any difficulty.

M_{zz} is usually the best resolved moment-tensor component from P wave data. Its radiation is azimuthally isotropic and the corresponding excitation functions $\underline{I}^0$ or $\underline{I}^0 - \frac{1}{2}\underline{I}^2$ are always of significant amplitude. The SH waves carry no information about M_{zz} or $M_{xx}+M_{yy}$ and cannot alone discriminate between a strike-slip or a 45° dipping dip-slip source mechanism. SH waves are, however, very helpful in determining the strike of a 45° dipping dip-slip fault because the P waves are dominated by the azimuthally isotropic radiation from the M_{zz} part of this mechanism and their resolution of the strike is poor (for the relation between geological fault parameters, strike, dip, and slip, and the moment-tensor see Aki and Richards [1980]).

The presence of the free surface also limits the resolvability of the isotropic component of the moment tensor. At the free surface $\underline{I}^0$ for the P-SV coupled waves equals $-\frac{1}{3}\underline{I}^2$. For waves which have much longer wavelengths compared to the depth of the source, equation 2.2.17a therefore reduces to

$$\underline{u} = \underline{I}^2[\tfrac{1}{2}(M_{xx}+M_{yy}) - \tfrac{1}{3}M_{zz} - \tfrac{1}{2}(M_{yy}-M_{xx})\cos 2\phi + M_{xy}\sin 2\phi] \qquad (3.2.2)$$

i.e., the relation between $M_{xx}+M_{yy}$ and M_{zz} cannot be resolved. This behavior of the $\underline{I}^0$ and $\underline{I}^2$ excitation functions as the source approaches earth's surface can be observed in Figure 3.1b; for the 0.5 km deep source the SV excitation functions $\underline{I}^0$ $\underline{I}^2$ and $\underline{I}^0 - \frac{1}{2}\underline{I}^2$ have essentially an identical shape. A similar behavior is seen for the Rayleigh wave excitation functions in Figure 3.2a. P waves are richer in high frequencies, and for the 0.5 km deep impulsive source the differences in

their excitation functions appear to still be sufficiently large that resolution of the moment tensor of an impulsive source using short-period data should be feasible.

The effect of the source duration is to broaden the observed seismic pulses and eliminate the high frequencies from the signal. This reduces resolvability of the M_{xz} and M_{yz} and isctropic components of the moment tensor but poses no serious problem in the resolution of the other components.

Resolution of Source Depth and Time Function: The resolution of the source depth hinges entirely on our ability to identify the signal contributions of the direct and the reflected phases from the free surface. In general any broadening and coalescence of the individual phases will result in the deterioration of the depth resolution. In practice, when the source duration becomes much larger than the travel time between the direct and reflected waves, the source depth becomes difficult to estimate.

The source depth is best resolved when the direct and reflected phases have opposite polarities. Unless we allow a back slip on the fault, a reversal in the polarity of a recorded pulse helps in identification of a reflected phase. The usual absence of a clear polarity reversal makes depth determination of shallow strike-slip events difficult. Except for pP which is small and usually buried in noise, for strike-slip events all other phases have the same polarity and we cannot easily distinguish between a simple source at a depth of, say, 10 km and a very shallow, multiple source (Figure 3.1). Unless pP can be clearly identified, one must usually make a decision which of the two solutions is more likely in a given situation.

Similar criteria apply to surface waves; the depth and time function effects are difficult to separate unless we observe a phase reversal with frequency (Figure 3.2).

Resolution of the Relative Location of the Source Centroid: The difficulties in resolving the source centroid location with respect to the source nucleation point are similar to those found in relative hypocenter location using the master event technique for teleseismic events. Due to steep take-off angles of the teleseismic body-waves, the vertical location should be better resolved compared to the horizontal location. On the other hand, we expect a trade-off between the source time function and the relative vertical location analogous to the origin-time v.s. depth trade-off in the master event techniques. For a good location, a complete azimuthal coverage is clearly required.

Effects of Source Finiteness: The simplest source parameterization used in this study is a point source with a varying source time function. The best fit point source for long-period waves is presumably located at the centroidal point of the actual source. Equation (2.2.15) tells us that by ignoring the source finiteness we are directly biasing the estimated source time function. The magnitude of the bias can be seen via the following simple examples.

(1) First we consider a unilateral horizontally propagating line source. The true far-field source time function in this case is a box function of duration $t_f = \frac{L}{v}$, where L is the length of the source and v the rupture velocity. The apparent duration, t, of the seismic pulse at a station at an azimuth, ϕ, with respect to the direction of the rupture is

$$t = L(\frac{1}{v} - p \cos\phi) = t_f(1 - vp \cos\phi)$$

where p is the ray parameter. With a good azimuthal station distribution,

the estimated point source time function $\hat{t}$ should approach the average of the apparent time functions over all azimuths. By carrying out the integration we obtain

$$\hat{t} = t_f(1 + \frac{1}{2} v^2 p^2)^{1/2}$$

Assuming $v=\beta$, $\alpha = \sqrt{3}\beta$ and 30° for average take-off angles of teleseismic waves, the estimated source duration using P and S waves will be

$$\hat{t} = 1.02\ t_f$$

$$\hat{t} = 1.06\ t_f$$

respectively. Thus for this type of rupture, the finiteness effect is on the order of a few percent and the estimated source time function is a good representation of the source time history.

(2) For a bilateral rupture, the true far-field time function duration is a box function of duration $t_f = \frac{L}{2v}$. The apparent duration measured at a given station is

$$t = t_f(1 + vp|\cos\phi|).$$

Averaging over all azimuths we obtain

$$\hat{t} = t_f(1 + 2vp + \frac{1}{2} v^2 p^2)^{1/2}.$$

The estimated source duration using P and S waves will therefore be

$$\hat{t} = 1.27\ t_f$$

$$\hat{t} = 1.46\ t_f$$

respectively. For a bilateral rupture the effect of finiteness significantly affects the estimated source time function. The estimated duration will be about 30-50% longer than the true rupture time. It should be pointed out that this is a rather extreme kinematic model which probably does not apply to most natural situations. It shows, however, that if slip occurs simultaneously at two distant points on the fault, the estimated source time function will be substantially smeared.

(3) As another extreme example we consider a case where the fault ruptures instantaneously along its full length, thus the true far field source time function is an impulse. Substituting $v \to \infty$ into the above equations we obtain

$$\hat{t} = \sqrt{2}\ Lp.$$

The apparent broadening of the P and S wave pulses due to an instantaneous rupture along a fault segment L is, therefore,

$$\hat{t} = 0.06L$$

$$\hat{t} = 0.10L$$

where L is measured in kilometers and $\hat{t}$ is measured in seconds. A 10 km long fault rupturing simultaneously will appear as a seismic pulse 0.6-1s long.

4) Due to steep take-off angles, the effect of source extent in the vertical direction on the source time function can be larger. Although the fault lengths of shallow earthquakes can be substantial, however, faulting in the earth's crust seldom extends deeper than 15 km. If the rupture propagates unilaterally in the vertical direction, the finiteness effect on the estimated source time function is averaged out between direct and reflected phases in a similar manner as we observed for the horizontal rupture.

5) For faults with large horizontal dimensions, the rupture along the vertical dimension may be essentially instantaneous. The effect of vertical finiteness can then be estimated analogously to (3), except that the ray parameter is replaced by the apparent vertical slowness of the P and S waves. The apparent broadening of the P and S wave pulses due to an instantaneous rupture along a fault of a vertical extent V is

$$\hat{t} = 0.10\ V$$

$$\hat{t} = 0.18\ V$$

respectively. For a fault extending from the surface to a depth of 15 km, the finiteness effect of such rupture on the source time function is, therefore, approximately 2-3s.

In general, although the effect of source finiteness and directivity due to rupture propagation may increase the high-frequency content of the signal in certain directions, when averaged over the focal sphere the effect is always to broaden the observed pulses. Under normal circumstances, the estimated point source time function is, therefore, always a smoothed version of the true time history.

3.3 EFFECTS OF BACKGROUND NOISE

Random background microseismic noise poses no serious problem for the inversions as long as the signal-to-noise ratio is large. The inversion techniques discussed in this study are based on a least-squares minimization of the differences between the data and the theoretical seismograms. In a linear problem, in the presence of Gaussian noise, the least-squares criterion gives an unbiased estimate of the parameters and the a posteriori estimate of the variance of the parameters gives an unbiased measure of their uncertainty. This should also hold for non-linear problems in the neighborhood of the true solution, but other relative minima may exist. For weakly non-linear and low-residual problems, the a posteriori parameter variance should give a good estimate of the uncertainties of the solution; otherwise other tests of the correctness of the solution are required. In our problem, the most non-linear parameter is the source depth. The formal error (variance) may, therefore, not always give the true uncertainty in the estimated value (it may be either higher or lower).

3.4 EFFECTS OF MULTIPLICATIVE AND PHASE ERRORS

The multiplicative (signal generated) errors, such as errors in the instrument magnification, in the receiver crustal response, or in the geometrical spreading pose more serious problems to the least-squares solution. If the probability distribution of the error is such that there is an equal chance of having a factor of e^N error or a factor of $1/e^N$ error, the least-squares criterion will give a biased solution for the strength of the source. Expressing the observed motion as $o(t) = e^{\pm N} y(t)$, where $e^{\pm N}$ is the multiplicative error and $y(t)$ is the motion if no errors were present, the average motion determined by the least squares criterion will be $\hat{y}(t) = \frac{(e^N + e^{-N})}{2} y(t)$

$$\hat{y}(t) = \frac{(e^N + e^{-N})}{2} y(t) = (1 + \frac{1}{2} N^2 + \ldots) y(t),$$

i.e., the estimated source strength will be overestimated. Patton and Aki [1979] made an extensive investigation of effects of multiplicative errors on the moment tensor estimates from surface waves. Although their analysis was conducted in the frequency domain, their conclusions apply verbatim to the time domain body wave analysis.

Patton and Aki [1979] also investigated the effect of multipathing and showed that at long-periods, to the first order, it causes multiplicative type errors. Small departures from our assumption that teleseismic body waves are well described by a single ray parameter will therefore manifest themselves as multiplicative noise.

Similarly, the results of Patton and Aki's investigation on the effects of phase incoherence of the signal on the inversion in the frequency domain apply equally to the time domain analysis. The phase incoherence between the observed and theoretical seismograms, in general,

causes an underestimation of the strength of the source.

3.4 NUMERICAL SIMULATIONS

The main purpose of the following numerical tests is to investigate the ability of different source parameterizations to recover the correct centroidal parameters of a finite fault. The tests are conducted on synthetic data which were generated for three finite fault models by numerical integration of point sources. The technique used to generate the synthetic long-period WWSSN and SRO data is described in Trehu, Nabelek and Solomon [1981] (Appendix G). In all examples only P waves are used.

Most of the basic tests are conducted on the first model (model M1) which is a rectangular source with the rupture spreading radially from its nucleation point. This model simulates simple large magnitude events with fault dimensions of the order of 10-20 km. The effect of the fault plane curvature on point source solutions is investigated using the second model (model M2) which is similar to model M1 except that the fault surface bends by 30° half way along its length. The third model (model M3) simulates a large complex event; it is a 48 km long, horizontal line source with a unilateral rupture and a 30-degree bend. We shall attempt to recover the point source parameters of its two segments.

The focal sphere coverage by the stations used in these numerical simulations is displayed in Figure 3.3. The station parameters and the crustal structure used in the calculations are summarized in Table 3.1. In all examples, the seismograms are sampled at 0.5s time intervals. The results of the following inversions are summarized in Table 3.3.

Inversion 1M1: In this inversion, the complete set of point source parameters (equation 2.2.25) of model M1 is estimated using data generated for WWSSN instruments. The model is shown in Figure 3.4 and its parameters (including its centroidal values) are summarized in Table 3.2. The model is a 25 km long and 11 km wide north-south oriented strike-slip fault with a dip of 80° E. The depth to the top of the fault is 2 km. The rupture initiates in the bottom of the southern end and spreads radially with a velocity of 3 km/s. The correct centroidal values to which the solution should converge (under ideal conditions and perfect station coverage) are: seismic moment = 1, strike = 0°, dip = 80°, rake = 0°, and depth 7.42 km. The source centroid is 11 km north, 2.95 km above and at an azimuth of 5° from the nucleation point.

The estimated best-fit model parameters are given in Table 3.3. The inversion gives the correct estimate of the seismic moment and the centroid's vertical distance from the nucleation point. The error in the source orientation is less than 1°. The centroid depth is over estimated by less than 0.5 km. Its azimuth from the nucleation point is in error by 2° and the horizontal distance is underestimated by 4.3 km.

Because of the steep take-off angles of the teleseismic P waves, we expect the estimate of the relative horizontal location of the centroid to be most susceptible to noise and incomplete station coverage; therefore, in many cases the recovery of the relative position of the nucleation and the centroidal points may be difficult, especially for smaller events.

In this inversion, and all subsequent inversions using WWSSN data, the triangular source time function parameterization with $\Delta\tau$ of 1.5s is used ($\Delta\tau$ of 3s is used with the SRO data). The estimated source time function for this inversion is shown in Figure 3.6a. The true "point source" time function for model M1 is also shown, it was calculated using the formula

$$\Omega(t) = \int_{\Sigma} \dot{\bar{u}}(t,\underline{\xi})d\Sigma_{\xi}$$

where $\dot{\bar{u}}(t,\underline{\xi})$ is the time derivative of the slip function.

Inversion 2M1. This inversion mimics the procedures used in most of the applications in this thesis. The initial point of the seismograms is assumed to be unknown and the alignment of the data with the synthetics is achieved by a cross-correlation. This inversion results in a -3° error in the estimated rake of the slip angle, and the centroid depth is overestimated by 1 km.

Inversion 3M1: This inversion is identical to inversion 1M1 except that the SRO data is used. The data and the seismograms for the best-fit point source model are shown in Figure 3.5b. The depth is overestimated by 1.4 km. The relative location of the nucleation and the centroidal points is reasonably well determined. The estimated source time function is shown in Figure 3.6a.

Inversion 4M1: In this inversion we assumed that the correct alignment of the data with the theoretical point source seismograms is given by the first motions. This assumption seriously affects only the source time function estimate (Figure 3.6b); the source duration is significantly overestimated.

Inversion 5M1: This inversion is identical to inversion 4M1 except that SRO data are used; the errors are slightly larger.

Inversion 6M1: In this inversion only the first two terms (up to total degree 1) of the Taylor series expansion of the moment tensor density are determined (the source strength, mechanism and the centroid time and location). Since we ignore the source duration, this parameterization is appropriate only for very long-period data (it is analogous to the inversion scheme of Dziewonski et al. [1981]). The match to the SRO data by the theoretical seimograms for the model found in this inversion are shown in Figure 3.5c. Visually, the match is almost indistinguishable from the one obtained in inversion 3M1. The estimated centroidal parameters are, however, substantially more in error. The error in fault dip is 4.3°, the seismic moment is underestimated by 5% and the centroid depth is overestimated by almost 4 km.

Inversion 7M1: This inversion illustrates the necessity of determining the centroid time and horizontal location if an unbiased estimate of source depth and mechanism are desired. In this inversion the far-field source time function is an impulse at the nucleation point and is not allowed to vary. Based on equation (2.2.15), the error in the centroid time should result in a bias in the depth estimate. Indeed, the inversion resulted in a 7.5-degree error in the estimated fault dip, a 14% error in the seismic moment, and the centroid depth was overestimated by more than 10 km. The match of the theoretical seismograms corresponding to this model to the data is displayed in Figure 3.5d.

Inversion 8M1: The purpose of this inversion is to estimate the effect of data errors which occur typically in "real earth" applications. In addition to source finiteness which appears as a data error in the estimation of point source properties, the data were contaminated by ±4° errors in station azimuths, ±3° errors in take-off angles, ±1s alignment errors (i.e., errors in determining the arrival time of the direct P wave from the short-period records). Multiplicative errors of a factor of 1.15 and 1/1.15 were also introduced. A sample of microseismic noise from WWSSN seismograms was digitized and added to the synthetic data. The r.m.s. amplitude of the added background noise is 15% of the r.m.s. amplitude of all the data. The data errors assigned to each station are given in Table 3.4.

With this rather severe noise contamination, the largest error occurs in the estimation of the horizontal location of the centroid, rendering this estimate practically meaningless. This severe error is not surprising and is mainly due to misalignments; the ±1s errors in the alignment that were arbitrarily introduced are greater than the maximum time shifts caused by the horizontal distance of 11 km from the nucleation point to the centroidal point and dominate the coherent information in the signal. The estimation error in the other parameters is: -2.8° in strike, 0.9° in dip, -0.7° in rake, 1% in seismic moment and 2 km in centroidal depth.

In general, these errors are larger than the formal uncertainties (2 standard deviations) of the estimated parameters as shown in Table 3.3. The only parameter for which the error in the estimated value is smaller than the formal uncertainty is the seismic moment, which is also the only linear parameter. On the basis of these results, it appears that 10 standard deviations are more representative of the uncertainty in the

non-linear parameters.

In order to investigate the effect of fault curvature on the estimated point source parameters, the inversions were performed on data corresponding to model M2 (Figure 3.7, Table 3.5). The fault dimensions of this model are similar to those of model M1. The main difference between these two models is the 30° bend in the fault plane half-way along the fault length. The source mechanism is a vertical strike-slip. The centroidal parameters for this model that we expect to recover using long-period data and point source approximation are: strike 15°, dip 90°, rake 0°, seismic moment 0.87, and depth 7.5 km. Note that although the seismic moment of each segment is 0.5, the total is not 1.0 but a value given by the scalar moment of the tensor sum of the moment tensors of each segment. The combined mechanism is a pure vertical strike-slip fault with the strike given by the average of the strikes of the two segments. Summaries of the following two inversions are given in Table 3.6.

Inversion 1M2: This inversion uses WWSSN data. Due to the curvature of the fault, the theoretical seismograms for the average solution give a poor match to the data for stations near the nodes of the radiation patterns of the two fault segments (e.g., stations S1 and S7, Figure 3.8). The estimated average fault parameters are nevertheless in good agreement with the expected values (Table 3.6).

Inversion 2M2: This inversion is identical to inversion 1M2 except that the SRO data are used. The results are similar to those obtained using WWSSN data.

In order to investigate our ability to recover point source parameters of segments of faults of large complex events, synthetic data using a two segment line source model M3 (Figure 3.8, Table 3.7) are generated. Each

segment of the source is 24 km long. The rupture is unilateral, initiating at the southern end of the north-south oriented segment. The rupture takes a 30° turn as it reaches the second segment. The centroidal values that we hope to recover using WWSSN data are given in Table 3.7. The source time function of each segment is parameterized by 5 box-cars of 2s duration each. In order to investigate the accuracy to which the time functions can be determined, they are allowed to take on longer durations than the known duration of the rupture on each segment.

The results of the inversion are shown in Table 3.8 and the seismograms are displayed in Figure 3.10. Except for the position of the centroidal point of the first segment with respect to the nucleation point and the time delay of the second segment, all the other parameters are determined correctly. Because of the short distance from the centroidal point of the first segment to the nucleation point, the uncertainty in its location (especially its azimuth) is large (see formal errors). The position of the centroid of the more distant second segment is better determined.

The correct and the estimated point source time functions for the two segments are displayed in Figure 3.11. We observe some overlap and trade-off between the two time functions but the overall fit is good.

3.6 SUMMARY

In summary, the above results indicate that in the absence of serious noise contamination and in the presence adequate station distribution (8-12 azimuthally distributed stations) teleseismic P waves carry sufficient information to determine the basic centroidal parameters of the source. Use of S waves should further help in constraining the source parameters.

The average source mechanism and the seismic moment are the source parameters which are the least sensitive to noise contamination. The centroid depth can be recovered to within ±2 km accuracy using long-period WWSSN and GDSN data if an estimate of source duration is also made. Inversions using only the first two terms of the Taylor series expansion result in significantly poorer estimates of the centroidal parameters of the source (the depth being biased towards larger values). Even a rough measure of the source duration can significantly improve the estimates of the lower order terms of the expansion.

For events of large dimensions, the estimate of the centroid location with respect to the nucleation point appears to be feasible. Inclusion of even a few S waves for which first motions can be unambiguously determined would greatly improve resolution of the relative location.

For large events, with energy release on fault planes of different orientations, the average parameters of the individual faults segments can be determined. For smaller complex events, the resolution of the individual fault segments using long-period data may not be feasible. In that case, however, although the matches to the data at the nodal stations may be particularly poor because the first motions of the average model are probably not of the same polarity as those observed in the actual data, the estimated parameters accurately correspond to the tensor sum of the moment-tensors of the individual fault segments.

Table 3.1 The Station Parameters and the Crustal Structure Used in the Numerical Simulations

Station	Azimuth (deg)	Take-off Angle (deg)
S1	10	30
S2	45	20
S3	70	35
S4	95	15
S5	130	25
S6	160	20
S7	190	35
S8	210	30
S9	250	25
S10	290	20
S11	330	15
S12	350	25

Crustal Structure in the Source and Receiver Regions:

V_p = 6.0 km/s V_s = 3.46 km/s density = 3.0 g/cm^3

t^* = 1.0s

Table 3.2 Parameters of the Finite Fault Model M1

M_o = 1

Strike = 0°

Dip = 80°

Rake = 0°

Depth to the top of the fault = 2 km

Length = 25 km

Width = 11 km

Nucleation point: 2 km along strike; 9 km down along width

Rupture velocity (circular rupture) = 3 km/s

Centroid location:

Depth (relative to the surface) = 7.42 km

Vertical distance* = -2.95 km

Horizontal distance* = 11.0 km

Azimuth* = 5.0°

*Relative to the nucleation point

Table 3.3 Results of the Inversions for the Centroidal Parameters of the Finite Fault Model M1*

Inversion**	Strike (deg)	Dip (deg)	Rake (deg)	M_o	Depth (km)	V-dis (km)	H-dis (km)	Azimuth (deg)
1M1†	0.2±0.4	80.8±0.4	-0.9±0.4	1.00±0.05	7.9±0.2	-2.9±0.9	6.7±0.8	7±9
2M1	0.2±0.3	80.5±0.4	-3.0±0.3	1.01±0.04	8.4±0.2			
3M1†	0.4±0.0	82.0±0.3	-0.3±0.1	0.99±0.04	8.8±0.2	-3.2±0.2	10.2±0.4	-3±2
4M1†	-0.7±0.4	80.8±0.6	-2.4±0.4	1.03±0.05	7.6±0.3			
5M1†	-0.5±0.2	82.1±0.6	-2.6±0.2	1.00±0.08	8.2±0.6			
6M1	0.5±0.0	84.3±0.0	-0.0±0.0	0.95±0.01	11.2±0.1		11 ±1	-1±1
7M1	-0.3±0.6	87.5±0.2	-0.6±0.2	1.14±0.03	17.9±0.2			
8M1	-2.8±0.6	80.9±0.5	-0.7±0.4	1.01±0.06	9.4±0.2	0.4±1.2	13 ±1	82±4

* correct centroidal values are shown in Table 3.2.

† fit to the source time function is shown in Figure 3.6

** 1M1 - inversion for all parameters; WWSSN instrument
2M1 - inversion with alignment by cross-correlation; WWSSN instrument
3M1 - same as 1M1; SRO instrument
4M1 - inversion assuming coincident nucleation and centroidal point (i.e. ρ=0); WWSSN instrument
5M1 - same as 4M1; SRO instrument
6M1 - inversion using centroid time, analogous to Dziewonski et al. [1981]; the centroid time delay was 5.1±0.1s; SRO instrument
7M1 - inversion with an impulse source at t=0, ρ=0; SRO instrument
8M1 - inversion for all parameters with typical noises in the data; WWSSN instrument

Quoted uncertainties represent 2 standard deviations

Table 3.4 Errors Introduced to the Data in Inversion 8M1

Station	Azimuth error (deg)	Take-off angle error (deg)	Magnification error (factor)	Alignment error (sec)
S1	+4	0	0.87	0
S2	0	+3	1.15	-1
S3	-4	-3	1.00	+1
S4	0	+3	1.15	-1
S5	-4	-3	1.00	+1
S6	+4	0	0.87	0
S7	-4	-3	1.00	+1
S8	+4	0	0.87	0
S9	0	+3	1.15	-1
S10	+4	0	0.87	0
S11	0	+3	1.15	-1
S12	-4	-3	1.00	+1

A sample of the recorded microseismic noise from WWSSN stations was added to the data. The rms amplitude of the noise was 15% of the rms amplitude of all the data. The data was generated for the finite fault model M1.

Table 3.5 Parameters of the Two-segment Finite Fault Model M2

	Segment 1	Segment 2
M_o	0.5	0.5
Strike (deg)	0	30
Dip (deg)	90	90
Rake (deg)	0	0
Depth to the top of the fault (km)	2	2
Length (km)	11	11
Width (km)	11	11

Nucleation point: 2 km along strike of segment 1;
9 km down along width

Rupture velocity (circular rupture) = 3 km/s

Centroid parameters:

Strike = 15°

Dip = 90°

Rake = 0°

M_o = 0.87

Depth (relative to the free surface) = 7.5 km

Table 3.6 Results of the Inversions For the Centroidal Parameters of the Two-segment Finite Fault Model M2*

Inversion**	Strike (deg)	Dip (deg)	Rake (deg)	M_o	Depth (km)
1M2	13.2±0.5	89.4±0.4	-1.2±0.5	0.85±0.12	6.9±0.4
2M2	14.3±0.3	89.1±0.3	-1.7±0.5	0.87±0.10	8.4±1.4

* correct centroidal values are shown in Table 3.5

** 1M2 WWSSN instrument; 2M2 SRO instrument

Quoted uncertainties represent 2 standard deviations

Table 3.7. Parameters of the Two-segment Horizontal Line Source Model M3.

	Segment 1	Segment 2
M_o	0.5	0.5
Strike (deg)	0	30
Dip (deg)	90	90
Rake (deg)	0	0
Depth (km)	10	10
Length (km)	24	24
Rupture Velocity (km/s)	3	3
Time Delay* (s)		8
Centroid Location:		
Depth* (km)	10	10
Horizontal Distance* (km)	12	35
Azimuth* (deg)	0	10

* Relative to the nucleation point

Table 3.8 Results of the Inversion for the Centroidal Parameters of the Two-segments of the Horizontal Line Source Model M3 (Inversion M3)†

	Segment 1	Segment 2
M_o	0.52± 0.01	0.47±0.01
Strike (deg)	0.9 ± 0.4	30.1 ±0.4
Dip (deg)	90.6 ± 0.2	90.5 ±0.2
Rake (deg)	-0.3 ± 0.3	1.0 ±0.2
Depth (km)	9.9 ± 0.3	10.2 ±0.2
Azimuth* (deg)	-1 ±10	12 ±1
H-distance* (km)	6 ± 1	37 ±1
V-distance* (km)	4 ± 1	
Time delay* (s)		6.9 ±0.1

† Correct centroidal values are shown in Table 3.7

* With respect to the nucleation point

Quoted uncertainties represent 2 standard deviations

FIGURE CAPTIONS

3.1 The excitation functions I^0, I^1 and I^2 of teleseismic body waves calculated for different source depths and epicentral distances. Also shown is the excitation function $I^0 - \frac{1}{2}I^2$ which is used for purely deviatoric sources. The relative maximum amplitude of each trace is indicated.

(a) P waves

(b) SV waves

(c) SH waves

3.2 The Fourier transforms of the excitation functions I^0, I^1 and I^2 of surface waves for various source depths (adopted from North and Fitch [1980]).

(a) Rayleigh waves

(b) Love waves

3.3 Station distribution used in the numerical simulations. The nodal planes shown are for model M1.

3.4 The finite fault model M1. The position of the centroid and the nucleation point is indicated by the star, and the solid circle, respectively.

3.5 Data (solid lines) and the corresponding best-fit seismograms (dashed lines):

(a) for inversion 1M1

(b) for inversion 3M1

(c) for inversion 6M1

(d) for inversion 7M1

(e) for inversion 8M1

3.6 (a) The true point source time function for model M1 (heavy solid line) and the source time functions estimated in inversions 1M1 (light solid line) and 3M1 (dashed line). The centroid time estimated in inversion 6M1 is indicated by the vertical line.

(b) The source time functions estimated in inversions 4M1 (light solid line) and 5M1 (dashed line).

3.7 The finite two-segment model M2.

3.8 The data (solid lines) and the corresponding best-fit seismograms for inversion 1M2.

3.9 The two-segment line source model M3.

3.10 The data (solid lines) and the corresponding best-fit seismograms for inversion M3.

3.11 The true point source time functions of the two line segments of model M3 (heavy solid line). The estimated source time functions (inversion M3) of segment 1 and 2 are indicated by the light solid and dashed line, respectively.

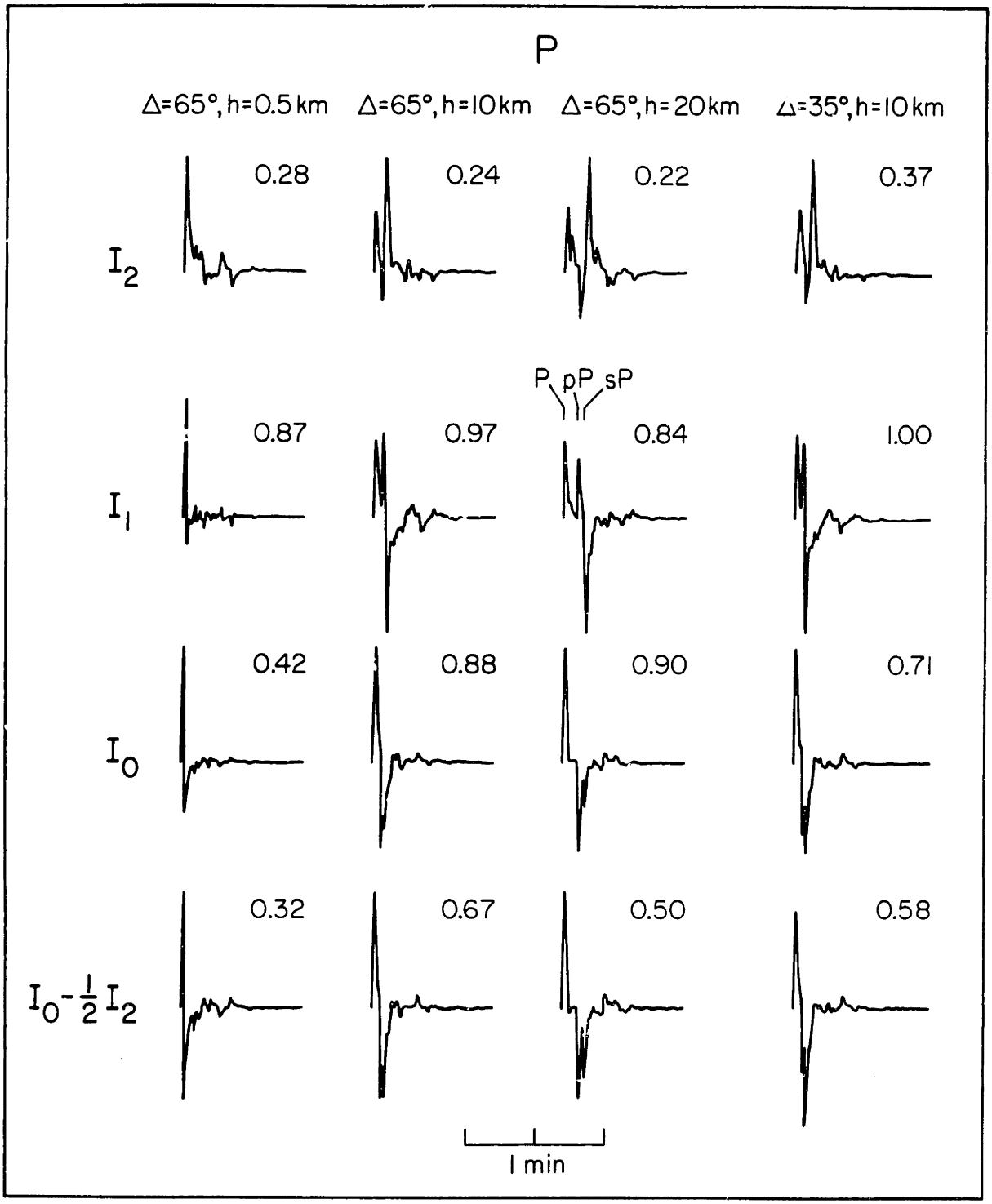
P
Δ=65°, h=0.5 km
Δ=65°, h=10 km
Δ=65°, h=20 km
Δ=35°, h=10 km
0.28
0.24
0.22
0.37
I_2
P pP sP
0.87
0.97
0.84
1.00
I_1
0.42
0.88
0.90
0.71
I_0
0.32
0.67
0.50
0.58
$I_0 - \frac{1}{2} I_2$
1 min

Figure 3.1a

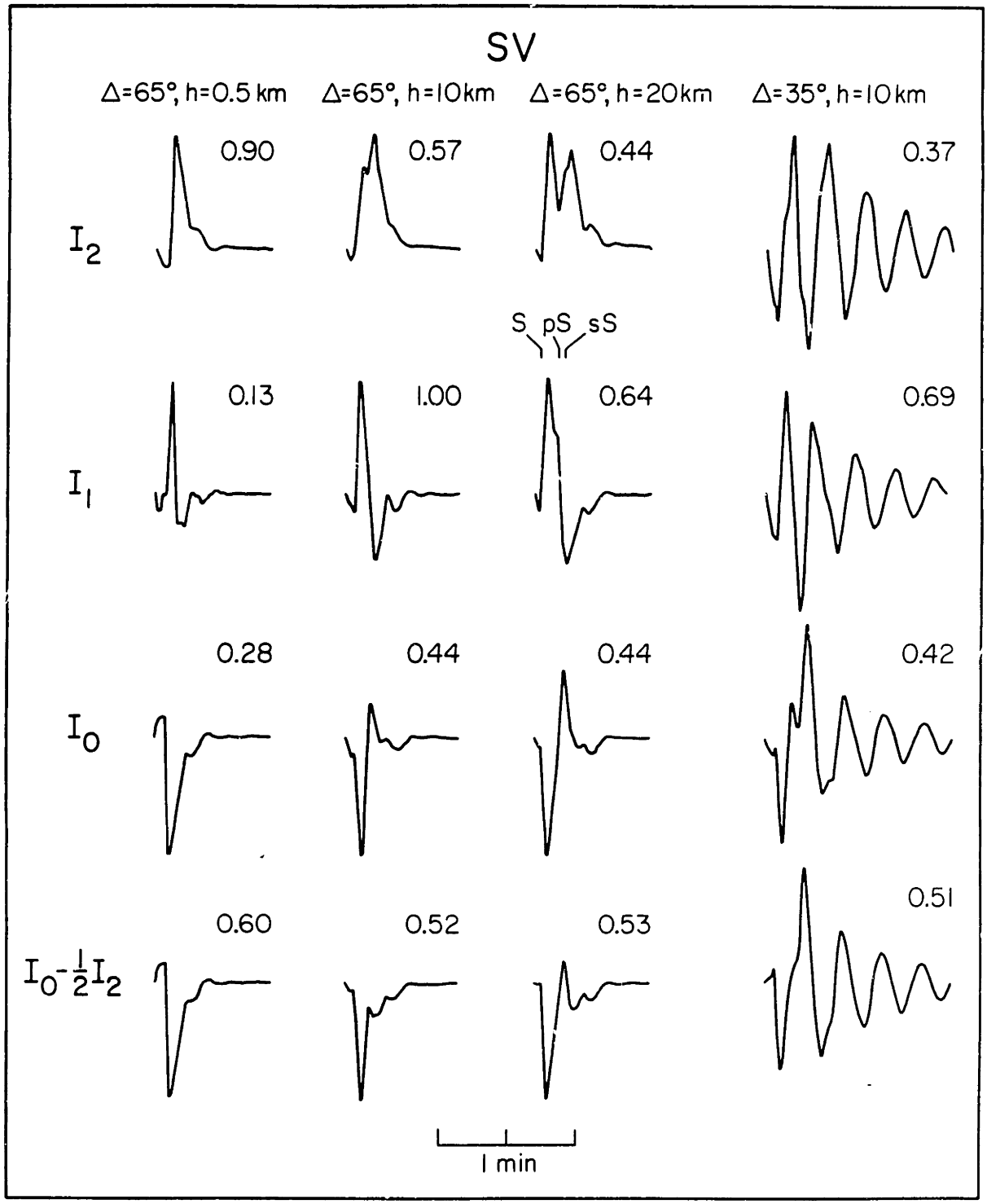
SV
Δ=65°, h=0.5 km
Δ=65°, h=10km
Δ=65°, h=20km
Δ=35°, h=10km
0.90
0.57
0.44
0.37
I_2
S pS sS
0.13
1.00
0.64
0.69
I_1
0.28
0.44
0.44
0.42
I_0
0.51
0.60
0.52
0.53
$I_0-\frac{1}{2}I_2$
1 min

Figure 3.1b


SH
Δ=65°, h=0.5km
Δ=65°, h=10km
Δ=65°, h=20km
Δ=35°, h=10km
0.88
0.54
0.42
0.56
I2
S
sS
0.21
1.00
0.78
0.91
I1
1 min

Figure 3.1c

Rayleigh

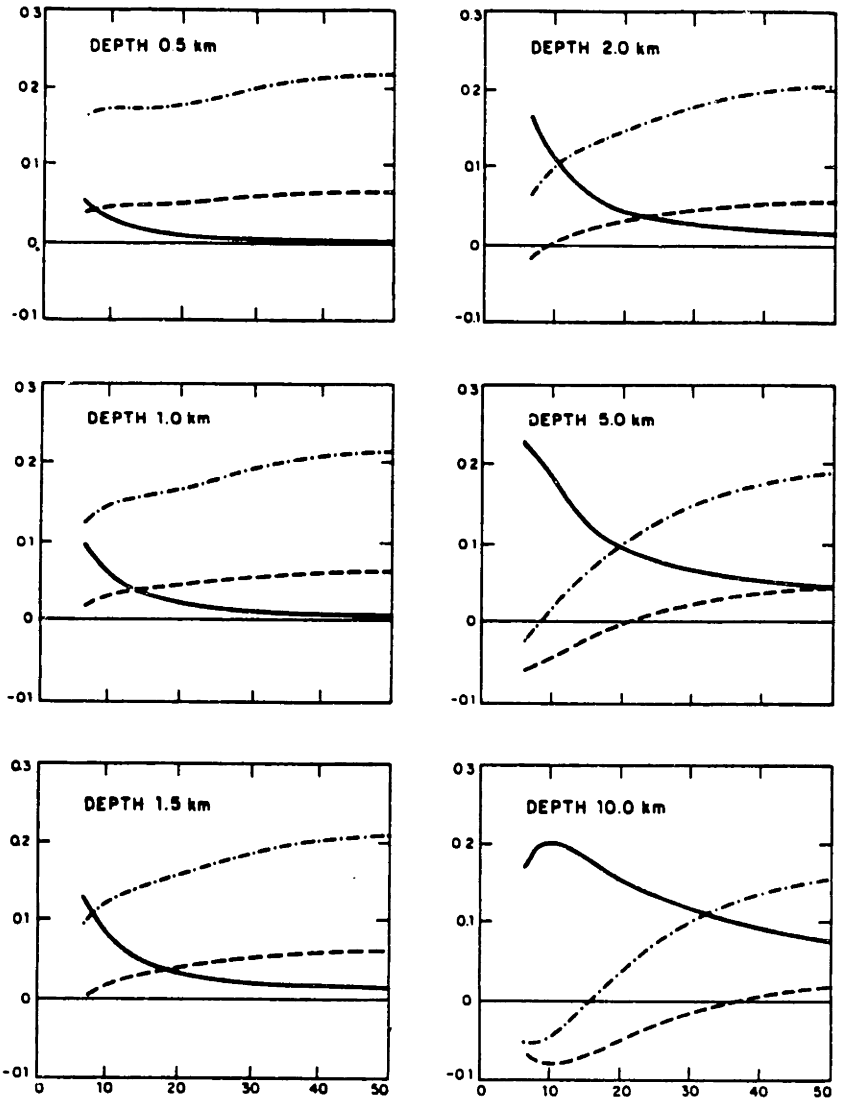

$I_2(\omega)$ ——·——·——

$i\ I_1(\omega)$ ————————

$-I_0(\omega)$ – – – – – –

Figure 3.2a

Love

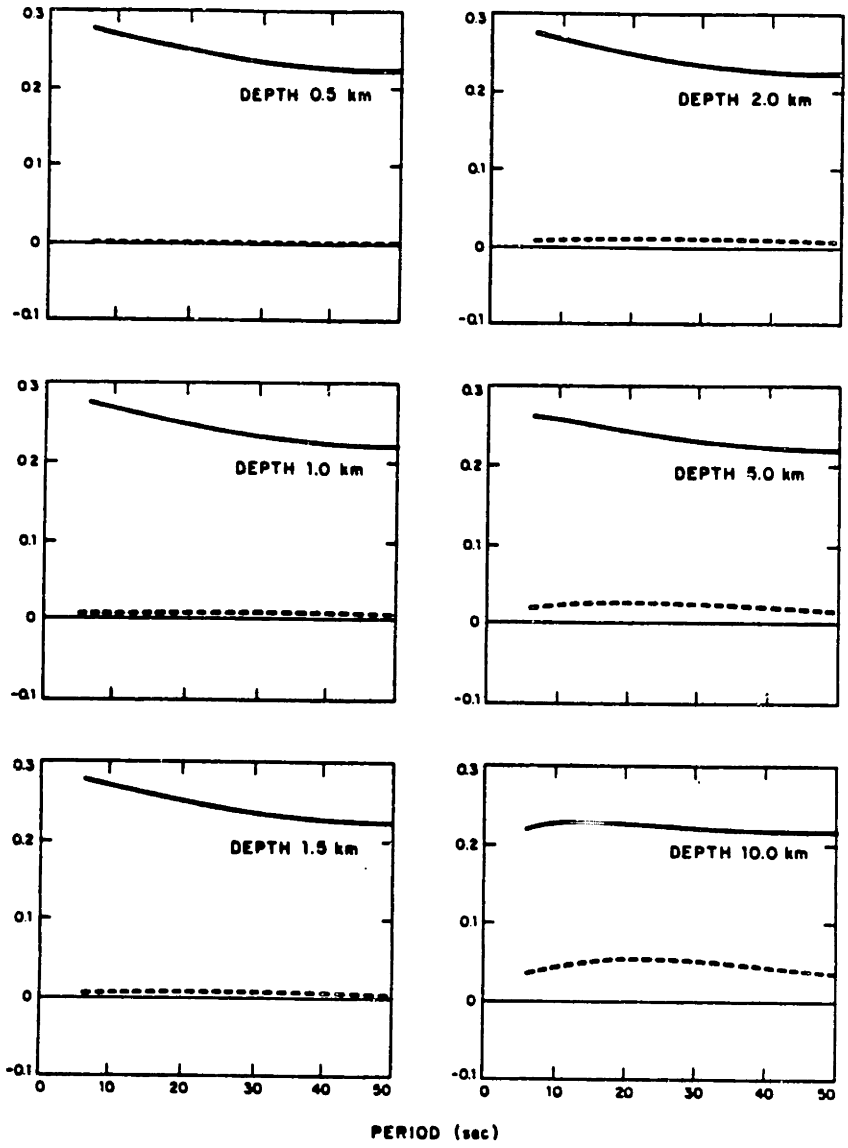

$I_2(\omega)$ ——————

$i\, I_1(\omega)$ - - - - - -

Figure 3.2b

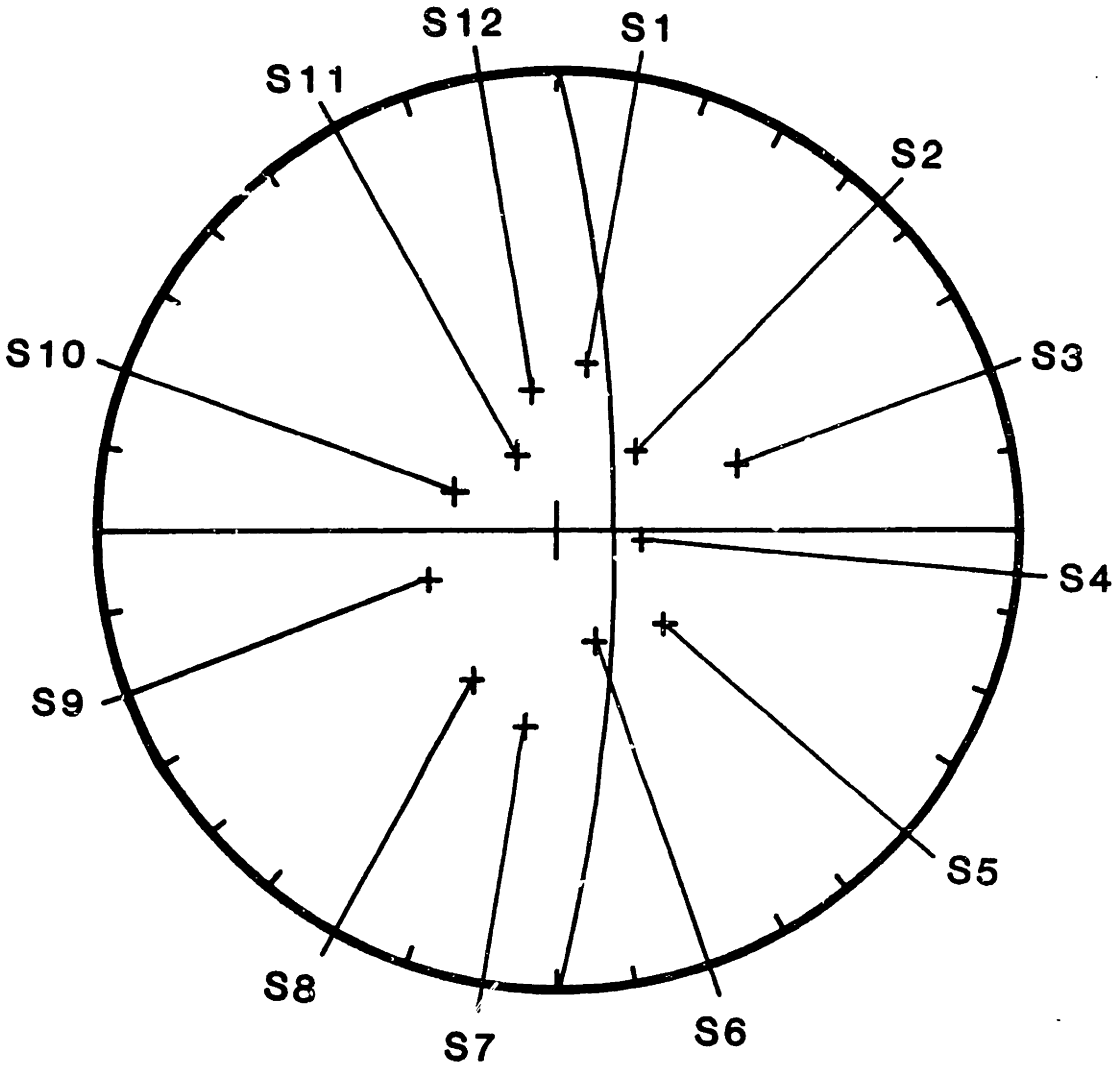

Figure 3.3

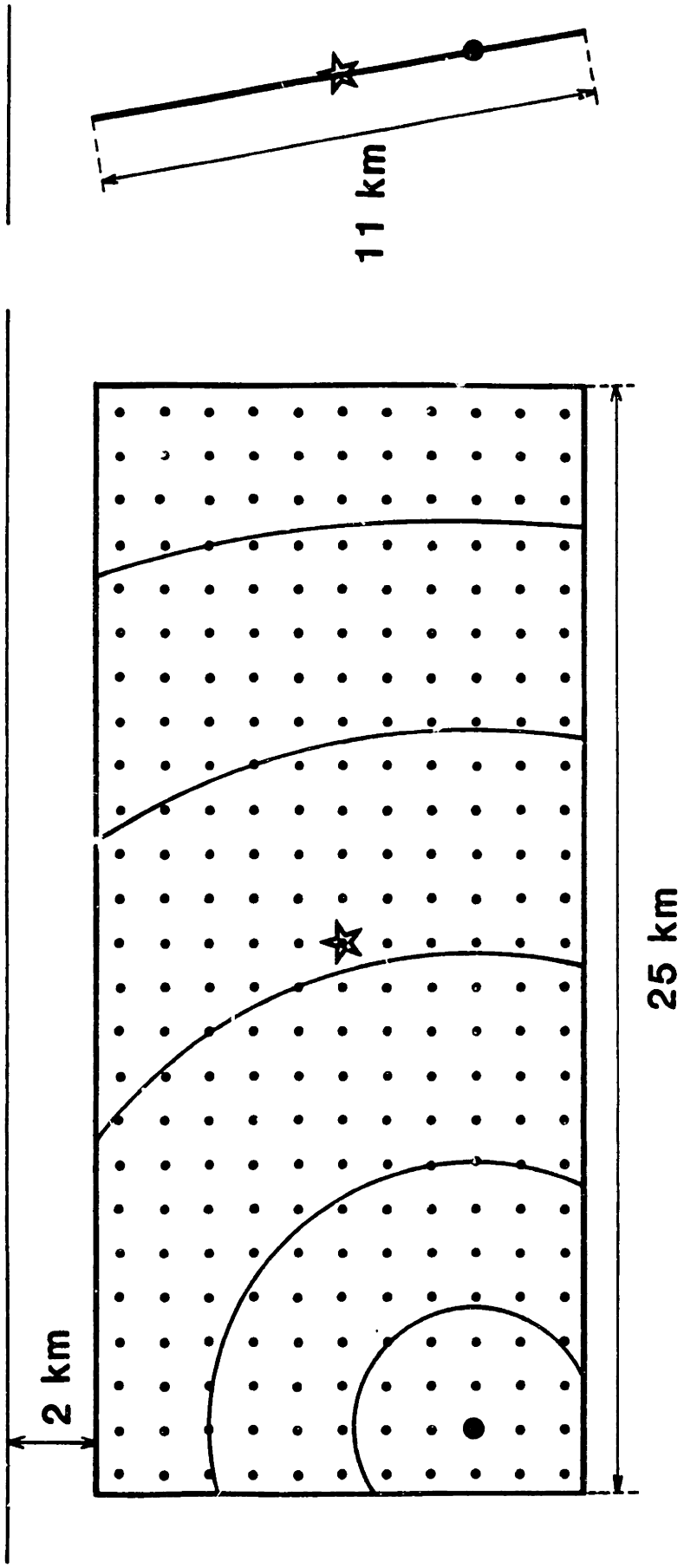

Figure 3.4

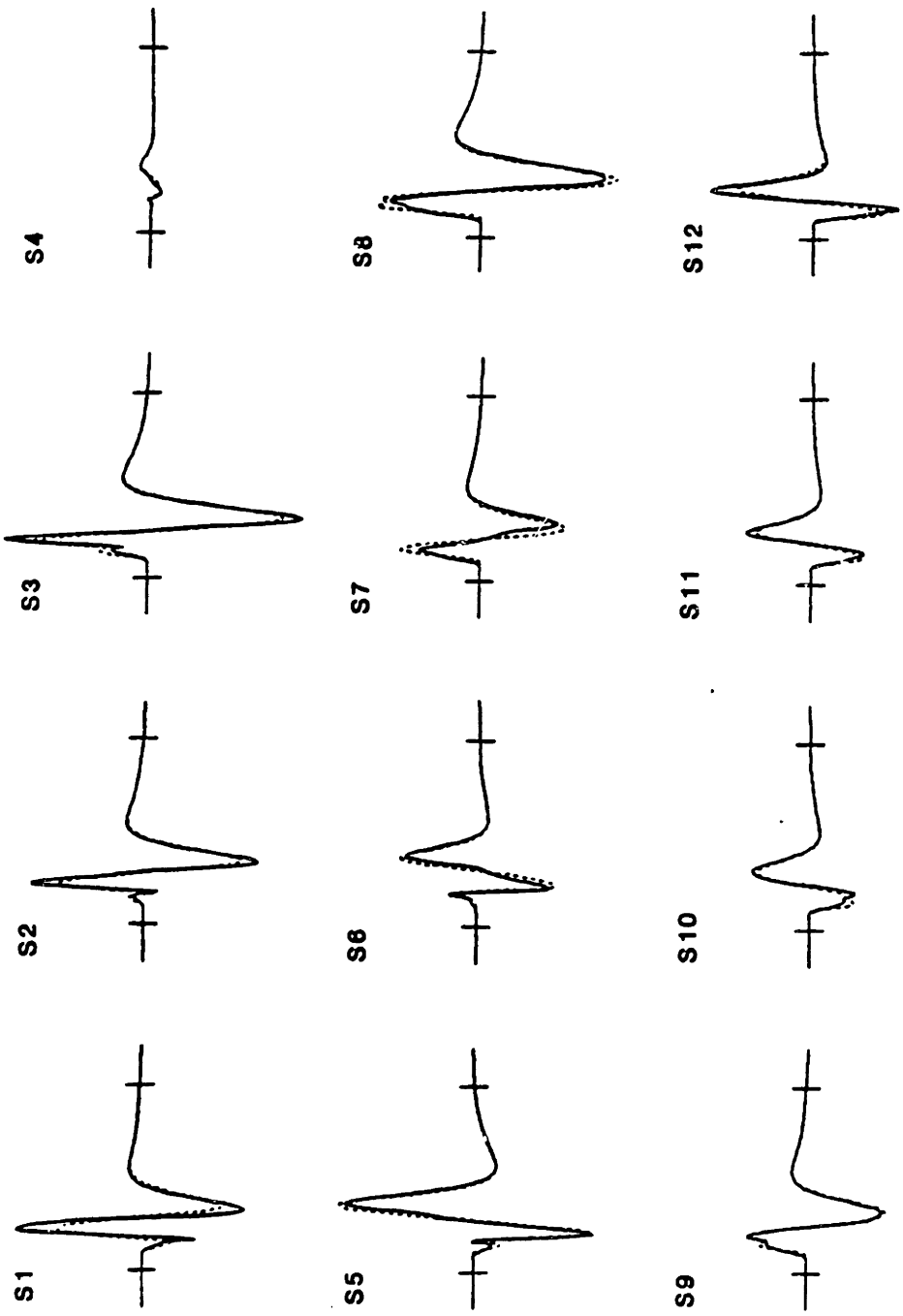

Figure 3.5a

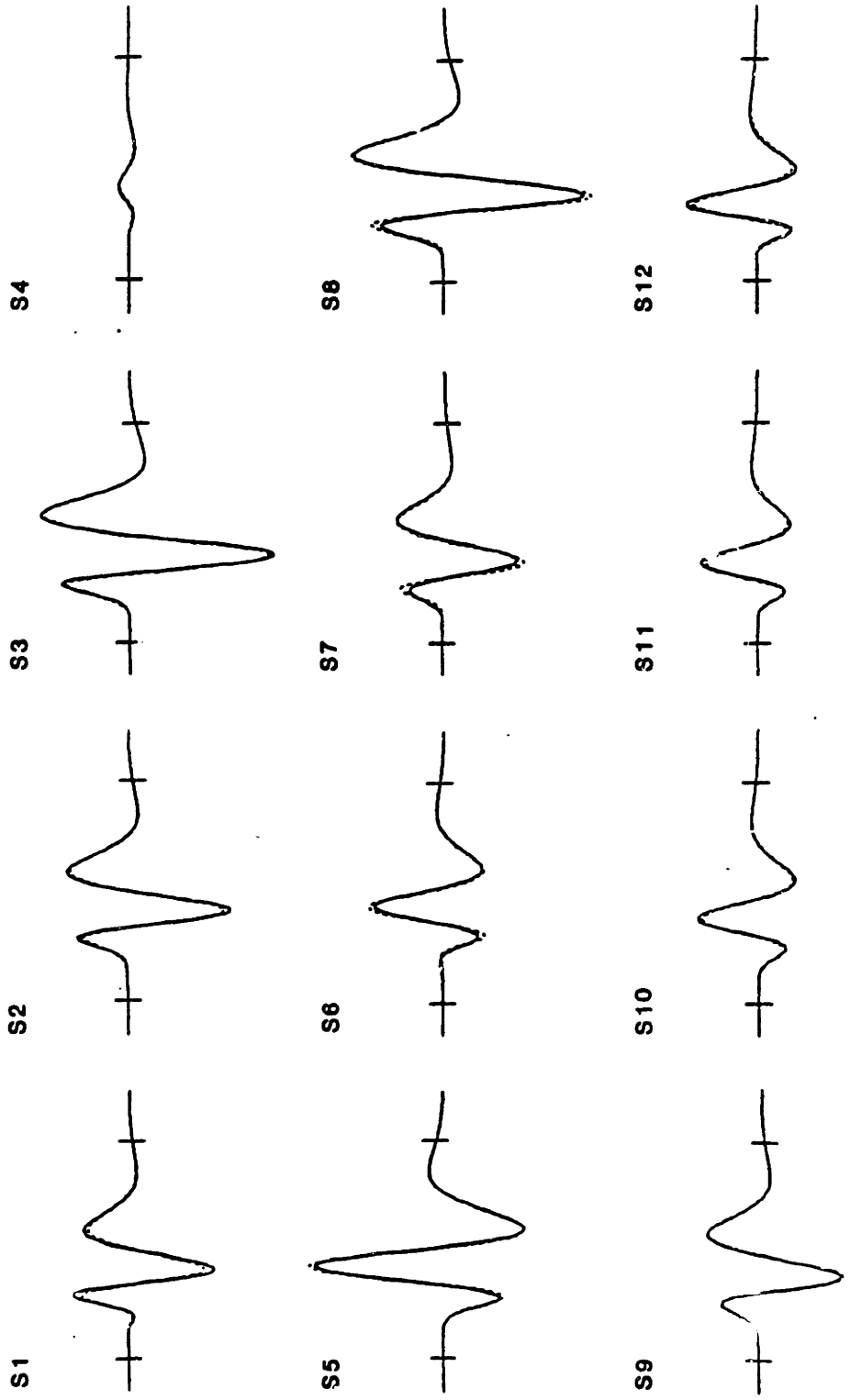

Figure 3.5b

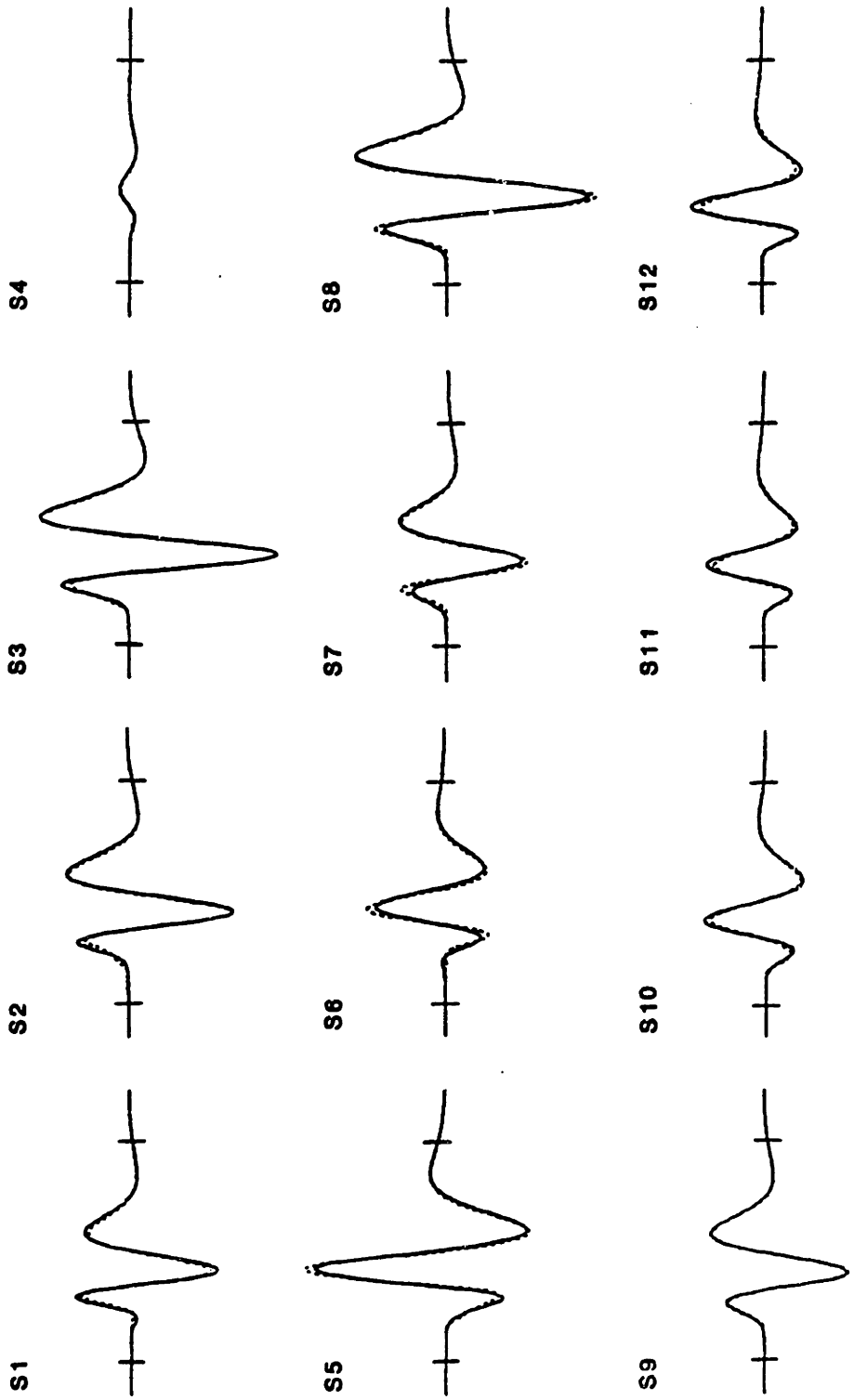

Figure 3.5c

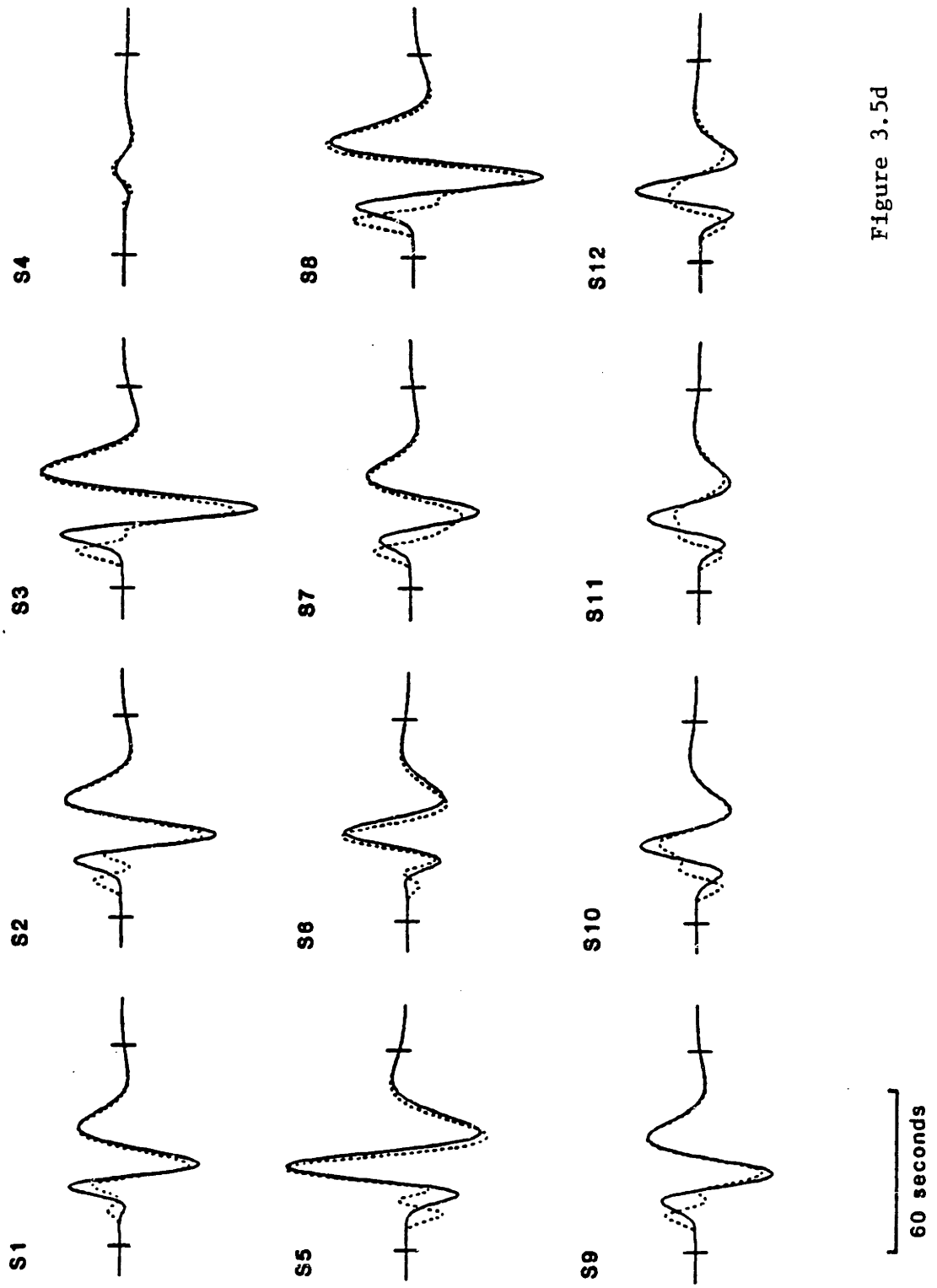

Figure 3.5d

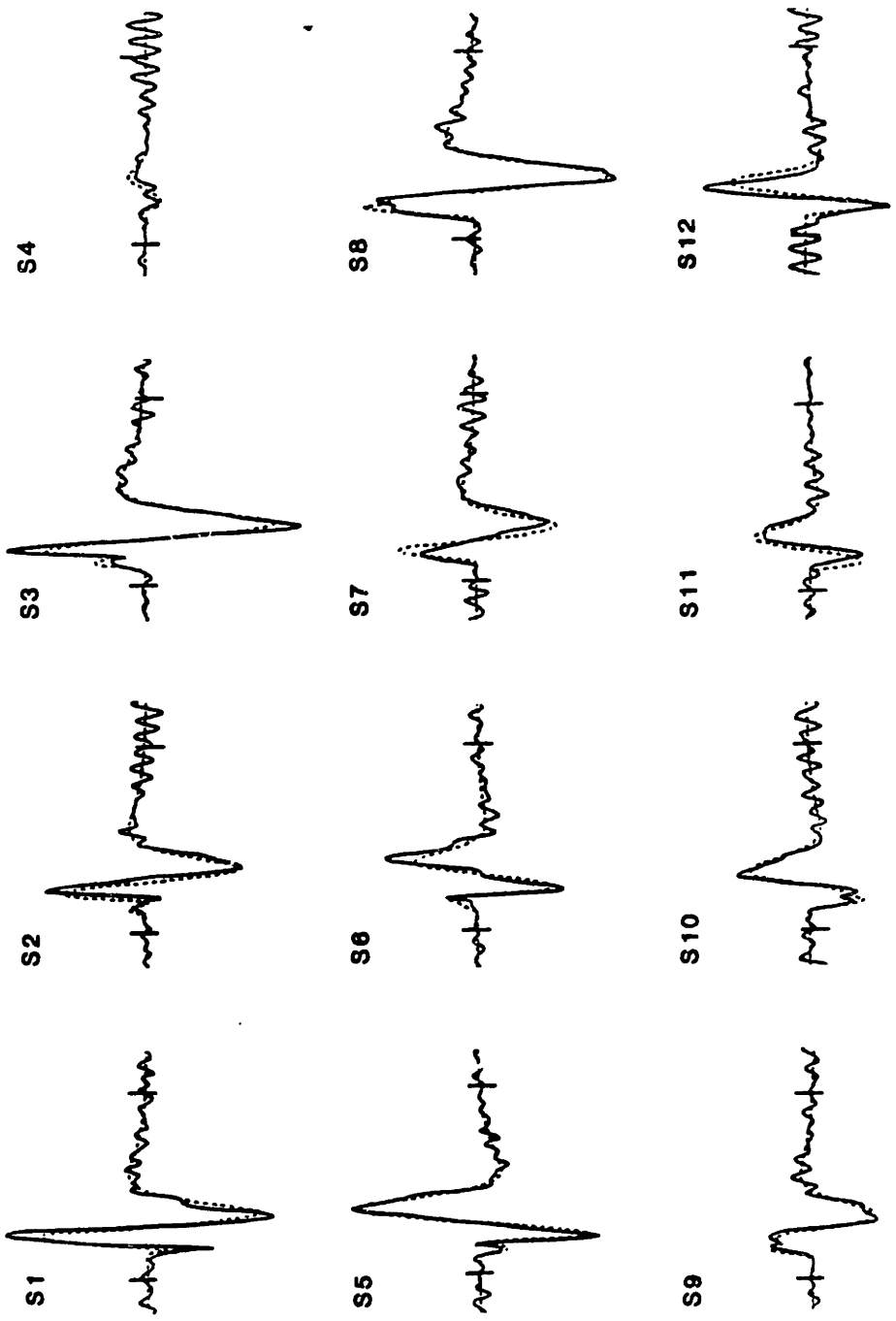

Figure 3.5e

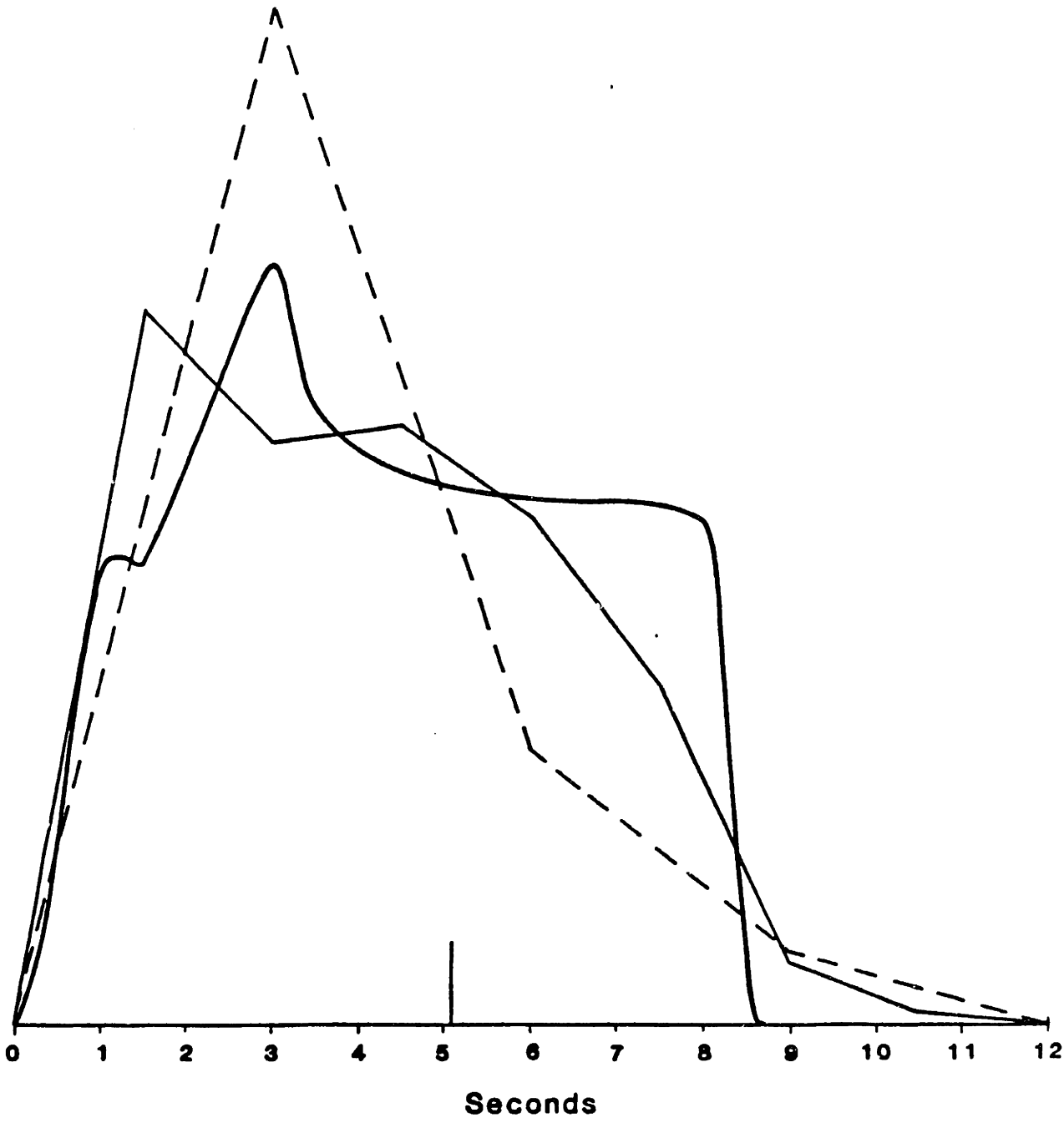

Figure 3.6a

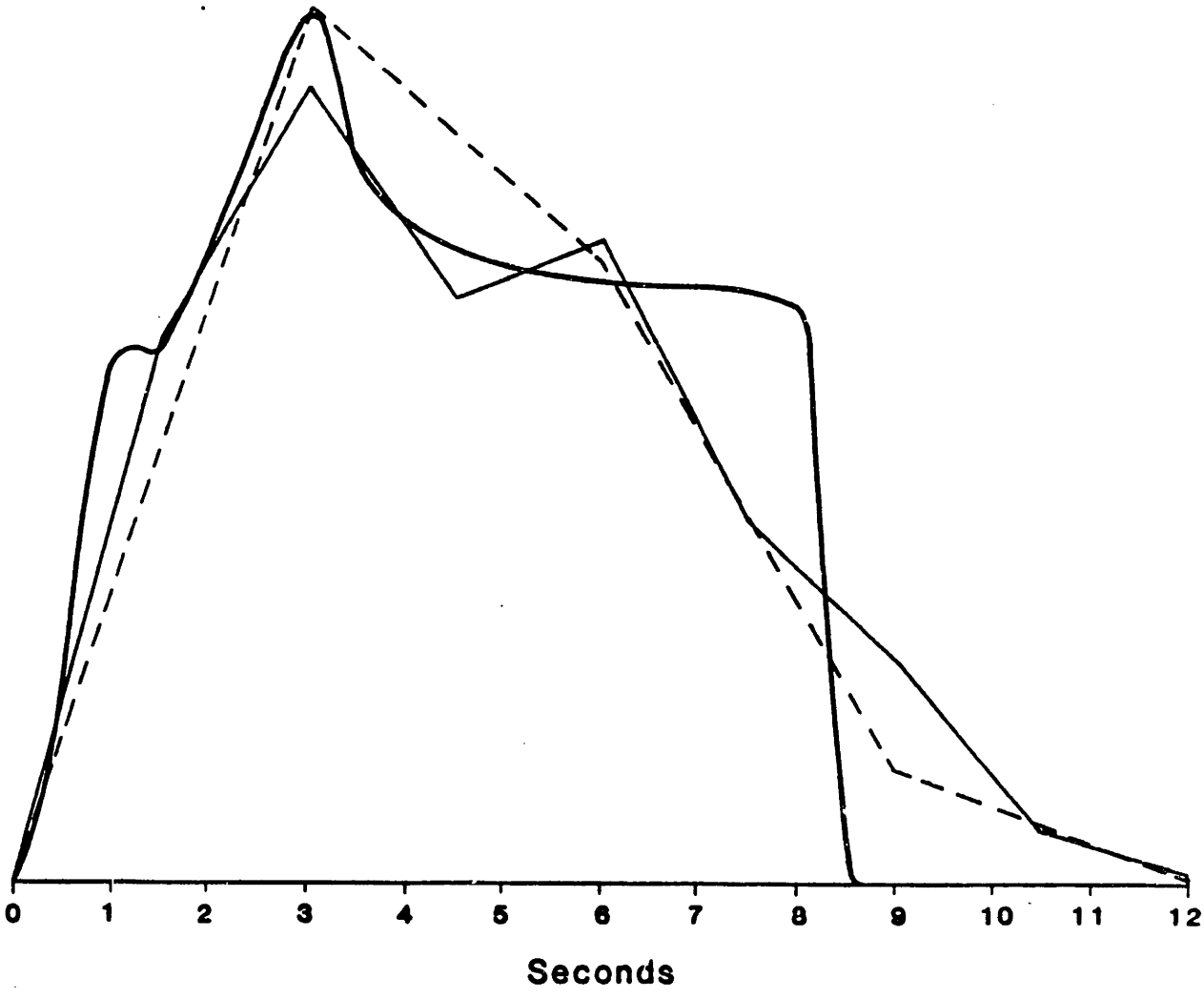

Figure 3.6b

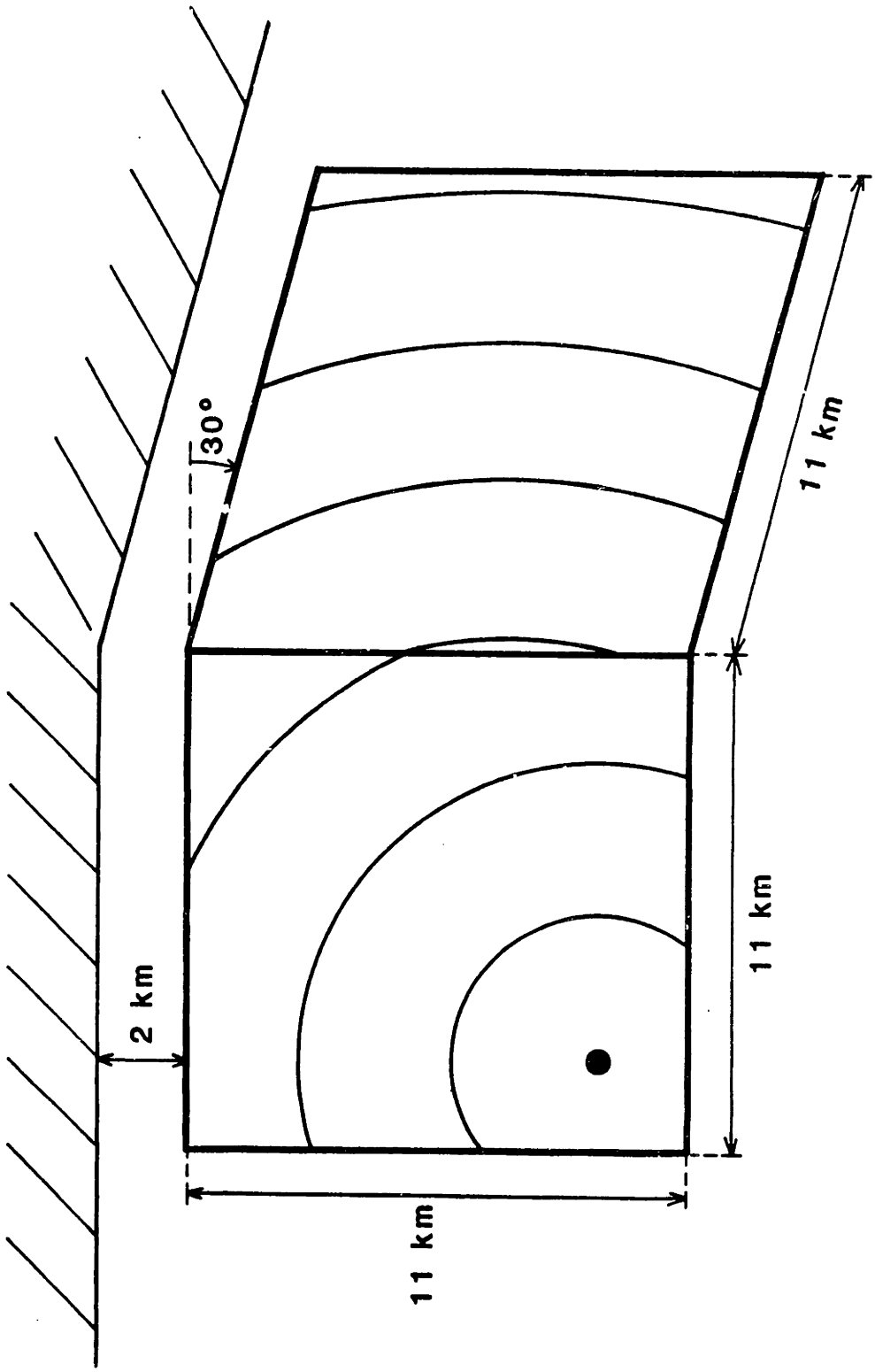

Figure 3.7

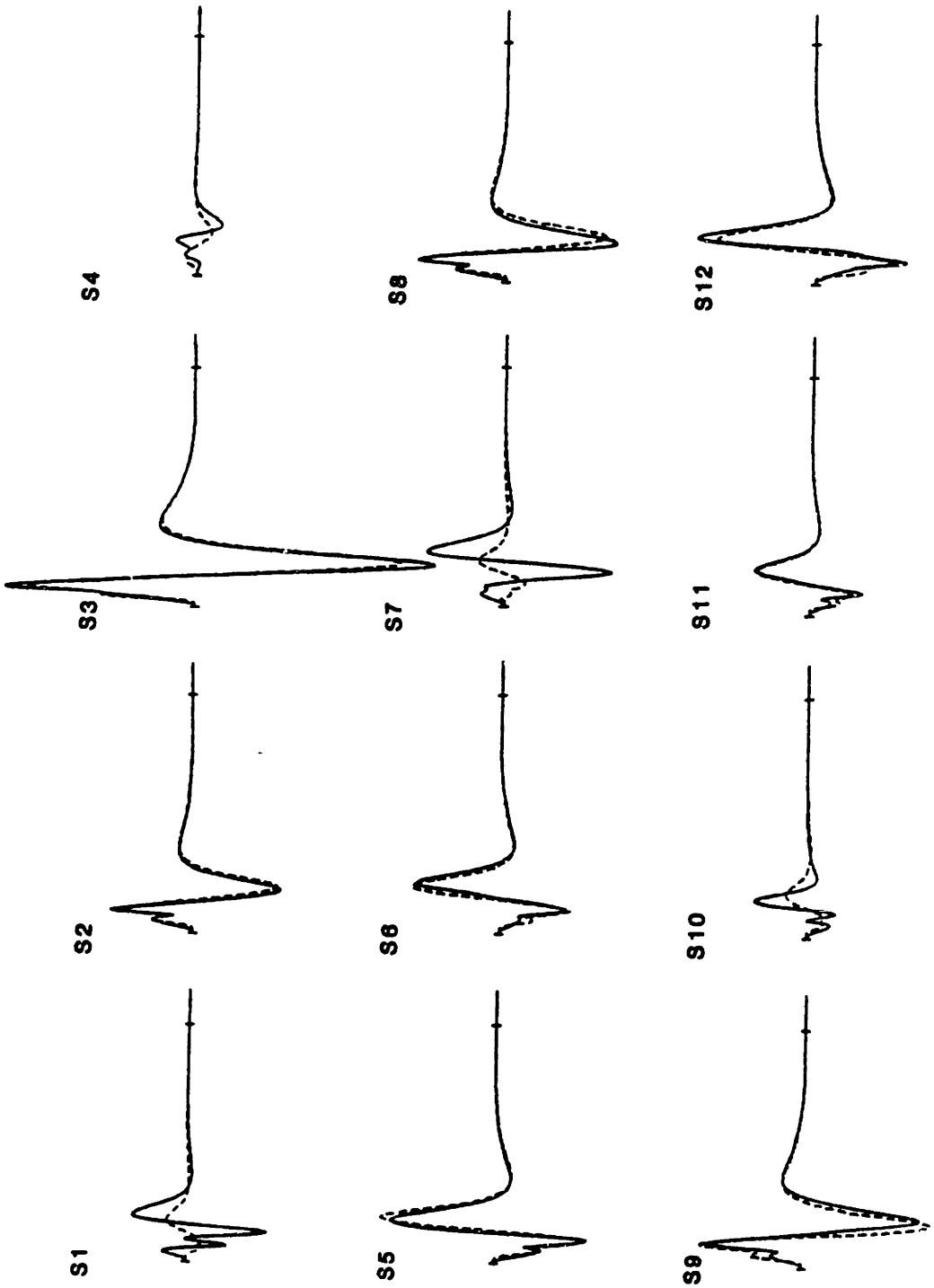

Figure 3.8

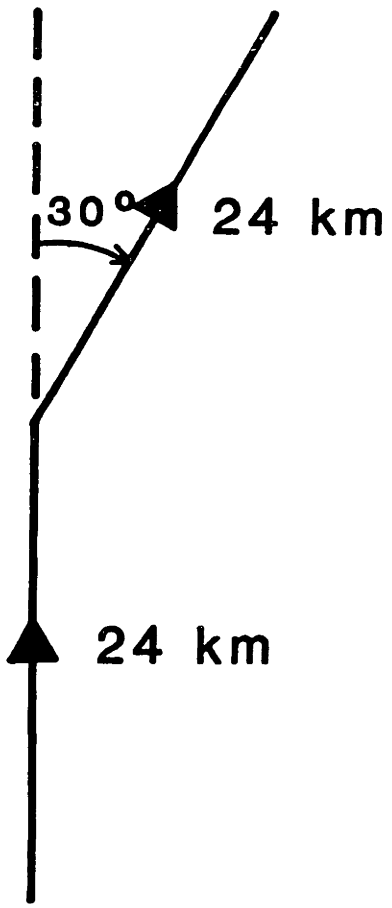

Figure 3.9

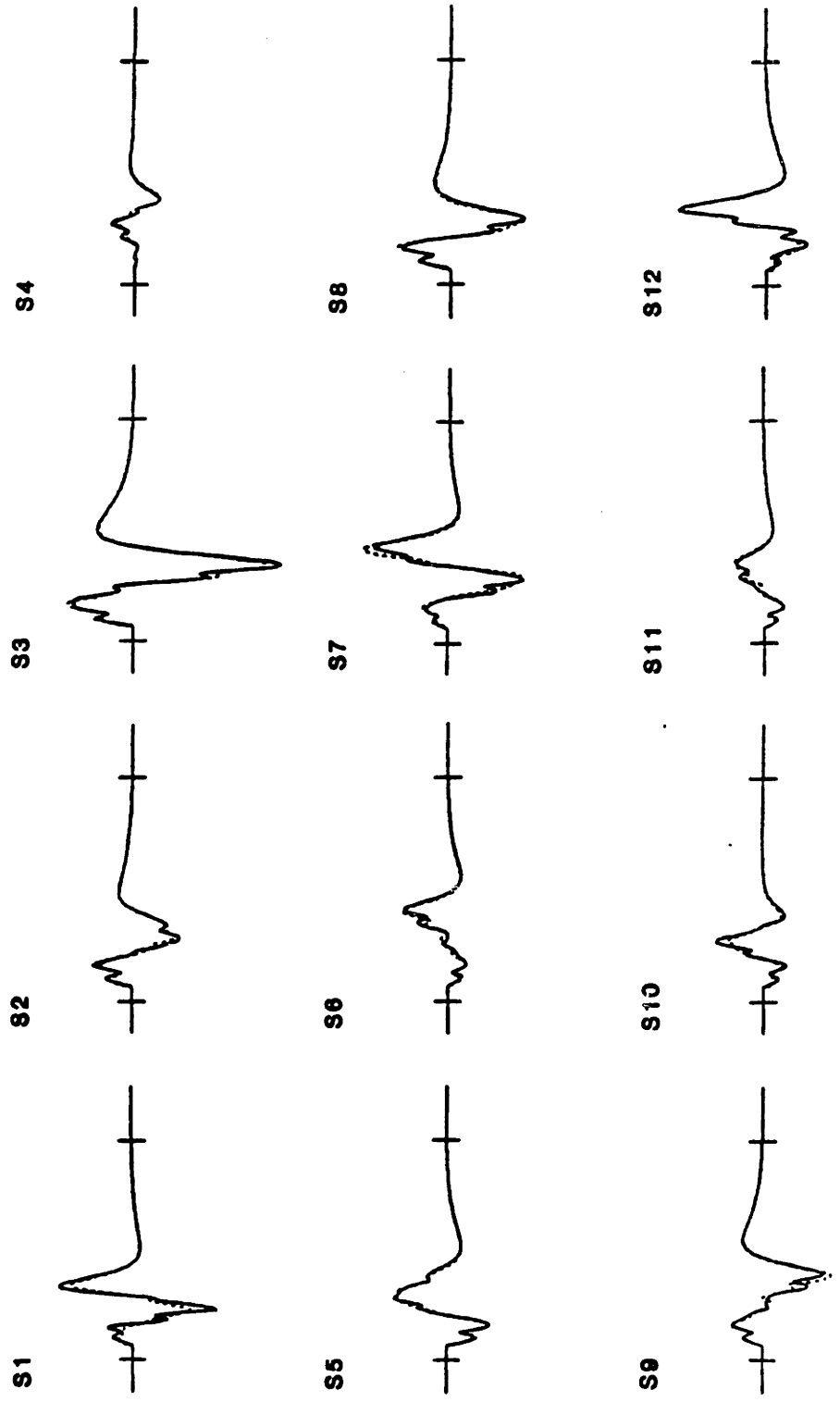

Figure 3.10

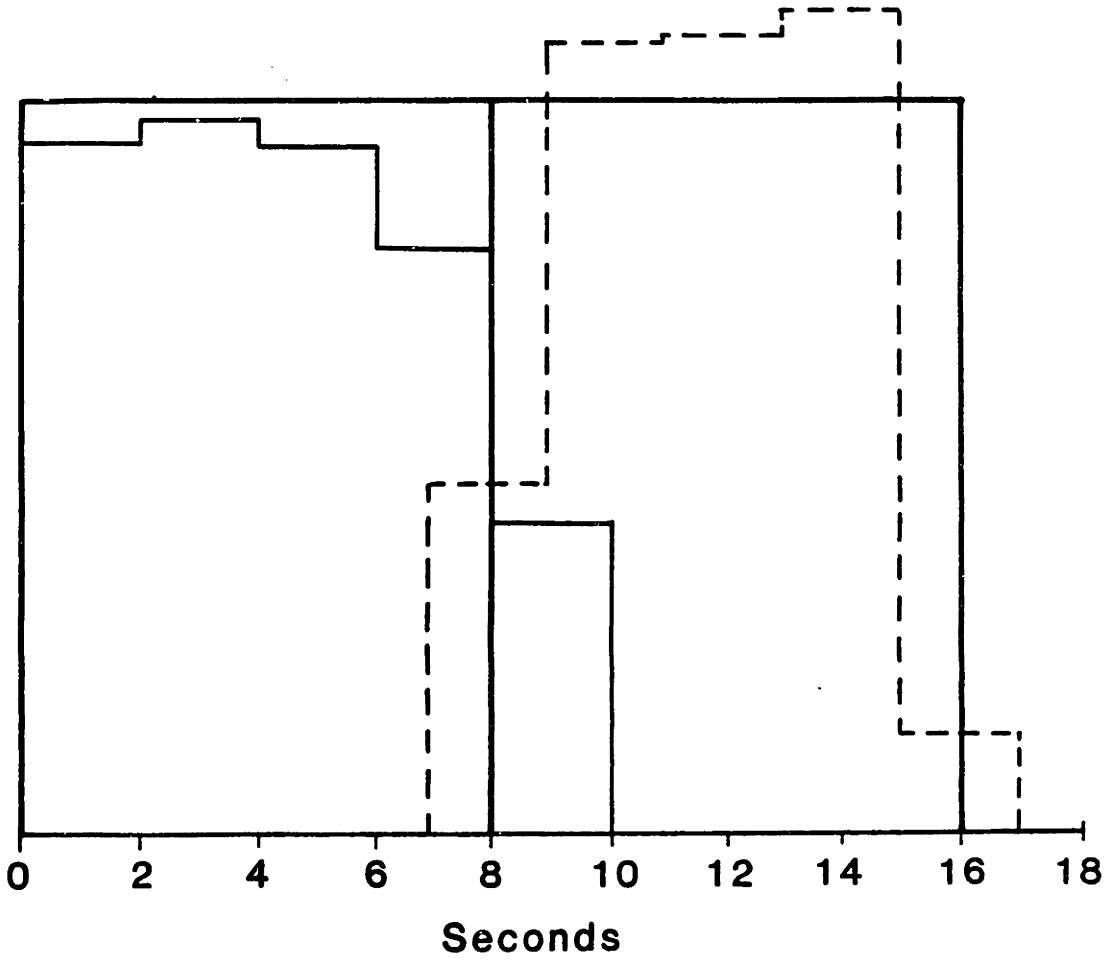

Figure 3.11

CHAPTER IV

APPLICATION TO EARTHQUAKES

4.1 INTRODUCTION

In this chapter techniques developed in the previous chapters are applied to four earthquakes of various size and complexity: the 1975, Lice, Turkey earthquake, the 1982, New Brunswick, Canada earthquake and its major aftershock, and the 1981 El Asnam, Algeria earthquake. The 1975 Lice earthquake (M_s = 6.7) is a relatively simple event. It was well studied in the field and provides a good test for the inversion techniques. Simple point source and line source models adequately explain the long-period body waves from this event.

The 1982 New Brunswick earthquake (m_b = 5.7) is much smaller than the Lice event, and the long-period data do not provide strong constraints on the time history of its rupture. This event is studied in detail using short-period and broad-band data which reveal small scale complexity of this event. The aftershock of the New Brunswick earthquake (m_b = 5.4) is too small for a long-period analysis. A successfully short-period inversion could, however, be performed.

The 1981 El Asnam earthquake (M_s = 7.3) is the largest and most complicated of the events studied in this thesis. This event is modeled as a multiple shock with fault-planes of different orientations. Although the unconstrained inversion is non-unique, a priori constraints based on field evidence can be used to stabilize the inversion and new information can be extracted from the data.

Chapter IV is written as three independent papers. Consequently, some of the discussions are repetitious. I apologize to the reader for the inconvenience.

4.2 THE SEPTEMBER 6, 1975, LICE, TURKEY EARTHQUAKE

4.2.1 INTRODUCTION

The Lice earthquake of September 6, 1975 (9:20:12 GMT; 38.5N, 40.7E; M_S = 6.7), named after the town of Lice in southeastern Turkey, destroyed the town and killed more than two thousand of its inhabitants. Lice lies at the western end of the Bitlis Thrust Zone, an east-west trending thrust belt defining the boundary between the Arabian and Anatolian tectonic plates. The thrust belt has been the site of frequent seismicity with several large events recorded in the past 60 years (Figure 4.2.1). The Lice earthquake is the largest to occur during this period. The relationship of the Bitlis Thrust Zone to the North and East Anatolian Fault systems is shown in Figure 4.2.2.

Following the Lice earthquake, several Turkish research teams inspected the epicentral region. Maps of the surface fault break, isoseismals and aftershock distribution are available and provide strong constraints on the orientation and the areal extent of faulting.

In this study, the source mechanism is investigated using the long-period P and surface waves recorded by the WWSSN network. P waves are analyzed using the methods described in previous chapters. The teleseismic and the field observations are very consistent, indicating thrusting along a 25 km east-west trending fault that dips to the north at approximately 50°. The centroidal (i.e. the average) depth was 4-5 km and the rupture propagated from east to west.

4.2.2 FIELD OBSERVATIONS AND AFTERSHOCK STUDIES

The surface faulting associated with the Lice earthquake was mapped by Arpat [1977] (Figure 4.2.3). In general, the surface disturbances follow the base of an escarpment of a well developed, steeply dipping geological thrust fault. The main segment of the fault, as defined by coseismic surface disturbances, is approximately 20 km long with a strike of approximately 255°. At the western end, the fault trace turns northward and continues along a strike of approximately 310° for another 5 km. As is commonly the case for thrust faults, it was difficult to estimate the exact amount of displacement and the exact slip direction during the Lice event due to landslides and slumping of the hanging wall [Yielding et al., 1981].

The intensity of shaking was mapped by Yanev [1975]. The strongest shaking reached intensity VIII (MMS). The contour of the strongest shaking, based on Yanev's study, is shown in Figure 4.2.3. It is approximately 25 km long and 5 km wide, with elongation in the east-west direction, that coincides with the main segment of the surface fault break. The shaking along the northwest trending segment of surface fault trace was not as severe.

A limited aftershock survey was carried out by Baysal [1977], two weeks after the main event (Figure 4.2.4). Most of the epicenters are located north of the escarpment in a band approximately 25 km long and 12 km wide that is shifted slightly westward with respect to the observed surface faulting. The largest concentration of aftershocks occurred westward of the the bend in the fault trace. Because only three recording instruments were used, hypocentral depths could not be determined.

In summary, the field observations in the epicentral area indicate that the Lice earthquake was caused by thrusting on a shallow east-west oriented plane that dips steeply to the north. The length of faulting was about 25 km.

4.2.3 BODY WAVE INVERSION AND MODELING

The fault plane solution based on P wave first motion polarities is shown in Figure 4.2.5. Because seismograms from regional stations north of the epicenter (Soviet Union) were unavailable, some readings reported as impulsive in the ISC Bulletin were also included (indicated by small symbols). The strike of the east-west fault plane was constrained to agree with the strike of the main segment of the observed fault trace. The fault plane solution indicates a thrust mechanism with a large left-lateral strike-slip component.

The Lice earthquake is of an ideal magnitude for P wave modeling. Good quality signal, well above the noise level, was recorded globally. The waveforms are simple, with no indication of source multiplicity.

The dataset for the inversion consists of long-period P waves from 24 well distributed WWSSN stations (Table 4.2.1). The waveforms were digitized at 0.25s intervals using the first 120 points (30s) from the onset of the direct P wave for the analysis. The onset of the P arrival was determined from the short-period records. After convergence, the assumed onset was allowed to vary by up to 1.5s if a better cross-correlation between the observed and synthetic waveforms was found. The computation was then restarted, resulting in the final solution.

The P waveforms were inverted for the source mechanism, depth, and source time function using methods described in previous chapters. The source time function is parameterized by a series of box function elements

(each of 2s duration) whose relative amplitudes are determined by inversion. The time length of the time function elements should be set to the minimum resolvable time interval, which depends on the frequency content of the signal. If the time length chosen is too short, the result is an instability in the estimated amplitudes. If, on the other hand, it is too long, the result is a poor description of the source and possibly biased estimates of other source parameters, most likely depth. In most applications using long-period WWSSN data, a value between 1.5 to 2s is appropriate. For small events the resolution is mainly controlled by the instrument response, but for large events, the high frequency roll-off due to a low corner frequency can further reduce the effective resolution of the data. The appropriate value can usually be found after a few trials. Because the power in the signal from the Lice earthquake was mainly concentrated at long-periods, a 2s discretization of the source time function was found to be sufficient.

The number of time function elements needed depends on the duration of the source. In all cases discussed below, the initial inversions were carried out using enough elements to observe their amplitudes decay back to zero or become negative, as is usually the case [Langston, 1981]. (Slight negative values of the elements at the tail end of the source time function should not be taken as evidence for back slip on the fault. They are usually the result of small errors in the assumed Green's functions, i.e. earth structure.) The final inversions were then performed using only the significant positive elements. It is important not to let the source time function be negative, because of the potential bias it can introduce in the depth estimate.

Although the coverage of the focal sphere is as good as one can expect to achieve with the present world wide network configuration, there is an imbalance in the number of stations at certain azimuths and take-off angles. A particularly large concentration of stations is found in the eastern quadrant of the focal sphere, corresponding to stations in eastern Asia (Table 4.2.1, Figure 4.2.6). Because such an imbalance may bias the estimated parameters, an attempt should be made to remove it. The situation is aggravated by the fact that the seismograms at the eastern stations have the largest amplitudes. Because the sensitivity of the least squares inversion is directly proportional to the power of the signal, these stations intrinsically carry the most weight in the inversion. The imbalance in station distribution could be partially removed by eliminating some of the stations from the inversion, but probably a better strategy is to downweight stations at a similar distance and azimuth. This decreases the effect of random noise contamination of any given station. In order to obtain an equitable weighting in a least squares sense, the station weights should be proportional to $1/\sqrt{N}$, where N is the number of stations in a given group of stations. The weights assigned to stations in this study (Table 4.2.1) reflect this strategy, except for DAV which was downweighted more because of its exceptionally large amplitude. No additional weighting proportional to the background noise was necessary because the signal at all stations was well above the background noise.

Five sets of inversions were performed. The results are summarized in Table 4.2.2. In order to investigate the extent to which the Lice earthquake can be approximated by a double-couple (as one would expect for a shear failure), the source was first parameterized as a moment tensor. Since there is no reason to expect any overall volume change

associated with the earthquake, the moment tensor was constrained to be purely deviatoric. Changes in the slip direction and fault curvature can (but do not necessarily have to) introduce a non-double couple (linear vector dipole) component into the point source mechanism.

The inversion indicates that the source was indeed essentially a pure double couple (Table 4.2.2). The inferred linear vector dipole component (7% of the total moment) is probably an artifact of imprecisions in the assumed Green's functions. The assumed crustal structure in this inversion and the following two sets of inversions was of a homogeneous halfspace with parameters given in Table 4.2.3. Examples of matches between the observed and theoretical seismograms for four representative stations from different azimuths are shown in Figure 4.2.6. As a quantitative measure of the goodness of fit of each model, the residual (using all stations) is also shown.

Because the moment tensor inversion (Model I) indicates a nearly pure double-couple mechanism the source mechanism was constrained to be a double couple in subsequent inversions. The parameterization of the source in Model II was identical to that of Model I, except for this constraint. As a consequence, the residual for Model II is slightly larger. The inferred double-couple orientation indicates thrusting with a substantial left lateral component (rake = 48°), on a east-west oriented fault plane (strike = 257°) that dips to the north (dip = 52°). The calculated moment is 1×10^{26} dyne-cm and the average source depth is 4.3 km. The most noticeable aspect of Models I and II is the large misfit to the western stations (e.g. station MAL in Figure 4.2.6); compared to the observed seismograms, the seismograms from these point source models are too rich in long periods and too small in amplitude. Most likely the reason for this

misfit is inadequacy of the point source approximation. We would expect that using a finite fault model with rupture initiating at the eastern end and propagating westward would correct both aspects of the misfit.

Finite faulting with predominantly lateral rupture propagation can be well approximated by a horizontally propagating line source. By virtue of the adapted time function parameterization, the effect of a horizontally propagating line source is easily introduced into the model simply by adjusting the assumed time length of the box functions comprising the time function at each station. The adjusted time length $\Delta\tau'$ for a given station depends on the station azimuth, ϕ, strike of the fault, θ, ray parameter, p, and rupture velocity, v_r, through the well-known relation [Ben-Menahem, 1961]

$$\Delta\tau' = \Delta\tau[1 - v_r p \cos(\phi-\theta)]$$

where $\Delta\tau$ is the original length chosen for the box functions. Since $\Delta\tau$ can be interpreted as the time it takes for the rupture to propagate along a line segment $\Delta\ell$, the deduced amplitudes of the box functions are a relative measure of the moment associated with each line segment.

In Model III, the point source is replaced by a horizontal line source oriented along the average strike of the fault, with rupture propagating east to west with velocity 2.5 km/s (0.7 v_s). The overall fit, especially the fit to the western stations, is considerably improved by this model. Improvement is also reflected in a more than 10% reduction in the residual. Inclusion of source finiteness into the model results in about 18° change in the estimated strike of the fault (275°), but the other parameters remain essentially unchanged.

Because of a persisting misfit in the second upswing of the western station waveforms a layered crust for the source region was introduced in

Model IV (Table 4.2.3). The fit is again improved, although the improvement in residual is not as substantial as it was when source finiteness was incorporated into the model. Inclusion of the layered crust results in a slightly larger estimate of the source depth (5 km) and consequently in a somewhat smaller seismic moment (0.9×10^{26} dyne-cm).

Model IV is considered to be the best fitting model. The data and the resulting match for all stations included in the inversion are shown in Figure 4.2.7. The model matches the absolute amplitudes of most stations quite well, in spite of the large azimuthal amplitude variation of the data. The largest amplitude misfit, seen for stations DAV, SNG and POO, is less than 50%. In trial-and-error modeling, amplitude fluctuations of a factor of 5 or more with respect to a "successful" model are normally regarded as acceptable, because many investigators consider only wave shape to be a reliable indicator of the source mechanism [e.g. Langston and Butler, 1976; Cipar, 1979; Stewart and Helmberger, 1981]. That such large amplitude misfits can be significantly reduced by careful adjustments of the source parameters indicates that the earth mantle is remarkably homogeneous at periods of 10-15 seconds (the dominant periods of the Lice P wave seismograms). A source model that exhibits large amplitude misfits should be accepted with caution, irrespective of how well the waveshapes are matched, because they could be due to some poorly modeled features of the source.

The most serious misfit in Model IV occurs for stations WES and BEC where the second upswing remains unmatched. This actually introduces ambiguity into the interpretation of this upswing as due to crustal structure in the source region. In Model IV this upswing is produced by the SV to P wave reflection from the second crustal interface at a depth of

26 km; it is observed only at the western stations because for the mechanism of Lice earthquake the downgoing SV wave has an antinode in western direction. This mechanism works well for stations with shorter epicentral distances, but for more distant stations (WES and BEC) the SV wave angle of incidence is too steep to generate a sufficiently large P wave reflection from a horizontal interface. For this mechanism to also be viable for stations WES and BEC, the 26 km interface must have a few degrees of dip in the northwest direction [Langston, 1977]. This is entirely plausible, since the Bitlis thrust is known to have northward vergence. Of course, one must also accept the possibility that the upswing is not due to structural effects but to some source effect, possibly related to the mapped complications at the western end of the fault trace. Although attempts to model the upswing as a source effect that would also be consistent with field observations were unsuccessful, one must admit to the nonuniqueness of the interpretation since we are dealing with strongly interfering signals.

In inversions I through IV, except for equilization to a common instrument magnification and common distance on the focal sphere, the signal was treated in its original form. The amplitude differences from station to station therefore played an important part in the estimate of the source parameters. In the final inversion discussed here (Model V), instead of minimizing the sum $(s_i-o_i)^2$, where s_i and o_i are the discrete synthetic seismogram and observed seismogram amplitudes, we minimize the sum $[s_i/(\sum_j s_j^2)^{1/2} - o_i/(\sum_j o_j^2)^{1/2}]^2$, where the summations with respect to j are carried out over the number of data points at a given station. This quantity is insensitive to the absolute amplitude of the data points at the station, and is sensitive only to their relative differences (i.e. the

shape of the seismogram). This inversion is analogous to the classical waveform modeling by trial-and-error. Since the information in the absolute amplitude is removed, the seismic moment must be estimated independently from the original data after the final iteration. This is again done in a least squares sense.

The result of this inversion and the resulting fit to the data are shown in Table 4.2.2 and Figure 4.2.6b. For comparison with the other models, the fit of this model to the original data and the corresponding residual is also shown.

With respect to the other models, in Model V the estimated source depth is considerably larger (9 km), the seismic moment, which strongly depends on the estimated source depth, is about one half, and the source time function is richer in short periods. The residual of Model V is about 8% larger than that for Model IV. Judging from the visual fits of Models IV and V to the original data in Figure 4.2.6, the main difference is the underestimate of the absolute amplitudes for the African stations (e.g. AAE) by Model V. If we admit the possibility that structural heterogeneity of the Earth can produce such a bias for stations at one azimuth, then Models IV and V become practically indistinguishable based on P wave data. Such a tradeoff between the estimated source depth and source time function, typical of large shallow events, is a result of strong interference between the direct and reflected phases. Because this tradeoff is non-linear, its effect on the formal uncertainties of the source parameters is difficult to estimate.

The only other parameter significantly affected by the choice of source depth is the seismic moment. The main reason for this dependence is that in the frequency band of observed P waves, the amount of destructive

interference between direct and reflected phases (and therefore the amplitude of the signal) is strongly dependent on the source depth. Including a longer period signal in the inversion would clearly improve the stability of the moment estimate and, at the same time, stabilize the depth determination. This is accomplished indirectly in the next section, using surface wave data. Based on the assumption that moment determined from T = 80s surface waves should match the moment from P-waves (dominant period ~15 s), the 4-5 km source depth determined from inversions I through IV using full amplitude data is most likely the correct estimate.

The least resolved parameter related to source orientation appears to be the fault strike. The estimates based on the five inversions discussed above are bimodal; inversions I, II and V indicate a strike of about 257°, whereas for inversions III and IV the best-fitting strike is about 273°. It is difficult to decide which one of the two values is correct. The value of 257° is appealing because it is consistent with the strike of the main limb of the observed surface fault trace. On the other hand, if significant slip also occurred on the western north-west trending limb, it could be expected to influence the average value which is measured by the point source or line source models. Thus, if the average strike was indeed 273°, as implied by inversions III and IV, it can be taken as supporting evidence for significant coseismic slip on the western limb of the mapped fault trace.

Compared to the strike, the estimates of the fault dip and the rake of the slip vector are stable. The estimates resulting from the five different inversions do not vary by more than 6° and are evenly distributed. As previously mentioned the faulting mechanism is a thrust

with a large left-lateral strike-slip component. The strike-slip component is, however, smaller than the first motion polarities indicate (Figure 4.2.5). Since the fault plane solution is constrained primarily by first motion readings taken from short period recordings at regional stations, the first motion solution represents the slip near the nucleus of the rupture. It is therefore apparent that the initial slip direction was somewhat different from the average slip determined from the full waveform modeling. There is, of course, a large uncertainty in the take-off angles assigned to regional phases, and since most of the take-off angles for these phases are close to the nodes it is likely that, in the presence of some background noise, the operators reporting the first motion polarities may have in fact missed the true first arrival [Aki, 1976].

The uncertainties in the parameters for each inversion result shown in Table 4.2.2 are formal errors, representing one standard deviation. These uncertainties represent only uncertainties propagating into the solution due to random errors in the data (equations B8 and B9 of Appendix B) and would represent true uncertainties only if all biases (systematic errors) are properly removed from the data prior to the inversion. The fact that they are small and that the solutions for different inversions change by more than one standard deviation indicates that random errors are relatively unimportant compared to biases introduced by different model parameterizations. In our problem, potentially the largest bias could be introduced by assuming the wrong crustal structure in the source region. It has been shown that the solution does not change appreciably when a layered structure instead of a homogeneous half-space is assumed. In both cases however, the medium properties directly at the location of the source were identical. Had the crustal structure at the location of the source

been changed or large discontinuities been introduced in the immediate vicinity, the changes in the solution (especially the estimate of source depth) would certainly be larger. It is somewhat surprising that the source orientation changed to such an extent when the point source model was replaced by the line source model, since finiteness effects should average out with a good station distribution (Chapter III). It appears that in spite of the effort to compensate for the lopsided station distribution, some imbalance still remains.

In general the results of the P-wave modeling are in very good agreement with the field data. The inferred strike of the fault plane falls within the bounds provided by the surface faulting data. The steep dip is also indicated by the attitude of the beds within the geological escarpment. There was no information provided on the sense or the amount of the strike-slip component of slip in the available field reports. The P-wave data suggests that the movement was substantial, and left lateral. The rupture had a duration of 10-12 s as indicated by the inferred source time function (Figure 4.2.7) and it propagated from east to west. Assuming the model rupture velocity of 2.5 km/s, the duration implies a fault length of 25-28 km which is in excellent agreement with the field data. Judging from the shape of the source time function, the maximum displacement did not occur at the initiation of faulting. The largest displacements occurred in the middle of the fault on a segment about 5 km long. If we assume that the average source depth of 5 km obtained in Model IV is correct, a dip of 50° implies an average fault width of about 13 km, since faulting extended to the earth surface. Using the estimated seismic moment of 1×10^{26} dyne-cm and the fault length of 28 km, an average stress drop of

about 18 bars and an average displacement on the fault of about 90 cm is obtained [Kanamori and Anderson, 1975; Chapter II].

4.2.4 COMPARISON WITH THE SURFACE WAVE DATA

The Lice earthquake was also of optimal magnitude for surface wave analysis since most lower gain WWSSN station produced clear R1 (Rayleigh waves travelling along the shortest path from the epicenter to the recording station) records, giving very good azimuthal coverage (Figure 4.2.8). Examples of four recorded seismograms are shown in Figure 4.2.9. The main reason for studying the surface waves is to obtain an estimate of seismic moment at longer periods than those that dominated the P-wave signal. Because the estimated moment at the dominant P-wave periods was very sensitive to the estimated source depth, long-period surface waves should provide a more stable moment estimate.

The observed radiation pattern of Rayleigh waves at a period of 80s is plotted in Figure 4.2.10. Theoretical patterns for different models derived from the P wave modeling and the first motion polarities are also shown. The Gutenberg earth structure for the continents was assumed [Aki and Richards, 1980]. The moment of 1.0-0.9 x 10^{26} dyne-cm obtained in Models I through IV is in excellent agreement with this data. The moment of 0.5 x 10^{26} dyne-cm, obtained in Model V, on the other hand would clearly be an underestimate. On the basis of this observation, we conclude that the depth obtained in the inversions which were sensitive to the absolute amplitude of the P wave seismograms (Models I-IV) is probably the correct centroidal depth for the Lice earthquake. The source mechanism based on best-fit Model IV also gives a good match to the Rayleigh wave radiation pattern.

4.2.5 TECTONIC IMPLICATIONS

The main geologic features controlling the tectonics of eastern Turkey are the Bitlis Thrust (site of the Lice earthquake), the left-lateral East Anatolian Fault and the right-lateral North Anatolian Fault. All three are easily recognizable on satellite photographs. Their relative geometry along with the fault plane solutions for major earthquakes in this region are shown in Figure 4.2.11. According to McKenzie [1972], the slip on this fault system is controlled by the northward motion of the Arabian plate. A striking feature of the recent seismicity is the relative lack of large events on the East Anatolian compared to the North Anatolian Fault (Figure 4.2.1) [Toksoz et al., 1979], although from the geometry of the McKenzie model a similar amount of offset and seismicity on both faults is expected. The only large event which occurred recently on the East Anatolian Fault was the Bingol, 1971 earthquake. The fault plane solution derived from P wave first motions indicates pure left-lateral slip on a nearly vertical fault plane [McKenzie, 1976]. Although 60 years of monitoring may not be representative of long term tectonic processes, other geological evidence also suggests that the total slip on the East Anatolian Fault is smaller than the total slip on the North Anatolian Fault [Arpat and Saroglu, 1972; Sengor, 1979]. This discrepancy may be accounted for if the left-lateral relative motion between the Turkish and Arabian plates is not strictly confined to the East Anatolian Fault but is partially taken up by the Bitlis Thrust and other less prominent faults in this region. The fault plane solution of the Lice earthquake, indicates that the northward thrusting assumed to take place on the Bitlis Thrust and the left-lateral strike slip motion assumed to be confined to the East Anatolian Fault are

not indeed completely decoupled. Other events on the Bitlis Thrust, at least those westward of Lice, probably behave in similar fashion.

The ISC determined depth for this event is 32 km. Even if we assume that the rupture initiated at the bottom of the fault plane, the depth of focus can not be much larger than 10 km, since the average (centroidal) depth was about 5 km. Jackson [1980] analyzed errors associated with focal depth determinations for this region using teleseismic arrival time data. He concludes that the depth of small events is very poorly determined, with possible errors up to 80 km, while very large events appear to be well located. For the 1978 Caldiran earthquake (Figure 4.2.11), the ISC depth is indeed in good agreement with that determined by waveform modeling (Chapter 4.6). Jackson's conclusion is violated for the Lice earthquake since the ISC location is significantly in error. A possible explanation for the hypocentral mislocation of the Lice earthquake may be its emergent source time function (Figure 4.2.6) which could lead to errors in determining the first arrival times. This result is important because several recent seismicity studies [Buyukasikoglu, 1980; Rotstein and Kafka, 1982] have used ISC locations of earthquakes with magnitudes less than 5 to infer the deep structure of the Bitlis Thrust Zone. If the ISC hypocenter for the Lice earthquake, by far the best recorded event in this region, is significaltly in error, the error in the ISC locations of small events may be large enough that conclusions of seismicity studies based on ISC focal depths should be questioned.

4.2.6 CONCLUSIONS

The Lice earthquake provides the opportunity to compare source parameters derived from teleseismic observations with those based on geological evidence and seismic observations in the immediate vicinity of

the earthquake fault. Those parameters which are well constrained by the field data (e.g. fault length and strike) are well matched by the P wave modeling. Other parameters which are known approximately (e.g. steep dip, shallow depth, sense of motion) are confirmed and more precisely determined. It was found that significant left-lateral motion is absorbed by this part of the Bitlis Thrust. We also pointed out that the focal depth published in the ISC bulletin is significantly in error. The source parameters determined in this study are summarized in Table 4.2.4.

Table 4.2.1 Parameters of Stations Used in the Body and Surface Wave Analysis

STATION	AZIMUTH (deg)	DISTANCE (deg)	WEIGHT*	WAVEFORMS USED**
COL	4	37	1.00	P,R
KIP	20	118		R
SHK	61	71	1.00	P,R
ANP	75	68	0.60	P,R
HKC	81	64	0.60	P,R
BAG	83	72	0.40	P,R
DAV	88	82	1.00	P,R
SHL	91	45	0.75	P,R
CHG	94	54	0.75	P,R
NDI	97	32	1.00	P
SNG	103	62	0.75	P,R
LEM	110	77	1.00	P,R
POO	115	35	1.00	P
MUN	123	99		R
AAE	184	30	1.00	P
NAI	186	40		R
PRE	193	65	0.75	P
BUL	193	60	0.75	P,R
LPB	168	115		R
MAL	282	35	1.00	P,R
TOL	287	34	0.75	P
PTO	290	37	0.75	P
BEC	305	81	1.00	P

Table 4.2.1 (cont'd)

STATION	AZIMUTH (deg)	DISTANCE (deg)	WEIGHT*	WAVEFORMS USED**
STU	305	25		R
VAL	308	37		R
ESK	315	34	1.00	P,R
WES	316	78	1.00	P
JCT	326	102		R
KON	327	29	1.00	P
ALQ	333	101		R
MSO	343	92		R
COR	349	96		R
KEV	351	32	0.75	P
KBS	352	42	0.75	P

* Weight assigned to stations in the body wave inversion. Weighting was used to compensate for uneven station distribution.

** P indicates vertical component P wave; R indicates vertical component Rayleigh wave.

Table 4.2.2 Summary of P-wave Inversions Using Different Source Parameterizations and Crustal Structure

MOMENT TENSOR

I. POINT SOURCE, HOMOGENEOUS CRUST*

Depth = 4.3 ± 0.1† km

Normalized moment-tensor components:

M_{xx} = −0.63±0.01 M_{xy} = −0.19±0.02
M_{yy} = 0.10±0.01 M_{xz} = −0.05±0.01
M_{zz} = 0.53±0.01 M_{yz} = 0.34±0.01

Moment-tensor norm = 1.43±0.04 x 10^{26} dyne-cm

Principal axes:

	Eigenvalue	Azimuth	Plunge
P:	−0.68±0.01	195±1°	2±0°
B:	−0.05±0.01	286±1°	30±0°
T:	0.73±0.01	102±1°	60±0°

Decomposition:‡ 93% double couple 7% linear vector dipole

Best double-couple:

Scalar moment = 1.01 x 10^{26} dyne-cm
Strike = 258° Dip = 51° Rake = 50°

Time-function amplitudes:**

0.012±0.006, 0.285±0.132, 0.011±0.005, 0.011±0.005, 0.020±0.009, 0.022±0.010

CONSTRAINED DOUBLE-COUPLE SOURCE

	II. POINT SOURCE HOMOGENEOUS CRUST	III. LINE SOURCE HOMOGENEOUS CRUST	IV. LINE SOURCE LAYERED CRUST	V. LINE SOURCE LAYERED CRUST WAVE SHAPE ONLY
Depth (km)	4.3±0.1	4.4±0.1	5.0±0.1	9.1±0.1
Strike (deg)	257±1	275±1	271±1	256±1
Dip (deg)	52±1	46±1	47±0	49±0
Rake (deg)	48±1	53±1	50±0	45±0
Scalar moment (10^{26}dyne-cm)	1.06±0.02	1.03±0.02	0.90±0.01	0.51±0.01
Time-function amplitudes	0.017±0.005	0.021±0.004	0.037±0.004	0.059±0.006
	0.097±0.005	0.112±0.004	0.299±0.004	0.201±0.007
	0.230±0.006	0.220±0.006	0.406±0.009	0.383±0.009
	0.310±0.009	0.312±0.010	0.158±0.007	0.233±0.012
	0.193±0.009	0.162±0.009	0.072±0.004	0.066±0.010
	0.091±0.006	0.069±0.006	0.028±0.004	0.056±0.009
	0.035±0.005	0.029±0.004		
	0.028±0.005	0.007±0.004		

---

* Values of the crustal parameters used are given in Table 4.2.3.
† All quoted uncertainties represent one standard deviation.
‡ Moment tensor was constrained to be purely deviatoric.
** Duration of the individual time function elements was 2 s.

Table 4.2.3 The Crustal Structure Used for the P-wave Modeling

	Thickness (km)	V_p (km/s)	V_s (km/s)	Density (g/cm^3)
Source Region:				
1. Homogeneous crust	half-space	6.00	3.46	2.5
2. Layered crust	10.0	6.00	3.46	2.5
	16.0	6.75	3.90	2.8
	half-space	8.05	4.65	3.0
Receiver Region:				
	half-space	6.00	3.46	2.5

Table 4.2.4 Summary of Source Parameters of Lice Earthquake Determined in This Study

$m_b = 6.0$, $M_s = 6.7$*	
Double couple mechanism	
Strike ≈270°, Dip ≈50°, Rake ≈50°	
Seismic moment ≈1.0×10^{26} dyne-cm	
Average depth ≈5 km	
Length ≈28 km	
Average width ≈13 km	
Average stress drop ≈18 bars	
Average slip ≈90 cm	
East to west direction of rupture propagation	

*ISC Bulletin

FIGURE CAPTIONS

4.2.1 The Seismicity map of Turkey. The location of the Lice earthquake is indicated by the diamond.

4.2.2 The map of major fault systems of eastern Turkey. The Lice earthquake occurred at the western end of the Bitlis Trust zone. The epicentral location is indicated by rough intensity contours [from Arpat, 1977].

4.2.3 The map of surface faulting and landslides associated with the Lice earthquake [from Arpat, 1977]. The dashed line indicates the intensity VIII contour of Yanev [1975].

4.2.4 The epicenter locations of aftershocks (triangles) following the Lice earthquake [from Baysal, 1977]. Filled circles indicate locations of the recording stations. Note the change of scale with respect to Figure 4.2.3.

4.2.5 The fault plane solution based on P wave first motion polarities (strike=255°, dip=52°, rake=36°). The open and filled circles indicate first motion dilitation and compression, respectively. The large symbols indicate my readings, while the small symbols indicate impulsive short-period first motions reported by ISC (International Seismological Centre). The strike of the northward dipping nodal plane was constrained to agree with the field observations. Also shown are the P wave nodal planes for the solution determined from the waveform inversion of long-period P waves (dashed lines). The projections are on the lower hemisphere of the focal sphere.

4.2.6 (a) The examples of the matches to the data by the different models given in Table 4.2.2. I is for a moment-tensor point source, II is for a double-couple point source, and III and IV are for a propagating line-source. In Models I-III, the assumed source crustal structure was a homogeneous half-space; IV is for a layered crustal structure. The residuals (normalized to the RMS amplitude of the data) for each model are indicated by Greek numbers.
(b) Va is the same as IV in Figure 4.2.6a, but the data and the synthetics were weighted inversely to the power in the individual seismograms. Vb is the same as Va but seismograms were scaled back to their true amplitudes. The residual is also indicated.

4.2.7 The observed (solid lines) and the best-fit theoretical (dashed lines) P wave seismograms for the 1975 Lice earthquake. The theoretical seismograms are for Model IV of Table 4.2.2. The seismogram amplitudes are normalized to instrument magnification of 3000 and epicentral distance of 40°. Also shown are the focal sphere projections of the rays and the nodal planes of the direct P waves. The inferred line-source time function is also shown. The rupture propagated from the east to west at a velocity 2.6 km/s.

4.2.8 The propagation paths of surface waves to the stations used in this study (equal angle equal distance projection).

4.2.9 Examples of the recorded surface waves (vertical component seismograms, normalized to the largest amplitude).

4.2.10 The observed radiation pattern of the Rayleigh waves at a period of 80 s (squares). The solid line indicates the theoretical pattern using the best-fit P wave solution (Model IV, Table 4.2.2). For comparison, the theoretical patterns corresponding to the P wave first motion solution (dot-dashed lines) and Model V (Table 4.2.2), based on matching P-wave shapes, but not their amplitudes (dashed lines), are also shown. Moment of 1×10^{26} dyne-cm was used for all three theoretical patterns.

4.2.11 The fault plane solutions of major earthquakes in eastern Turkey. The directions of present tectonic plate motions are indicated by arrows. Except for the 75.9.6 (Lice) and 76.11.24 (Caldiran) earthquakes which are invesigated in this thesis, the fault plane solutions for the other events were determined from P wave first motion polarities by McKenzie [1972, 1976].

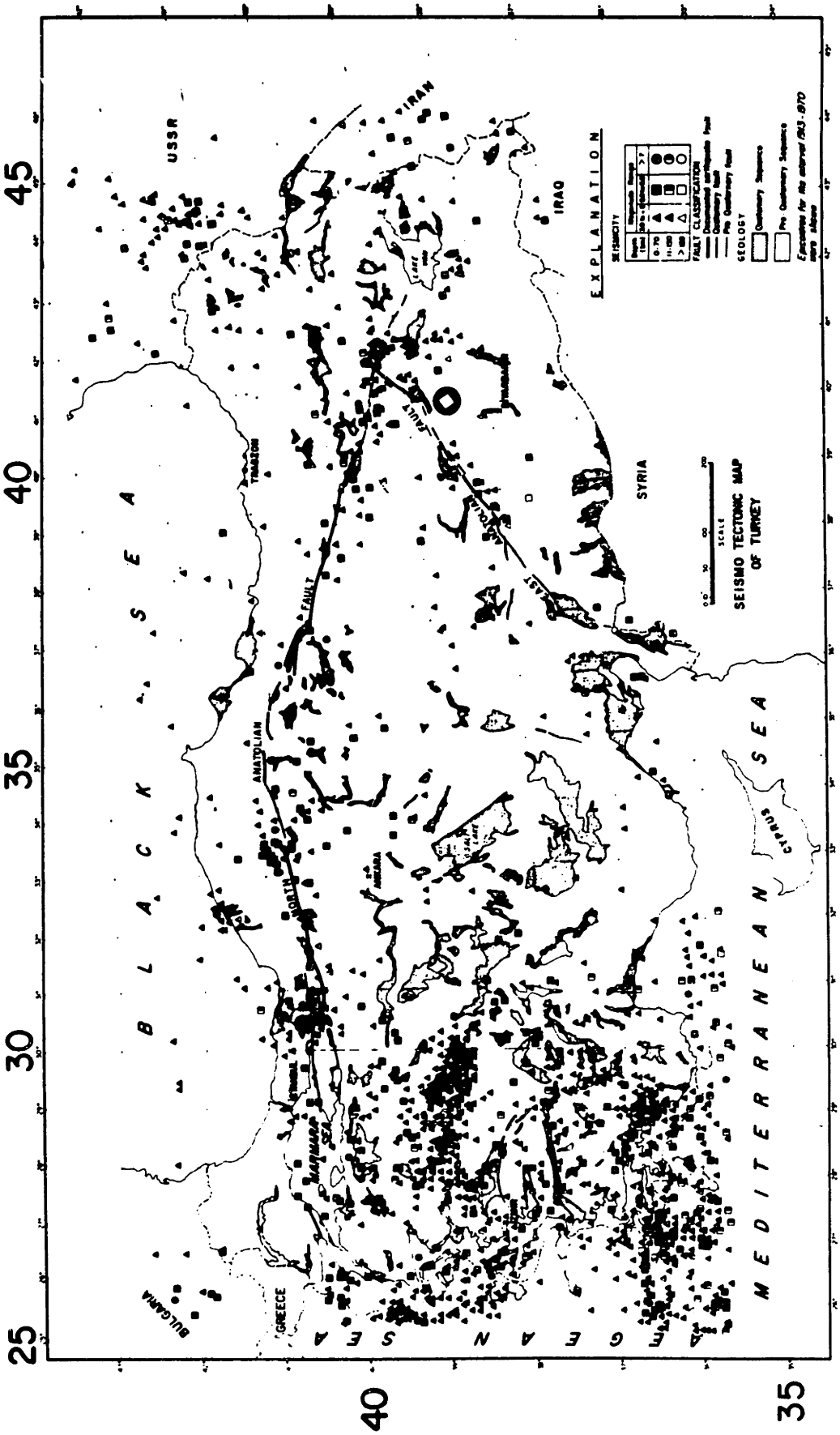
BLACK SEA
MEDITERRANEAN SEA
AEGEAN SEA
USSR
IRAN
IRAQ
SYRIA
GREECE
BULGARIA
CYPRUS
NORTH ANATOLIAN FAULT
EAST ANATOLIAN FAULT
TIMARSON
ANKARA
EXPLANATION
SEISMICITY
FAULT CLASSIFICATION
GEOLOGY
SCALE
SEISMO TECTONIC MAP OF TURKEY
25
30
35
40
45
40
35

Figure 4.2.1

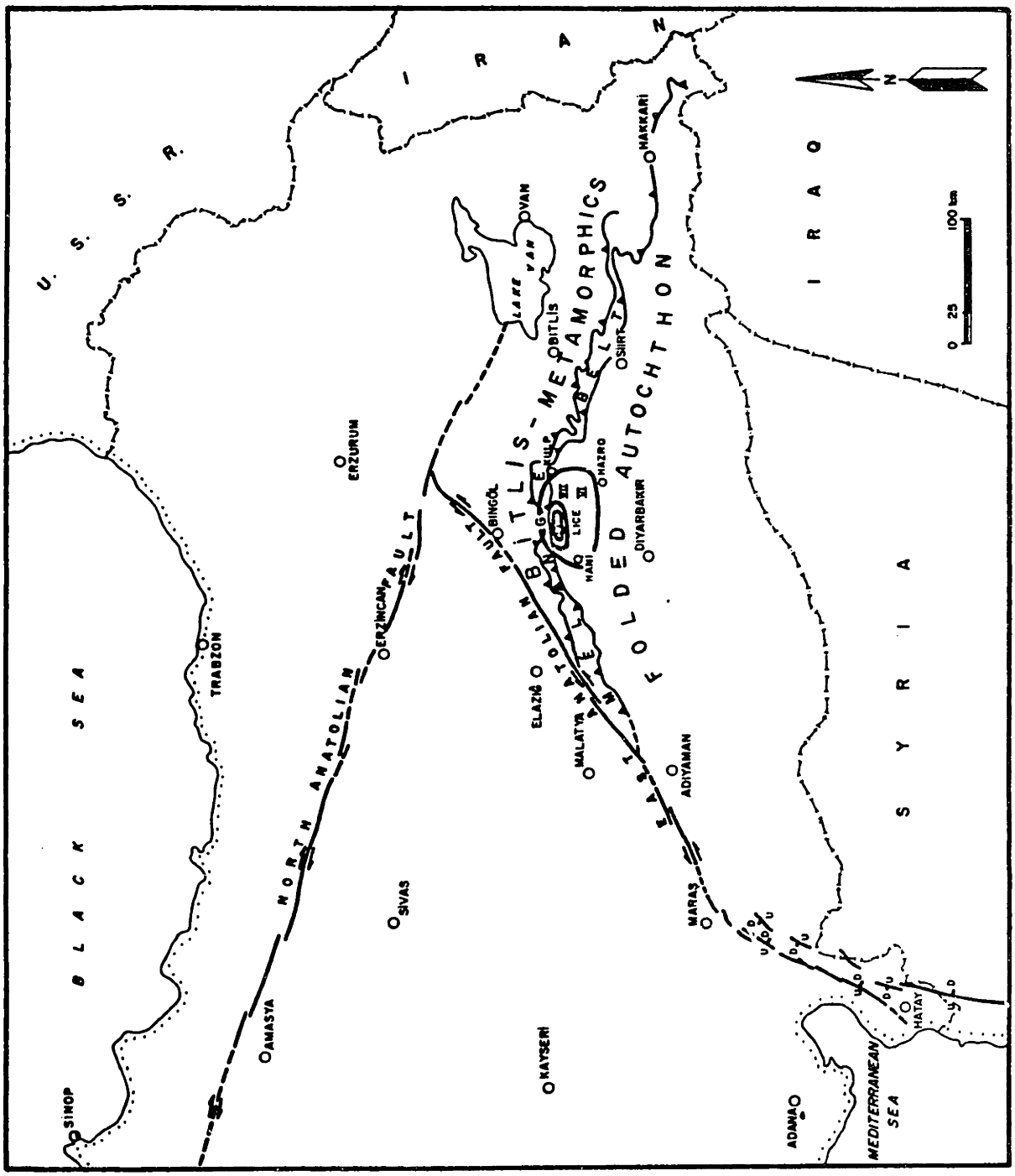
U. S. S. R.
I R A N
I R A Q
S Y R I A
BLACK SEA
MEDITERRANEAN SEA
LAKE VAN
VAN
BITLIS
SIIRT
HAKKARI
ERZURUM
BINGÖL
MUŞ
MAZRO
LICE
DIYARBAKIR
ELAZIĞ
MALATYA
ADIYAMAN
MARAŞ
ERZINCAN
TRABZON
SINOP
AMASYA
SIVAS
KAYSERI
ADANA
HATAY
NORTH ANATOLIAN FAULT
EAST ANATOLIAN FAULT
BITLIS-METAMORPHICS
FOLDED AUTOCHTHON
N
0 25 100 km

Figure 4.2.2

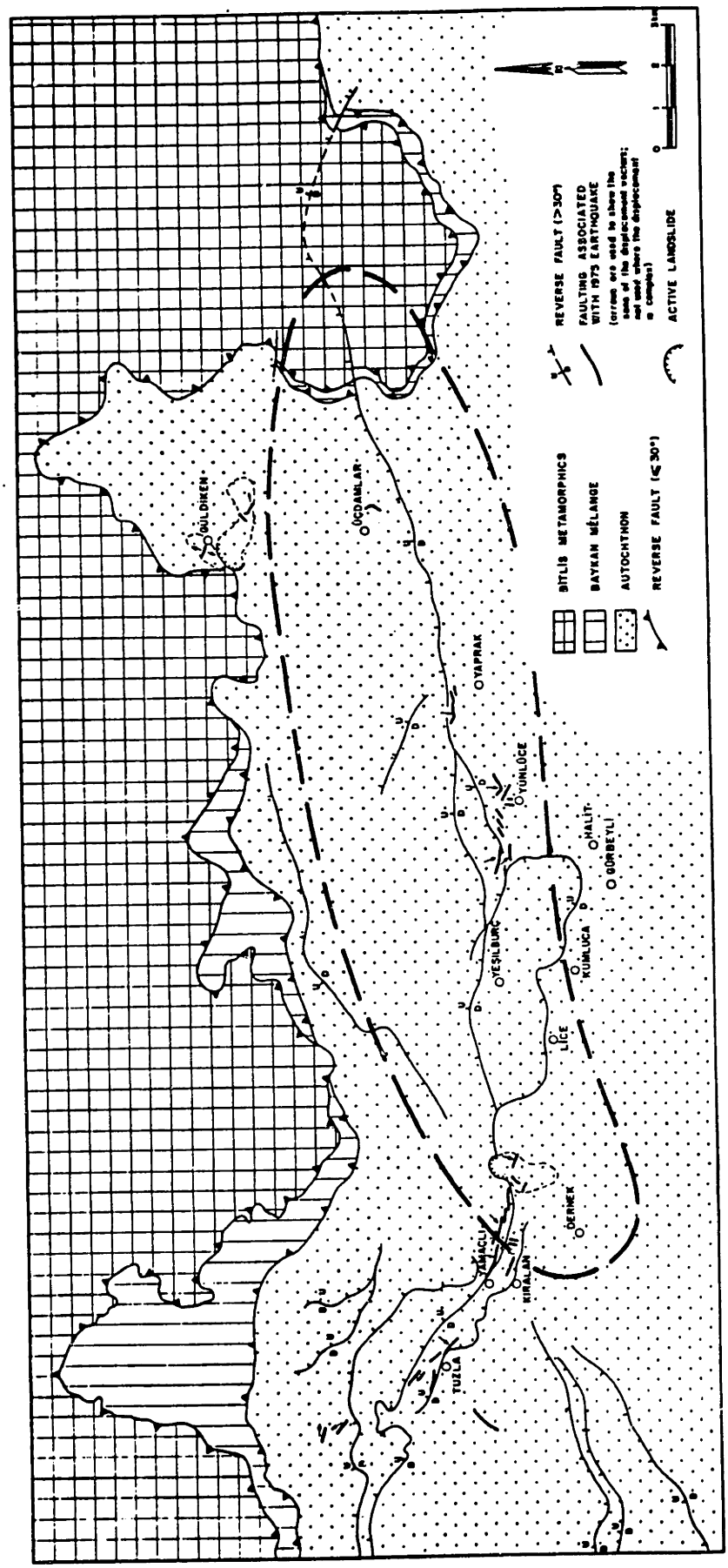
BITLIS METAMORPHICS
BAYKAN MÉLANGE
AUTOCHTHON
REVERSE FAULT (≤ 30°)
REVERSE FAULT (> 30°)
FAULTING ASSOCIATED WITH 1975 EARTHQUAKE
ACTIVE LANDSLIDE
GÜLDIKEN
ÖDAMLAR
YAPRAK
YÜNLÜCE
HALIT-
GÖRBEYLI
YEŞILBURÇ
KUMLUCA
LICE
DERNEK
YAYACLI
KIRALAN
TUZLA

Figure 4.2.3

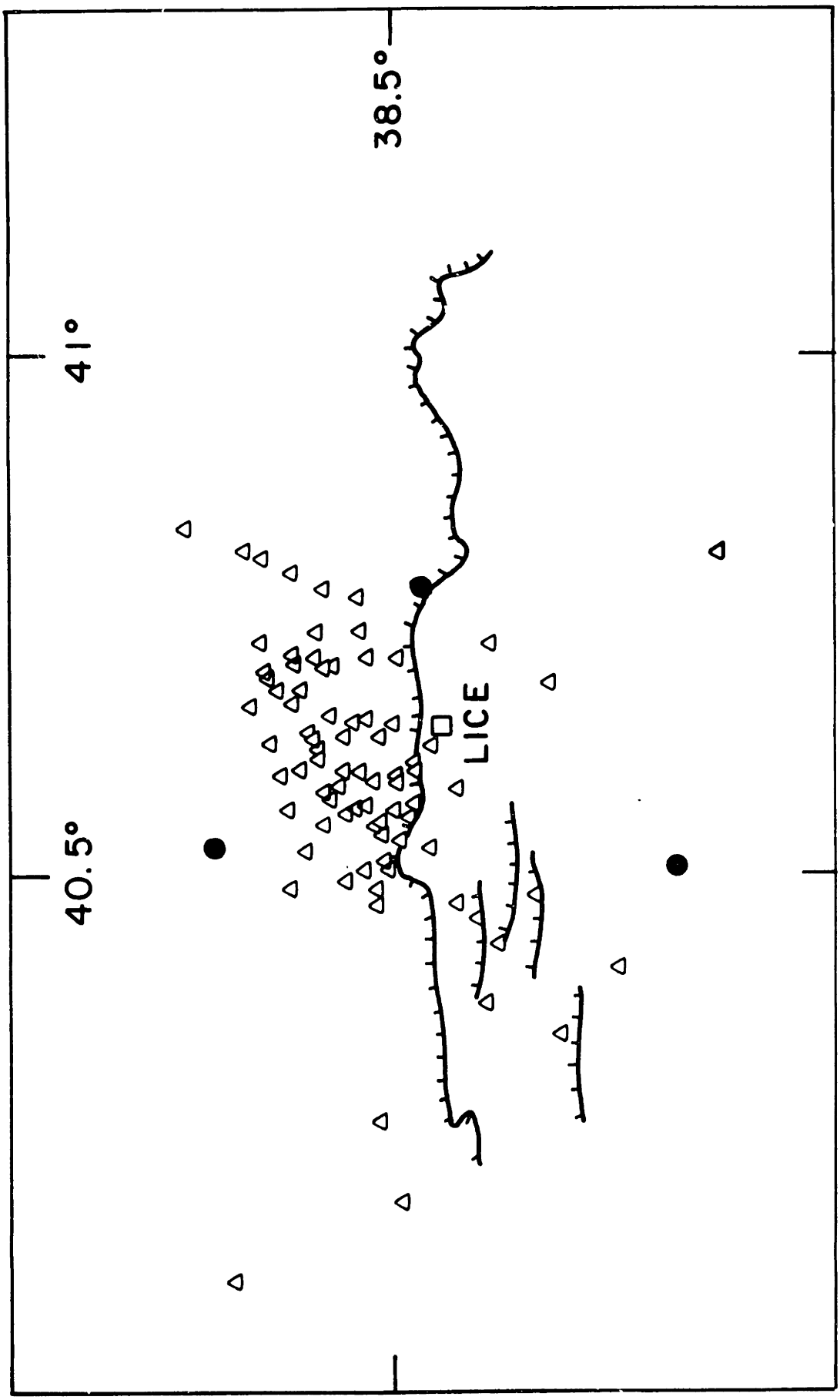

Figure 4.2.4

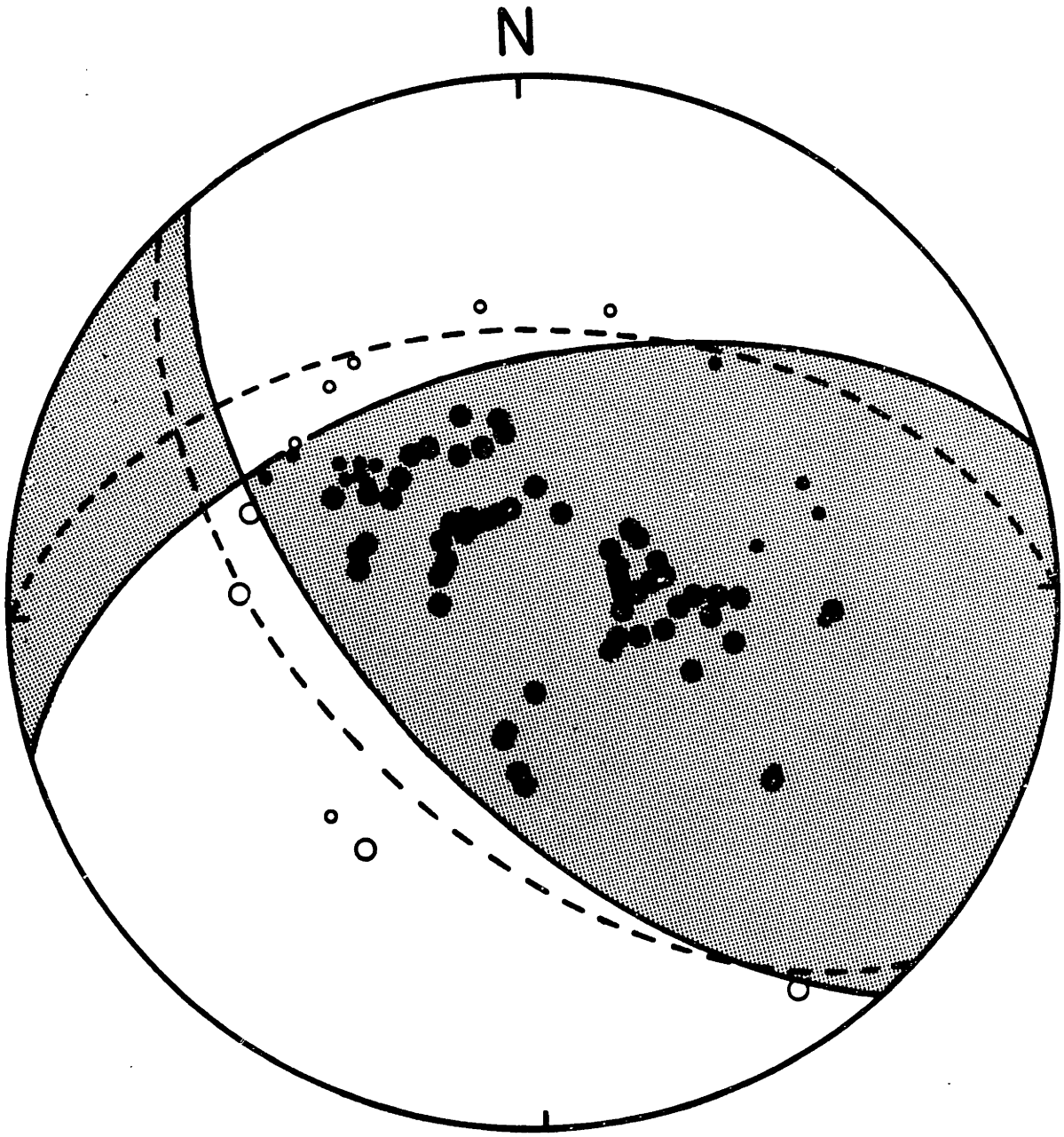

Figure 4.2.5

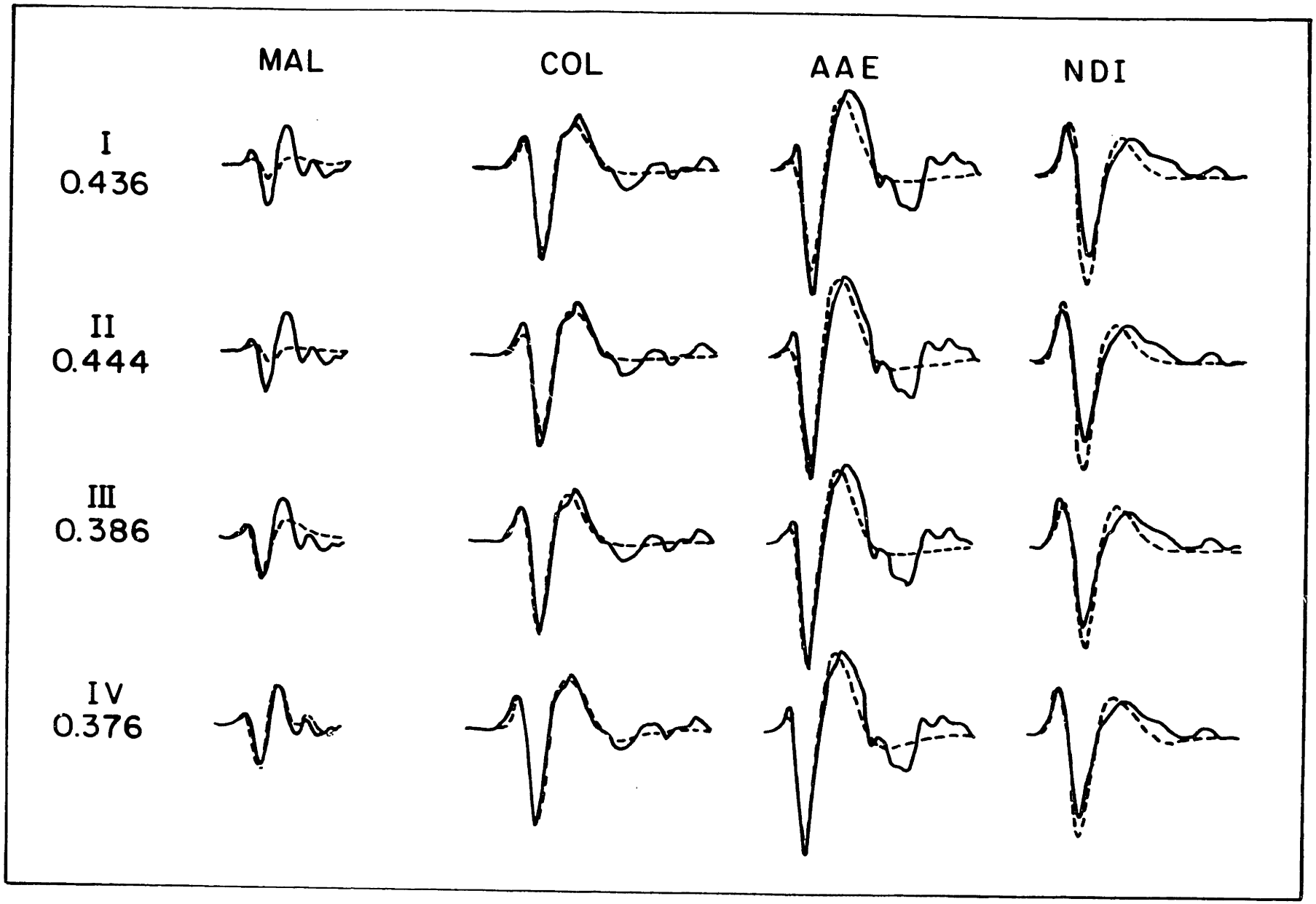

Figure 4.2.6a

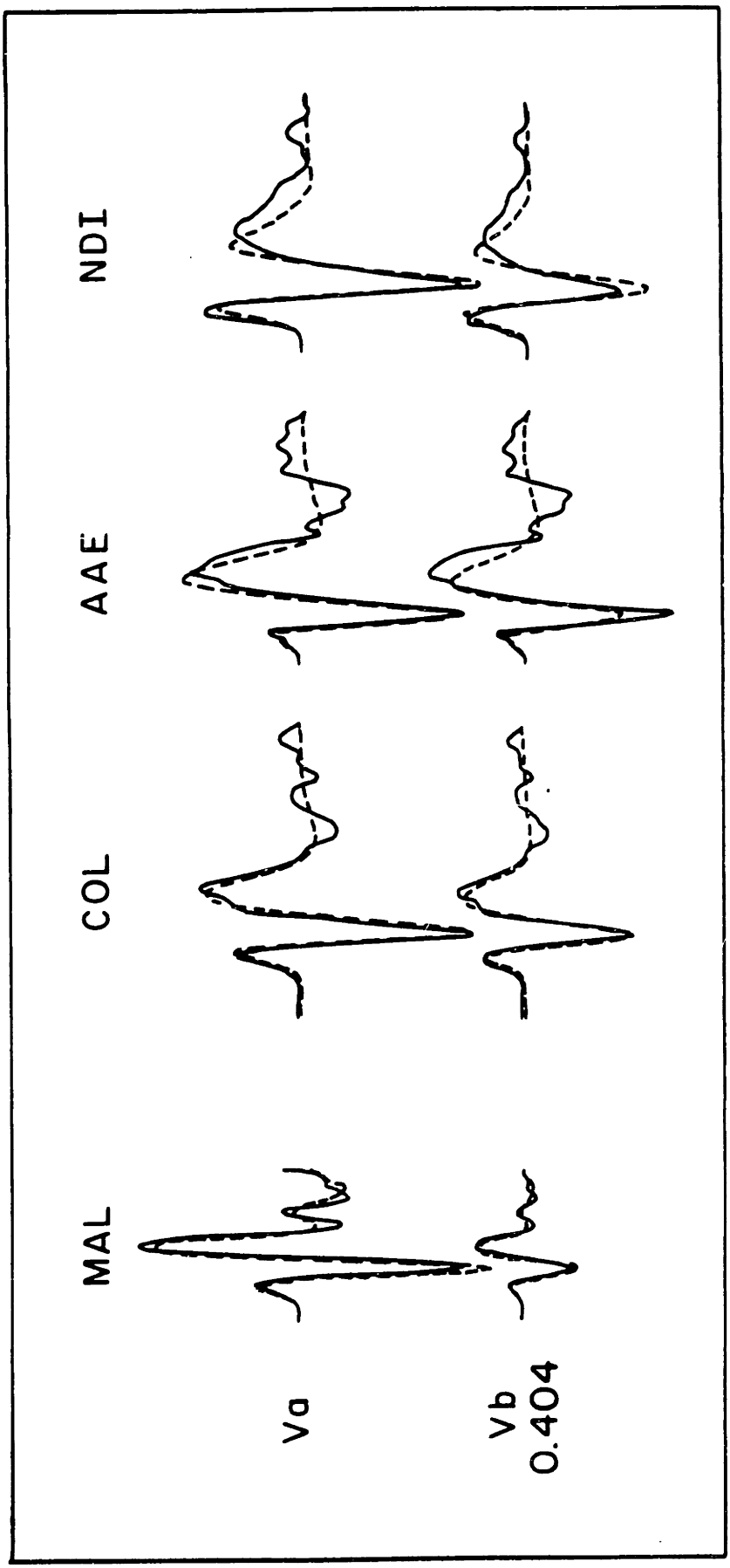

Figure 4.2.6b

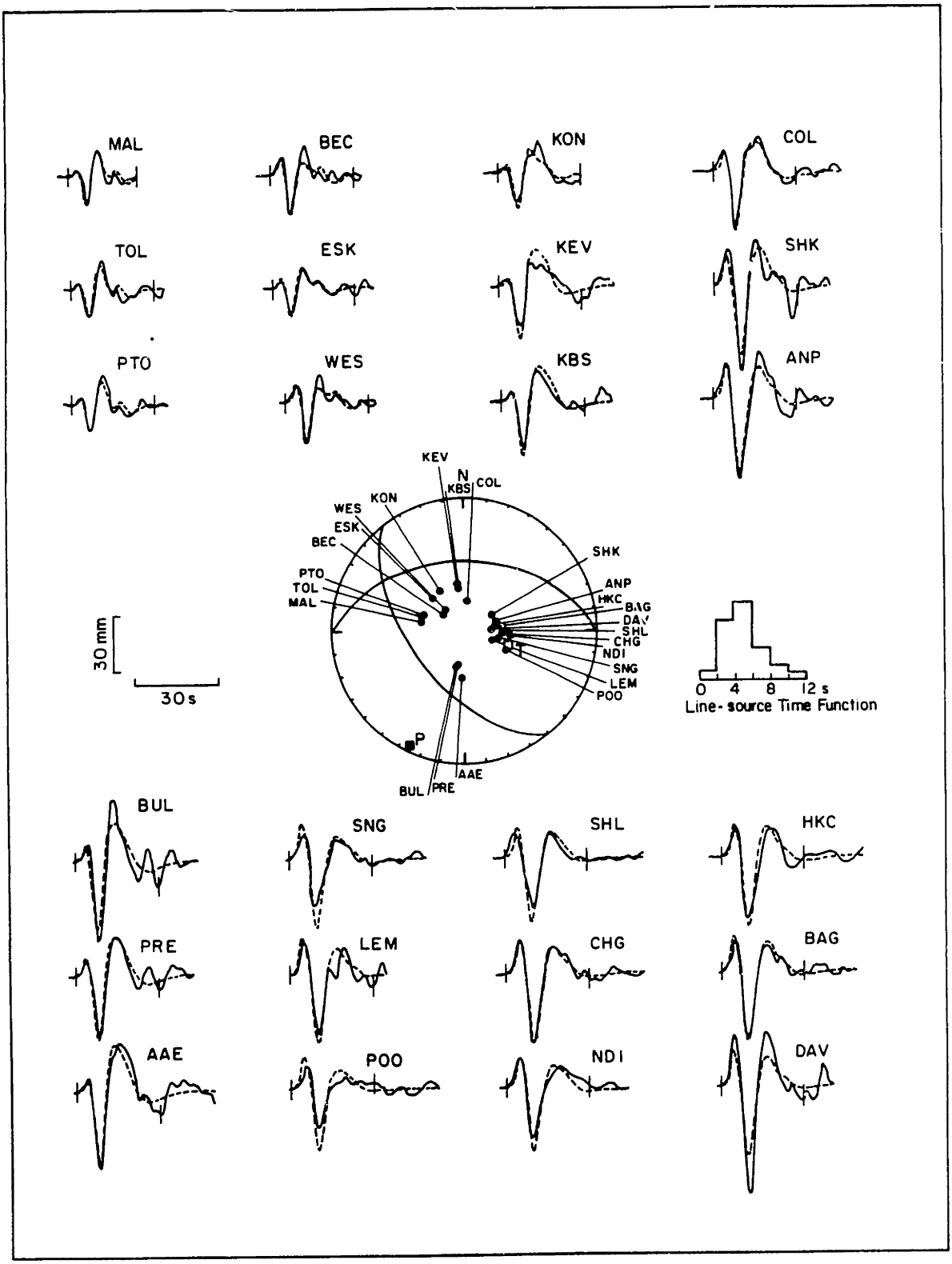
MAL
BEC
KON
COL
TOL
ESK
KEV
SHK
PTO
WES
KBS
ANP
KEV
N
KBS
COL
KON
WES
ESK
BEC
PTO
TOL
MAL
SHK
ANP
HKC
BAG
DAV
SHL
CHG
NDI
SNG
LEM
POO
P
BUL
PRE
AAE
30 mm
30 s
0 4 8 12 s
Line-source Time Function
BUL
SNG
SHL
HKC
PRE
LEM
CHG
BAG
AAE
POO
NDI
DAV

Figure 4.2.7

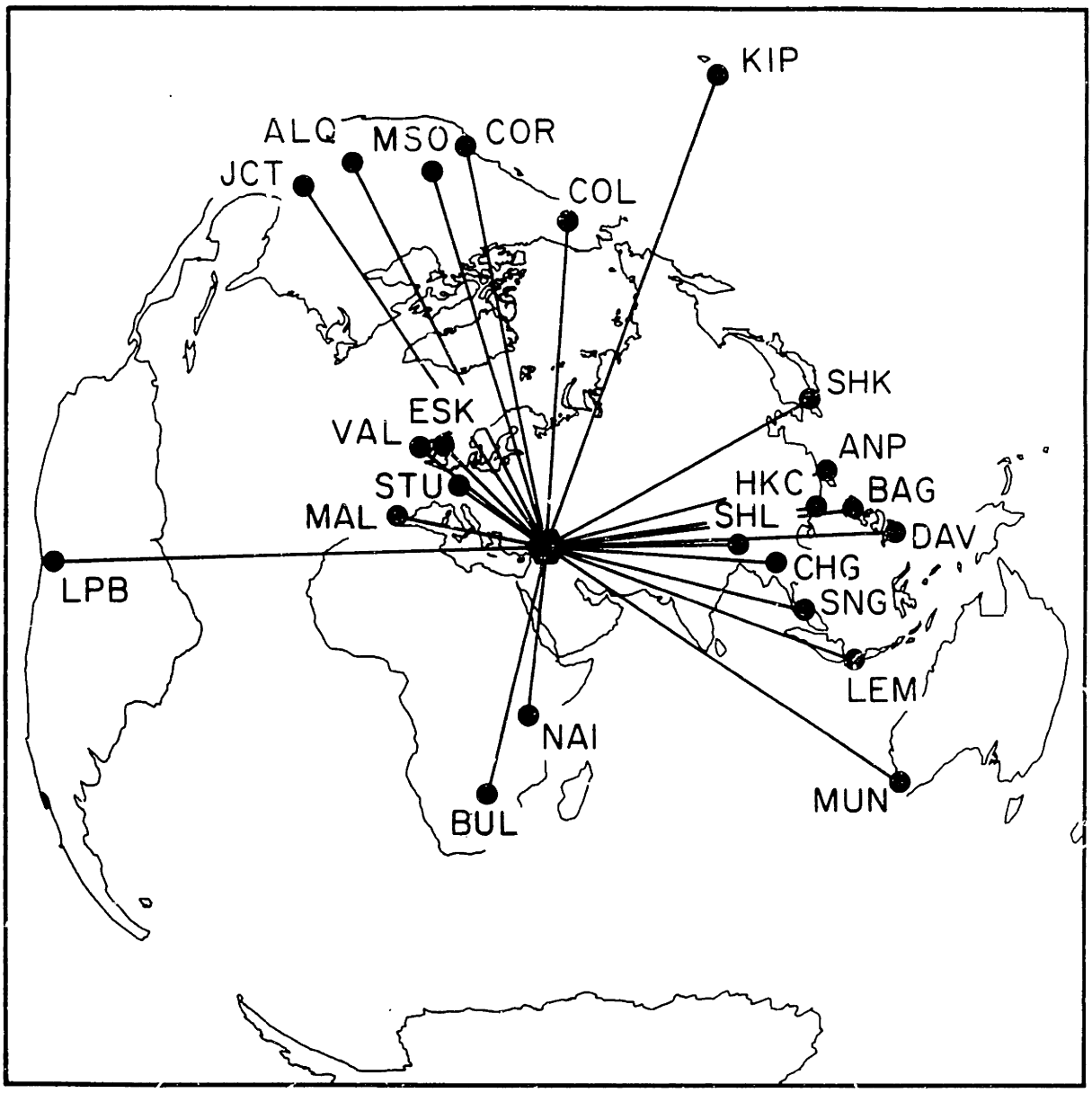
KIP
ALQ
MSO
COR
JCT
COL
SHK
ESK
VAL
ANP
HKC
BAG
STU
SHL
MAL
DAV
CHG
LPB
SNG
LEM
NAI
MUN
BUL

Figure 4.2.8

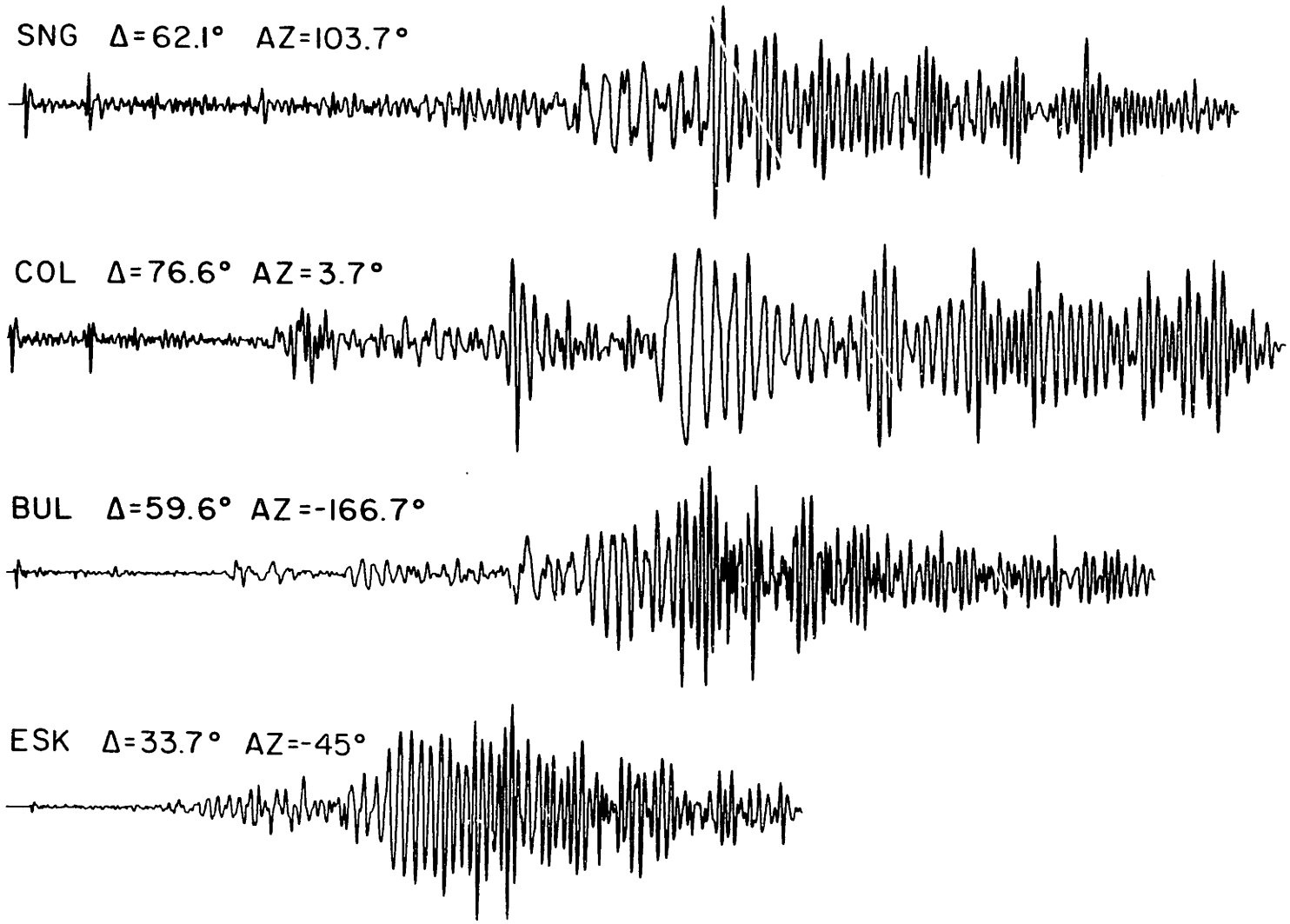
SNG Δ=62.1° AZ=103.7°
COL Δ=76.6° AZ=3.7°
BUL Δ=59.6° AZ=-166.7°
ESK Δ=33.7° AZ=-45°
5 min

Figure 4.2.9

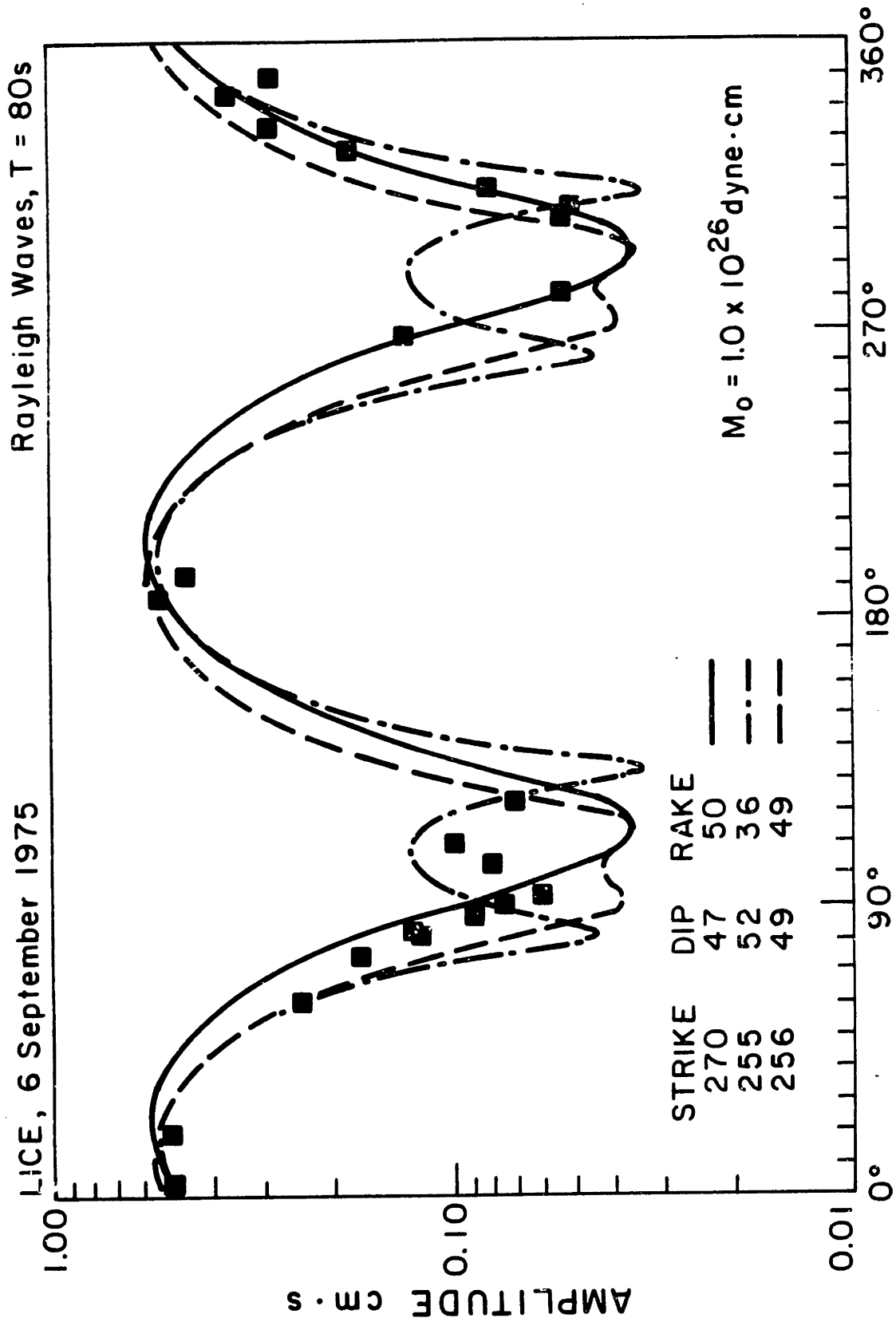
LICE, 6 September 1975
Rayleigh Waves, T = 80s
$M_o = 1.0 \times 10^{26}$ dyne·cm
STRIKE DIP RAKE
270 47 50
255 52 36
256 49 49
AMPLITUDE cm·s
1.00
0.10
0.01
0°
90°
180°
270°
360°
AZIMUTH

Figure 4.2.10

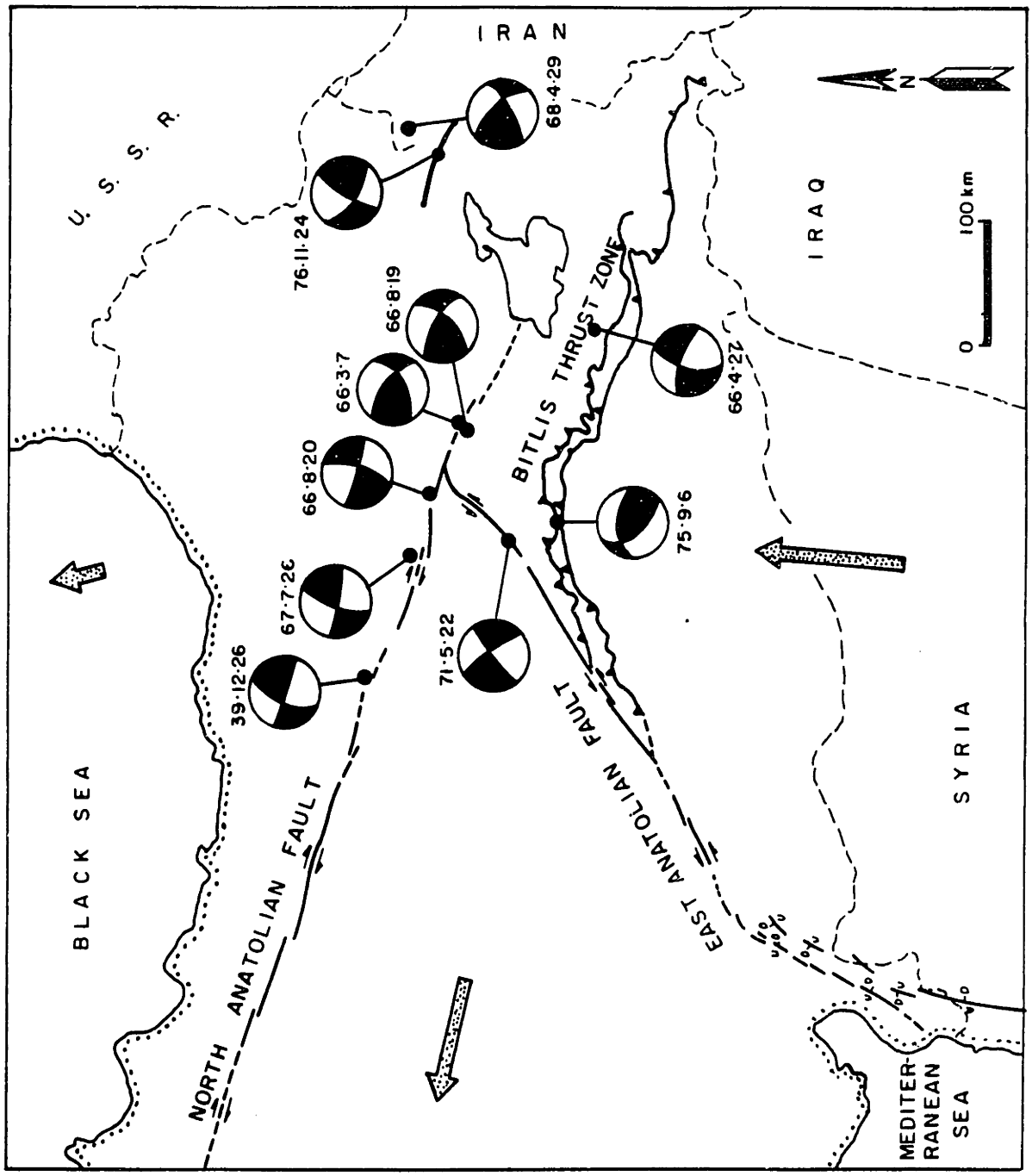
U. S. S. R.
IRAN
IRAQ
SYRIA
BLACK SEA
MEDITER-
RANEAN
SEA
NORTH ANATOLIAN FAULT
EAST ANATOLIAN FAULT
BITLIS THRUST ZONE
39·12·26
67·7·26
66·8·20
66·3·7
66·8·19
76·11·24
68·4·29
71·5·22
75·9·6
66·4·22
N
0
100 km

Figure 4.2.11

4.3 THE JANUARY 9, 1982, NEW BRUNSWICK, CANADA EARTHQUAKE

4.3.1 INTRODUCTION

The New Brunswick earthquake, although of only intermediate size (m_b=5.7; 12:53:52 GMT; 47.0°N, 66.7°W), is an important event because it is the first event in eastern North America large enough to be recorded globally since the inception of the major global seismic networks. Because the propagation of regional phases in eastern North America is still poorly understood, source parameters of smaller earthquakes are subject to large uncertainties [Aggarwal and Sykes, 1978; Yang and Aggarwal, 1981; Pulli and Toksoz, 1981; Pulli, 1983]. Prior to the New Brunswick earthquake the best recorded event was the m_b=5.2 1980 Sharpsburg, Kentucky earthquake [Herrmann et al., 1982]. The New Brunswick earthquake provides the first opportunity to study an event from this region using well-developed techniques of teleseismic source analysis, thus permitting a more reliable estimate of the source parameters which can be directly compared with the results of similar source studies in other regions.

Eastern North America has been the site of infrequent, but large and potentially damaging earthquakes in the past (e.g. 1886 Charleston, m_b=6.8; 1925 Grand Banks, M_s=7.2; 1925 St. Lawrence, M_s=6.7). Because of the high population density, it is important to estimate the potential hazard from such large events. Studies of typical source properties for smaller events, especially stress drop, can provide important clues to the potential hazard from larger events.

This paper presents the results of modeling the short- and long-period body waveforms (P and SH) and Rayleigh wave spectra of the New Brunswick earthquake, using data from the GDSN, WWSSN and Canadian networks. The dataset spans periods of about 0.1 to 80s. The use of short-period data is

particularly important because it allows much better resolution of the source duration, which is usually shorter than 2s for an earthquake of this size. The minimum resolvable source duration using data from long-period WWSSN instruments is about 1.5-2 s. A major obstacle in using short-period wave to infer source properties is that they are quite sensitive to variations in anelastic attenuation. Observed values of t^* (Travel time/$Q_{average}$) for P waves seem to vary from about 1.5 to about 0.3s depending on the propagation path and location of the source [Helmberger and Hadley, 1981; Der et al., 1982] and may be also frequency dependent, with lower values at higher frequencies [Lundquist and Cormier, 1980; Der et al., 1982; Cormier, 1982]. Thus one of our tasks will be to determine the appropriate value(s) of t^* for paths from the New Brunswick region.

The results can be summarized as follows. The New Brunswick earthquake was caused by thrust faulting at a depth of 7 km on a fault plane striking in the north-south direction. The seismic moment was $1.6\pm0.1 \times 10^{24}$ dyne-cm, released over a period of about 0.6s, from which a stress drop of 960 bars is inferred. The short period waveforms indicate the presence of a small precursor about 1 second before main rupture, but the parameters of the precursor are not well resolved. Its moment is approximately 10 times smaller than that of the main event, and its orientation appears to be slightly different. The average value of t^* for paths to stations used in the short-period P wave analysis appears to be approximately 1s, but with large azimuthal variations. The largest values (1.2-1.3s) were observed in the western U.S. and the smallest values (0.6-0.8s) were observed for South American stations.

The site of the New Brunswick earthquake has been a region of scattered seismicity with events of magnitude up to 3 in the past (Figure 4.3.1). The epicenter was located in the middle of a granitic pluton of the Miramichi Anticlinorium, at a site with no observable geologic faulting (Figure 4.3.2). The nearest significant geologic fault is the Catamaran Fault, an east-west trending lineament about 20 km south of the epicenter (Figure 4.3.2). From the offset of geologic features cut by the Catamaran Fault, it appears that the sense of displacement is mainly right-lateral strike slip but it is not known if the fault is still active.

4.3.2 INVERSION AND MODELING OF TELESEISMIC BODY WAVES

The inversion procedure has been described in Chapter II and Appendices A and B. I shall again make use of the two objective functions (i.e. measures of misfit)

$$o_i - s_i \tag{4.3.1}$$

and

$$o_i/(\sum_j o_j^2)^{1/2} - s_i/(\sum_j s_j^2)^{1/2} \tag{4.3.2}$$

which are minimized in a least squares sense. The second objective function, which is insensitive to the absolute amplitudes, will be particularly useful in the analysis of the short-period data, where poorly understood variations in t^* and other path effects dominate the amplitude signature of the source. In preliminary inversions of the short-period data, positivity constraints (Chapter II; Appendix 3) were applied to the source time function. This stabilized the inversion and facilitated rapid convergence.

4.3.3 LONG-PERIOD P AND SH WAVES

The data set for the long-period body-wave inversion included seismograms from the GDSN, WWSSN and Canadian seismic networks (Table 4.3.1). To remove very long-period noise and D.C. offset, the GDSN seismograms were high-pass filtered with a three-pole (zero phase) Butterworth filter with a cut-off period of 60 sec, well outside of the dominant period range of the observed body waves. The analog WWSSN and Canadian network seismograms were hand digitized at 0.5 sec intervals. The S-wave seismograms were rotated in order to retrieve the transverse component for the SH analysis.

To deal with variations in data quality at different stations, a weighting scheme which reflects our ability to predict the contributions of the various sources of error in the data was implemented. The signal S generated by the source and recorded on receiver R is affected along its path by the crustal structure in the source region C^s, anelastic attenuation A, geometrical spreading and other losses G, and receiver crustal structure C^r. The recorded signal d can be considered as a convolution of these terms,

$$d = R*C^r*G*A*C^s*S \qquad (4.3.3)$$

The errors in d are mainly due to imprecise knowledge of the path effects, the presence of some background microseismic noise, incomplete parameterization of the source, errors in the assumed source crustal structure and misalignment of the data with the synthetics (it is sometimes difficult to determine exactly where the observed seismogram begins). The errors due to path effects and background noise can be estimated in advance and are reflected directly in our weighting scheme; the others are

difficult to determine in advance and are investigated after the best estimate of the model parameters is made.

To first order, the errors in R, C^r, and G are amplitude factors (small phase errors, to first order, are also reflected in amplitude fluctuations: Chapter III) which are independent of each other and can be summed in quadrature. The error in attenuation is negligible for long-period data. The background noise level can be estimated from the seismogram trace prior to the arrival of the signal. The fractional error of the individual data points due to these uncertainties is,

$$\frac{\Delta d_i}{|d_i|} = \sqrt{\left(\frac{\Delta R}{|R|}\right)^2 + \left(\frac{\Delta C^r}{|C^r|}\right)^2 + \left(\frac{\Delta G}{|G|}\right)^2} + \frac{N}{|d_i|} = M + \frac{N}{|d_i|}, \qquad (4.3.4)$$

where N is the estimated background noise level. When the background noise is small, d_i can be approximated by the observed signal x_i. The final expression for the estimated error of data point d_i at station s becomes

$$\Delta d_i^s = M|x_i^s| + N^s. \qquad (4.3.5)$$

The error increases linearly with amplitude of the signal from a minimum determined by the background noise, N^s. The errors in C^s are not random and cannot be treated statistically; they will be discussed later.

The uncertainty in the instrument magnification is assumed to be about 5%. At long periods, the effect of likely variations in the receiver crustal structure for angles of incidence corresponding to the distance range of 30 to 80° is also about 5%, and the uncertainty in the geometrical spreading and other losses is assumed to be about 10-15%. The combined error M is therefore approximately 15%. The weight,

$$w_i^s = w^s/\Delta d_i^s \qquad (4.3.6)$$

assigned to each data point is inversely proportional to the estimated error; the term w^s allows additional weighting and can be used to compensate for biases such as poor station distribution or systematic variations in the amplitudes of different phases. In this study, w^s was 1.0 for P waves and 0.7 for SH waves. SH waves were given lower weight because of their larger average amplitudes.

For the long-period analysis the source time function is parameterized by a series of box functions of 1.5 seconds duration. This is approximately the time resolution limit of the long-period WWSSN and Canadian network instruments. The assumed source and receiver crustal structure is a halfspace with compressional velocity of 6.0 km/s, shear velocity of 3.46 km/s and density of 2.8 g/cm^3 Five sets of inversions were performed: (1) first both P and SH waves simultaneously using moment tensor parameterization of the source; (2) after confirming that the source is well-characterized as a pure double couple, as one would expect for an earthquake, the inversion was repeated using a double-couple constraint; then in order to test the stability of the inversion, (3) P and (4) SH waves were inverted individually, and (5) the inversion was performed using the second objective function (eq. 4.3.2) which is sensitive to the shapes but not to the absolute amplitudes of the seismograms. The results are summarized in Table 4.3.2. The synthetic waveforms for the joint P and SH inversion (2) (Table 4.3.2) are compared with the observed data in Figure 4.3.3. The matches are within the estimated uncertainty in the data; the worst matches are obtained for the noisiest stations (e.g. ANMO) which also carried the least weight in the inversion.

The data indicate essentially pure thrust faulting at a depth of 7 km on a fault striking in the north-south direction. The dips of the P-wave

nodal planes are approximately 54° west and 30° east. The seismic moment is 1.6 x 10^{24} dyne-cm. The source time function obtained from the inversion is only 1.5 seconds (1 unit) long, implying that the far-field time function was essentially an impulse with respect to long-period instruments.

The P and SH waves complement each other in constraining the orientation. Because of deficient station distribution and dip-slip source mechanism, the P waves alone provide little constraint on the strike and rake of the fault. This is reflected in large standard errors of the strike and rake angles when only P waves are used in the inversion (Table 4.3.2). Since three of the four lobes of the SH radiation pattern are sampled by the data, the SH waves are much more sensitive to changes in these angles. The SH waves alone, however, cannot distinguish between a vertical strike-slip and a 45° degree dipping normal or thrust fault.

The a posteriori standard deviation of the weighted data (for definition, see Appendix B) is approximately one, which indicates that the a priori data error estimates were reasonably accurate, and that the source is sufficiently parameterized. The formal standard errors of the source parameters for the combined P and SH inversion are very small and most likely underestimate the true uncertainty in the estimated parameters. The estimated errors do not include uncertainties in the source crustal structure and misalignment of the synthetics with the observed data.

Although the effect of misalignment tends to average out when a large number of stations is used, it can cause a substantial bias in the estimated source parameters if it is azimuthally dependent. In this study, the onset of the waveform was first assumed to be the theoretical arrival

time. After convergence to a solution, it was allowed to vary by up to 2s if a better cross-correlation between the observed and synthetic waveforms could be found. The computation was then restarted, resulting in the final solution.

In order to obtain a more realistic picture of the uncertainties in the source parameters, I performed additional inversions using different source crustal models, longer time function elements, and altered weighting of individual stations. The effect of misalignment was investigated by varying the assumed initial time of the observed seismograms. The misalignment of the P waves was minimized by comparing the long- and short-period P wave arrival times. The results of these inversions suggest that more realistic uncertainties in the estimated source parameters inferred from the long-period body wave data are: strike ±10°, dip ±3°, rake ±10° and depth ±1 km. The time function duration appears to be less than 2.0 seconds (with the strongest constraints coming from stations of the WWSSN and Canadian network) but the long-period data cannot resolve how much shorter it might be.

The long-period description of the source within the above uncertainties is certainly sufficient for most geotectonic studies. In order to estimate the stress drop or displacement on the fault, however, we must improve the resolution of the fault dimensions. For this it is necessary to consider shorter period data.

4.3.4 SHORT-PERIOD P WAVES

Because of the small size of the event and some instrument malfunctions, the azimuthal coverage of the long-period P-wave data was poor. The azimuthal distribution of well-recorded short-period P waves is considerably better. After high-pass filtering with a cut-off at 0.4 Hz, the short-period waveforms at adjacent stations show remarkable coherency. The wave shapes change smoothly across the focal sphere, suggesting that the source radiation pattern is the dominant factor (good coherency of short-period records has been noted and successfully utilized by Hartzel [1980], Cipar [1981], and Ebel and Helmberger [1982] in studies of other events). The high-pass filtering was done only on the GDSN data to remove D.C. offset and long-period noise present at some stations; stations with good signal-to-noise ratio were not visibly affected by this filtering. The observed data and the best-fit theoretical seismograms are shown in Figure 4.3.4. Because the absolute amplitudes of the waveforms appear to be mainly controlled by path effects, only the wave shapes were inverted. The inversion was performed on the first 6 seconds of the waveform after the onset of the direct P arrival. The inferred source parameters and their formal uncertainties are summarized in Table 4.3.3.

With the improved time resolution of the short-period records, we can see that the earthquake is composed of two discrete subevents 0.7 seconds apart. The seismic moment of the first subevent is approximately 10 times smaller than the second and it can be identified only as a small oscillation prior to the larger arrivals at stations in the northern, southern and western quadrants of the focal sphere. This oscillation is not observed at eastern stations, suggesting that the dip of first subevent was slightly different from that of the second. The mechanism of this

small precursor is poorly resolved and was fixed in the inversion; the dip was adjusted to satisfy the amplitude and the polarity of the initial part of the records, while the strike and rake were kept approximately equal to the strike and rake of the second subevent. The exact duration of the first subevent is not well determined; the main portion of the energy appears to be released in about 0.2-0.4s. The seismic moment is 0.15 x 10^{24} dyne-cm. The source depth is poorly resolved because the depth phases (pP, sP) are buried in the signal from the second subevent. The inversion indicates two possible depths: one at 8 km, and one at 6 km (Figure 4.3.5). For the reasons discussed below, I prefer the deeper solution as the more likely of the two.

An emergent character of the small precursory event and background noise make it difficult to identify the initial time of the seismograms at some stations. In these cases, the initial time was determined by correlation with less noisy stations (e.g. DUG, ALE, BOCO). A comparison with the signal from an aftershock, which will be discussed later, helped distinguish source effects from path effects and helped determine the initial time of the direct arrival at the Albuquerque, N.M. stations ANMO and ALQ. It will be shown that the energy arriving prior to the assumed initial time at ANMO and ALQ is probably related to a crustal or mantle heterogeneity below these stations.

The parameters of the second subevent are well resolved by the short-period data and agree with those determined from the long-period records. The best-fitting double-couple orientation has strike 174°, dip 54°, and rake 85°; the seismic moment is 1.4 x 10^{24} dyne-cm; the average (centroidal) depth is 6.9 km; the time delay with respect to the origin time of the first subevent is 0.7s; the rupture duration is 0.4s. The

centroidal depth is particularly well-resolved by the short-period dataset. The inferred moment and rupture duration are very sensitive to the assumed value of t^*. These results assume a value for t^* of 1.0s at all stations; the reasons for this choice will be discussed in the next section.

In order to obtain a better estimate of the fault dimensions and to determine if directivity is resolvable in the observed waveforms, the source was modeled as a propagating line source. Because of the steep take-off angles of the rays contributing to the seismograms at teleseismic distances and the small size of the event, the waveforms are expected to be sensitive mainly to the vertical component of rupture. The effect of rupture propagation along the dip of the fault is introduced into our formulation by varying the time function duration of each elementary seismogram $H_i(t)$ according to the formula

$$\Delta\tau_i = \Delta\tau\{1 - v^{\delta}[-\eta_i \sin\delta + p \cos\delta \sin(\phi-\theta)]\} \qquad (4.3.7)$$

$H_i(t)$ and all other parameters are defined in Chapter II and Appendix A. The term containing the ray parameter p represents the directivity due to the horizontal component of the propagating line source, and is very small; it was kept in the formulation because, if observable, it could help in distinguishing the fault plane from the complementary plane of the double couple. The assumed rupture velocity v^{δ} is 2.5 km/s. Figure 4.3.6 illustrates the effect of source finiteness on the short-period waveforms. Up-dip propagating rupture increases the amplitude of the reflected phases and decreases the amplitude of the direct arrival. The reverse is observed for down-dip rupture. (Due to narrow bandwidth of the short-period data, the effect on the pulse width is less apparent.) The residual relative to the observed waveforms is essentially identical for the upward propagating line source models and the point-source model, but the downward propagating

models are inferior (Figure 4.3.6). A scenario that is consistent with these results and the bounds on the possible depths of the two subevents (Figure 4.3.5) is that the precursor occurred at a greater depth than the main event and the rupture propagated upward, but the evidence is far from being conclusive. The data cannot resolve which P-wave nodal plane corresponds to the actual fault plane; I choose to present the results in terms of the west-dipping fault plane because it is preferred by some other investigators [Wetmiller et al., 1982; Choy et al., 1983] and thus allows an easier comparison with their results.

4.3.5 t_p^* FOR MANTLE TRAVEL PATHS FROM THE NEW BRUNSWICK REGION

Values of t^* for P waves at 1 Hz are known to vary between 1.3 and 0.5s depending on the propagation path [Der et al., 1982; Cormier, 1982]. At higher frequencies, t^* is much less certain because in order to generate enough energy to be observed at teleseismic distances, the source has to be of considerable size, and the source time function cannot be considered to be an impulse, even for explosions. All t^* measurements at frequencies higher than 1 Hz, therefore, depend strongly on assumptions about the behavior of the source. Many studies indicate, however, that t^* may decrease with frequency, dropping to values of 0.2-0.3 s at about 8 Hz for some paths [Der et al., 1982; Cormier, 1982].

The results of the modeling constrain the duration of the main subevent to less than 1s. This result is independent of the assumed t^* within the bounds of values discussed above. Due to the lack of t^* measurements for paths from eastern North America, we must be able to estimate the correct value from our data if better constraints on the source time function are desired. Because of the trade-off between the

source time function and t^*, certain assumptions about their behavior are necessary. The first assumption is that t^* is constant from long-periods to a period of about 1s; the second assumption is that the source has a flat amplitude spectrum from long periods to about 2-1.5s (the longest significant periods in the short-period records). The second assumption is crucial, because it implies that the seismic moments determined from the long- and short-period records should be equal. The moment determined at long periods is not very sensitive to the assumed attenuation and can be used as a standard for the shorter periods if this assumption is correct.

After the best match to the waveshapes of the short-period data was determined, the seismic moment was estimated by matching the absolute amplitudes in the least squares sense. An excellent match between the long- and short-period moments can be obtained when the average t^* to all stations is about 1s. For a t^* of 0.6s, the short-period moment is under-estimated by about 40%. The t^* of 1s is average in a crude sense, because the scatter in the absolute amplitudes of the short-period seismograms with respect to the average model is large (that was why we inverted only wave shapes, when originally determining the source mechanism). The match of the best-fitting average model (Table 4.3.3 and t^* = 1s for all stations) to the absolute amplitude short-periods data is shown in Figure 4.3.7. Also shown are the matches after the correction to t^* for individual stations was made, assuming the amplitude differences are mainly due to attenuation along a given path. The highest attenuation (t^* of 1.2-1.3s) is observed for paths to stations in California (JAS) and New Mexico (ANMO and ALQ); the least attenuation (t^* of 0.6-0.8s) occurs for stations in South America (BOCO and ZOBO). Since the power of the short-period data is concentrated around a period of 1s, the t^* determined

here applies only for those periods. Although the absolute values of t^* quoted in Figure 4.3.7 are probably less certain because they depend on the assumption we made about the source (i.e. that the long- and short-period moments should be equal), the relative differences in t^* among stations are probably correct because the source orientation and its radiation pattern are well constrained by the waveforms of the observed records.

4.3.6 BROAD-BAND P WAVES

Due to the response characteristics of the long-period and short-period instruments (further accentuated by high-pass filtering of the short-period data) there is little information about the behavior of the source at very short periods and periods in the range of about 1.5-3s. Thus any source complexities in these bands might have gone undetected. These undesirable instrumental characteristics strongly limit our view of the true ground motion and must be removed by deconvolving the instrument response. Since we are primarily interested in periods shorter than 5s, only deconvolution of the short-period traces is necessary. Due to background noise, only stations ZOBO and BOCO could be successfully deconvolved. The resulting broad-band traces (flat in the period range of 0.1 to 10s) of the ground displacement and velocity are shown in Figure 4.3.8. Nearly all of the energy arrives in the first 5 seconds at these stations. According to our model, the observed positive displacement pulse corresponds to the direct P arrival and the negative pulse to the pP; the sP is very small and is difficult to identify. The precursor blends with the main event in the displacement records but can be easily distinguished in the velocity records.

Since the source mechanism was well constrained in the previous analysis, the mechanisms of both the precursor and the main event were fixed during the analysis of the broad-band records. Fortunatelly, the sP phase is nodal for these two stations, thus reducing interference between phases and improving the resolution of the source time function. Although the sP corresponding to the overall best-fitting source mechanism is close to being nodal, its amplitude is somewhat larger than that actually observed at these two stations (a discrepancy possibly due to a small error in the ray parameter or small inclination of the free surface in the source region [Langston, 1977]; such errors become significant only when a phase is near its node; the P and pP, being further from the nodes, should not be as sensitive to local structural deviations with respect to the average earth model). Care must be taken not to alias this discrepancy into the estimate of the source time function. In order to avoid this problem, only the time window before the arrival of the sP was considered.

Both displacement and velocity records were inverted simultaneously. The velocity records were given half the weight of the displacement records, because of their larger amplitude. A t^* of 0.7s, the average value for these two stations determined in the previous analysis, was used (Figure 4.3.7). Because these two stations do not show significant directivity, the point source model was used. The source time function determined in this inversion is very similar to that obtained from the standard short-period records (Figure 4.3.8). The duration of the main event (0.4s) remains unchanged. The main difference between the results of the broad-band and short-period analyses is the partitioning of the moments between the subevents; the broad-band data requires a relatively larger

moment for the precursor (0.4 : 1.2 x 10^{24} dyne-cm; which may simply be an artifact of errors in the mechanism for the precursor and limited station distribution). The total moment of the two events is 1.6 x 10^{24} dyne-cm.

In view of the possibility that t^* decreases at high frequencies, the constant t^* attenuation operator [Futterman, 1962] was replaced by a band-limited attenuation operator [Liu et al., 1976; Minster, 1978] in which at high frequencies $t^* \approx t_m^* \frac{2}{\pi} \tan^{-1}(\frac{1}{2\pi f \tau_m})$. I take t_m^* = 0.8s and τ_m = 0.08s; thus the t^* at 1 Hz is 0.7s and falls to 0.12s at 10 Hz (these values approximately satisfy the results of the previous analysis and Der et al. [1982]). The inversion using this frequency dependent t^* indicates a somewhat longer source duration (0.6s) while the match to the data is indistinguishable from that obtained for the constant t^* case (Figure 4.3.8). Because the attenuation at periods longer than 1s is not affected by this operator, the seismic moment estimate was unchanged.

Had we, however, assumed a constant t^* of 0.4s (the value used by Choy et al. [1983]), the moment would be underestimated by about 30%. Although one might expect that because we are working with a broad-band signal it should contain long enough periods to be insensitive to the assumed attenuation, the presence of the pP free surface reflection causes a peaked spectrum even in the broad-band signal. The power of the broad-band signal at these two stations is concentrated between periods of 2 to 4 seconds, causing the absolute amplitudes of the synthetics to be scaled mainly to the signal at those periods. If we assume that the long-period seismic moment determined in section 4.3.3 should be equal to the seismic moment determined here, the t^* of 0.4s at periods of 4-2s is inadmissible.

Based on the results discussed above it can be concluded that the duration of the rupture of the main subevent was 0.4-0.6s. The rupture duration of 0.8s obtained by assuming the constant (frequency independent) t^* of 0.4s is probably a conservative upper bound.

4.3.7 COMPARISON WITH THE SURFACE WAVE DATA

In this section we shall check the consistency of the source model inferred from short- and long-period body waves with the observed surface wave radiation. The New Brunswick earthquake has an ideal magnitude and location for a surface wave study. The data quality is high, with good azimuthal coverage and paths which are shorter than 40° and generally cross only a single tectonic province. The station coverage is displayed in Figure 4.3.9. The dataset consists of the digital GDSN data, supplemented by hand-digitized WWSSN and Canadian Network seismograms. The consistency of the dataset can readily be seen from Figure 4.3.10; the seismograms in this figure were equalized to a common distance, phase velocity dispersion, and seismometer type and magnification. The equilization was accomplished in the frequency domain using the formula:

$$u_o(\omega) = u(\omega)\, F(\omega) \frac{\sqrt{\sin \Delta/a}}{\sqrt{\sin \Delta_o/a}} e^{i\omega(\frac{\Delta}{c} - \frac{\Delta}{c_o})} e^{\frac{\omega}{2Q(\omega)}(\frac{\Delta}{\omega} - \frac{\Delta_o}{\omega_o})} \frac{R_o(\omega)}{R(\omega)} \qquad (4.3.8)$$

- $u(\omega)$ spectrum of the observed Rayleigh waves
- $F(\omega)$ 3-pole Butterworth band-pass filter with cutoff periods of 80 and 20s
- ω angular frequency
- $c(\omega)$ phase velocity
- $u(\omega)$ group velocity

$Q(\omega)$ quality factor

$R(\omega)$ receiver response

Δ epicentral distance in km

a Earth radius (6371 km)

The reference values are indicated by a subscript of zero. The phase and group velocity model assumed for the continental paths as well as the reference model are for the Gutenberg continental structure [Aki and Richards, 1980]. For the oceanic paths we assumed the velocity dispersion model of Weidner [1974] (normal ocean basin). The Q model is from Tsai and Aki [1969]. The reference distance and instrument are 40° and SRO, respectively. This equilization is analogous to that of Kanamori and Stewart [1976] except that we have accounted for the significantly different phase velocity dispersion in the period range considered between oceanic paths and continental paths.

The spectra of the wavetrains appear to be flat, except for the obvious hole in the mid-periods at JAS in California. This spectral hole is apparently due to passage across the low-Q Basin and Range Province, since DUG, with similar azimuth but on the near side of the Basin and Range Province (Figures 4.3.9 and 4.3.10), does not show such a hole. Using spectral ratios between these two stations, values of Q in the range 15-30 were obtained for periods between 25 and 40 seconds, with the lowest values occurring at T≈30s. This result correlates with P waves which also showed high attenuation for the path to JAS ($t^* = 1.3$s, the largest recorded value).

The azimuthal variation of amplitudes of the wavetrains shown in Figure 4.3.10 is clearly two-lobed and consistent with a north-south oriented thrust-type source mechanism. This observation is further

confirmed in Figure 4.3.11, where the theoretical T=50s Rayleigh-wave radiation pattern matches the data very well (using the P-wave solution as the source model). The seismic moment (2-2.2 x 10^{24} dyne-cm) at T=50s is somewhat larger than was obtained in the body wave analysis. Using the same data set but a moment-tensor inversion procedure over a wider period range, Suarez [1982] obtained a moment of 1.1 x 10^{24} dyne-cm. His estimate of the source mechanism is in good agreement with the one obtained in this study. Discrepancies of this size in the seismic moment are expected when entirely different data sets or wave types are compared, and mainly reflect biases introduced into the analysis by making different assumptions about the earth response.

4.3.8 THE STRESS DROP

The stress drop (Chapter II) is very difficult to estimate because it depends on the least certain quantity we could directly determine, the far-field source time function, which must be further interpreted (with large uncertainty) in terms of the fault geometry. The situation is further complicated by the presence of the precursor. Does the asperity model [Kanamori, 1978] or the barrier model [Das and Aki, 1977] apply? Can we distinguish between the two? Although the asperity model [Kanamori, 1978] and the barrier model in which all barriers (strong areas in the fault zone) break during an earthquake (model P-SV-3 of Das and Aki [1977]) differ in details, they cannot be distinguished either by the teleseismic radiation or the final static displacements. In both models, passage of the rupture releases a portion of the accumulated tectonic stress and the residual stress is equalized over the entire fault area. The average stress drop for both models is, therefore, well-represented by a single crack model [Madariaga, 1979]. Since both models lead to the same static

stress-drop estimate, for our purposes, the distinction between them is not important (subsequently, I will refer to both of these models as model A). Model A must, however, be distinguished from the barrier model in which the barriers are left unbroken by the slip on the fault (model P-SV-2 of Das and Aki [1977]); this model results in a drasticly different slip distribution on the fault (subsequently, this model will be referred to as model B).

Figure 4.3.12 depicts the slip displacements which would result from the precursor (first subevent) and the main (second) subevent of the New Brunswick earthquake using both model B and model A. The rupture durations in both cases would be approximately the same. For the same moment, however, the displacement and the stress drop associated with the second subevent would be about 4 and 8 times larger in model B, respectively. Perhaps the strongest argument that can be presented against of model B for the New Brunswick earthquake is that if this model applied, the stress drop associated with the main event would be more than 6 kilobars which would most likely be sufficient to break the barrier. I shall continue the analysis under the premise that model A is a better representation for this event.

Although it appears that the centroidal depth of the precursor was different from that of the main subevent (Figure 4.3.5), the confidence in the precursor's depth is insufficient to give a reliable constraint on the fault dimensions. Taking advantage of the fact that the second subevent was much larger than the first, a more reliable estimate of the fault size can, however, be obtained from the duration of the pulse of the second subevent. Guided by model A (Figure 4.3.12) we can see that all information about the total fault dimension is contained in the pulse shape of the second subevent, since the large stress release from it most likely

resulted in a slip across the entire fault surface. The duration and the relative timing of the small precursor is therefore irrelevant. For the estimate of the average slip displacement and stress drop resulting from both the precursor and the main subevent, however, the total moment of both must be used.

In the analysis of the broad-band records we found that the source time function of the main subevent had a duration of about 0.6s or less, assuming the values of t^* determined in this study are correct. For a circular rupture, the fault radius r can be obtained simply from

$$r = \frac{v_r v_h}{v_r + v_h} t_d$$

where v_r is the velocity of the rupture front, v_h is the velocity of the healing front and t_d is the duration of the source time function [Madariaga, 1976]. If $v_r = 0.75\beta$ and $v_h = \beta$, we obtain a fault radius of 0.9 km. For this radius and the moment of 1.6×10^{24} dyne-cm, we obtain the stress drop of 960 bars and average fault displacement of 190 cm. Since the results are sensitive to errors in the assumed attenuation, we also calculated stress drop and displacement using the time function duration of 0.8s (obtained by assuming a frequency independent t^* of 0.4s) as its upper bound. The corresponding values of 400 bars for average stress drop and 100 cm for average displacement, are probably a good representation of the lower bounds for these parameters. Thus we must conclude that, for an earthquake of this size, the New Brunswick earthquake had an above average stress drop [Kanamori and Anderson, 1975]. That this event is unusual is also evident from the m_b v.s. M_s plot shown in Figure 4.3.13. The m_b/M_s ratio increases with increasing stress drop, and the New Brunswick earthquake clearly falls outside of the field defined by North American earthquakes. The implications of the high stress drop will be discussed further in the conclusions.

4.3.9 COMPARISON WITH PREVIOUS BODY WAVE STUDIES

The source mechanism of the New Brunswick earthquake has been studied by Dziewonski and Woodhouse [1983] and Choy et al. [1983]. These mechanisms differ from the detailed source model derived in this study. Because of the importance of this earthquake for understanding the seismicity of eastern North America I will examine the other proposed models in some detail. Figures 4.3.14a-d compare the match to the data by the preferred model of this study with the matches produced by the preferred models of the above studies. The average model from this study is a pure double-couple with the following parameters: strike 175°, dip 54°, rake 85°, depth 7 km, and moment 1.6 x 10^{24} dyne-cm. I shall refer to this model as model N. First the Dziewonski and Woodhouse model is discussed in detail, followed by the Choy et al. model. To facilitate a better comparison between different source mechanisms, the seismic moment (i.e. the scale factor) determined in this study was used for theoretical seismograms (unless otherwise stated in the figure captions). The seismic moments determined in the other studies, especially the moment preferred by Choy et al., result in a much larger misfit.

The Dziewonski and Woodhouse model

Dziewonski and Woodhouse [1983] presented their result as a part of a larger study of global seismicity. Their preferred source moment tensor for the New Brunswick earthquake is characterized by quite a large linear-vector-dipole component (16%). Its best double-couple component has the orientation: strike 202°, dip 61°, rake 129°; and moment 1.9 x 10^{24} dyne-cm. They set the depth arbitrarily to 10 km. This double-couple orientation implies a large strike-slip component of displacement on the fault. The synthetics corresponding to this model (model DW) tend to

substantially underestimate the observed long-period P wave amplitudes, especially those for the northern stations (Figure 4.3.14a), while the long-period SH wave amplitudes are generally overestimated (Figure 4.3.14b). The short-period P-wave misfit is markedly large for the northern and southern stations (Figure 4.3.14c). The solution produces a large sP arrival in the broad-band records of the southern stations (Figure 4.3.14d).

The Dziewonski and Woodhouse technique is designed to obtain a rough estimate of the mechanism of large earthquake in "real" time, i.e. for rapid distribution to various agencies. It involves matching the entire body wave seismogram up to the arrival of surface waves. In order to avoid large phase misalignments due to deviations of the body-wave travel times with respect to the average earth model, they must, however, work only with very long period signal. For the New Brunswick earthquake they applied a low-pass filter with the cut-off at T = 45s. Because of this filtering and the small size and shallow focus of the New Brunswick event, this earthquake is at the lower limit of epplicability of their method. Although more time consuming, the approach taken in this study that involved working with data with periods shorter than 45s is more appropriate for an event of this size. In order to avoid the phase mismatch I had to treat each body wave phase individually and allow adjustment for variations in their travel time. For small, shallow events, the resolution in the Dziewonski and Woodhouse method is much worse than that of the analysis presented here. The similarity between our results is a testimony to the utility of their method for obtaining a first estimate of fault mechanisms.

The Choy et al. model

The Choy et al. [1983] investigation of the source mechanism involved essentially two independent studies. One was visual analysis of the long-period and broad-band body wave data, and the other was an inversion of the long-period body waves (similar to one presented in section 4.3.3 of this paper). I shall refer to the results of the former as model CBDS1 and of the latter as model CBDS2. The discrepancies between the Choy et al. study and mine are troubling, because essentially the same data set was used in both.

The CBDS2 model, based on inversion of long-period P and SH waves, is the most similar to the model obtained in this study. It is characterized by a pure double-couple mechanism with a strike of 169°, dip of 65°, rake of 81° and moment of 3.2×10^{24} dyne-cm (a value of 5.3×10^{24} dyne-cm was obtained when only P waves were considered). The depth of 9 km was found by trial-and-error. This solution indicates a slightly larger strike-slip component of displacement and a somewhat steeper dip of the west-dipping nodal plane than the solution N. The moment is considerably larger than that determined here, Dziewonski and Woodhouse [1983] or by Suarez [1982].

There are some obvious serious problems with CBDS2, since the synthetics presented are clearly not compatible with the source orientation they are supposed to represent (e.g. the P synthetic waveform for ANMO has a clear upward first motion when, allowing for the uncertainty in the take-off angle, the first motion should be negative or at most nodal; similarly the SH synthetic for KEV clearly has an incorrect first motion polarity). According to S. Sipkin (personal communication) the error occurred in the last stage of the inversion, in which only the final waveforms and moment are calculated; the inferred orientation should not be

affected, although the moment is significantly smaller. The difference in the source orientation between our two models may be due to several factors, e.g. slightly different data handling (I filtered the signals with a high-pass filter with the cut-off at T = 60s), different alignment of seismograms and different source depth (they did not invert for the source depth).

What I believe to be the correct synthetics for CBDS2 are shown in Figure 4.3.14. Visually, the CBDS2 model matches the long-period P waveforms quite well, although due to the steeper dip of the fault plane the amplitudes are somewhat underestimated at the western stations and overestimated at the eastern stations (Figure 4.3.14a). For the long-period SH waves the mismatch is largest at KEV and BOCO (Figure 4.3.14b; the amplitude mismatch is also particularly large at COL, not shown in the figure). Due to the steeper dip of CBDS2, the amplitude of direct P waves is significantly underestimated in the western short-period waveforms (e.g. JAS, Figure 4.3.14c). Of all models presented, CBDS2 produces the smallest sP arrival for the broad-band r cords (Figure 4.3.14d), but because the P/pP amplitude ratio is not correct the residual is larger than for N or CBDS1.

Choy et al. [1983] place considerable weight on the CBDS1 model, which is based on a visual examination of waveforms. The model is characterized by a strike of 195°, a dip of 65°, a rake of 70°, a moment of 4.7×10^{24} dyne-cm, and a focal depth of 9 km. For this model, their data set consisted of short-period and broad-band P waves and long-period SH waves. The P, pP, sP, S and sS were identified and their polarities read directly from the seismograms. The stations used are not specified, but it appears from the distribution of the readings on their focal sphere plots that the

P waves from the western stations were completely disregarded. Considering the extremely long-period response of the long-period GDSN stations it is quite difficult to believe that unambiguous polarity picks are possible, not only of the direct S arrivals but also the free surface reflections. Moreover, such picks are presented for the high-noise stations such as ANMO and BOCO, but not for KEV, the station with one of the clearest signals.

The CBDS1 model underestimates amplitudes of the western long-period P waves and overestimates those of the eastern long-period P waves (Figure 4.3.14a). The matches to the long-period SH waveforms, as well as their amplitudes are particularly poor (Figure 4.3.14b). The amplitude of the direct P wave in the short-period records is clearly underestimated (Figure 4.3.14c). Choy et al. [1983] put considerable weight on the fact that the sP appears to be nodal on the broad-band records at BOCO and ZOBO, but model CBDS1 does not fit this feature any better than model N of this study (Figure 4.3.14d). Choy et al. also obtained an estimate of the moment, apparently based on the area under the pulses of these stations. The value of 4.7×10^{24} dyne-cm appears to be a severe overestimate. Since Choy et al. [1983] assumed a much lower attenuation than that used in this study, an overestimate of the seismic moment is especially puzzling.

Using directivity arguments Choy et al. [1983] determined the westward dipping plane of the double-couple to be the actual fault plane. Since based on visual comparison of the models shown in Figure 4.3.5 one could perhaps argue that some upward directivity appears to be present, e.g. upward propagating models match better the waveform at ALE (based on residuals, the evidence is not convincing), for their source mechanism which has one very steeply dipping and one very shallow dipping fault plane, such a conjecture would perhaps be justified. In the source

mechanism found in this study, the westward dipping double-couple plane starts with a dip of 45° for the precursor and ends with a dip of 54° for the main subevent. The corresponding values for the eastward dipping plane are 45° and 35°, respectively. The selection of the west-dipping plane as the fault plane therefore depends on aspects of the focal mechanism with which this study is in conflict; rupture propagation along either plane of solution of this study could produce the observed directivity. (Although the choice of the fault plane is arbitrary for models in this study, the model parameters presented in this paper are for the westward dipping nodal plane, to provide an easier comparison with the previous investigations.)

One of the major discrepancies between Choy et al. and the present study concerns the estimate of stress drop. In spite of the fact that they used a moment three times larger in their calculation, the estimated stress drop is only 41 bars, and would be 14 bars if a moment of 1.6×10^{24} dyne-cm determined in this study were used. The source of this discrepancy is the difference in fault dimensions which were estimated from the source time function. The different attenuation assumed in these studies is clearly one of the factors leading to a different estimate of the source time function duration, but, as was shown in the previous section, the assumption of the constant $t^* = 0.4$s still resulted in a time function duration of approximately 0.8s and stress drop of several hundred bars. The main reason for the discrepancy between the two studies is the different treatment of the precursor. Although Choy et al. [1983] recognize the precursor and point out that the P-SV-3 model of Das and Aki [1977] probably applies, in their calculations they treat both the small precursor and the main subevent as a continuous breaking of a single asperity. In other words, they take the total time from the initiation of

the rupture of the precursor to the stopping of the main subevent as representative of the dimension of the fault area, although, as I have argued in the previous section, only the duration of the main subevent should be considered. To stress this point, consider a case in which the small precursor occurs 10 minutes prior to the much larger main event. Clearly, one would not assume that the rupture had a radius of 1500 km. Since the main event would most likely cause additional motion on the fault plane ruptured by the precursor, the total dimension of the fault plane would be entirely given by the dimension of the main event, but the total displacement would be the sum of the two. On the basis of the above arguments I believe that the stress drop of 14 bars, which one would obtain using the Choy et al. fault dimensions and moment of 1.6×10^{24} dyne-cm obtained in this study, is substantially underestimated.

4.3.10 THE JANUARY 11, 1982 AFTERSHOCK

The January 11, 1982 event is the largest aftershock ($m_b = 5.4$) of the New Brunswick earthquake, but it is too small for a long-period study. An analysis of the short-period P waves, identical to that described for the main shock, was performed. The data and the synthetics for the best fit solution are shown in Figure 4.3.15 and the inferred source parameters are summarized in Table 4.3.4. The event has a similar mechanism to the main shock but is simpler and shallower. The aftershock distribution has been used to infer that the eastward dipping nodal plane was the actual fault plane [Wetmiller et al., 1982]. Because fewer stations were available, the inferred parameters for this event are less certain. The main reason to study this event is that it helps distinguish source effects from structural effects in the observed waveforms of the January 9 earthquake. By comparing these two events, we see that the initial oscillation in the

waveforms of the January 9 event that we identified as the first of two subevents, was indeed a source effect, because it is not observed for the aftershock. On the other hand, structurally-related coda is observed for both events at staton ZOBO, while at BOCO (with similar azimuth) the waveforms are consistently simpler. Note also an arrival at the Albuquerque stations (ALQ and ANMO) which arrives at exactly the same time (about 1 s) ahead of what was identified as the direct arrival. This arrival appears to be caused by multipathing near the receiver, since nearby noise-free stations DUG (Figure 4.3.4) and JAS (Figure 4.3.15) do not exhibit this phenomenon.

4.3.11 DISCUSSIONS AND CONCLUSIONS

In this study I have derived a detailed model of the source process of the New Brunswick earthquake. The body and surface wave data considered in this study covered periods from 0.1 to 80s. The best constrained parameters of the model are the average source mechanism (pure double-couple with strike 172-182°, dip 53-55°, rake 80-95°), seismic moment ($1.6\pm0.1 \times 10^{24}$ dyne-cm) and the average depth (6.9±0.1 km). The presence of a small precursor (first subevent) of slightly different orientation is indicated by the short-period and broad-band data. The duration of the source time function of the main (second) subevent is clearly less than 1s but a precise determination would require precise estimate of the attenuation along individual propagation paths rather than simply assuming a worldwide average t^* for paths from a source in New Brunswick.

Based on the assumption that the source has a flat spectrum down to periods of 1-1.5s we concluded that the average t^* for the paths from New Brunswick is about 1s. The t^* at T=1s appears to fluctuate between high

values of 1.2-1.3s for the western North American stations and low values of 0.65-0.8s for the South American stations; intermediate values were obtained for the European stations. Based on the less stringent assumption that the source has a flat spectrum down to periods of 2-4s we concluded that the constant $t^* = 0.4$s for the paths to the South American stations is probably not correct, instead a value of 0.7-0.8s appears more appropriate for those periods. Assuming a frequency dependent t^* [Liu et al., 1976] with $t^*_m = 0.8$s and $\tau_m = 0.08$s in the analysis of the broad-band South American records, a time function duration of 0.6s was inferred for the main subevent, leading to a stress drop estimate of 960 bars. A larger value than this is acceptable by the data. A conservative lower bound on the stress drop, found by assuming frequency independent $t^* = 0.4$s, is about 400 bars.

The stress drop of the New Brunswick earthquake is large when compared with the average stress drops commonly found for large events [Kanamori and Anderson, 1975; Hanks, 1980]. It is not, however, inconsistent with stress drops found in some studies of events similar in magnitude to the New Brunswick earthquake [Fletcher et al., 1980] or in studies of local stress concentrations on fault planes of some large events [Hanks, 1974; Bouchon, 1978; Hanks, 1980; Papageorgiou and Aki, 1983b].

The coseismic stress drop is of interest because it has a direct bearing on the magnitude of strong ground motion felt in the epicentral area. A critical question is whether the average stress drop value found for this event would also apply to a larger, potentially more damaging earthquake? I believe it would not, since many studies indicate that the average stress drop of events with fault radii of more than a few kilometers never attains a level as high as that found for the New

Brunswick event [Kanamori and Anderson, 1975; Hanks, 1980]. Nevertheless, local stress drop concentrations as large as the one found for the New Brunswick earthquake can occur and should be included in models for predicting strong ground motion for larger events in eastern North America (e.g. the patch model of Aki et al. [1977] or Papageorgiou and Aki [1983a]). The possiblity exists, of course, that the stress drop associated with the New Brunswick earthquake may not be typical of the earthquakes in the region since the event occurred in a pluton with no apparent prior faulting.

The causes of seismic activity in the eastern U.S. are poorly understood. Although historical records show several large events [Street and Turcotte, 1977], the seismicity of the past two hundred years has been characterized by scattered small and intermediate events. Several concentrations of seismic activity do occur, e.g. the New Madrid region, the Charlevoix zone, the Ottawa northern New York region [Stauder et al., 1976; Basham et al., 1979; Yang and Aggarwal, 1981; Pulli, 1983] but the activity can seldom be associated with any well-defined fault system. There have been attempts to identify linear trends, e.g. Alabama-New Brunswick, St. Lawrence River, Boston-Ottawa [Woollard, 1969, Sbar and Sykes, 1973], but their existence remains controversial. A controversy also exists about correlations of the seismic activity with such features as mafic and ultramafic intrusive bodies [Kane, 1976; McKeown, 1978], alkaline intrusions, or oceanic fracture zones extending into the continental margins [Sykes, 1978]. Recently, Yang and Aggarwal [1981] proposed two distinct seismotectonic provinces, 1) the Adirondack-western Quebeck province and 2) the Appalachian province, which respond to two distinctly different stress systems (see also Zoback and Zoback [1980]). They also suggest that intrusive bodies tend to inhibit earthquake activity.

The New Brunswick earthquake occurred within an intrusive body; it may, therefore, be is a result of local thermal stresses due to the cooling of the body. On the other hand, the orientation of the principal compression appears to be consistent with the east-west compression generally found for earthquakes throughout eastern North America (Figure 4.3.16) indicating that the earthquake may be a response to a regional stress field.

One of the striking aspect of the New Brunswick earthquake is the simplicity and coherency of the short-period records. Because of the location of the event within a granitic pluton and the lack of sediment cover, the structural complexity of the source region is minimal. The fact that some stations show significant coda but a few, such as BOCO or ALE (Figures 4.3.4, 4.3.15), show practically no coda suggests that, to a large extent, the teleseismic coda is generated by reverberations within the crustal layering at the source and the receiver. The multipath arrival at the Albuquerque stations (ANMO and ALQ), prior to what was identified as the direct P arrival from the January 9th and 11th events, is interesting and probably results from structural heterogeneity below these two stations.

Notwithstanding some unexplained complexities, the short-period waveforms were matched with a reasonable success and led to important constraints on the source process of the New Brunswick earthquake and its largest aftershock. This success suggests the possibility of studying intermediate size events using short-period teleseismic body waves and techniques developed for long-period studies of larger events. The recent availability of well-calibrated short-period data (that can be easily filtered to suitable frequency bands) should facilitate teleseismic studies of remote regions characterized by intermediate size earthquakes.

Table 4.3.1 Stations Used in the Analysis of the New Brunswick Earthquake

Station	Type‡	Δ (deg)	ϕ_{ES} (deg)	ϕ_{SE} (deg)	$P_{first\ motion}$	Waveforms used†
			DIGITAL			
ALQ	WWSN	32.0	262.5	55.7	Ce	P_{sp}, R
ANMO	SRO	32.0	262.5	55.7	Ce	P_{sp}, P_{lp}, SH
BER	WWSSN	42.4	44.3	285.4		P_{lp}, R
BOCO	SRO	42.8	190.9	7.5	Ci	P_{sp}, SH, R
COL	WWSSN	45.1	323.6	72.3	Ce	P_{sp}, SH
GRFO	SRO	49.5	56.4	298.6	Ce	P_{sp}, P_{lp}, SH, R
JAS	WWSSN	39.9	277.1	59.2	Ce	P_{sp}, P_{lp}, R
KEV	WWSSN	48.0	27.8	293.7		P_{lp}, SH
KONO	ASRO	44.6	45.5	289.1	Ce	P_{sp}, P_{lp}, SH, R
LON	WWSSN	37.0	290.5	68.8		SH, R
SCP	WWSSN	10.2	236.6	48.8	Ce	R
TOL	WWSSN	44.9	75.2	300.7	Ce	P_{sp}, P_{lp}, R
ZOBO	SRO	63.1	181.6	1.1	Ci	P_{sp}
			ANALOG			
ALE	CN	35.6	1.0	185.0	Ci	P_{sp}, P_{lp}, SH, R
BEC	WWSSN	14.7	173.4	354.7		R
DAG	WSSSN	35.3	17.1	241.2	Ci	
DUG	WWSSN	33.7	275.6	62.8	Ci	P_{sp}, R
FCC	CN	20.1	315.9	113.7	Ci	

Table 4.3.1 (cont'd.)

Station	Type‡	Δ (deg)	ϕ_{ES} (deg)	ϕ_{SE} (deg)	$P_{first\ motion}$	Waveforms used†
			DIGITAL			
FRB	CN	16.8	357.2	175.7	Ci	
FVM	WWSSN	19.6	251.4	55.2	Ce	
GEO	WWSSN	11.1	272.1	40.0	C	
GOL	WWSSN	28.8	269.7	62.5	Ci	R
INK	CN	39.0	327.1	88.0	Ci	R
KBL	WWSSN	89.4	35.1	331.5	C	P_{lp}
LHC	CN	15.3	283.7	86.9		R
MBC	CN	36.1	341.2	112.7	C	R
PNT	CN	34.7	293.9	73.1	Ce	P_{sp}, R
PHC	CN	39.1	298.6	71.0		R
SCH	CN	7.8	359.5	179.4	Ce	
SES	CN	29.1	293.3	79.2	Ci	R
STJ	CN	9.5	81.3	271.6	De	
STU	WWSSN	48.8	58.3	298.3	C	
WES	WWSSN	5.7	217.6	34.3	Ce	
YKC	CN	30.9	320.2	99.7	Ce	

Δ is the distance between station and the epicenter; ϕ_{ES} is the azimuth of station from the epicenter; ϕ_{SE} is the azimuth of the epicenter from the station.

* C, D, i and e indicate compressive, dilitational, impulsive and emergent readings. Except for KBL all first motions were determined from the short-period records.

† P_{sp} indicates short-period P wave, P_{lp} indicates long-period P wave, SH indicates long-period SH wave, and R indicates Rayleigh wave.

‡ CN is abbreviation for the Canadian network stations.

Table 4.3.2 Summary of Long-period Body-wave Inversions for the New Brunswick Earthquake

MOMENT TENSOR

Depth = 7.0±0.1 km

Normalized moment-tensor components:

M_{xx} = 0.05±0.01 M_{xy} = -0.00±0.01
M_{yy} = -0.64±0.01 M_{xz} = 0.05±0.01
M_{zz} = 0.69±0.01 M_{yz} = 0.22±0.01

Moment-tensor norm = 2.32±0.09 x 10^{24} dyne-cm

Principal axes:

	Eigenvalue	Azimuth	Plunge
P:	-0.68±0.01	269±1°	9±1°
B:	-0.05±0.01	179±1°	4±1°
T:	0.73±0.01	67±6°	80±1°

Decomposition:* 93% double-couple 7% linear-vector-dipole

Best double-couple:

Scalar moment = 1.6 x 10^{24} dyne-cm
Strike = 176° Dip = 54° Rake = 86°

Residual = 0.48‡

CONSTRAINED DOUBLE-COUPLE

	P AND SH	P ONLY	SH ONLY	P AND SH WAVE SHAPE ONLY
Depth (km)	7.1±0.1	7.0±0.2	7.1±0.1	7.0±0.1
Scalar moment (10^{24} dyne-cm)	1.57±0.03	1.76±0.06	1.48±0.05	1.52±0.24†
Strike (deg)	175±1	170±4	175±1	176±0
Dip (deg)	55±1	54±1	56±1	54±0
Rake (deg)	84±1	104±4	82±1	90±0
Residual	0.85	0.82	0.81	0.86

Conventions as in Aki and Richards [1980].
Quoted uncertainties represent one standard deviation.
Residuals are normalized to the RMS amplitude of the data.
The source time function was a box-car of 1.5 s duration.
* Moment tensor was constrained to be purely deviatoric.
† Moment was determined after the last iteration.

Table 4.3.3 Summary of Short-period P-wave Inversion for the New Brunswick Earthquake

Event	Depth** (km)	Strike	Dip (deg)	Rake	Source Time Function*		Time Delay†	Moment (dyne-cm)
					w_1	w_2		
1	8.41±0.02 (8.06)	177	45	90‡	1.00			0.15±0.02 x 10^{24}
2	7.34±0.00 (6.90)	174±3	54±0	85±1	0.44±0.09	0.66±0.09	0.72±0.01	1.38±0.04 x 10^{24}

* Each element of the source time function had a duration of 0.2s.
† Time delay of the second subevent is with respect to the origin time of the first subevent.
‡ Orientation (strike,dip,rake) of the first event was determined by trial-and-error by matching the amplitudes and polarities of the first motions.
** Depth of the initial point of the rupture; rupture propagated up-dip with velocity of 2.5 km/s. Numbers in the parenthesis indicate the centroidal depth.

Table 4.3.4 Summary of the Short-period P-wave Inversion for the 11 January 1982 Aftershock of the New Brunswick Earthquake

MOMENT TENSOR

Depth = 5.25±0.01 km

Normalized moment-tensor components:

M_{xx} = -0.34±0.03	M_{xy} = -0.22±0.05
M_{yy} = -0.37±0.03	M_{xz} = 0.08±0.02
M_{zz} = 0.71±0.01	M_{yz} = -0.26±0.01

Moment-tensor norm = 6.1±0.7 x 10^{23} dyne-cm

Principal axes:

	Eigenvalue	Azimuth	Plunge
P:	-0.59±0.05	50±3°	6±1°
B:	-0.20±0.05	141±3°	14±1°
T:	0.79±0.01	296±3°	75±1°

Decomposition:* 78% double couple 22% linear vector dipole

Best double-couple:

Scalar moment = 4.2 x 10^{23} dyne-cm
Strike = 332° Dip = 53° Rake = 108°

Source time function: 1.16±0.03, -0.16±0.04

RMS residual = 0.059

CONSTRAINED DOUBLE-COUPLE

Depth = 5.30±0.02 km

Scalar moment = 4.1±0.3 x 10^{23} dyne-cm

Strike = 345±4° Dip = 53±1° Rake = 98±3°

Source time function: 0.92±0.01, 0.002±0.01

RMS residual = 0.059

Quoted uncertainties represent one standard deviation.
Each element of the source time function had a duration of 0.2 s.
* Moment tensor was constrained to be purely deviatoric.

FIGURE CAPTIONS

4.3.1 Seismicity map of the northeastern United States and Canada for the period 1975 to 1981. The epicenter of the New Brunswick earthquake (m_b=5.7) is indicated by the star.

4.3.2 Geotectonic map of the epicentral region. The earthquake epicenter (star) falls within the granitic pluton of the Miramichi Anticlinorium (the north-east trending structure in the center of the map).

4.3.3 The observed (solid lines) and the corresponding theoretical (dashed lines) long-period P and SH wave seismograms. The longer-period waveforms are the GDSN data, the shorter-period waveforms are analog recordings. The theoretical seismograms are for the joint P and SH double-couple inversion (Table 4.3.2). All seismograms were normalized to an instrument magnification of 5000 and epicentral distance of 40°. Larger vertical scales are for the digital data, the smaller ones are for the analog data.

4.3.4 The observed (solid lines) and the corresponding theoretical (dashed lines) short-period P wave seismograms. The sketch in the upper right-hand corner shows the geometry of the model; further details are given in Table 4.3.3. The assumed first arrivals are indicated by the vertical marks. The presumed precursor causes the first small oscillation immediately following the marks. The arrival prior to the mark at ANMO and ALQ is real and appears to be due to some earth heterogeneity (see also Figure 4.3.15); a similar arrival at JAS is an artifact of the zero phase filtering (it is not observed on the original record). The arrival time of P, pP and sP of the main subevent is also indicated. All traces are normalized to the power$^{1/2}$.

4.3.5 Effect of the depth of the precursor on the short-period waveforms (dashed lines are the data, solid lines are the synthetics). In each row, synthetics were calculated using the indicated depth of the precursor. In all exaples, the depth of the main event was 7 km. Point sources an other parameters given in Table 4.3.3 were used in all calculations. The RMS residual for each model using all stations is also shown. The models with the precursor depth of 6 and 8 km correspond to the two relative minima found in the inversion.

4.3.6 Effect of the source finiteness and rupture propagation on the short-period waveforms (dashed lines are the data, solid lines are the synthetics). Model I is for an upward propagating westward dipping line source with precursor (the best-fit model). In the subsequent models the small precursor was not included. Model II is for the same geometry as I; III is for an upward propagating eastward dipping line source; IV is for a point source; V is for a downward propagating eastward dipping line source; and VI is for a downward propagating westward dipping line source. The numbers are the RMS residuals using all stations. We cannot distinguish between the point and the upward propagating models from the residuals, but the downward propagating models are clearly inferior.

4.3.7 Traces on the left show the fluctuations of the short-period absolute amplitudes with respect to the average model with a $t^* = 1s$ (solid lines are the data, dashed lines are the synthetics). Traces on the right were generated with the same source model, but the t^*'s were adjusted to fit the absolute amplitudes at each station. The t^*'s used are indicated.

4.3.8 The broad-band records of the ground displacement and velocity due to P waves at the South American stations (solid lines are the data, dashed lines are the synthetics). The amplitudes are normalized to a distance of 40°. The source time functions shown were obtained by matching the shapes of the observed P and the pP pulses at these stations.

4.3.9 The surface wave paths to the stations used in the analysis (equal distance equal angle projection).

4.3.10 Equalized Rayleigh wave traces for the New Brunswick earthquake. The azimuthal amplitude variation is consistent with north-south striking thrust faulting. Note the spectral hole in the mid-periods at JAS, most likely due to high attenuation in the region between DUG and JAS.

4.3.11 The observed (squares) and the theoretical (solid line) radiation pattern of Rayleigh waves at a period of 50s. The theoretical radiation pattern was calculated for the source mechanism and the moment determined in the body wave analysis.

4.3.12 Interpretation of the source time function of the New Brunswick earthquake in terms of the barrier and asperity models of faulting. The concentric lines depict the growth of the slip displacement along the fault. The slip resulting from the precursor is indicated by dashed lines. In the asperity model [Kanamori, 1978] or barrier model P-SV-3 of Das and Aki [1977] (here shown together as a single model A), the slip due to the precursor and the main subevent become distributed over the whole fault surface, but in the barrier model P-SV-2 of Das and Aki (here shown as model B), high stress areas with no slip remain on the fault surface even after the passage of

the rupture. "0.5" marks the displacement distribution at the time when the stopping (healing) phase is initiated, approximately at the half time of the duration of motion [Boatwright, 1980].

4.3.13 The m_b v.s. M_s plots for earthquakes and explosions. The New Brunswick earthquake is indicated by the squares. (Adapted from Douglas [1980].)

4.3.14 (a) Examples of the fit to the long-period P wave data by the DW model (Dziewonski and Woodhouse [1983]), the CBDS1 and CBDS2 models (Choy et al. [1983]), and the N model (present study). Dashed lines are the data and solid lines are the theoretical seismograms. To facilitate a better comparison between different source mechanisms, the seismic moment (i.e. the sale factor) of 1.6×10^{24} dyne-cm was used for all theoretical seismograms (the preferred moments, especially those for CBDS1 and CBDS2 result in a very large misfit). The source depths are those determined in each study.

(b) Examples of the fit to the long-period SH data by the DW, CBDS1, CBDS2, and N models. The seismic moment of 1.6×10^{24} dyne-cm was used for all theoretical seismograms.

(c) Examples of the fit to the short-period P wave data by the DW, CBDS1, CBDS2, and N models. Only the main subevent is modeled. Because the source depths determined in the previous studies were not sufficiently precise for a meaningful comparison, the source depth determined in this study was used in all models. The source time function determined in this study was used. The absolute amplitudes of all traces were normalized to the power$^{1/2}$ of each trace.

(d) Examples of the fit to the broad-band P wave data by the DW, CBDS1, CBDS2, and N models. The source time function depth and seismic moment determined in this study were used in all theoretical seismograms.

4.3.15 The observed (solid lines) and the corresponding theoretical (dashed lines) short-period P wave seismograms for the January 11, 1982 aftershock. The constrained double-couple model given in Table 4.3.4 is used for the theoretical seismograms. The arrival prior to the direct arrival at ANMO and ALQ is identical to that observed for the January 9, 1982 event (Figure 4.3.4).

4.3.16 The orientation of the principal compression for the eastern North American earthquakes. The New Brunswick earthquake is indicated by the open symbol. (Adapted from Yang and Aggarwal [1981]).

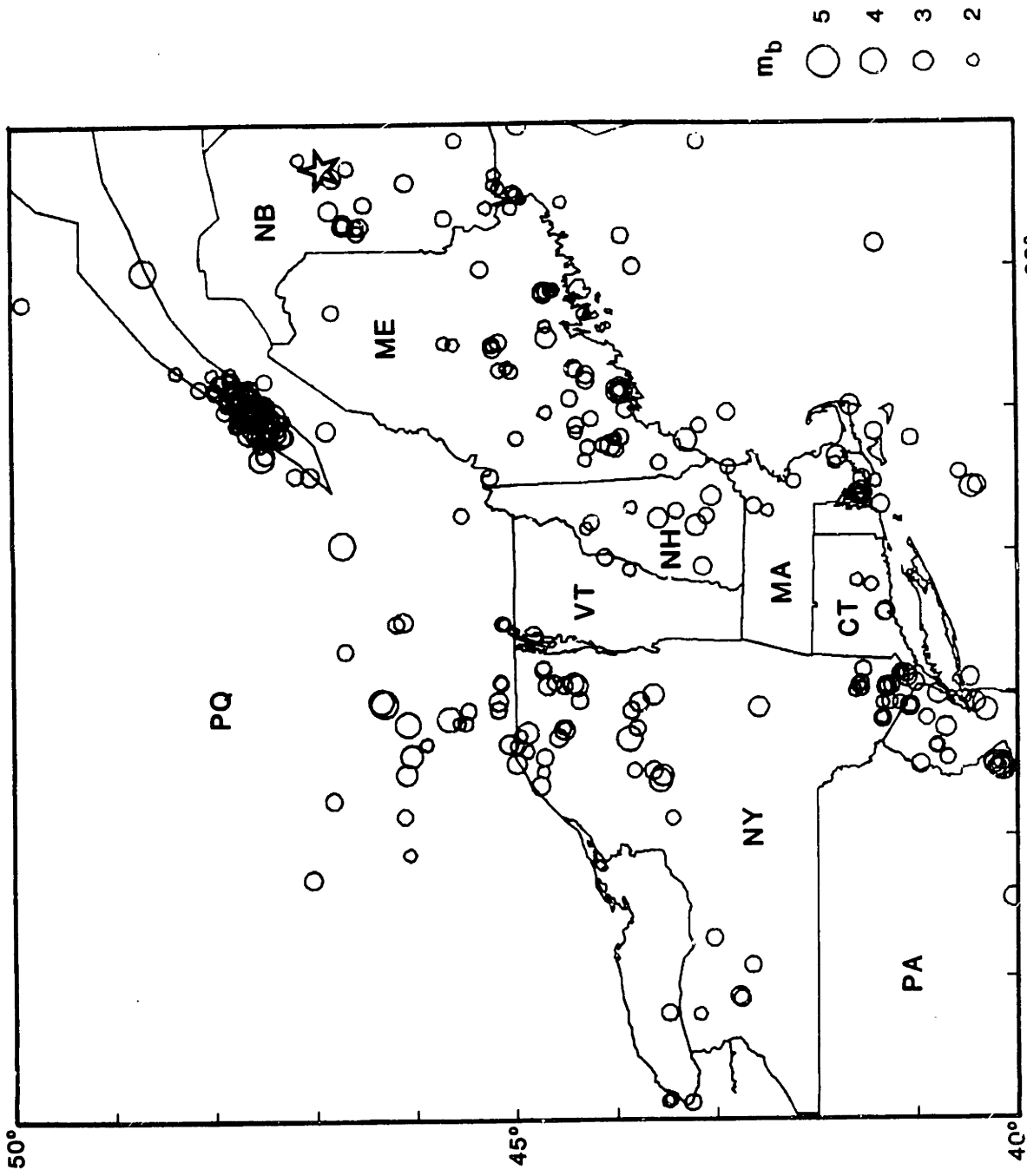

Figure 4.3.1


Gaspé Synclinorium
Grand Pabos Fault
Maquere Dome
QUEBEC
NEW BRUNSWICK
Restigouche Synclinorium
Millstream Fault
Climtree Anticline
Dunnage Zone
Gander Zone
BATHURST
Rocky Brook
Chaleur Bay
Aroostook Matapedia
Synclinorium
Synclinorium
Catamaran Brook Fault
Miramichi
CHATHAM
New Brunswick Basin
MAINE
NEW BRUNSWICK
Moncton Basin
FREDERICTON
Pokiok Batholith
Fredericton Trough
Fredericton Fault
St George Batholith
Belle Isle Fault
Caledonia Fault
Clover Hill
Caledonia Highlands
Harvey-Hobe
SAINT JOHN
BAY OF FUNDY
Minas
Valley
50 km

Figure 4.3.2

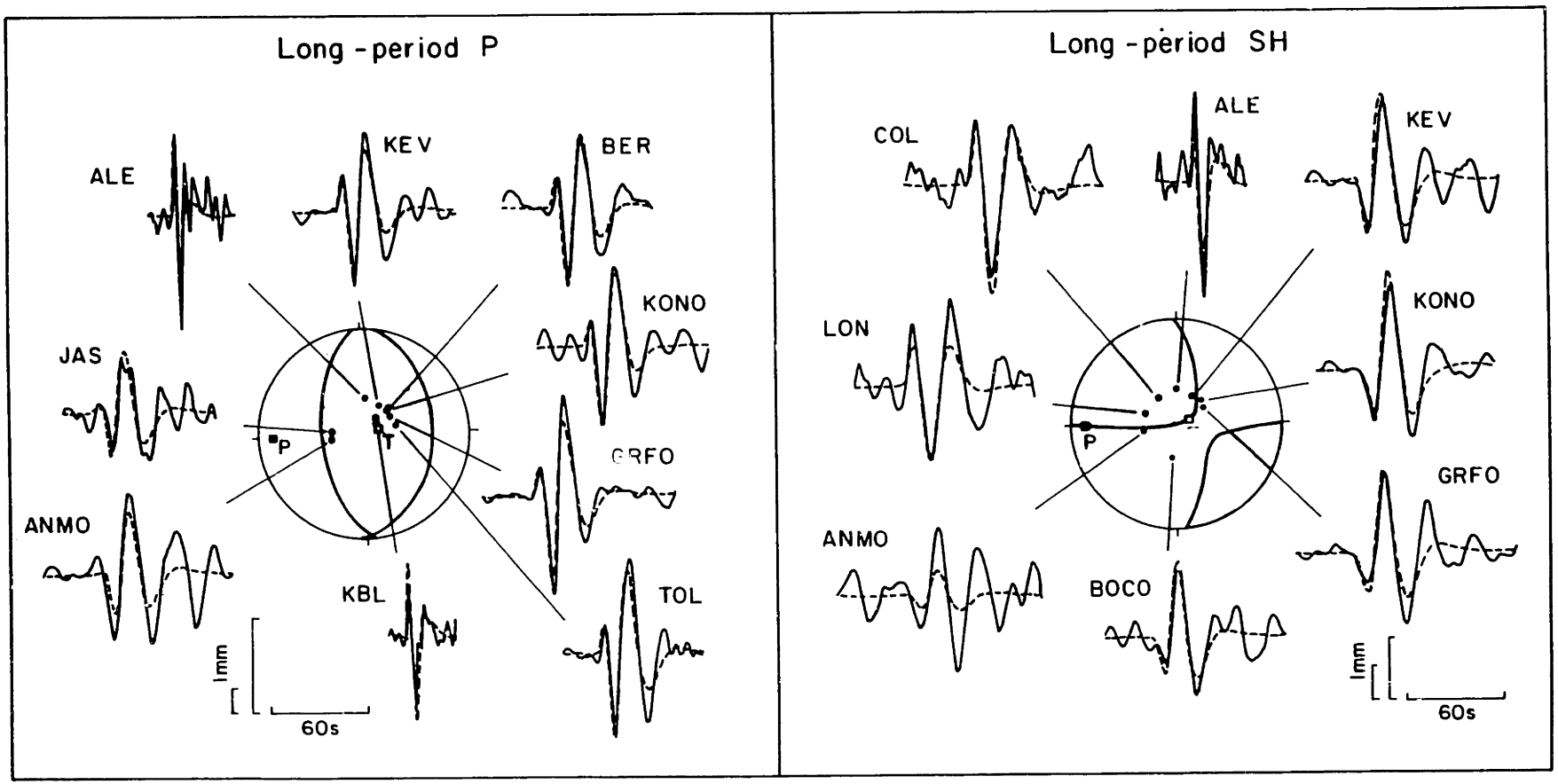
Long - period P
ALE
KEV
BER
KONO
JAS
P
T
GRFO
ANMO
KBL
TOL
1mm
60s
Long - period SH
COL
ALE
KEV
LON
KONO
P
GRFO
ANMO
BOCO
1mm
60s

Figure 4.3.3

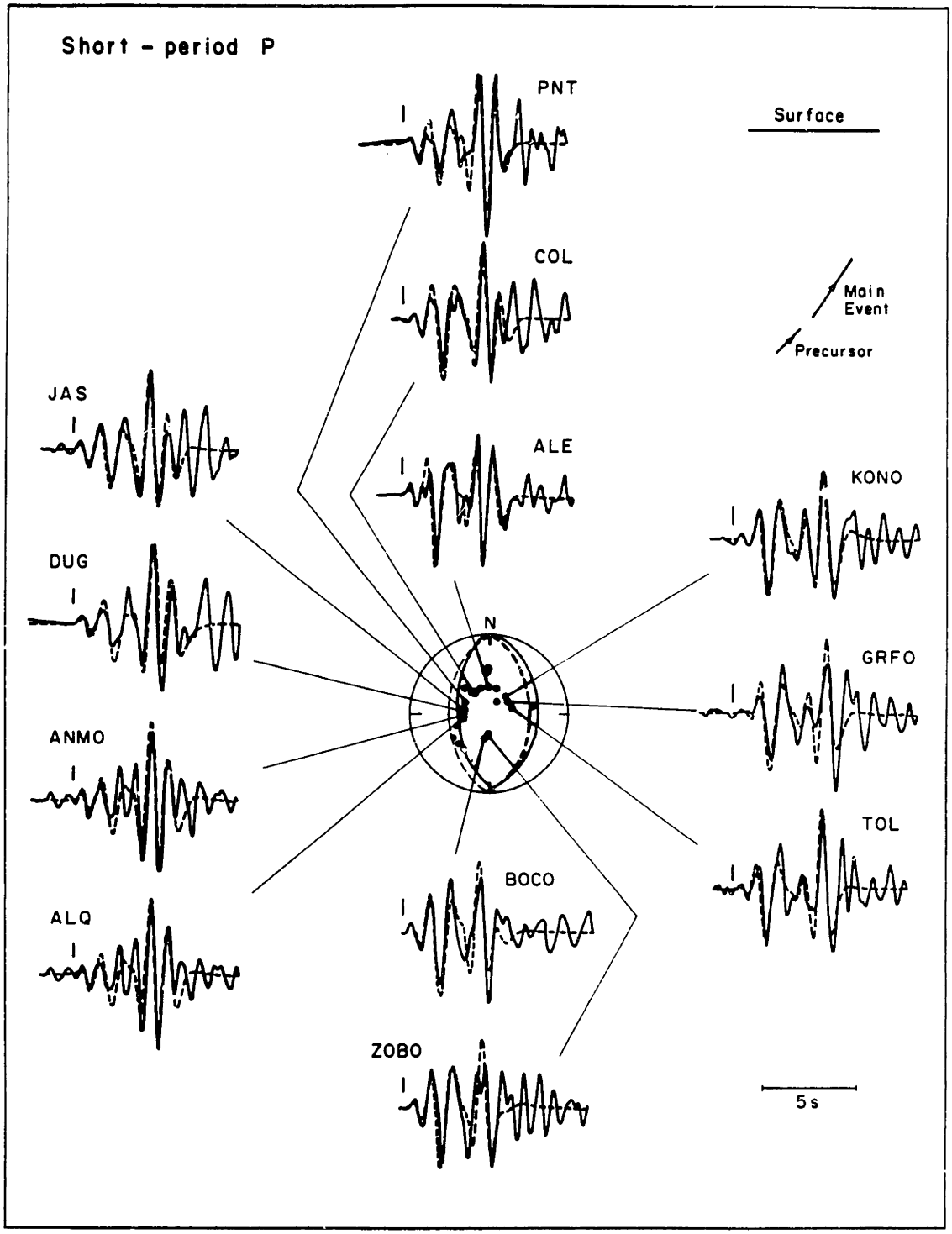
Short - period P
PNT
Surface
COL
Main Event
Precursor
JAS
ALE
KONO
DUG
N
GRFO
ANMO
TOL
BOCO
ALQ
ZOBO
5s

Figure 4.3.4

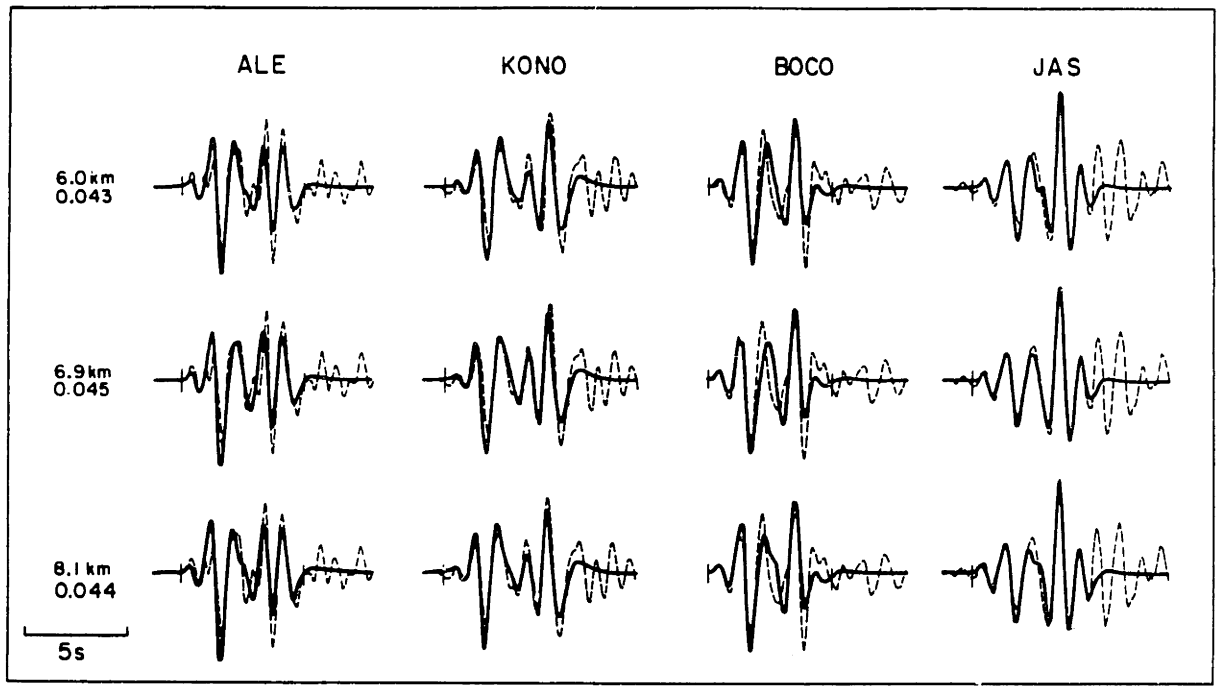

Figure 4.3.5

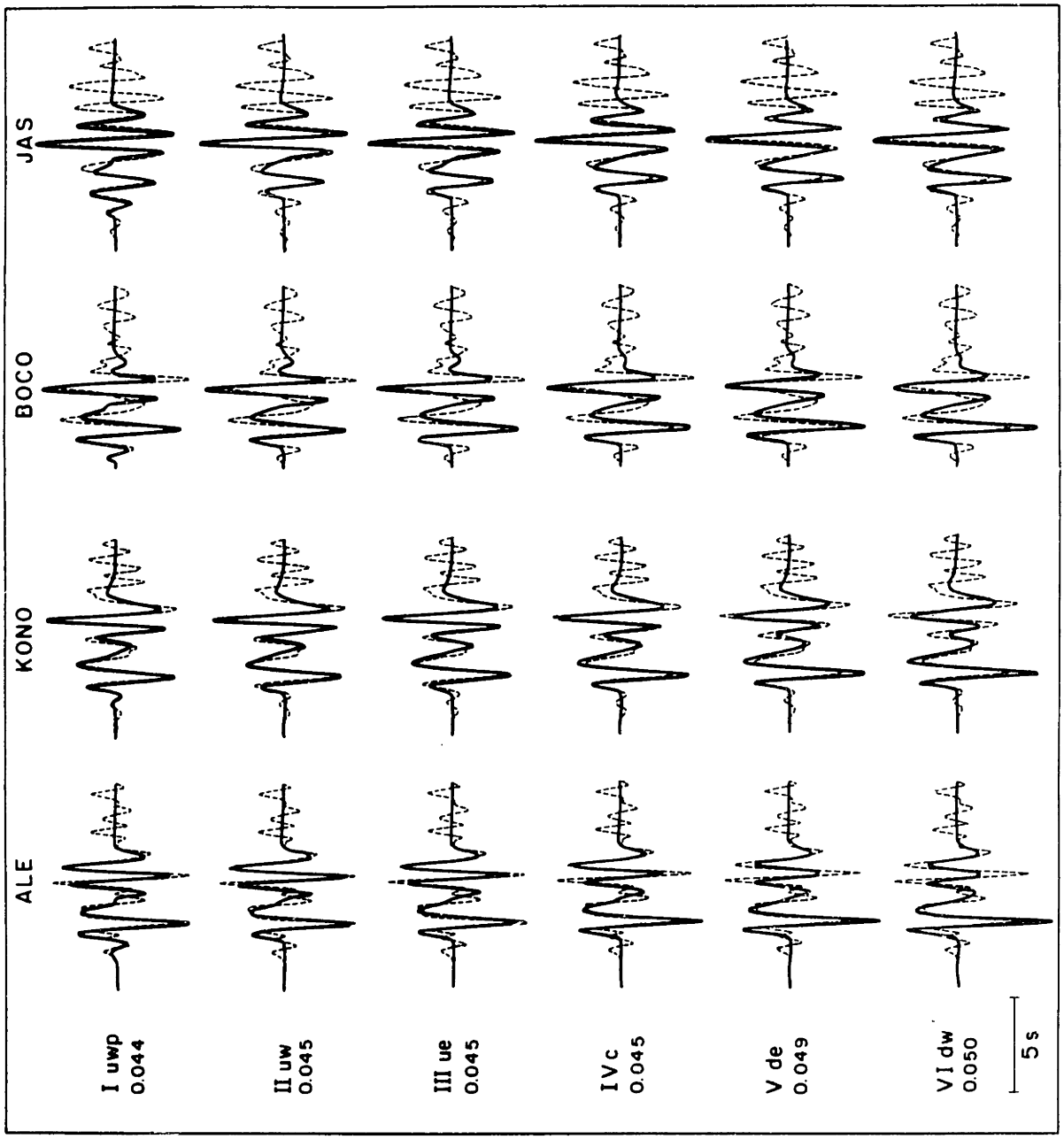
ALE
KONO
BOCO
JAS
I uwp
0.044
II uw
0.045
III ue
0.045
IVc
0.045
V de
0.049
VI dw
0.050
5s

Figure 4.3.6

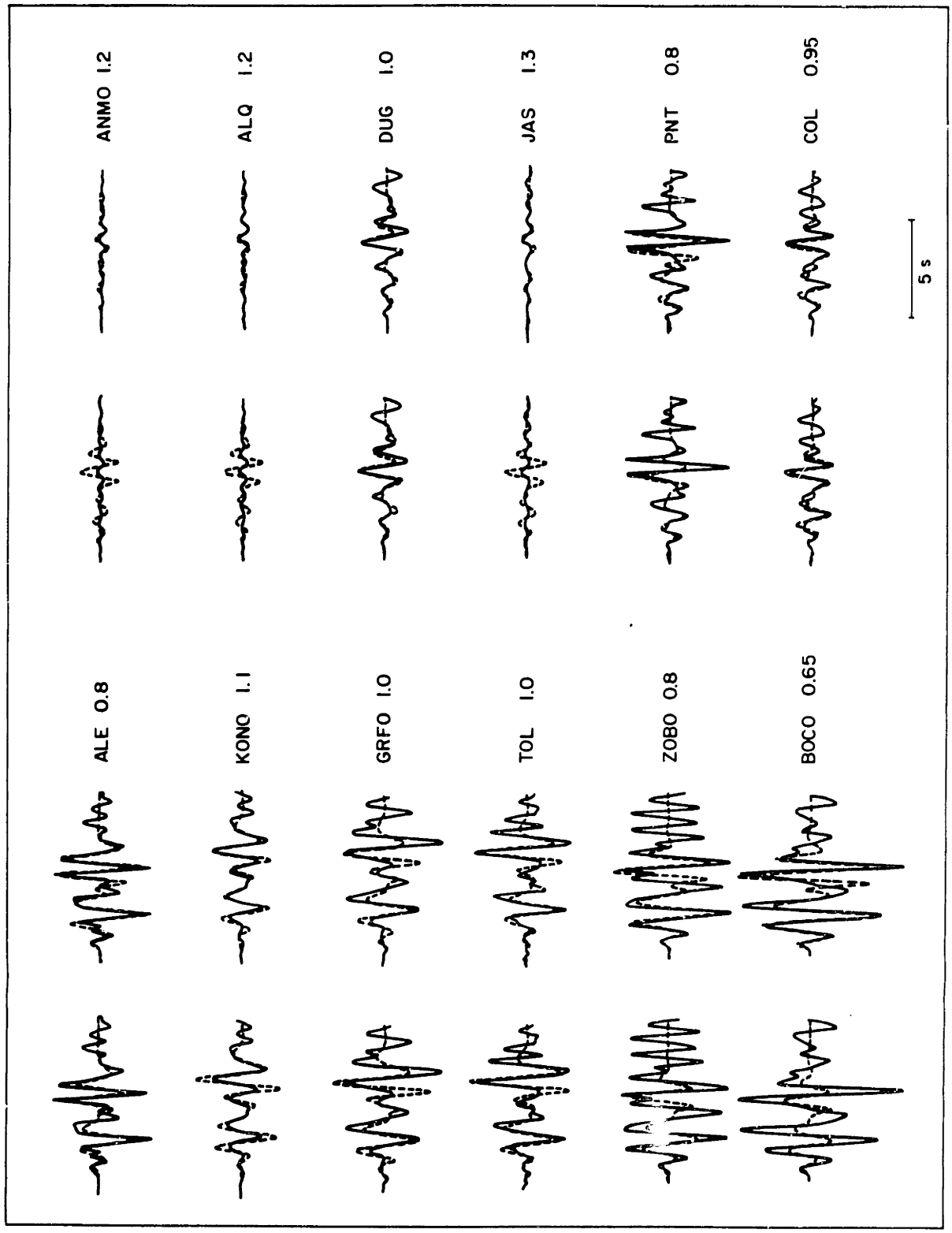
ALE 0.8
KONO 1.1
GRFO 1.0
TOL 1.0
ZOBO 0.8
BOCO 0.65
ANMO 1.2
ALQ 1.2
DUG 1.0
JAS 1.3
PNT 0.8
COL 0.95
5 s

Figure 4.3.7

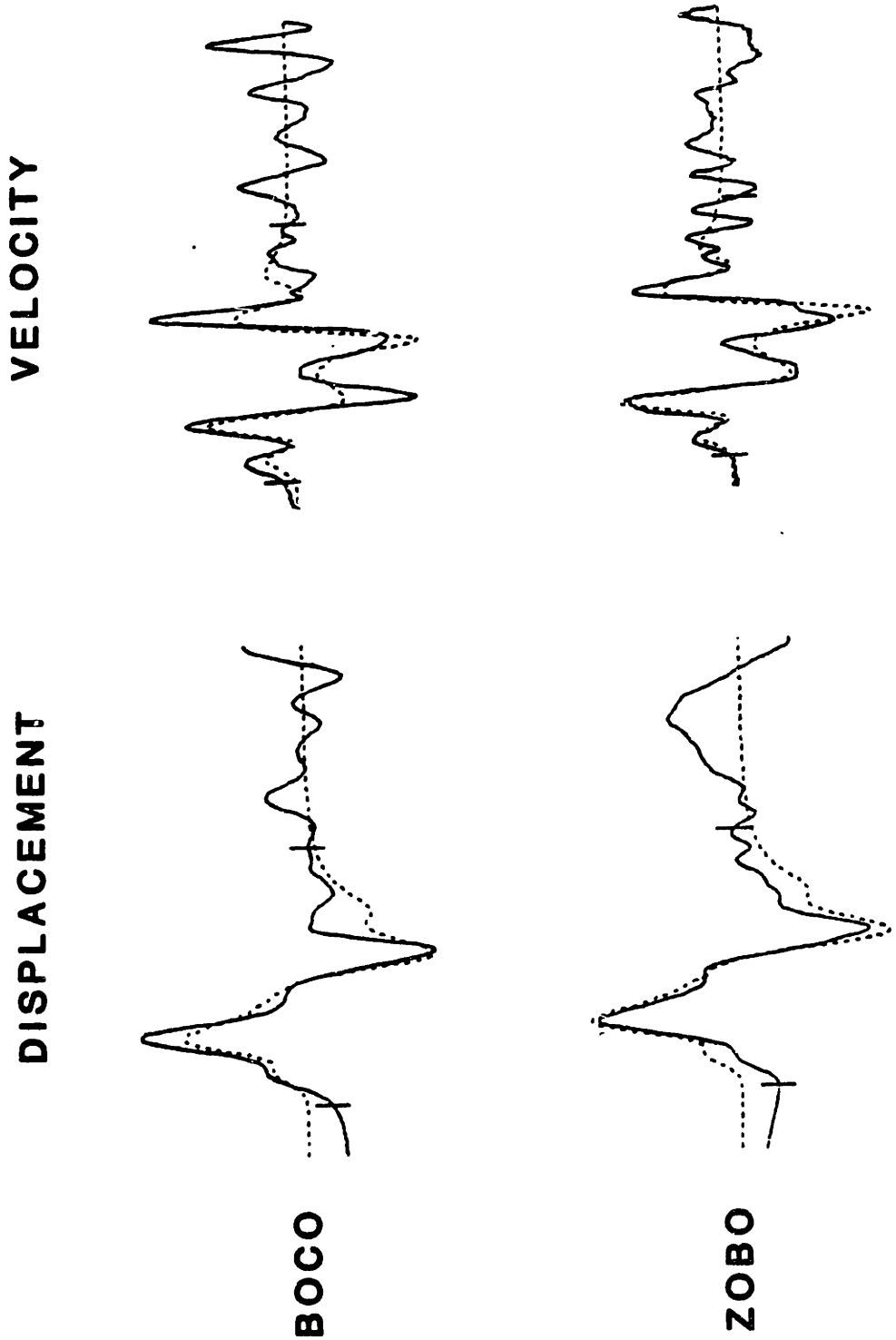

Figure 4.3.8

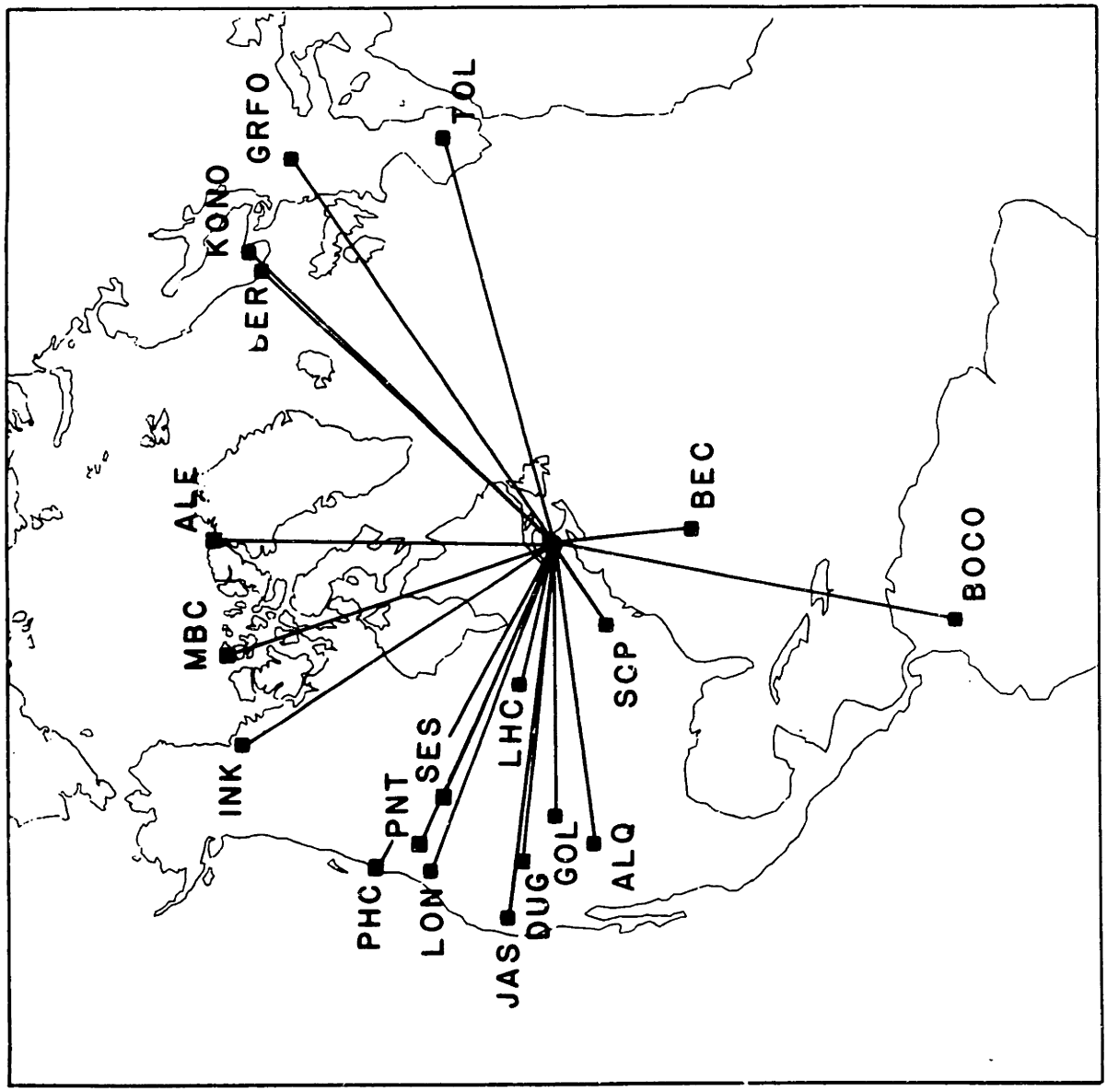
GRFO
TOL
KONO
BER
ALE
BEC
BOCO
MBC
SCP
INK
LHC
SES
PNT
GOL
ALQ
PHC
LON
DUG
JAS

Figure 4.3.9

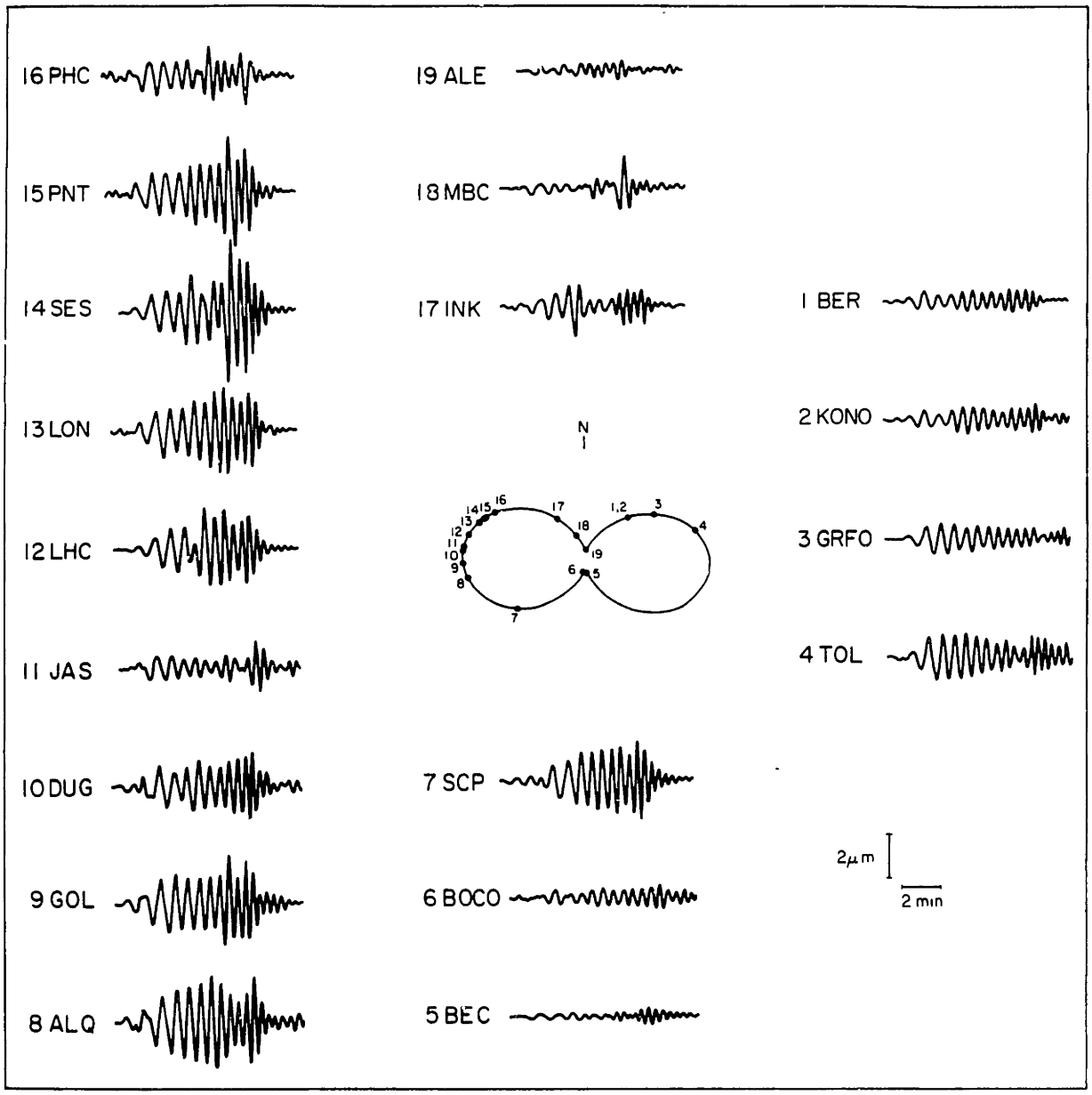
16 PHC
15 PNT
14 SES
13 LON
12 LHC
11 JAS
10 DUG
9 GOL
8 ALQ
19 ALE
18 MBC
17 INK
7 SCP
6 BOCO
5 BEC
N
1 BER
2 KONO
3 GRFO
4 TOL
2μm
2 min

Figure 4.3.10

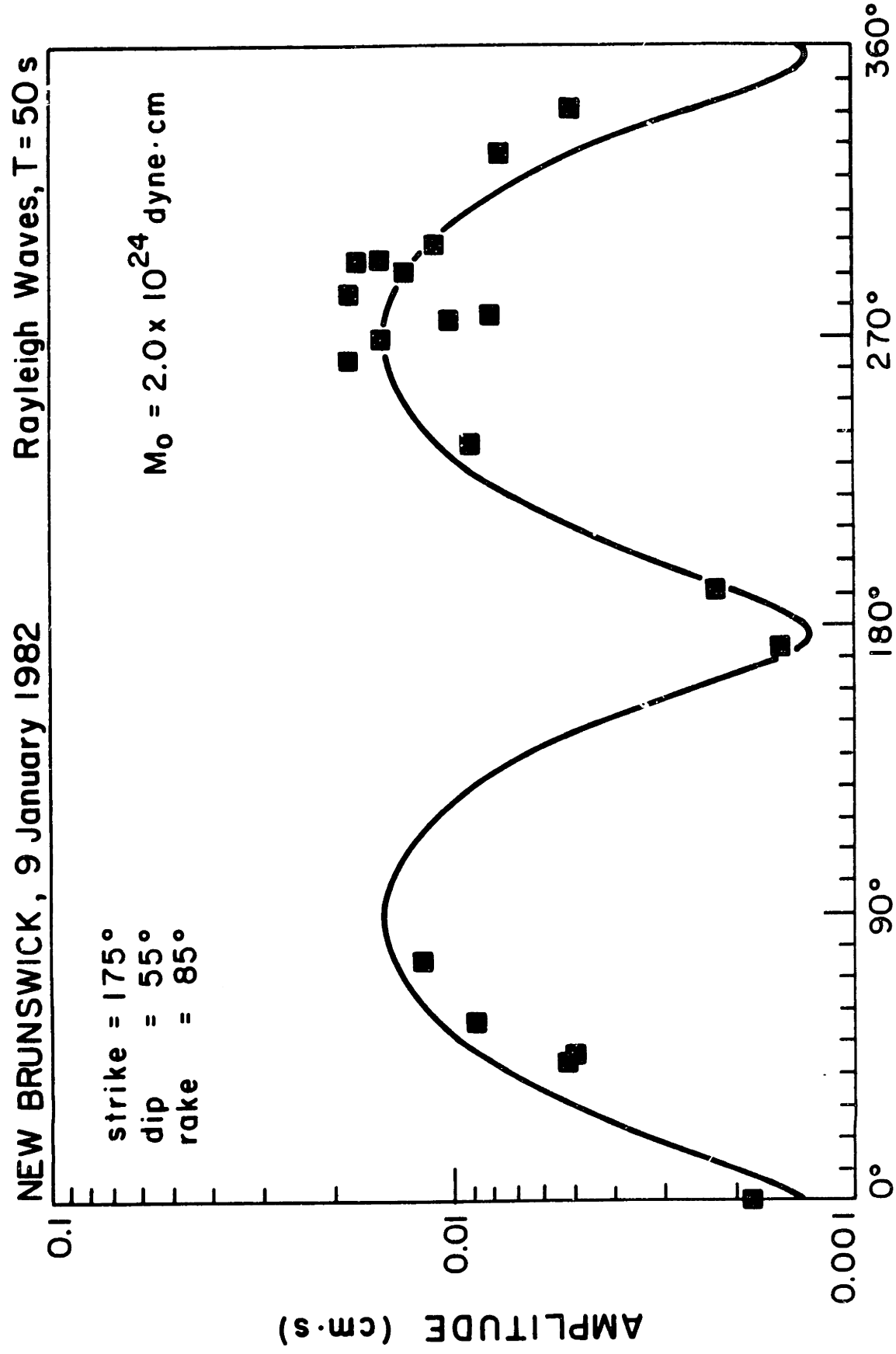
NEW BRUNSWICK, 9 January 1982
Rayleigh Waves, T = 50 s
$M_o = 2.0 \times 10^{24}$ dyne·cm
strike = 175°
dip = 55°
rake = 85°
AMPLITUDE (cm·s)
0.1
0.01
0.001
0°
90°
180°
270°
360°
AZIMUTH

Figure 4.3.11

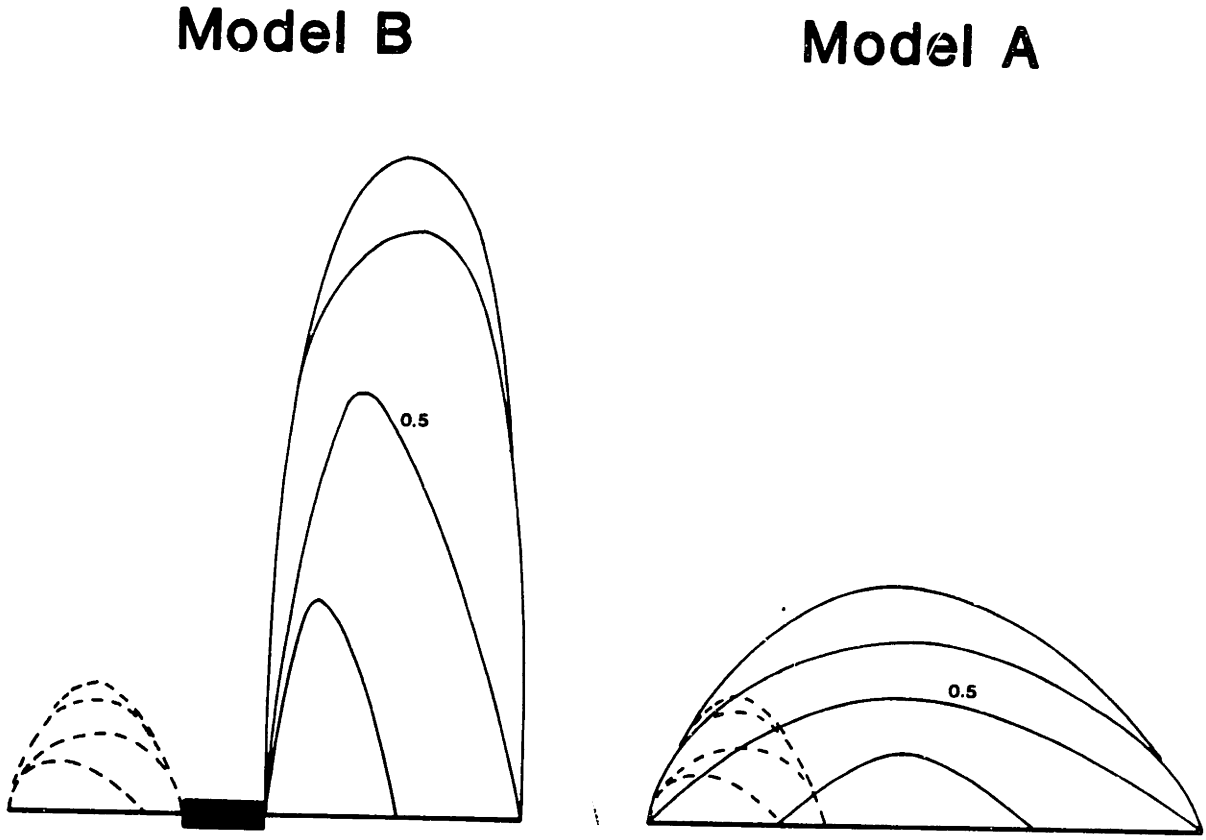

Figure 4.3.12

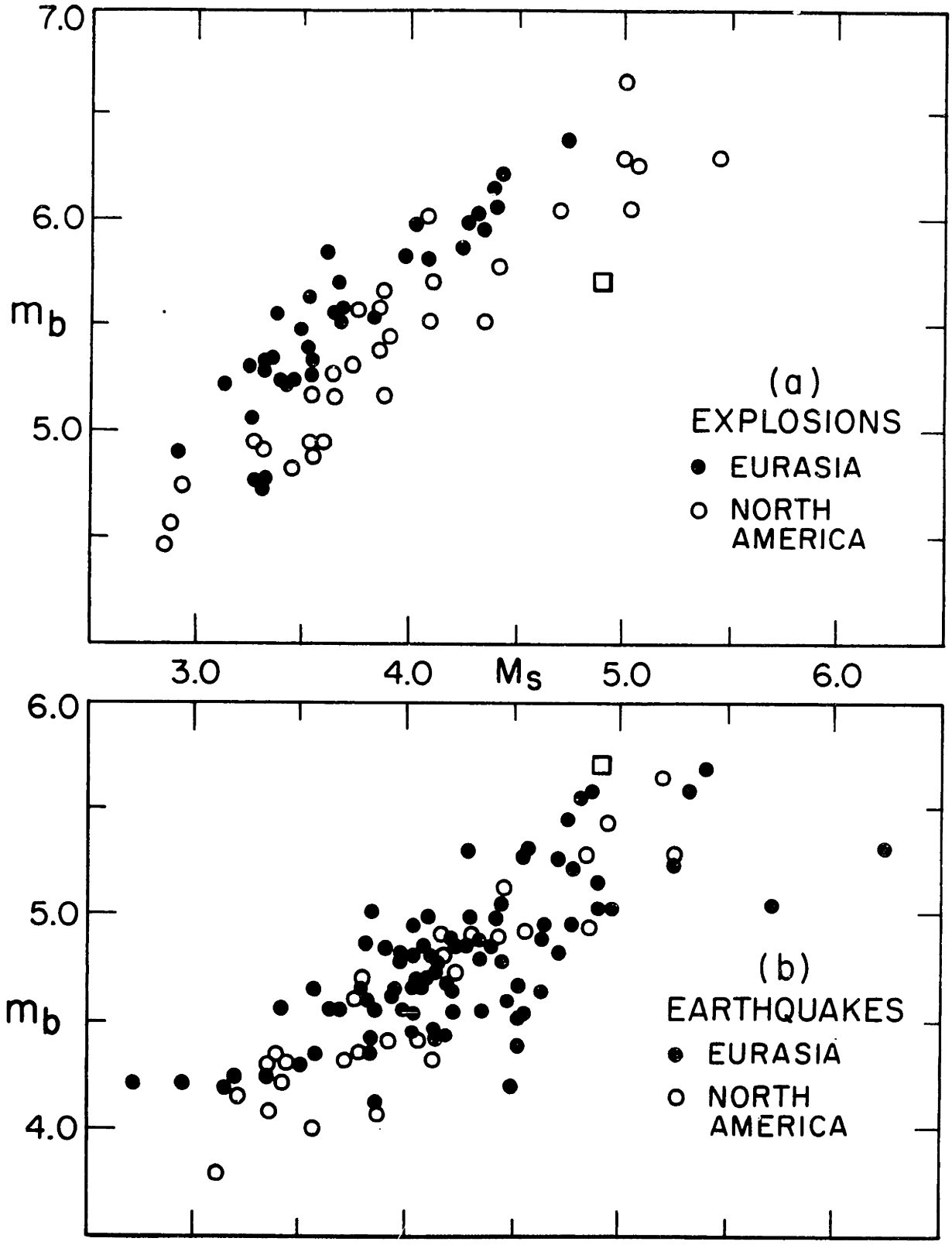
7.0
6.0
5.0
m_b
(a)
EXPLOSIONS
EURASIA
NORTH AMERICA
3.0
4.0
M_S
5.0
6.0
6.0
5.0
4.0
m_b
(b)
EARTHQUAKES
EURASIA
NORTH AMERICA

Figure 4.3.13

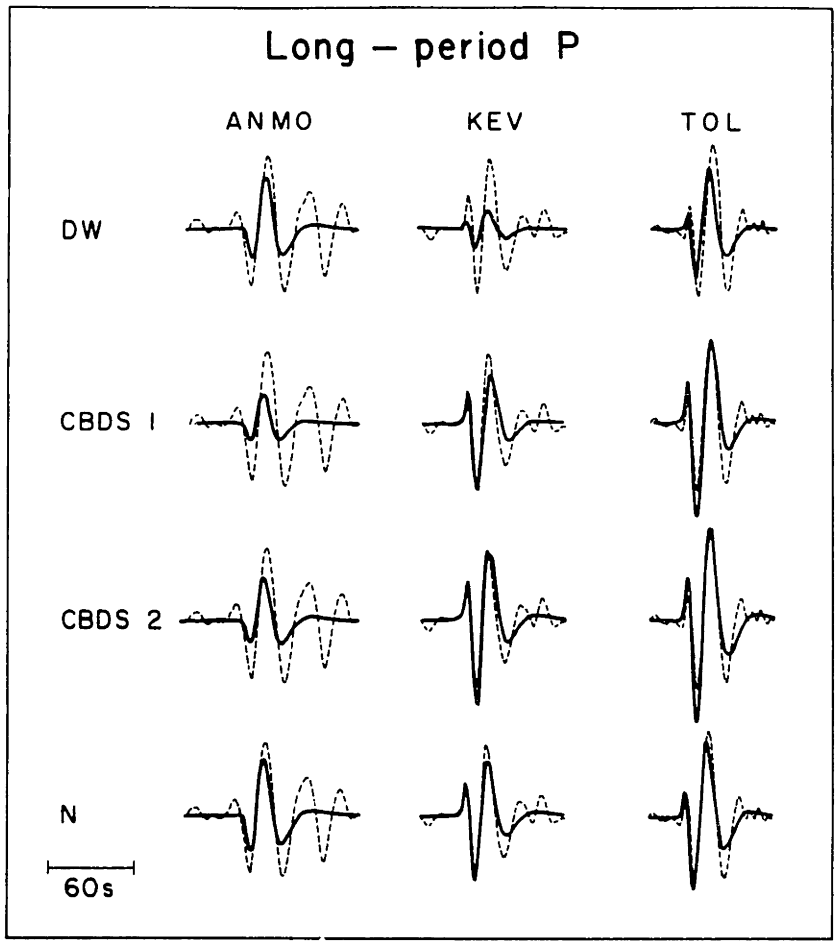

Figure 4.3.14a

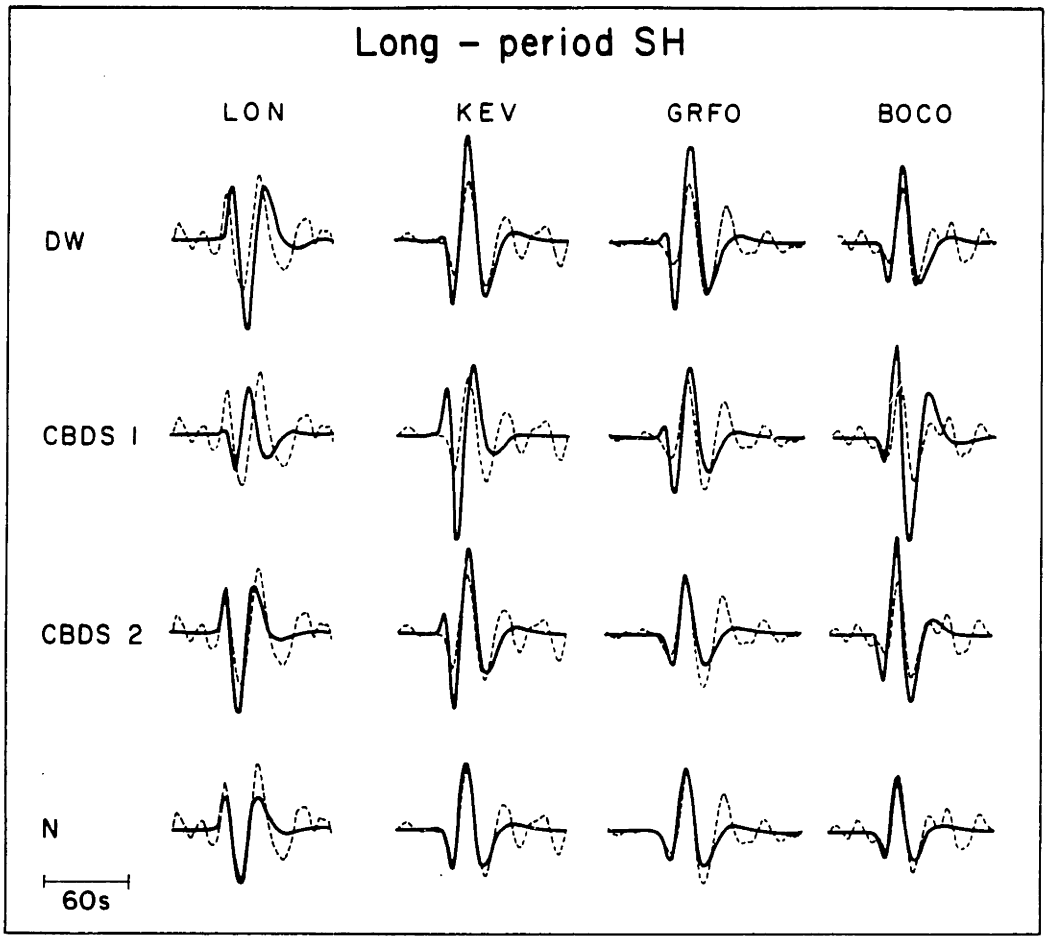

Figure 4.3.14b

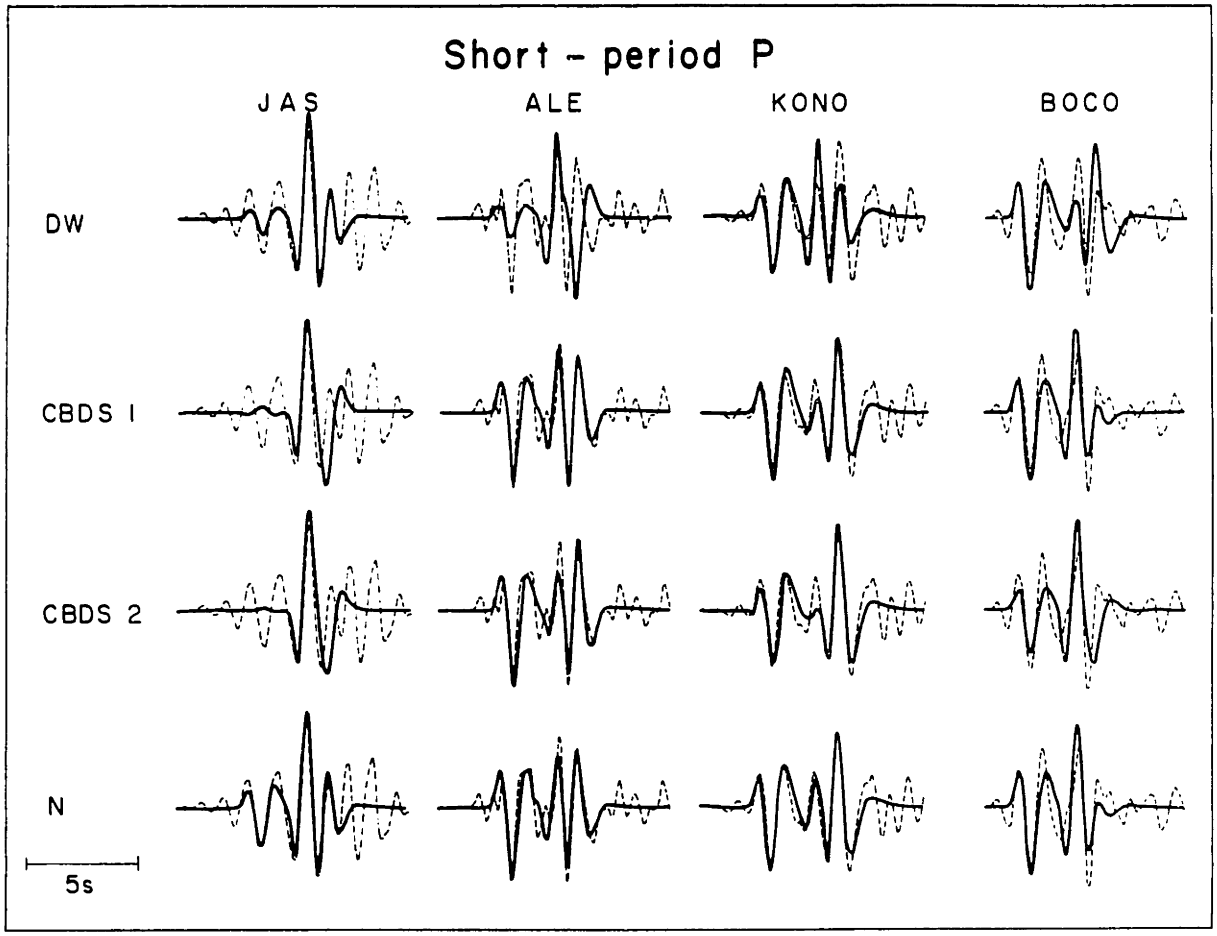

Figure 4.3.14c

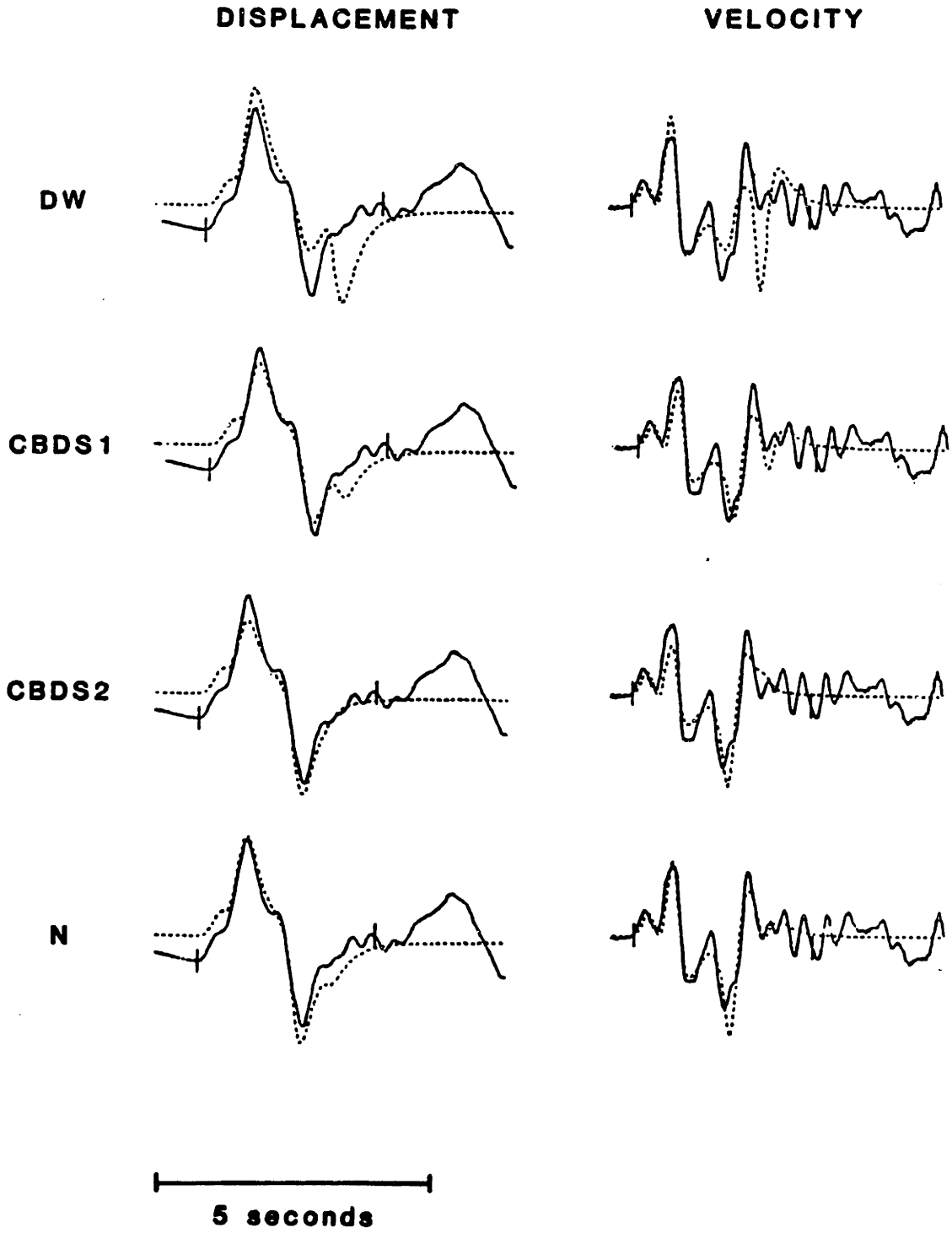

Figure 4.3.14d

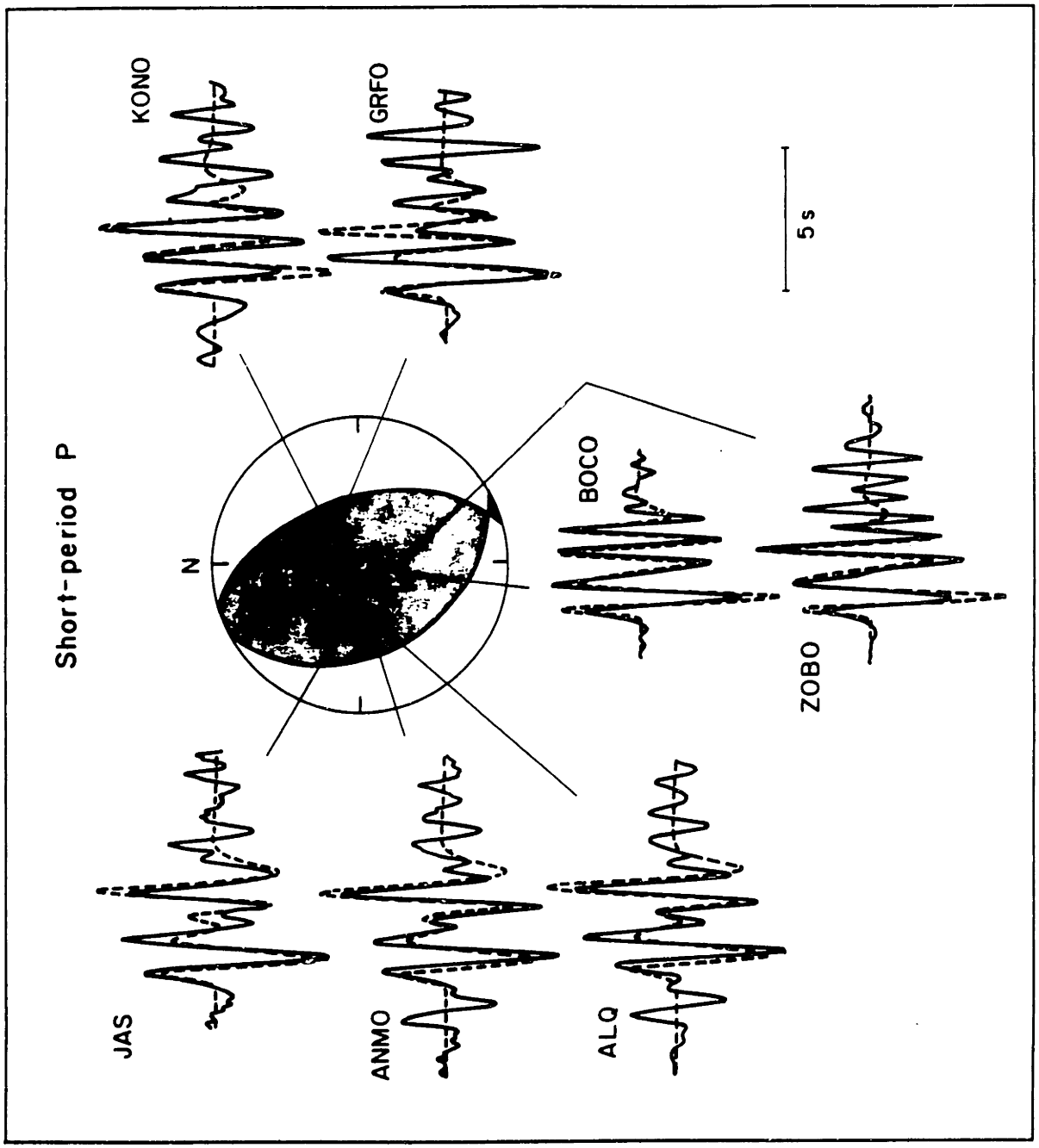

Figure 4.3.15

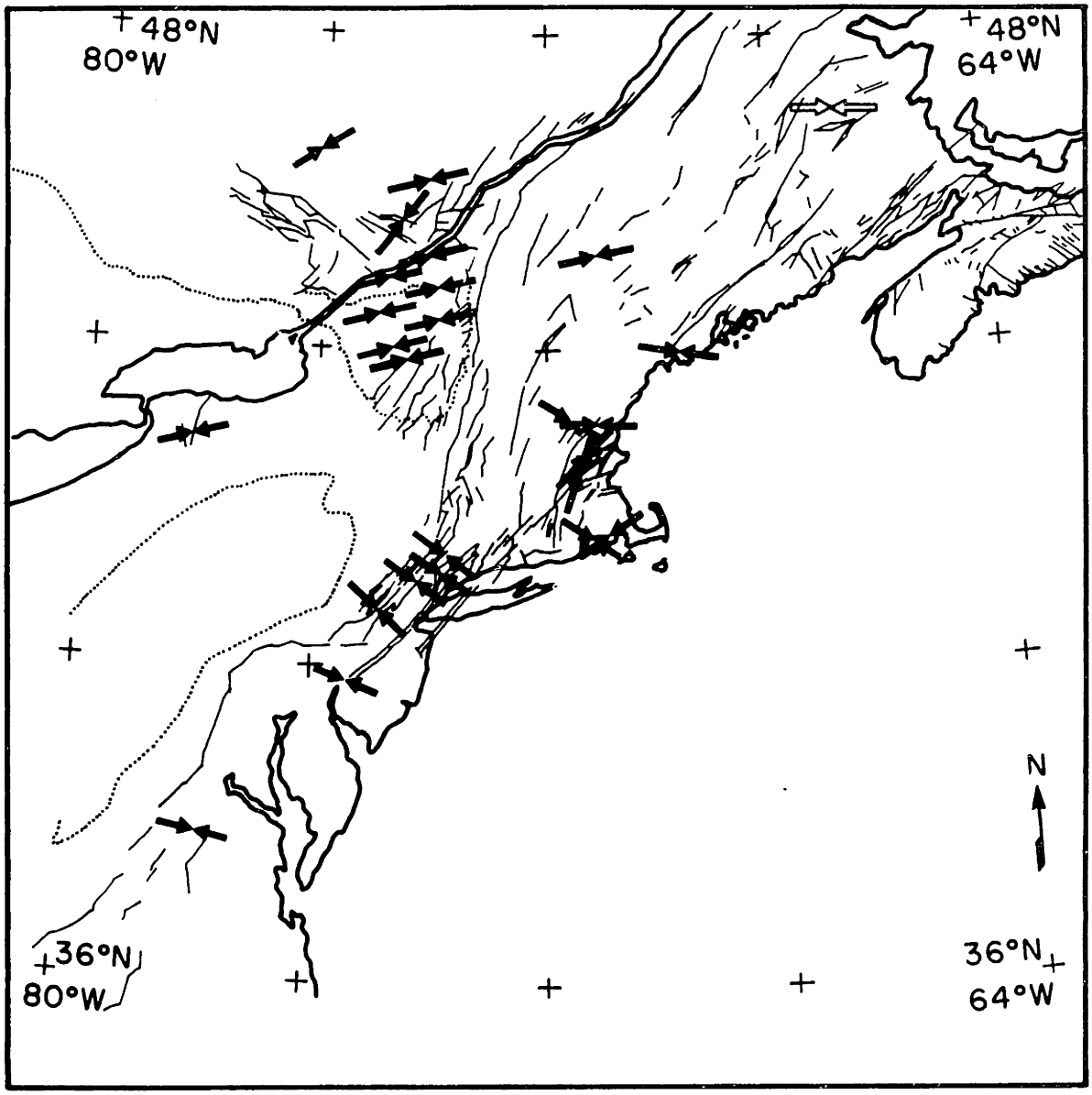

Figure 4.3.16

4.4 THE OCTOBER 10, 1980, EL ASNAM, ALGERIA, EARTHQUAKE

4.4.1 INTRODUCTION

The El Asnam, Algeria earthquake (M_S = 7.3; 12:25:23 GMT; 36.2°N, 1.4°E) has by now become one of the most extensively studied large events. The earthquake produced widespread surface faulting. The geological mapping and detailed aftershock monitoring were conducted primarily by teams from France and England [Ambraseys, 1981; King and Vita-Finzi, 1981; Ouyed et al., 1981, 1984; Yielding et al., 1981; Philip and Meghraoui, 1983]. Geodetic measurements and interpretations were discussed by Ruegg et al. [1982]. The results of teleseismic P-wave modeling were presented by Yielding et al. [1981], Nabelek [1981] and Deschamps et al. [1982]. Surface waves were analyzed by Deschamps et al. [1982], Kanamori and Given [1982] and Romanowicz and Guillemant [1984]. Although in many respects the above studies corroborate each other's conclusions, many uncertainties in the interpretations still remain.

The purpose of this paper is to reassess the constraints on the mode of faulting provided by the long-period teleseismic body waves giving particular attention to the inconsistencies in the previous studies. Attention will be given mainly to the late parts of the seismograms which apparently contain information about the slip at the north-east end of the El Asnam fault break. The faulting in this region is the least understood and was the subject of varied interpretations. The least squares inversion of the P and SH waves discussed in previous chapters is again the main tool in this analysis. It will be shown that although the inversion of the later parts of seismograms is quite unstable, meaningful results can be obtained if constraints based on the geological studies are applied to the model. The two main results of this study are: 1) the thrust plane of the

north-east fault segment dips at a much shallower angle than the thrust plane of the south-west segment and 2) the seismic moments associated with both fault segments are approximately equal.

4.4.2 FIELD OBSERVATIONS AND AFTERSHOCK STUDIES

Detailed field investigations of the surface faulting and aftershock activity commenced three days after the event. The comprehensive results of the mapping of surface fault displacements were presented by Yielding et al. [1981], Ouyed et al. [1981], and Philip and Meghraoui [1983]. A simplified map of their observations is shown in Figure 4.4.1.

The main thrust follows the base of a well-developed geological escarpment with an average strike of 230°. It is composed of two segments, each approximately 11 km long; here, as in the previous studies, they will be referred to as southern and central segments (or segments A and B, respectively). The average of the observed slip displacements was approximately 3 m, with a maximum of approximately 6.5 m. No significant strike-slip component was noted. A well developed system of secondary normal faults with slip displacements of up to 1 m parallels the central segment. Based on the location of the epicenter (also shown in Figure 4.4.1) it appears that the rupture initiated at the south-west end of the fault and propagated towards the north-east.

At the northern end, the strike of the fault escarpment changes abruptly from 230° to 250°. Unambiguous evidence for continued thrust faulting in this region is found along a segment approximately 3 km long, but the large extent of the secondary faulting indicates thrusting over a wider area [Yielding et al., 1981; King and Yielding, 1984]. This region is referred to as the northern fault segment (or segment C). The largest normal fault displacements of all were observed in the northern region, at

Beni Rached (2 m) and Kef el Mes (3-5 m, Figure 4.4.1). Beni Rached is believed to be a massive landslide [Ouyed et al., 1981; Yielding et al., 1981; Philip and Meghraoui, 1983]. Kef el Mes, on the other hand, has been subject to several interpretations (Figure 4.4.2). Yielding et al. [1981] believe it to be a secondary normal fault with motion along the bedding planes within the hanging wall of the main thrust (Figure 4.4.2a), while Philip and Meghraoui [1983] believe that the normal fault is actually the main thrust that has been redirected by the bedding planes to give it the appearance of a normal fault near the surface (Figure 4.4.2b).

The aftershock distribution found by Ouyed et al. [1984] is shown in Figures 4.4.3 and 4.4.4. The aftershocks form a narrow band along the southern and central segments of the fault, but are considerably more spread out in the north. The northern region is also unusual in that a large number of aftershocks occurs south of the geological escarpment. In general, however, the aftershock distribution is consistent with a north-west dip of the fault. Most of the activity appears to die out at a depth of 10-12 km.

4.4.3 PREVIOUS BODY WAVE STUDIES

Yielding et al. [1981] modeled the first cycle of the observed P waveforms, which corresponds to the energy release from the southern and central fault segments. They show evidence for a temporary arrest of the rupture propagation that exhibits itself as a small glitch in the first half-cycle of the waveforms recorded at stations to the west (Figure 4.4.5a). They interpret this to be the breaking of a barrier and correlate the barrier with the discontinuity in the escarpment defining segments A and B. Based on the modeling of the waveforms, they also argue that the fault-plane of segment B must be dipping at a shallower angle than that of segment A.

Deschamps et al. [1982] also include segments A and B in their model, but only in a pro forma fashion, since they assign them an identical source mechanism and propagate the rupture in an essentially continuous manner. Consequently, heir calculated waveforms do not strongly reflect this secondary feature. Deschamps et al. [1982], however, consider a longer portion of the waveforms than did Yielding et al. [1981]. They argue that additional faulting is necessary in order to explain the later parts of the wave forms. They include segment C in their model and argue that it ruptured about 7.5 s after the rupture on segment B ceased. Based on field evidence, they consider only a thrust mechanism as a viable explanation of the observed seismograms.

Nabelek [1981], using an inversion scheme similar to the one described in this thesis, also put forward evidence for continued energy release in the later parts of the seismograms. He concluded that the main mode of deformation in the north was characterized by steeply dipping normal faults, which he correlated with the large amplitude normal faulting observed at the surface in this part of the fault zone. Like Deschamps et al. [1982], he merged segments A and B into one and reached similar conclusions about faulting in that part of the fault. All of the above studies agree that the faulting initiated at the southernmost point of segment of A.

As mentioned earlier, the main the purpose of this paper is to further investigate the models of faulting in the northern segment of the fault zone. The Deschamps et al. [1982] model, although geologically consistent, does not adequately explain certain basic features of the observed seismograms (these will be further discussed later in the text). On the other hand, although the Nabelek [1981] model does fit the seismograms

better, it is not consistent with the concensus reached by the field investigators about the seismogenic mode of faulting in the northern region. This model is presented here again as one of the alternatives because, seismologically, it is an acceptable model and points out fundamental instabilities associated with the analysis of large, complex events using teleseismic data.

4.4.4 INVERSION AND MODELING OF TELESEISMIC BODY WAVES

Data preparation: This study utilizes long-period P and SH wave data from the WWSSN and GDSN networks, supplemented by a few stations of similar characteristics (Table 4.4.1). All data were digitized and interpolated into 0.5s time intervals. Amplitudes were equilized to an instrument magnification of 5000 and a distance of 40°. The entire data set can be viewed in Figures 4.4.5a and 4.4.5b. Station weights (Table 4.4.1) were assigned on the basis of the focal sphere coverage and the average amplitude of the waves in the subsets of the total data sets (the subsets being P and SH waves, and digital and analog records). As mentioned before, such weighting reduces the possibility of introducing bias into the solution because of an imbalance in the data coverage.

Inversion strategy: The results of the previous studies indicated the need for introducing complicated source time histories in order to explain basic features of the observed body waves. The present analysis is divided into 7 inversions. In the first two inversions only the early portion of the seismograms is analyzed with relatively simple models. The need for introducing additional model complexities in order to explain the later part of the waveforms will become apparent. The next two inversions will indicate the possibility of two alternative models which could explain the observed waveform complexities and the following two inversions will be

refinements of these two models. It will be shown that a meaningful result can be obtained only by putting some a priori bounds on the model based on the field investigations. The final model will show that some still unmatched complexities in the waveforms from the African stations may perhaps be due to crustal layering in the source region.

The models in the earlier studies were based solely on P-wave analysis. The SH waves used in this study help considerably in narrowing down the field of acceptable models. The models presented here attempt to explain only the first-order, long-period features of the seismograms. The short-period features associated with the breaking of fault segments A and B were adequately modeled by Yielding et al. [1981]. For the purposes of this study it will be sufficient to model the rupture on this part of the fault by a single (average) source mechanism.

Source parameterization: Two types of source parameterizations are used, a point source and a line source. The point source time function $\Omega(t)$ is parameterized by a series of overlapping isosceles triangle functions $T_{\Delta\tau}(t)$ of duration $2\Delta\tau$ and adjustable relative amplitudes w_k (Figure 2.6)

$$\Omega(t) = \sum_{k=1}^{N_{\Delta\tau}} w_k T_{\Delta\tau}(t-\tau_k), \quad \tau_k = (k-1)\Delta\tau \tag{4.4.1}$$

$N_{\Delta\tau}$ being the number of the time function elements. $N_{\Delta\tau}$ and $\Delta\tau$ are prescribed a priori and w_k are determined by the inversion.

$T_{\Delta\tau}(t-\tau_k)$ can be also written as a convolution of two box functions $B_{\Delta\tau}(t)$, of equal duration $\Delta\tau$

$$T_{\Delta\tau}(t-\tau_k) = B_{\Delta\tau}(t-\tau_k) * B_{\Delta\tau}(t). \tag{4.4.2}$$

The effect of a propagating horizontal line source is achieved by varying the duration of one of the box functions according to the well known

formula (Ben Menahem, 1961)

$$\Delta\tau' = \Delta\tau\,[1 - v_r p \cos(\phi-\theta)] \qquad (4.4.3)$$

where p is the ray parameter, v_r is the rupture velocity, ϕ is the station azimuth and θ is the fault strike. $\Delta\tau$ is chosen a priori as in the case of the point source. For the line source, however, $\Delta\tau$ can be also interpreted as the time it takes for the source to propagate along a segment $\Delta\ell = \Delta\tau\, v_r$ and w_k as the relative moment release from the individual line source segments. The duration of the second box car $\Delta\tau_r$ is constant; it corresponds to the rise time in Haskell [1964] type models and is also set a priori. Equation (4.4.2) becomes

$$T_{\Delta\tau'}(t-\tau_k) = B_{\Delta\tau'}(t-\tau_k) * B_{\Delta\tau_r}(t), \quad \tau_k = (k-1)\Delta\tau' \qquad (4.4.4)$$

Thus an element of the effective source time function of a line source at a given station is a trapezoid (Figure 2.7). All models were calculated using a double-couple constraint.

Inversion results: The main results of the individual inversions which will be discussed in this section are summarized in Table 4.4.2. Deduced source time functions are displayed in Figure 4.4.6. Examples of the matches to the data achieved by the models are shown in Figures 4.4.7a and 4.4.7b.

Model I was obtained using a single point source. The length of the source time function was limited to the time frame in which the amplitudes of all elements remained positive (about 12s). The deduced source mechanism is in very good agreement with the field data for fault segments A and B. This simple model matches the waveforms in the first cycle of the data reasonably well. We notice, however, a discrepancy in the amplitude and dominant period for stations along the fault strike (e.g., the amplitude of TAB is underestimated by a factor of 2). The directivity of the observed misfits supports the earlier conjecture based on the

published epicenter location estimates (Figure 4.4.1) that the rupture originated at the southern end of the fault. In inversion II the source is modeled by a horizontally propagating line source (otherwise, the parameterization is the same as in model I). The rupture velocity is assumed to be 2.75 km/s (0.75 v_s). The rise time of 2.5s approximates the effect of fault width on the source time function. We notice that the line source parameterization substantially improves the data fit in the first cycle. (The improvement is not well represented by the tabulated residuals because they include the later portion of the seismograms which is not being affected by these two simple models. For consistency, the inversion time windows were kept constant in all of the seven models; see Figure 4.4.5a,b). With the assumed rupture velocity, the inversion indicates a fault length of 27 km (determined by the number of consecutive, positive time function elements), in excellent agreement with the total length of fault segments A and B. In order to speed up the convergence and improve the stability of the inversion in the subsequent, more complex source parameterizations, the depth determined in this inversion (6 km) was used.

The single event models I and II are inadequate for explaining the waveforms beyond the first cycle. In order to investigate possible source activity at a later time, the number of elements in the source time function in Model III was increased to cover a time window of 50 s. Because continuous rupture over such a large time window would be clearly inconsistent with the field data, the point source model was used again. We notice that the source time function becomes strongly negative approximately 12 s after the origin time and remains negative for additional 12 s; after 24 s, no significant energy is released. Assuming that no back slip took place, the negative excursion implies faulting with

a significantly different mechanism, most likely in the north, triggered by the rupture of segments A and B.

Model V (skipping model IV for a moment) was obtained by explicitly introducing two subevents into the inversion. The first subevent was modeled by a propagating line source. The second subevent is a point source located 30 km north of the nucleation point of the first subevent at an azimuth of 40°. Because the depth of the second subevent is very poorly resolved, it was also set to 6 km; this is consistent with the observed depths of the aftershocks. The deduced source mechanism is a steeply dipping normal fault with a strike of 55° [Nabelek, 1981]. This result would imply that the large amplitude normal faults at Beni Rached and Kef el Mes (Figure 4.4.1) are not simply shallow secondary features but must extend to a considerable depth to account for the large seismic moment. Model V is successful at reproducing both the shapes and absolute amplitudes of the first two cycles of the data at all stations (except for some misfit at the African stations, which will be discussed later). Tectonic considerations, the morphology of the normal faults, and the aftershock distribution and fault-plane solutions, however, do not support this model [Yielding et al., 1981; Philip and Meghraoui, 1983; Cisternas et al., 1983; Ruegg et al., 1983]. The uniqueness of this seismically derived model must therefore be investigated.

In order to find a starting model which could lead to a solution with a thrust type mechanism, the inversion was carried out using a single source with a long source time function, adding the constraint that the elements of the source time function be positive [Lawson and Hanson, 1974]. The inversion (Model IV) indicates the possibility of a second thrust event of very long duration starting approximately 20s from the origin time of the

first event (Figure 4.4.6). Using this solution as an initial point for the two source inversion, the inversion leads again to an answer which is not consistent with the field studies. It appears that the noise (signal generated) in the later parts of the seismograms forces the inversions into unacceptable solutions. To obtain meaningful results, a priori constraints based on the field observations must be applied.

The maximum likelihood inverse discussed in Chapter II and Appendix B provides a means of applying constraints in an objective manner. From the field studies, the best known fault parmeters are the strike and the slip angle. The dip angle is difficult to estimate from the surface data due to slumping of the nose of the thrust [Yielding et al., 1981]. The a priori model for the first subevent corresponding to fault segments A and B is strike 230±5°, dip 50±15° and rake 90±5°. The a priori model for the second subevent presumed to be a result of the faulting on segment C, is strike 250±5°, dip 45±15° and rake 90±5°. As mentioned previously, nowhere do the aftershocks extend beyond a depth of 12 km, providing good bounds on the possible vertical fault extent. The average depth of 6 km determined earlier and used in the previous models is probably a reasonable choice, it is fixed in this inversion. The parameterization of the first subevent as a propagating line source is justified by the observable directivity and the general agreement with the field studies. On the other hand, a point source parameterization of the second subevent is required by its very long duration. Its relative location with respect to the epicenter is assumed to be the same as for the second subevent in model V.

Model VI was obtained by conducting the inversion under the above constraints. The model reproduces the observed data quite well although the residual is somewhat greater than that for model V. The most

important new information obtained about the second subevent is the dip angle (20°) and the seismic moment (3.6×10^{26} dyne-cm). It appears that the thrusting in the northern region had a seismic moment comparable to that of the thrusting in the south and central regions, but it took place on a much shallower dipping fault plane and over a relatively longer time span.

None of the above models satisfactorily explain the large arrivals in the later parts of the waveforms observed at the African stations (e.g., BUL). Modeling of these features in terms of different source effects was entirely unsuccessful which suggests that they may be due to unmodeled structural effects. Such a conjecture is supported by the fact that the waveforms from an $m_b = 6.1$ aftershock (October 10, 1980; 15:39 GMT) show identical late arrivals (Figure 4.4.8).

In Model VII we introduce a layered crustal structure in the source region. It shows that crustal reverberations could be partially responsible for the observed complexity, since the strongest effect is indeed felt by the African stations. The amplitudes of the reverberations, however, are not sufficiently large. This and the fact that an unusually large crustal thickness (48 km) is necessary to produce the required period of the oscillations suggests that they may be due to some other structural effect along the paths to the African stations. Model VII is the final model of this study. Its match to all the data is shown in Figures 4.4.5a and 4.4.5b.

4.4.5 DISCUSSION AND INTERPRETATION

The results of the analysis of the rupture on fault segments A and B are in excellent agreement with the previous body wave analyses and field investigations. The dip of the fault (46°) is an average for the two segments and is in agreement with the dip obtained from the composite focal-mechanism solution from the aftershocks in this region by Cisternas et al. [1983]. Comparison with the observed short-period first motions indicates that the dip at the epicenter was somewhat steeper which indicates that the fault dip is shallowing as it progresses to the north. This conclusion was also reached by Yielding et al. [1981]. Deschamps et al. [1982] obtained a steeper dip (54°) for the average of segments A and B but in visually matching of the observed and calculated seismograms they may have biased their solution somewhat to the early parts of the wave forms. The point source depth of about 10 km determined by Yielding et al. [1981] and Deschamps et al. [1982] is deeper than the depth of 6 km determined here. This discrepancy may again be due to the fact that in visual modeling the tendency is to concentrate on the early and short period aspects of the waveforms, thus biasing the solution towards the parameters at the source nucleation point. On the other hand, inversions tend to match the longer-period aspects of the waveforms, and the obtained solution represents the centroidal (average) aspects of the faulting. The centroidal depth of 6 km obtained in this study is in excellent agreement with the vertical extent of the aftershocks. The centroidal depth and the dip of 46° imply an average fault width of about 17 km. It is interesting to note that if the dip of the fault plane determined from the teleseismic analysis is indeed correct, it implies that almost all aftershock activity in segments A and B occurs in the foot wall of the thrust (Figure 4.4.4).

It was mentioned earlier that the fault-length of 27 km determined here correlates well (within the uncertainty on the assumed rupture velocity) with the 24 km total length of segments A and B observed in the field. The seismic moment released from segment A and B was about 3.9×10^{26} dyne-cm. This value is larger than that determined by both Yielding et al. [1981] (2.5×10^{26} dyne-cm) and Deschamps et al. [1982] (1.5×10^{26} dyne-cm). This discrepancy is due primarily to the difference in source depth; although the source depth has only a small effect on the estimated source mechanism, the decrease in destructive interference between direct and reflected phases for deeper source results in a large decrease in the seismic moment estimate).

Using the above fault parameters (length = 24 km, width = 17 km, and $M_o = 3.9 \times 10^{26}$ dyne-cm) we can estimate an average slip displacement of 3.2 m and an average stress drop of 48 bars for segments A and B. The value of 3.2 m for average slip displacement is in excellent agreement with the 3 m determined from the field measurements [Yielding et al., 1981; Oued et al., 1981].

It was shown in the previous section that the interpretation of the later parts of the waveforms is non-unique. The solution with the lowest residual (using a half-space crustal model) indicates significant normal faulting in the northern-region of the fault zone (Model V). This was the solution reported earlier [Nabelek, 1981]. Although large normal faulting is observed at the surface in the northern region (Beni Rached, Kef el Mes; Figure 4.4.1), most field investigators argued against these faults extending to depth [Yielding et al., 1981; Philip and Meghraoui, 1983]. Seismologically, the best argument against this model comes from the investigations of very long period surface waves (~300 s) from the IDA

network [Kanamori and Given, 1982; Deschamps et al., 1982; Romanowicz and Guillemant, 1984]. At these periods, the waves from the two subevents are almost in phase and the calculated moment should represent the sum of the two. If the second subevent had a normal faulting mechanism, the very long period moment would be smaller than the moment for the first subevent. The reported moments (>5 x 10^{26} dyne-cm) in the surface wave studies are for a double-couple mechanism with a similar orientation to that of subevent 1 of this study and can be compared directly with the single-event-long-time-function inversions III and IV. That inversion IV agrees better with the very long period surface wave moment is a strong argument in favor of the thrust type models for the northern region (models VI and VII).

Since no unconstrained inversion leads to a geologically acceptable solution, constraints based on field investigating were employed. The most important constraints were the strike and the slip angle of faulting in segment C; the *a priori* values of 250±5° and 90±5°, respectively, were based on studies by Yielding et al. [1981] and Oued et al. [1981]. It should be pointed out that a small relaxation of the constraints rotates the strike of segment C counterclockwise, producing an improvement in the fit of the second downswing of the SH waves from PAL and ANMO.

We have obtained an estimate of the fault dip, the least known parameter of the faulting mechanism. It appears that the northern fault segment is not only rotated in strike with respect to the southern and central segments, but that its dip also changes abruptly to a much smaller value. This change in dip, however, follows the already documented northward shallowing trend in the south and central fault segments [Yielding et al., 1984]. The significant shallowing of segment C correlates well with the spreading out of the aftershock distribution in

the north (Figure 4.4.3). The deduced dip of 20° implies that the aftershock activity occurs mainly in the footwall, in agreement with the pattern observed for the south and central segments (Figure 4.4.4).

The long duration of the source time function and the lack of observable directivity preclude an estimate of the fault dimensions for segment C from the body wave data. The extent of aftershock activity in this region indicates a fault length of approximately 15 km and a width of approximately 25 km. These dimensions and the moment of 3.6×10^{26} dyne-cm imply average slip displacement on the fault of about 3.2 m. Due to many assumptions, the uncertainty in this value is large, but it implies comparable displacements to those on segments A and B. The absence of a single clear surface break in segment C suggests that the fault may break up into a number of smaller faults as it reaches the surface because of its shallow dip. The large amplitude and areal extent of the secondary normal faulting, however, indicate a substantial slip on this fault segment. The same conclusion is also reached on the basis of geodetic measurements [Ruegg et al., 1982].

The results of the above analysis of the faulting on segment C conflict with those obtained by Deschamps et al. [1982]. In their preferred solution, the rupture on segment C initiated about 3 s earlier than the rupture on segment C in the model determined here and had a duration of only slightly more than 4 s. The moment determined by them is only 0.73×10^{26} dyne-cm.

Deschamps et al. [1982] claim to follow field evidence as closely as possible. Nevertheless, for some reason, they fixed the least known parameter, the fault dip, at an arbitrary value (54°) and tried to estimate the best known parameter, the fault strike.

In order to facilitate a comparison between these two models, examples of synthetic seismograms corresponding to the Deschamps et al. [1982] model are shown in Figure 4.4.9. The model appears to fail at the time of the initiation of faulting on segment C, at which point the synthetic and the observed seismograms become strongly out of phase. This is also reflected in the very large residual (0.90; only 10% improvement with respect to a straight line fit through the data). In terms of the residuals, adding segment C to their model is not warranted since the residual is in fact considerably smaller (0.77) when only segments A and B are included. It should be pointed out that the main reason for the unfavorable performance of this model is poor timing, which is not important in terms of geological interpretation. Changing the start time and the duration of the rupture on segment C does not, however, remove all the serious misfits, most notably those in the SH waves. Those can be removed only by a change in the source mechanism.

Yielding et al. [1981] and King and Yielding [1984] interpret the large extent of the aftershock seismicity in the north in terms of many en echelon steeply dipping thrusts. Although listric type faulting and movement along pre-existing bedding planes can explain the complexity of faulting as the main thrust reaches the surface, the body wave data does not allow seismogenic high angle thrusting in this region. The data do not disallow complex faulting within a volume, but the net strain must be that of a shallow dipping thrust. Independent support for shallow dip angle of the northern fault segment comes from the first motion focal-mechanism solution by McKenzie [1972] for the September 9, 1954 earthquake (m_b = 6.7) which occurred in the Beni Rached area. This solution indicates a dip of approximately 30° for the northward dipping nodal plane.

An interesting feature of models VI and VII is the 10 s quiescence of the source between the time the rupture reaches the northern end of segment B and the time of initiation of rupture on segment C. The drastic change in the rupture direction which was imposed by the pre-existing fault system in the north [Cisternas et al., 1982], apparently formed a geometric barrier which had to be overcome before rupture could proceed [Aki, 1979b; King and Yielding, 1984].

Finally, I would like to point out once again the striking agreement between the normal faulting mechanism derived in inversion IV and the observed faulting at Kef el Mes and to some extent at Beni Rached. In terms of residual, this is the preferred solution based on body wave information. If these faults extend to a depth of about 5 km, their combined seismic moment could be on the order of 0.5×10^{26} dyne-cm. It is, therefore, quite possible that the teleseismic body waves do in fact pick up some of this complexity, and that a model using three subevents (first, representing segments A and B; second, representing normal faulting at Kef el Mes and Beni Rached; and third, representing shallow thrust faulting in the north) would be appropriate.

4.4.6 CONCLUSIONS

Although the surface faulting from the El Asnam earthquake is well exposed, due to its complexities it provides a challenge for both the geologist and seismologist. By and large, where the geological information is unambiguous it can be also unambiguously derived from the seismological observations. It then comes as no surprise that when the geological complexities increase and their interpretation becomes ambiguous we are also faced with such problems in the seismological interpretation. It is interesting, however, how similar indeed the ambiguities in the

interpretation of the normal faulting in the north are in both data sets, and that merging of the information does not entirely remove the ambiguity. Nevertheless, there is clear evidence for continued thrusting in the north and this study provides evidence that it probably occurs at a shallow angle. A summary of the fault parameters derived here is given in Table 4.4.4. The match between the field evidence on segments A and B and the corresponding parameters deduced from the teleseismic body waves is remarkable and adds confidence to the interpretations based on the later parts of the waveforms, which, although non-unique, allow only certain types of mechanisms. Finally, this study underscores the need for good quality very long period data in investigations of large complex events; it is the only practical seismological means of introducing stability into the modeling of shorter periods.

Table 4.4.1 Parameters of Stations Used in the Body Wave Inversion

Station	Azimuth (deg)	Distance (deg)	Weight	Waves Used
CHTO	70	85	0.7	P,SH
KAAO	70	54	0.7	P,SH
TAB	73	36	0.7	P
BCAO	149	35	1.0	P
BUL	150	62	0.6	P
PRE	154	67	0.6	P
WIN	163	60	0.6	P
ZOBO	245	84	1.7	P,SH
TRN	263	62	0.7	P
BOCO	265	76	1.0	P,SH
BTG	268	60	0.5	P
SHA	295	72	0.5	P
PAL	300	57	0.7	SH
WES	300	55	0.5	P
ANMO	308	82	0.7	P,SH
PHC	330	82	0.7	P
AKU	345	32	0.7	P

Table 4.4.2 Summary of Body-wave Inversions Using Different Source Parameterizations and Crustal Structure

Inversion	Event 1									Event 2										Residual
	Strike (deg)	Dip (deg)	Rake (deg)	Depth (km)	Moment (10^{26}dyne-cm)	$N_{\Delta\tau}$	$\Delta\tau$ (s)	$\Delta\tau_r$ (s)	v_r (km/s)	Strike (deg)	Dip (deg)	Rake (deg)	Depth (km)	Moment (10^{26}dyne-cm)	$N_{\Delta\tau}$	$\Delta\tau$ (s)	τ_r (s)	v_r (km/s)	t_d (s)	
I	222±2	45±1	74±2	6.2±0.4	3.7±0.1	4	2.5	-	-											0.59
II	222±2	46±1	74±2	6.0±0.4	3.8±0.1	4	2.5	2.5	-2.75											0.58
III	221±2	45±1	73±2	6.0	2.1±0.3	17	3.0	-	-											0.53
IV	222±2	44±1	72±2	6.0	6.3±0.3	17	3.0	-	-											0.58
V	215±2	52±1	71±2	6.0	3.4±0.1	5	2.5	2.5	-2.75	55±4	64±2	-92±3	6.0	1.6±0.1	3	3.0	-	-	11±0	0.45
VI	221±1	46±1	73±1	6.0	4.0±0.1	5	2.5	2.5	-2.75	235±4	21±2	92±6	6.0	3.9±0.2	8	4.0	-	-	19±0	0.47
VII	219±1	46±1	72±1	6.0	3.9±0.1	5	2.5	2.5	-2.75	226±5	19±2	90±6	6.0	3.6±0.2	8	4.0	-	-	19±0	0.44

$N_{\Delta\tau}$ - number of time function elements
$\Delta\tau$ - time spacing of the time function elements (see text for details of the point source and line source parameterizations)
$\Delta\tau_r$ - rise time
v_r - rupture velocity of a propagating line source (positive along the strike)
t_d - time delay with respect to the origin time

The quoted uncertainties represent 95% confidence limits (2 standard deviations).
Parameters showing no uncertainties were fixed in the inversion.
Residuals were normalized to the RMS amplitude of the weighted data.
See Figure 4.4.6 for the deduced source time functions.

Table 4.4.3 The Crustal Structure Used for the P-wave Modeling

	Thickness (km)	V_p (km/s)	V_s (km/s)	Density (g/cm^3)
Source Region:				
1. Homogeneous crust	half-space	6.00	3.46	2.5
2. Layered crust	15.0	6.00	3.46	2.5
	33.0	6.75	3.90	2.8
	half-space	8.05	4.65	3.0
Receiver Region:				
	half-space	6.00	3.46	2.5

Table 4.4.4 Summary of Source Parameters of El Asnam Earthquake Determined in This Study

$m_b = 6.5^*$ $M_S = 7.3^*$

	Segments A and B	Segment C
Strike	220°	230°
Dip	46°	20°
Rake	72°	91°
Seismic moment	3.9×10^{26} dyne cm	3.6×10^{26} dyne cm
Average depth	6 km	6 km†
Length	24 km	15 km†
Average width	17 km	25 km†
Average slip	3.2 m	3.2 m
Average stress drop	48 bars	33 bars
Rupture velocity (south-to-north)	2.4 km/s	

* USGS

† from aftershock distribution

FIGURE CAPTIONS

4.4.1 A map of the surface faulting associated with the El Asnam earthquake, based on studies by Yielding et al. [1981] and Philip and Meghraoui [1983] (adapted from King and Yielding [1984]). Numbers indicate estimates of the main shock epicenter location by various agencies. The extents of the southern, central and northern fault segments are indicated by arrows and marked by A, B, and C, respectively.

4.4.2 Two interpretations of the normal faulting at Kef el Mes. The interpretations are due to (a) Yielding et al. [1981] and (b) Philip and Meghraoui [1983].

4.4.3 A map of the aftershock epicenters of the El Asnam earthquake [Ouyed et al., 1984] (adapted from King and Yielding [1984]).

4.4.4 Horizontal and vertical cross-sections of the aftershock distribution, based on locations by Ouyed et al. [1984] (adapted from King and Yielding [1984]). The presumed dip of the fault plane at different locations along the fault is indicated.

4.4.5 (a) The observed (solid lines) and synthetic (dashed lines) P-wave seismograms for the model VII (Table 4.4.2). The amplitudes of the seismograms were normalized to an instrument magnification of 5000 and epicentral distance of 40°. The larger vertical scale is for the digital stations (four letter names); the smaller scale is for the WWSSN stations (three letter names). The portions of the seismograms used in the inversion are indicated by triangles. The fault-plane solutions shown are for the first (solid line) and second (dashed line) subevents of the model. The observed first-motion polarities are also indicated.

(b) The corresponding figure for the SH waves. The vertical lines over the waveforms indicate the theoretical ScS-wave arrival. The circle in the center of the focal sphere indicates the bound on the take-off angles for ScS waves. Note that for this source model the ScS waves are nodal.

4.4.6. Plots of the far-field point-source time functions (scaled by the seismic moment) derived from Inversions I through VII as discussed in the text and summarized in Table 4.4.2. An element of the equivalent point-source time for the fault segmants which were modeled by a propagating line source is given by $T_{\Delta\tau} = B_{\Delta\tau} * B_{\Delta\tau R}$ where $\Delta\tau = \Delta\ell/v_r$. In order to obtain the effective source time function at each station, $\Delta\tau$ must be replaced by $\Delta\tau'$ (see equations 4.4.1 through 4.4.4).

4.4.7 (a) Matches to P waves from selected stations at different azimuths for the models discussed in the text and Table 4.4.2. The residual using all available data (normalized to the RMS amplitude of the data) for each model is also indicated.

(b) Matches to SH waves for the same models as in (a).

4.4.8 P waveforms recorded at African stations for the El Asnam main shock (solid line, station PRE) and the largest aftershock (dashed line, station GRM). Note the presence of similar large amplitude late arrivals for both events, indicating their path-related origin. (Good quality records were not available for both events from a common station).

4.4.9 An example of the match to the data by the model of Deschamps et al. [1982]. The residual shown is for all available data.

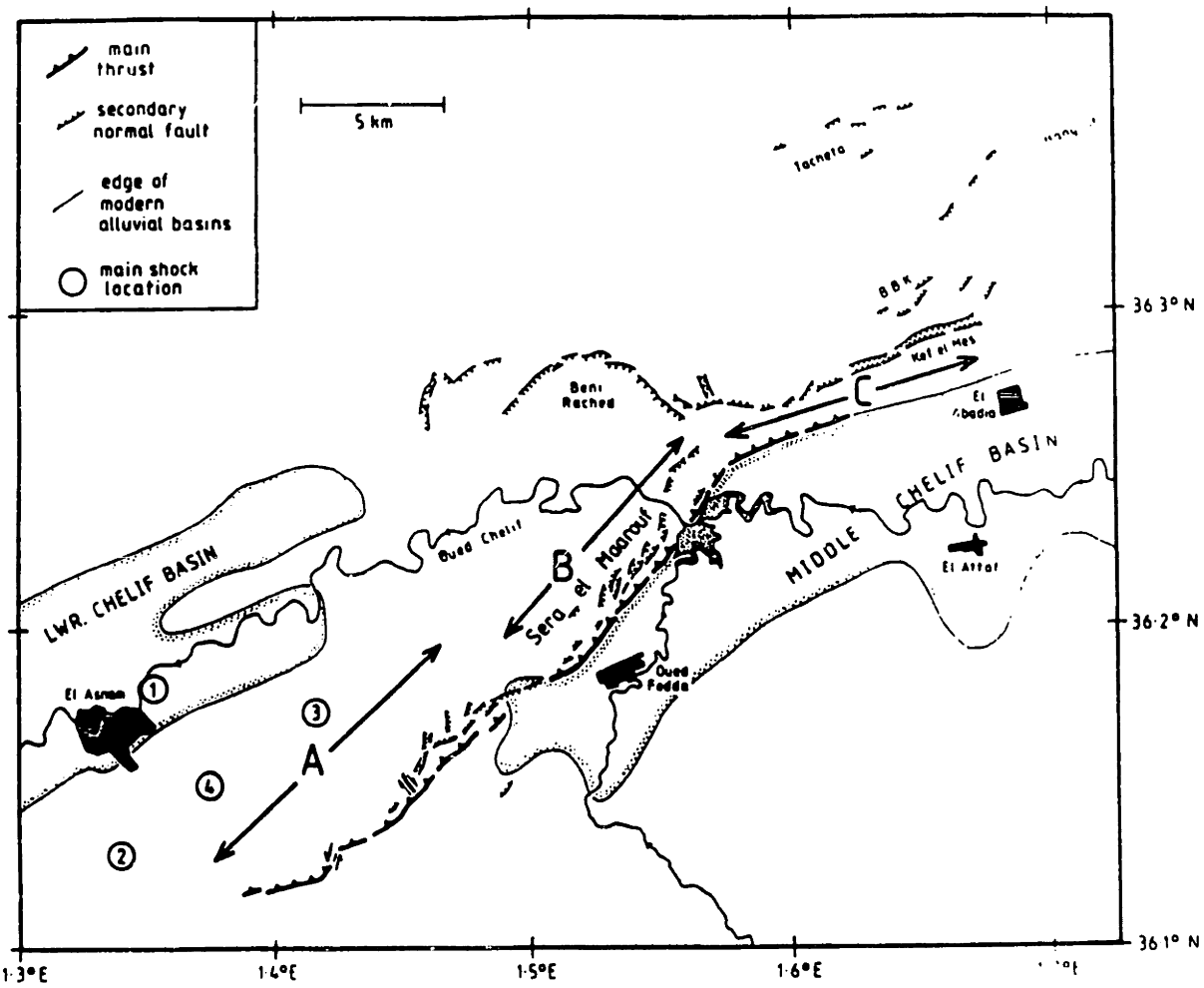
main thrust
secondary normal fault
edge of modern alluvial basins
main shock location
5 km
Tarnata
BBK
Kef el Hes
Beni Rached
El Abadia
LWR. CHELIF BASIN
Oued Chelif
Sera el Maarouf
MIDDLE CHELIF BASIN
El Affroi
El Asnam
Oued Fodda
A
B
C
1
2
3
4
36·3° N
36·2° N
36·1° N
1·3°E
1·4°E
1·5°E
1·6°E

Figure 4.4.1

(a)

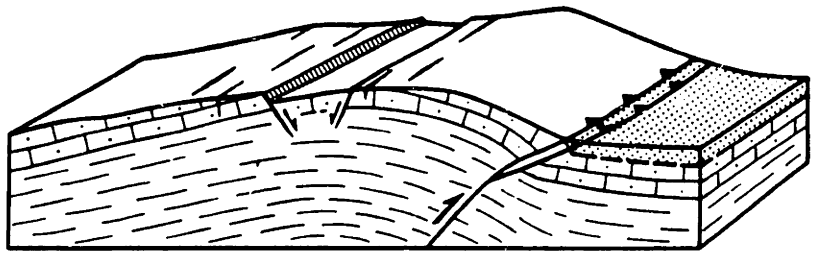

(b)

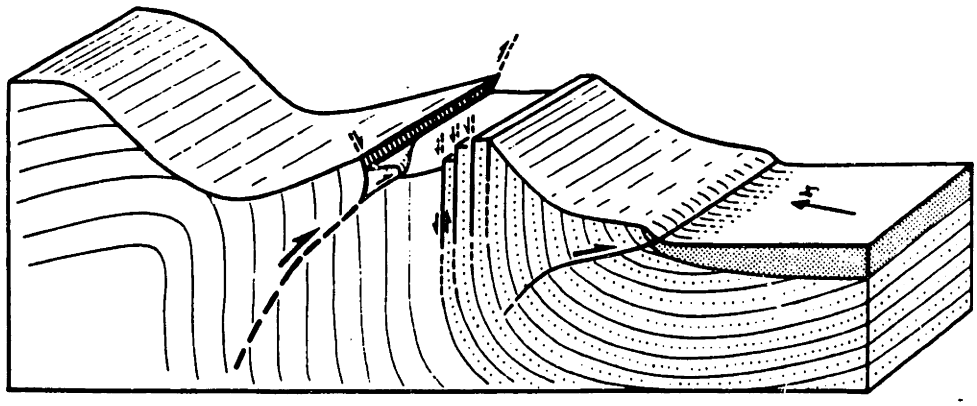

Figure 4.4.2

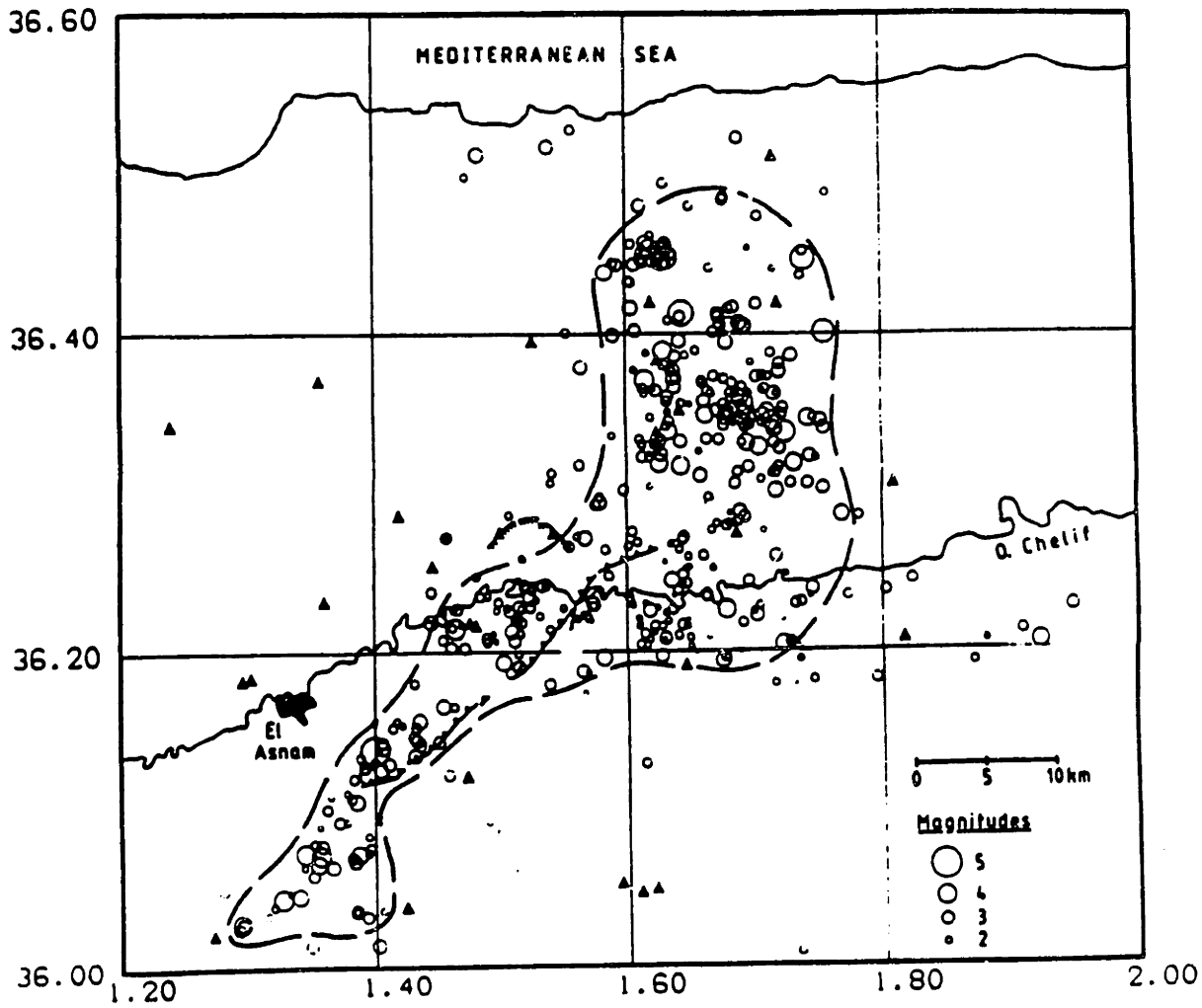
36.60
36.40
36.20
36.00
1.20
1.40
1.60
1.80
2.00
MEDITERRANEAN SEA
Q. Chelif
El Asnam
0 5 10km
Magnitudes
5
4
3
2

Figure 4.4.3

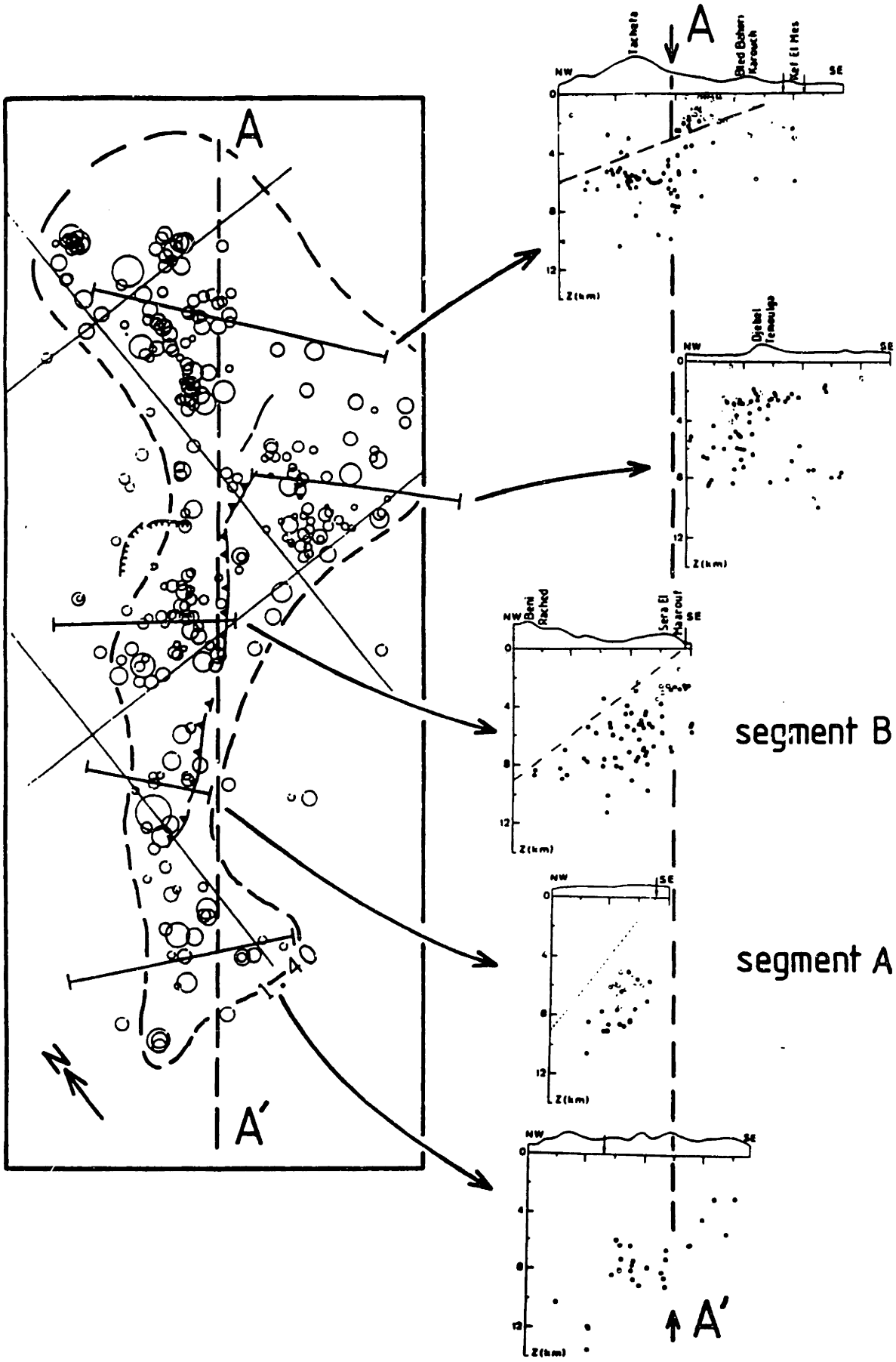

Figure 4.4.4

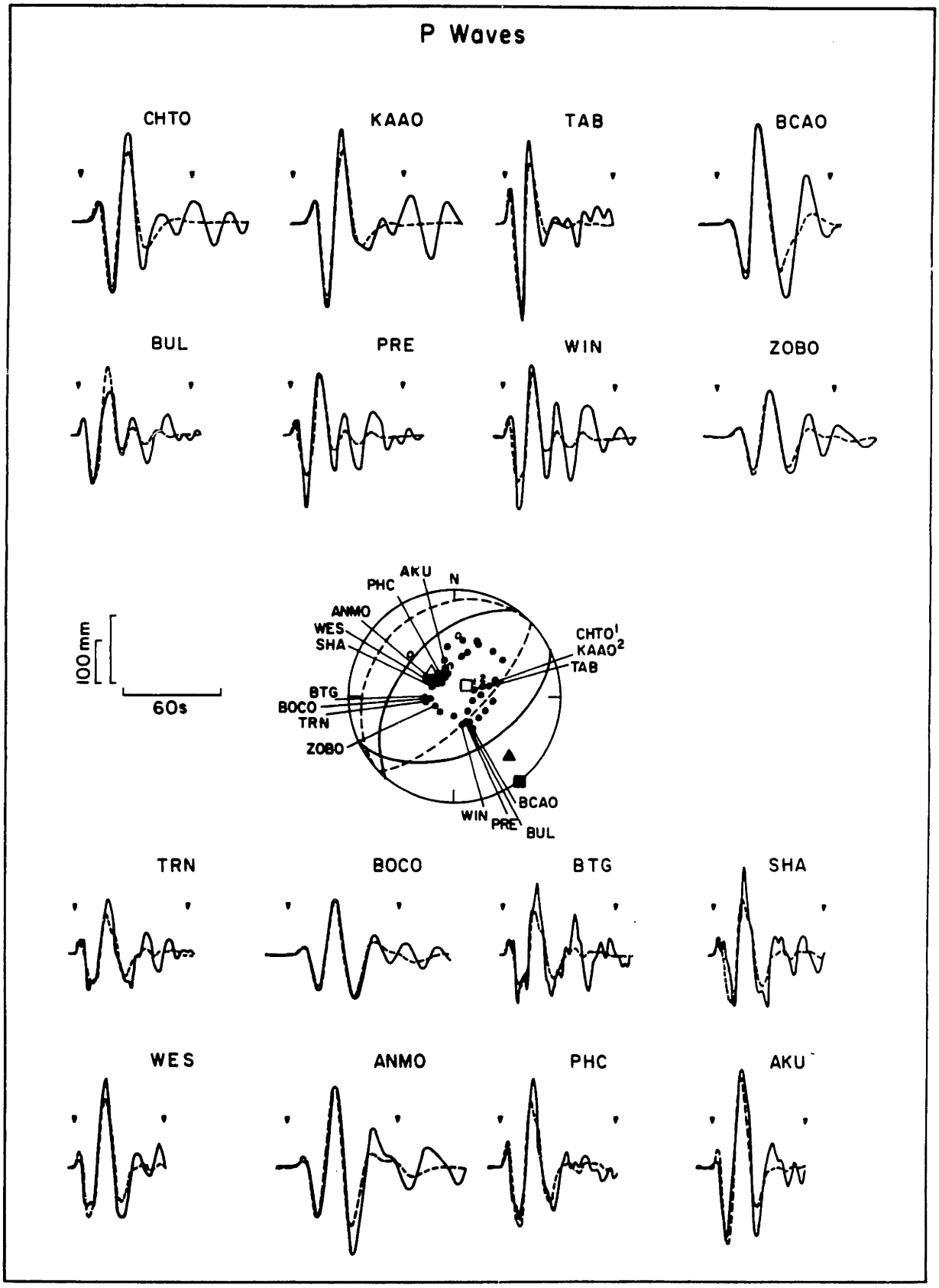
P Waves
CHTO
KAAO
TAB
BCAO
BUL
PRE
WIN
ZOBO
100 mm
60s
AKU
N
PHC
ANMO
WES
SHA
BTG
BOCO
TRN
ZOBO
CHTO1
KAAO2
TAB
BCAO
WIN
PRE
BUL
TRN
BOCO
BTG
SHA
WES
ANMO
PHC
AKU

Figure 4.4.5a

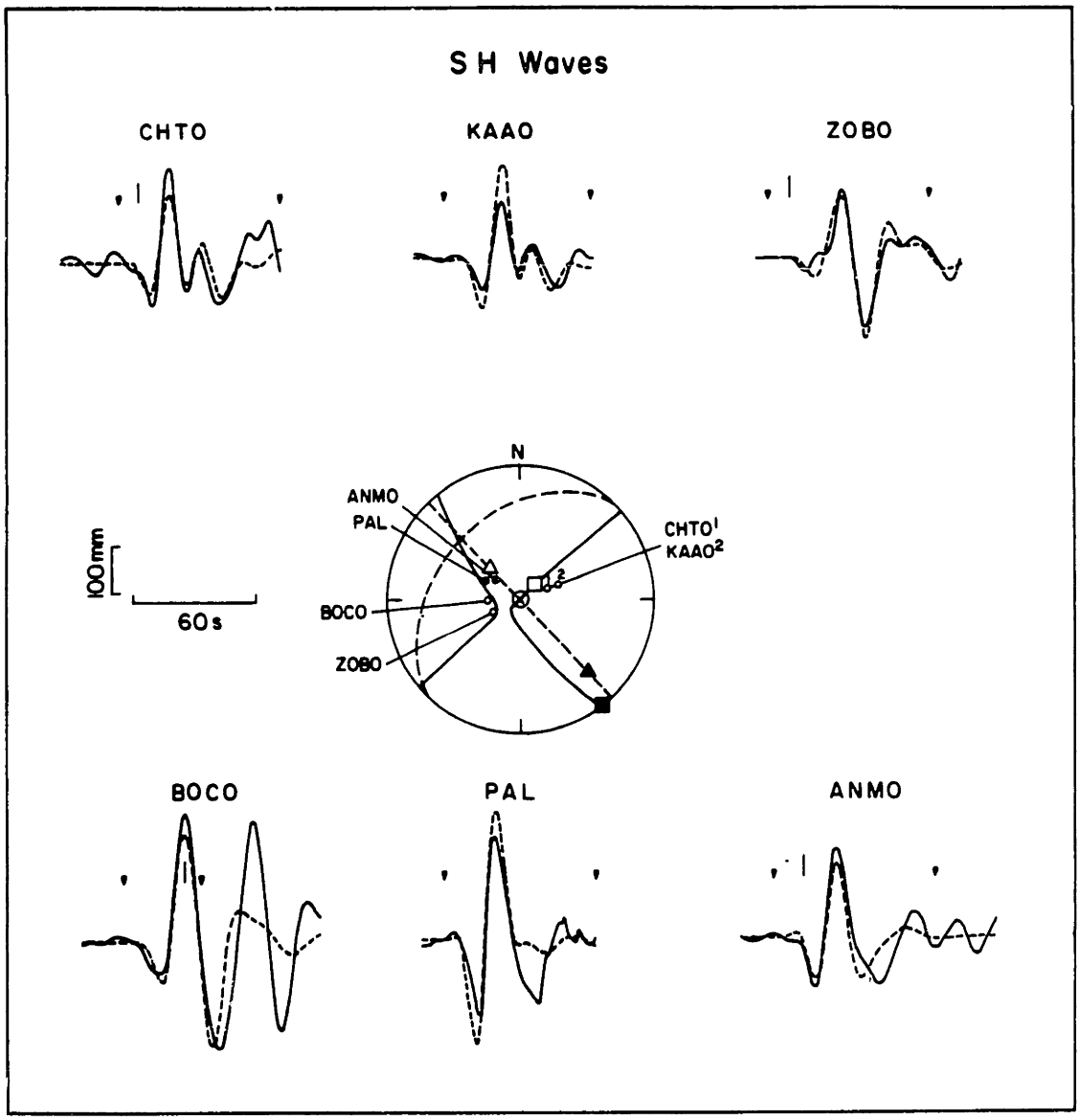
S H Waves
CHTO
KAAO
ZOBO
N
ANMO
PAL
CHTO1
KAAO2
100mm
60s
BOCO
ZOBO
BOCO
PAL
ANMO

Figure 4.4.5b

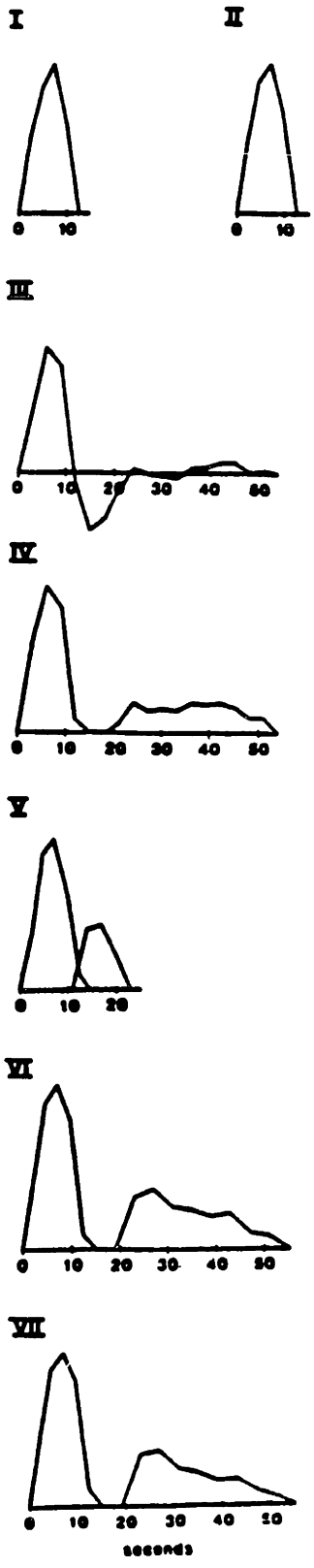
I
II
0 10
0 10
III
0 10 20 30 40 50
IV
0 10 20 30 40 50
V
0 10 20
VI
0 10 20 30 40 50
VII
0 10 20 30 40 50
seconds

Figure 4.4.6

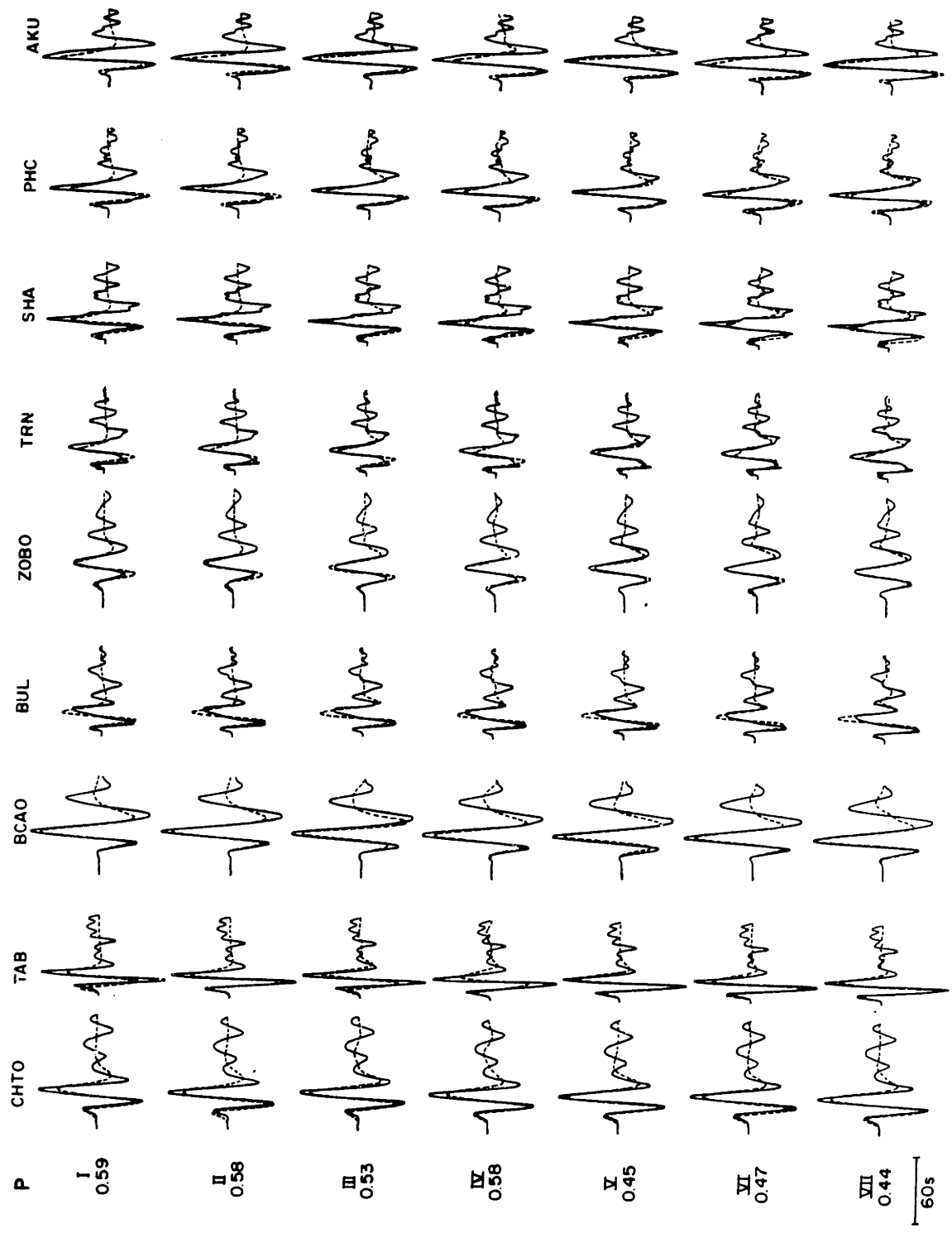
P
CHTO
TAB
BCAO
BUL
ZOBO
TRN
SHA
PHC
AKU
I 0.59
II 0.58
III 0.53
IV 0.58
V 0.45
VI 0.47
VII 0.44
60s

Figure 4.4.7a

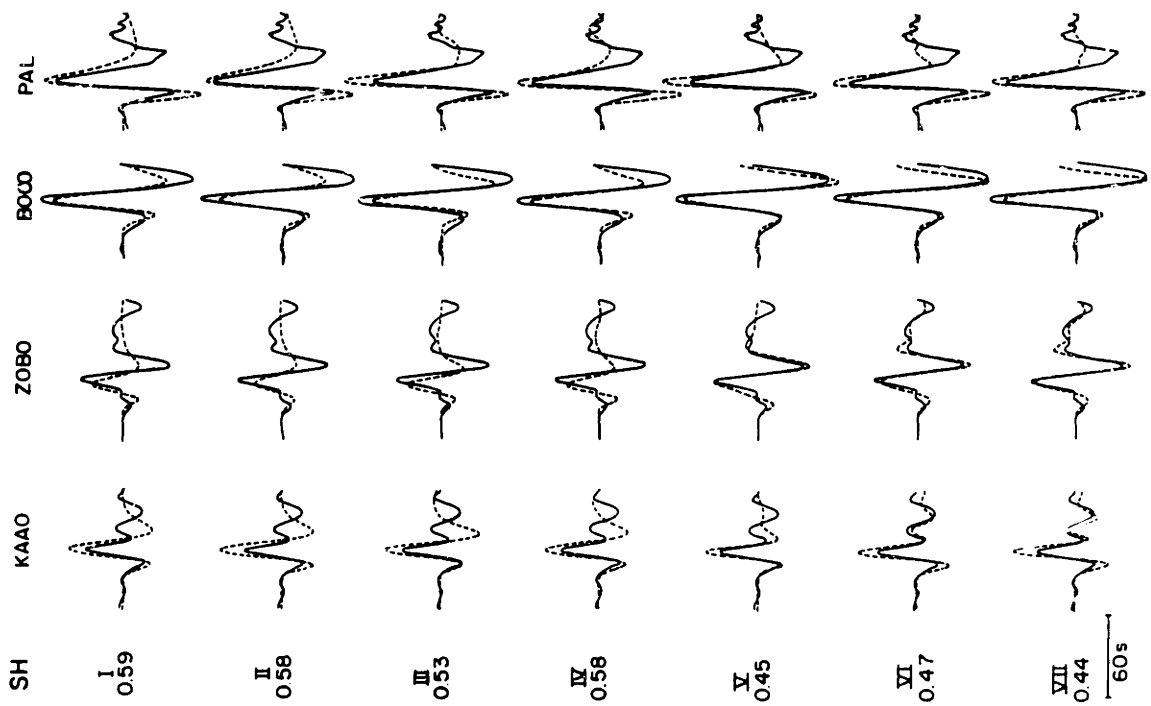
SH
KAAO
ZOBO
BOCO
PAL
I 0.59
II 0.58
III 0.53
IV 0.58
V 0.45
VI 0.47
VII 0.44
60s

Figure 4.4.7b

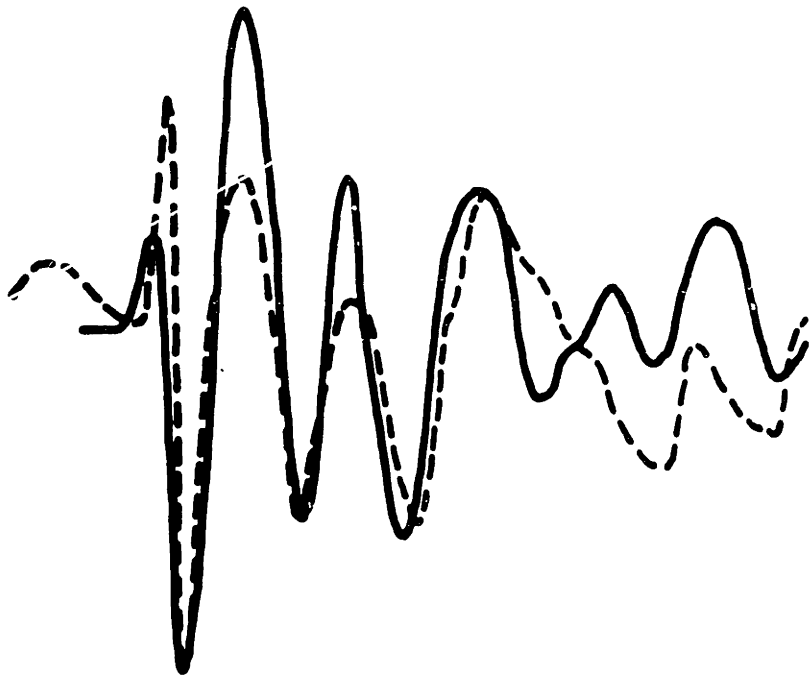

Figure 4.4.8

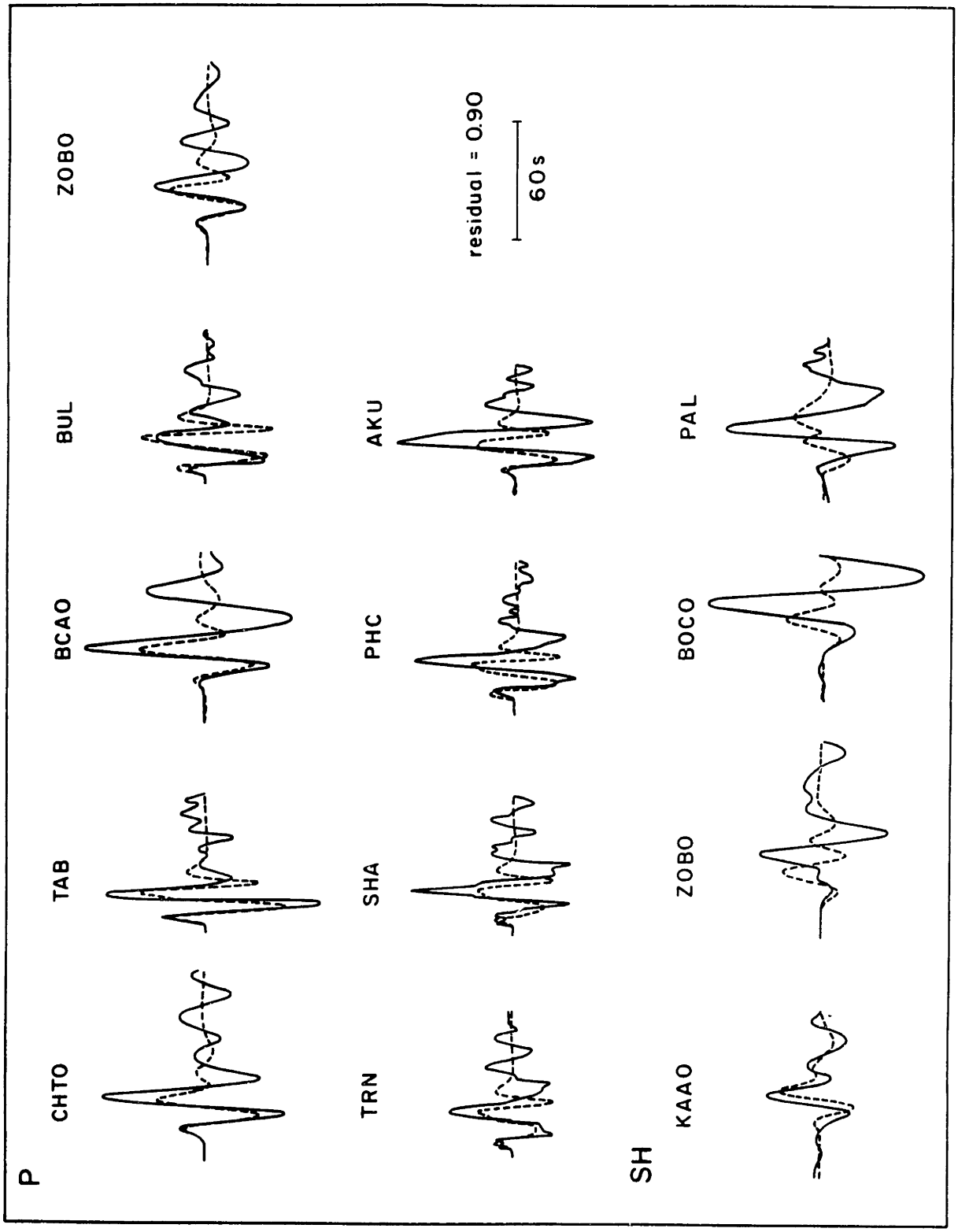
P
CHTO
TAB
BCAO
BUL
ZOBO
TRN
SHA
PHC
AKU
residual = 0.90
60s
SH
KAAO
ZOBO
BOCO
PAL

Figure 4.4.9

CHAPTER V

APPLICATION TO UNDERGROUND NUCLEAR EXPLOSIONS

5.1 INTRODUCTION

Determination of source parameters such as depth and mechanism for shallow seismic sources is a difficult task. The resolution of the depth and the m_{xz}, m_{yz} and isotropic moment tensor components hinges on our ability to separate the contributions of the direct arrival and the reflections from the free surface. For extremely shallow sources such as nuclear explosions, with typical source depths of less than one kilometer, we must be able to resolve pulses with time separations of about 0.5 s, which requires the use of short-period instruments.

This chapter presents studies of two underground nuclear explosions. In the first study we use short-period GDSN data to investigate source characteristics of the August 18, 1979 Shagan River (Kazakhstan, U.S.S.R., m_b=6.2) event, presumed to be a nuclear explosion. It will be shown that the short-period waveforms are sufficiently correlated to give reasonable estimates of the source parameters. The absolute amplitudes show considerable scatter, which in most cases appears to be due to variations in attenuation (t^*), because the frequency content of the signal changes accordingly. In several cases, however, the amplitude anomaly appears to be caused by some unknown effect.

The second study is of the March 26, 1970 Handley (Nevada, U.S.A.) event. Because of the structural complexity of the Nevada Test Site [Taylor, 1983], the short-period data lacks sufficient coherency to be analyzed independently. Handley is a large (>1 Mt) event from before the time of the yield limitation treaty. It was buried deeper than 1 km and excited sufficiently strong long-period waves for the analysis. Although

the scatter in the data is considerable, we find that a well constrained solution can be obtained by using a data set of short- and long-period P waves and long-period SH waves.

5.2 THEORETICAL CONSIDERATIONS

As mentioned in Chapter III, because of the stress free boundary condition at the surface, the $\underline{I}^1$ excitation function (equation 2.2.17) for all waves essentially vanishes for very shallow sources (depth << wavelength), and for the P-SV coupled waves the other two excitation functions are related by $\underline{I}^0 \approx -\frac{1}{3}\underline{I}^2$. Consequently, for long wavelengths the expression for displacement due to a shallow moment-tensor source reduces to

$$\underline{u} = \underline{I}^{PSV^2}[\tfrac{1}{2}(M_{xx}+M_{yy}) - \tfrac{1}{3}M_{zz} - \tfrac{1}{2}(M_{yy}-M_{xx})\cos 2\phi + M_{xy}\sin 2\phi]$$

$$\underline{u} = \underline{I}^{SH^2}[\tfrac{1}{2}(M_{yy}-M_{xx})\sin 2\phi + M_{xy}\cos 2\phi] \qquad (5.1)$$

We have no information at all about the behavior of the M_{xz} and M_{yz} moment-tensor components; nor can we resolve the relation between the $M_{xx}+M_{yy}$ and the M_{zz} components. In the absence of *a priori* information about the source, we cannot resolve the strength of the isotropic component since identical displacements could be produced by a purely deviatoric compensated linear vector dipole. Inversion under these circumstances will be unstable.

All examples in Chapter IV dealt with earthquakes. An earthquake, most often caused by shear failure of a rock masss, is expected to be characterized by a purely deviatoric moment-tensor. Only results of the moment-tensor inversions with a deviatoric constraint were therefore given. In order to test the stability of the isotropic component, the inversions

were also performed using no constraints. The percentages of the isotropic and deviatoric components obtained for the four events in Chapter IV are tabulated in Table 5.1. Although all four events had approximately equal centroidal depths, because of their different durations the characteristic wavelengths of the data are different. The effective depths of these events are, therefore, quite different. The unconstrained inversions of the New Brunswick earthquakes, the events with the largest effective depths, give essentially pure deviatoric solutions. The Lice earthquake, with an intermediate effective depth, gives 17% isotropic component, and the "shallowest" El Asnam earthquake gives 33% isotropic component. Since inversions with the deviavoric constraint imposed produce an equally good fit to the data, we suspect that the apparent large isotropic component for the Lice and El Asnam is a result of an instability of which equation (5.1) is the limiting case.

With this as a preamble, one would probably conclude that for inversions of explosions which have a depth of burial of about 1 km our chances of resolving the moment tensor are poor. Fortunately, however, explosions excite considerably more high-frequency energy than earthquakes. In Chapter III (Figure 3.1) it was shown that for impulsive events, in absence of structural contamination, teleseismic P waves should, in principle, carry enough information to resolve the complete moment tensor.

Nuclear explosions are not the ideal test of the resolvability of the moment tensor components. Common observations of large amplitude Love waves indicate significant source heterogeneity [Toksoz and Kehrer, 1972]. The isotropic component of the moment-tensor is, however, expected to be dominant.

5.3 THE AUGUST 18, 1979 SHAGAN RIVER EXPLOSION

This event is much larger in magnitude (m_b=6.2) than the New Brunswick events studied in Chapter IV, and consequently its signal-to-noise ratio is much better. High-pass filtering which was used to remove the long-period noise from the New Brunswick records is not necessary. In fact, stable deconvolution of the instrument can be achieved for most stations; this increases the bandwidth of the data and stabilizes the inversion. Compared to the New Brunswick events, the analysis is complicated 1) by the extremely shallow source depth, and 2) because the site of the explosion is in relatively low velocity sediments, and the take-off angles of the teleseismic waves are considerably steeper than they would be in a hard rock site. This reduces the coverage of the focal sphere and results in poorer resolution of the source mechanism (Figure 5.1).

The P waveforms are inverted for the source mechanism, the source time function and the source depth. The mechanism is obtained either in terms of a totally unconstrained moment tensor or with appropriate constraints to improve stability. The source time function is parameterized by a series of box cars (Chapter II). The waveforms are inverted by minimizing

$$o_i/(\Sigma o_j^2)^{1/2} - s_i/(\Sigma s_j^2)^{1/2}$$

in a least-squares sense, where o_i are the amplitudes of the digitized observed waveforms and s_i are the corresponding synthetic seismogram amplitudes. The summations are carried out over the number of data points at a given station. The inversion is therefore sensitive only to the shape of the seismograms at the individual stations. The source strength is determined by matching the absolute amplitudes in a least squares sense only after the solution for source depth, mechanisms and time function has been determined. We use this procedure because the absolute amplitudes of

the short-period data show great fluctuations, probably because of variations in the attenuation along the different travel paths, and probably not because of the source radiation pattern.

Figure 5.2 shows the original waveforms together with the best-fit synthetics for the source parameters obtained from the unconstrained moment tensor inversion. The inversion is performed using the first 2.5 seconds of the waveforms after the onset of the direct P wave. Station SHIO is included in the data set in spite of its short epicentral distance, since the arrival of the upper mantle phases can be clearly recognized in the later part of the waveform and can be excluded from the inversion window. The crustal structure at the source is a half-space with the parameters given in Table 5.2.

The inferred source parameters are summarized in Table 5.3. The best fit source mechanism is characterized by about 40% explosive, 40% double-couple, and 20% linear vector dipole components. The inversion using a purely explosive source results in an equally good fit to the data, and solving for all six moment tensor parameters is probably not justified.

The poor resolution of the moment tensor is due mainly to the limited coverage of the focal sphere and unmodeled structural complexity. An inversion based on narrow-band data may be strongly biased by noise at the dominant frequency; this risk is minimized with broad-band data which is unlikely to be uniformly contaminated. The use of longer period data should also decrease the sensitivity of the inversion to errors caused by unmodeled fluctuations in small scale earth structure.

In this study, the bandwidth of the data is extended by deconvolving the instrument. The deconvolution was stable for high frequencies, but had

to be limited to 0.2-0.1 Hz at the low frequency end. The deconvolved traces are displayed in Figure 5.3. (Large background noise level precluded deconvolution of stations MAJO, CTAO, and NWAO). The moment-tensor inversion of the deconvolved waveforms resulted in 60% explosive, 34% double-couple and 6% linear vector dipole components (Figure 5.3, Table 5.3). We take the larger size of the isotropic component to be an indication of improved stability of this procedure.

The average t^* and the regional variability about this average are investigated in the same manner as for the New Brunswick events. The t^*'s are adjusted to simultaneously match both the narrow-band and the broad-band data. The moment-tensor norms determined from the short-period and the broad-band data can be matched if the average t^* for all stations is 0.6s. Figure 5.4 shows the fit to the narrow-band data obtained with a single value of t^* (0.6 s) for all stations and with the best-fit value of t^* at each station. The source mechanism is a pure explosion. As was the case with the New Brunswick earthquake, the largest t^*(1.1 s) was obtained for the station ANMO (New Mexico). At stations CHTO (Thailand), BCAO (Central America), and ANTO (Turkey) the best-fitting value of t^* is only 0.3 s. These values are similar to those obtained by Farrell and Stevens [1982] from an analysis of explosions at the same test site. Variability in t^* can explain most of the misfit to the data, except for the European stations GRFO and KONO. The waveforms at these two stations have large amplitudes, indicating low attenuation, but at the same time are dominated by low frequencies, indicating high attenuation. No frequency-independent t^* can account for the absolute amplitude and frequency content at these stations. This problem is illustrated in Figure 5.5. In the absence of other independent data, both path and source effects could be invoked to

explain the focussing of long-period energy at these two stations, but since Farrell and Stevens [1982] experienced problems with these same two stations, we suspect that some unknown path effect is responsible.

Finally, let us turn our attention to the other estimated source parameters: seismic moment, depth and time function. Assuming that the attenuation was estimated correctly, the norm of the moment tensor for this event is stable (~9 x 10^{23} dyne cm) regardless of the constraints imposed. For a pure explosion, this can be related to the reduced displacement potential using the relation $\Psi(\infty) = M_{norm}/\sqrt{3}4\pi\rho\alpha^2$, where α and ρ are the compressional velocity and density at the source. For the Shagan River explosion, $\Psi(\infty) = 1.0 \times 10^{11} cm^3$. For the assumed source crustal velocity, the source depth of 830 m is well constrained by the data.

As a result of near-field studies of underground nuclear explosions, the far-field source time function of an explosion is expected to show an overshoot after the initial impulse [Haskell, 1967]. Figure 5.6a shows the inferred source time function for a constrained isotropic source. No overshoot is observed. It has been recognized that non-elastic behavior of the material in the vicinity of the source can sometimes reduce the amplitude of the pP reflection [Perl et al., 1979; Bache et al., 1980]. The inferred source time functions when the theoretical pP amplitude is reduced by factors 1.5 and 2 are also shown in Figure 5.6. We observe a complete trade-off between the amount of overshoot and the decrease in the pP amplitude; these two effects cannot be resolved by our data, since the data is matched identically in all three cases.

The main conclusions of the study of this event are:

(1) Short-period teleseismic waveforms can significantly improve the resolution of the m_{xz}, m_{yz}, m_{zz} and $m_{xx}+m_{yy}$ moment tensor components

and thus facilitate discrimination between various types of seismic sources.

(2) Fluctuations in the absolute amplitude due to the regional variability of attenuation and other path effects need to be better understood before the information contained in the absolute amplitudes can be used reliably in the determination of source mechanisms.

(3) The stability of the inversion can be significantly improved by using broad-band data.

(4) The average t^* at 1 Hz for the P wave travel paths from Kazakhstan is 0.6 s.

(5) The t^* for station ANMO is large (1.1 s; similar to that obtained from the analysis of the New Brunswick earthquake indicating high attenuation below this station); the smallest t^* value (0.3 s) was found for CHTO, BCAO, and ANTO.

(6) Strong trade-off between the non-linearity of pP and the overshoot of the source time function complicates investigation of these phenomena.

5.4 THE MARCH 26, 1970 HANDLEY EXPLOSION

The approach taken in the analysis of the Handley event differs somewhat from that used for the Shagan River event because of the lack of digital data. The hand-digitized analog data available are not of sufficiently good quality to permit deconvolution of the instrument response. Because of the structural heterogeneity of Pahute Mesa (the site of the explosion) [Taylor, 1983] the short period waveforms are complex and difficult to explain. Although long-period P waves were excited by this large event, the azimuthal coverage is limited (Table 5.4). A helpful constraint in the inversion, however, is provided by the SH waves (or the lack thereof) at the long-period stations which contribute the

observations of long-period P waves. Because the absolute amplitude ratio between the P and SH contains information on the source, inversions are conducted on absolute amplitude data.

The results of the inversions are summarized in Table 5.5. The matches to the data by the best fit model are shown in Figure 5.7. The assumed crustal structure for the source region is based on study by Taylor [1983] (Table 5.6). A t^* of 1 or 5s is used for long-period P and SH waves, respectively. The t^* for the short-period P waves are adjusted to match the absolute amplitudes at each station. The unconstrained inversion yields 88% isotropic and 12% deviatoric components. The deduced source depth is 1240 m, in good agreement with the true depth of 1203 m. The norm of the moment-tensor is 2.2×10^{24} dyne-cm. This implies a reduced displacement potential $\psi(\infty)$ of 3.2×10^{11} cm^3.

In conclusion, the unconstrained moment tensor inversion using the combined data set of long- and short-period P and SH waves is successful in isolating the isotropic moment-tensor component for the Handley nuclear explosion. The deduced source depth is in good agreement with the known depth of burial of the nuclear device. This supports one of the main conclusions of this thesis that teleseismic body waves provide very good estimates of depth of seismic sources. The t^* value of approximately is for P waves at 1 Hz is somewhat smaller than the value of 1.3 s obtained by Helmberger and Hadley [1981] from a study of the same event. The discrepancy is probably mainly due to the fact that they assumed that the source time function has a substantial overshoot. The source time function in this study did not exhibit this phenomenon.

Table 5.1 Percentages of the Isotropic and the Deviatoric Moment Tensor Components for the Earthquakes Studied in Chapter IV

	Isotropic	Deviatoric	
New Brunswick (mainshock)	3	97	LP
New Brunswick (aftershock)	3	97	SP
Lice	17	83	LP
El Asnam	34	66	LP

Unconstrained inversions using:
LP - long-period data
SP - short-period data, wave shapes only

Table 5.2 The Crustal Structure Used For the Analysis of the Shagan River Explosion

Source Region:	Thickness	V_p (km)	V_s (km)	Density (g/cm^3)
	half-space	4.0	1.9	2.5
Receiver Region:	half-space	6.0	3.46	2.5

Table 5.3 The Inversion Results For the August 18, 1982 Shagan River Nuclear Explosion

	Narrow-band	Narrow-band	Broad-band
Constraint	none	isotropic	none
Normalized moment-tensor components:			
M_{xx}	0.41	0.58	0.70
M_{yy}	0.69	0.58	0.32
M_{zz}	0.19	0.58	0.55
M_{xy}	0.40	0.00	0.21
M_{xz}	0.02	0.00	0.01
M_{yz}	-0.04	0.00	-0.09
Moment-tensor norm (dyne-cm)	1.1×10^{24}	9.1×10^{23}	1.0×10^{24}
Principal axes:			
P(λ,azimuth,plunge)	0.11,144,27	-	0.20,144,15
B	0.21,328,63	-	0.57,319,74
T	0.97,235,02	-	0.80,205,06
Decomposition:			
Isotropic,dc,lvd (%)	40,40,20	100,0,0	60,34,06
Depth (m)	840	810	820
Time function ($\Delta\tau$=0.15s)	0.90,0.33, -0.35,0.04,0.08	0.68,0.12,0.02, 0.02,0.16	0.08,0.13,0.06, 0.00,0.00
Residual	33	38	4.6

Table 5.4 Stations Used in the Analysis of the Handley Nuclear Explosion

Station	Azimuth	Distance	Waves Used
GDH	26	46	P_{lp}, P_{sp}
TRI	32	86	P_{sp}
VAL	39	70	P_{sp}
TOL	46	81	P_{sp}
WES	67	35	P_{lp}, S_{lp}
OGD	70	32	P_{lp}, S_{lp}
BOG	119	51	P_{lp}, P_{sp}, S_{lp}
LPS	126	33	P_{lp}, S_{lp}
QUI	128	51	P_{lp}, P_{sp}, S_{lp}
AFI	237	73	P_{sp}
HNR	259	91	P_{lp}

Table 5.5 The Inversion Results For the March 26, 1970 Handley Nuclear Explosion

Constraint	none	isotropic
Normalized moment-tensor components:		
M_{xx}	0.60	0.58
M_{yy}	0.53	0.58
M_{zz}	0.60	0.58
M_{xy}	-0.04	0.00
M_{xz}	0.00	0.00
M_{yz}	-0.03	0.00
Moment-tensor norm (dyne-cm)	2.2×10^{24}	2.2×10^{24}
Principal axes:		
P(λ,azimuth,plunge)	0.50,066,15	-
B	0.60,176,51	-
T	0.63,326,35	-
Decomposition:		
isotropic,dc,lvd(%)	88,9,3	100,0,0
Depth (m)	1250	1260
Time function ($\Delta\tau$=0.25s)	0.816,0.309,-0.125	0.833,0.325,-0.158

Table 5.6 The Crustal Structure Used For the Analysis of the Handley Explosion

	Thickness	V_p	V_s	Density
Source Region:	(km)	(km/s)	(km/s)	(g/cm^3)
	0.9	2.70	0.75	2.6
	1.1	3.40	1.20	2.7
	0.5	4.40	2.50	2.8
	2.5	5.10	2.90	2.9
	half-space	6.10	3.50	3.0
Receiver Region:				
	half-space	6.00	3.46	2.7

Table 5.7 t^* Used for Modeling of the Short-period P Waves From the Handley Explosion

Station	t^* (s)
GDH	1.0
TRI	1.5
VAL	1.1
TOL	0.9
BOG	0.9
QUI	0.9
AFI	0.9

FIGURE CAPTIONS

5.1 Focal sphere coverage by the direct P wave for the Shagan River explosion.

5.2 Short-period waveforms (solid lines) and the corresponding synthetic seismograms (dashed lines) for the August 18, 1979 Shagan River nuclear explosion. The synthetic seismograms were calculated for the model determined by the unconstrained moment-tensor inversion (Table 5.3).

5.3 The same as in Figure 5.2 but using broad-band waveforms with deconvolved instrument response. (Due to noise, stations MAJO and CTAO could not be deconvolved but were included in the inversion).

5.4 The effect of attenuation on the absolute amplitude of the short-period P waves. Absolute amplitudes of the observed seismograms (solid lines) were equilized to a common epicentral distance and instrument magnification. The synthetic seismograms (dashed lines) in the left-hand columns were computed using a single t^* (0.6 s) for all stations. The synthetic seismograms with the adjusted t^* are shown in the right-hand columns. The values of the best-fit t^* are also shown. Stations GRFO and KONO are anomalous (see Figure 5.5).

5.5 The effect of attenuation on the amplitude and frequency content of waveforms at GRFO and KONO. No frequency-independent t^* can match the observations.

5.6 The effect of the reduction of the pP amplitude on the inferred source time function:

a) purely elastic pP, b) pP/1.5, c) pP/2.

5.7 The data (solid lines) and the corresponding theoretical seismograms (dashed lines) for the model found by the unconstrained moment-tensor inversion of P and SH waves from the Handley nuclear explosion (Table 5.5). The observed seismogram amplitudes are normalized to a common epicentral distance and instrument magnification.

a) Long-period P waves

b) Long-period SH waves

c) Short-period P waves

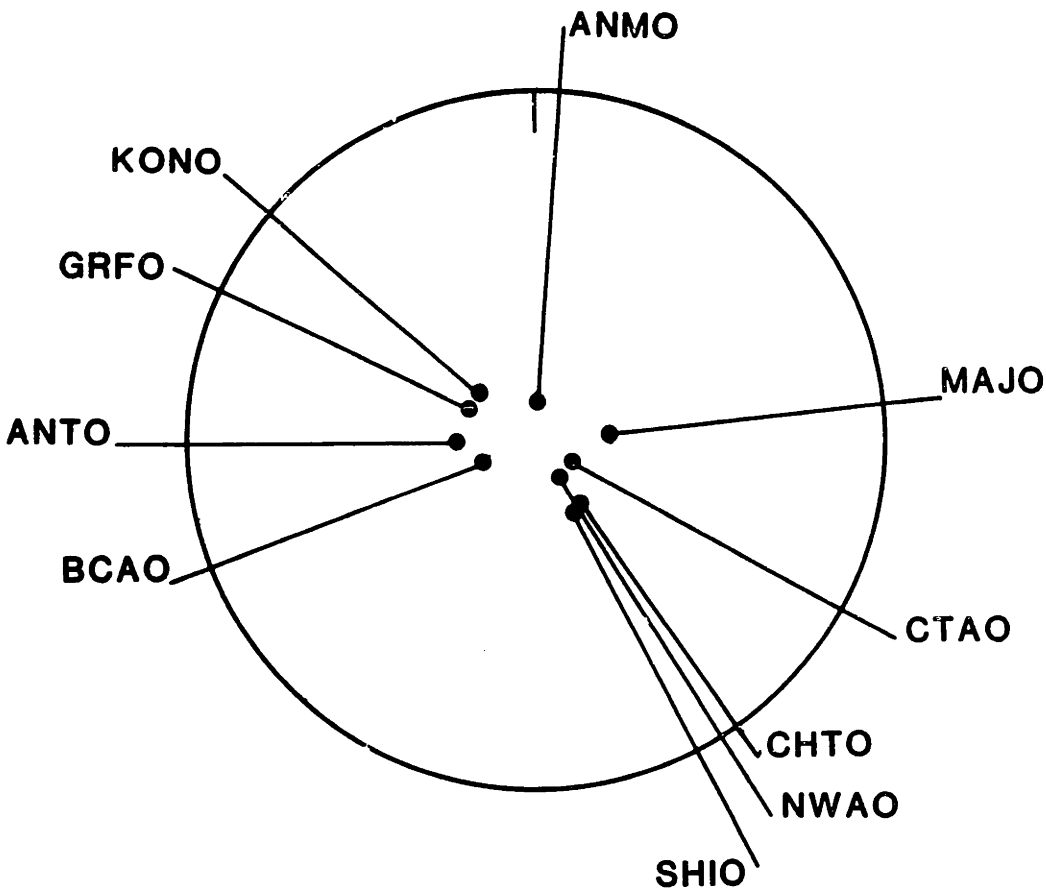

Figure 5.1

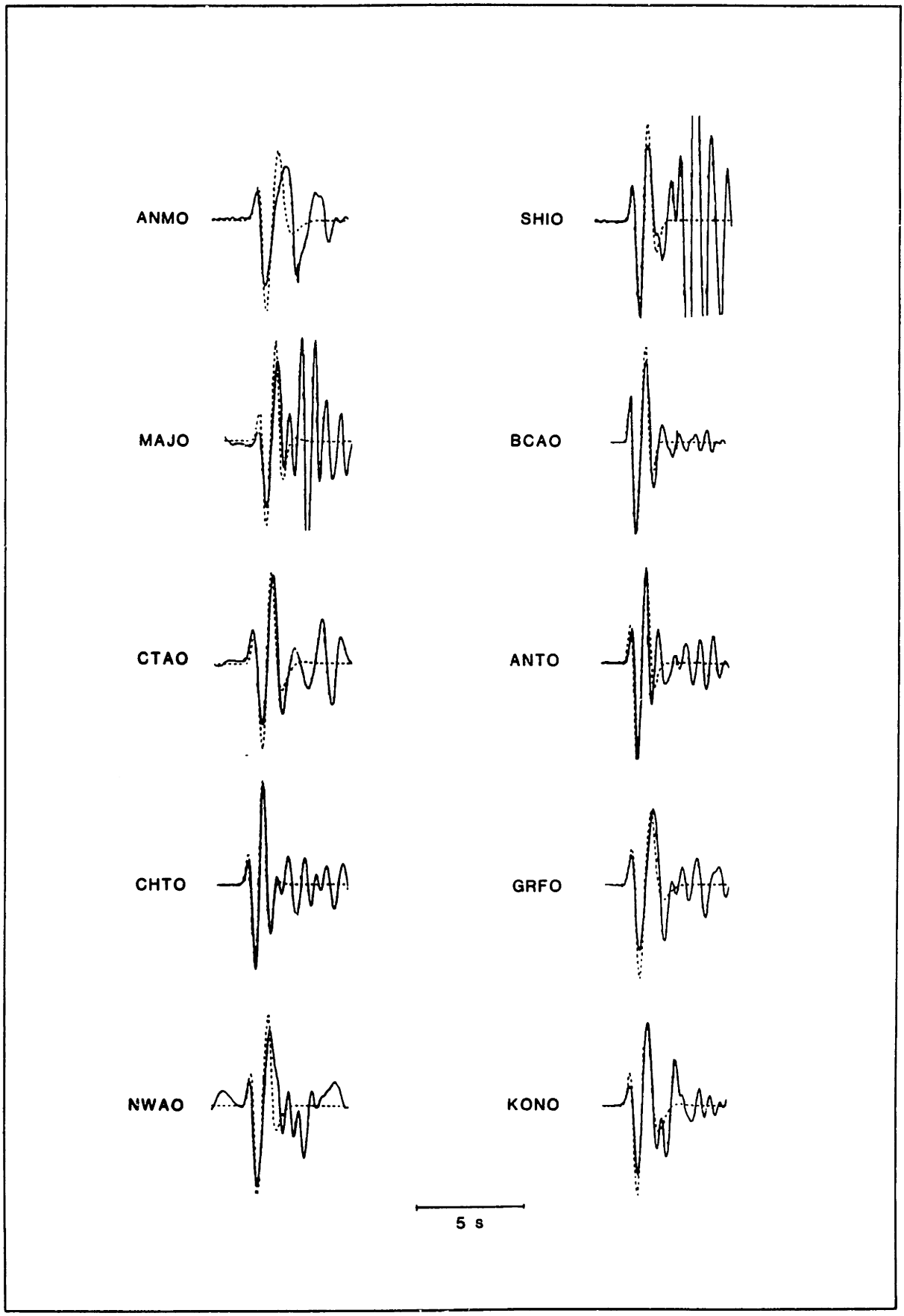

Figure 5.2

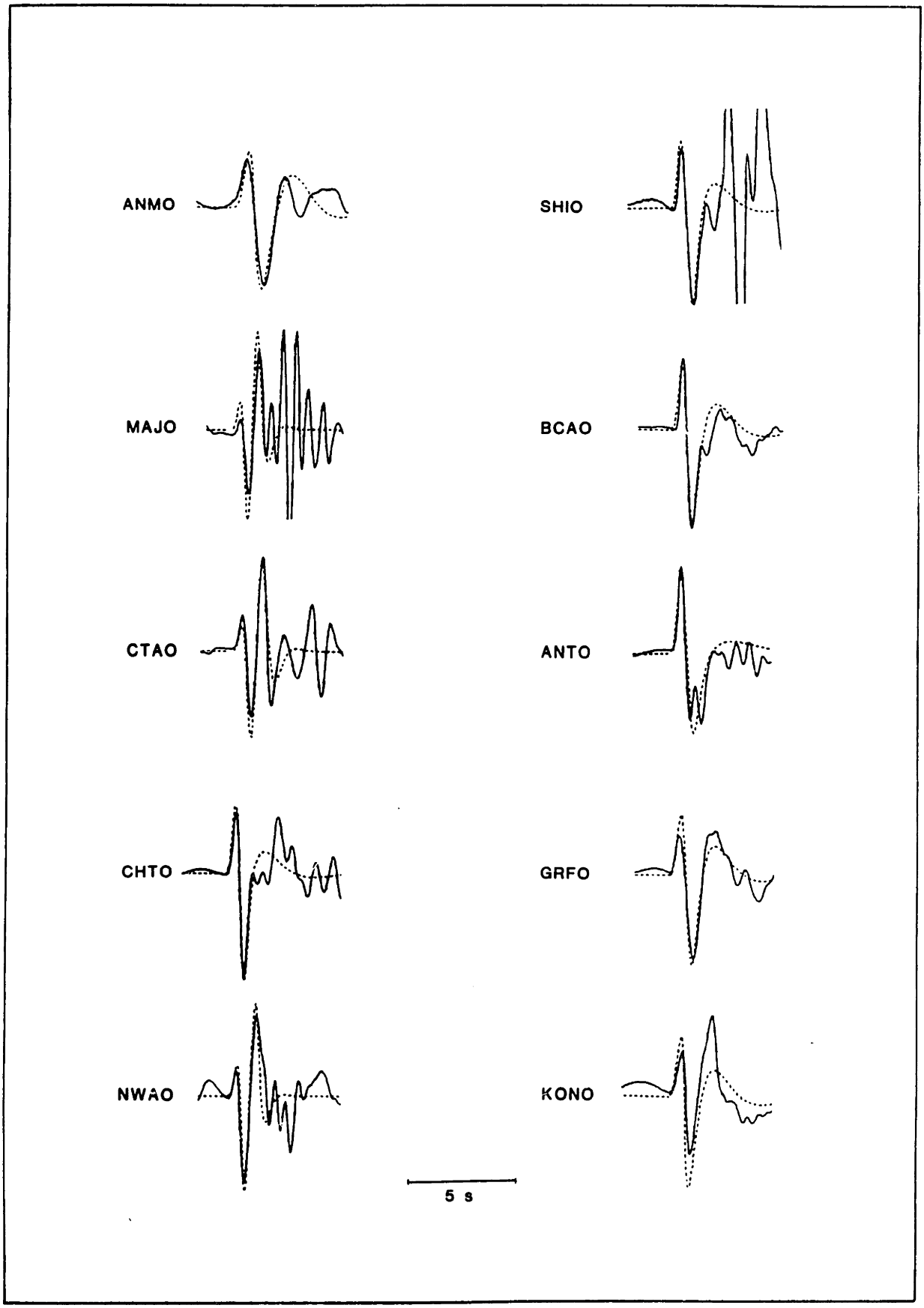

Figure 5.3

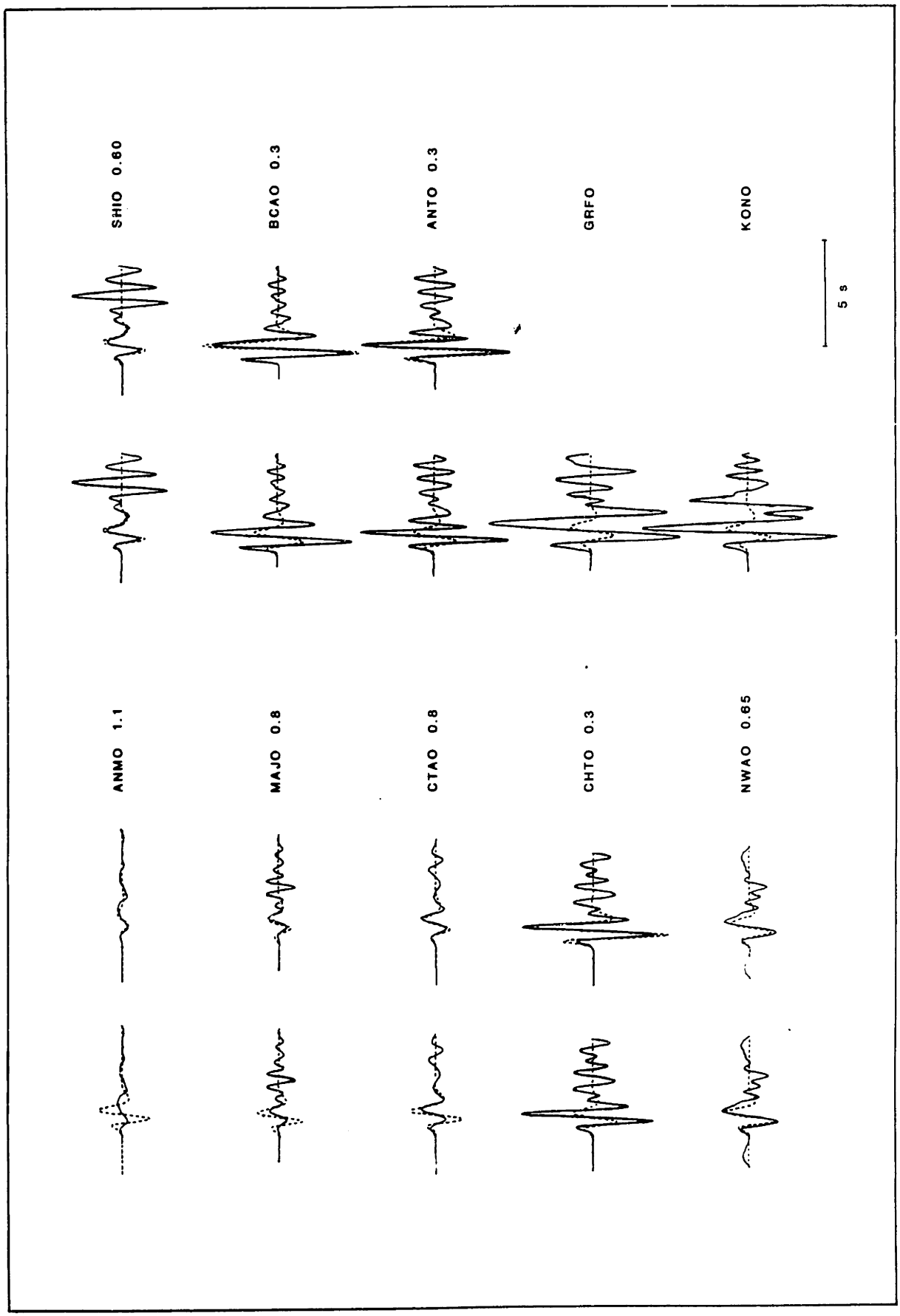
SHIO 0.80
BCAO 0.3
ANTO 0.3
GRFO
KONO
5 s
ANMO 1.1
MAJO 0.8
CTAO 0.8
CHTO 0.3
NWAO 0.65

Figure 5.4

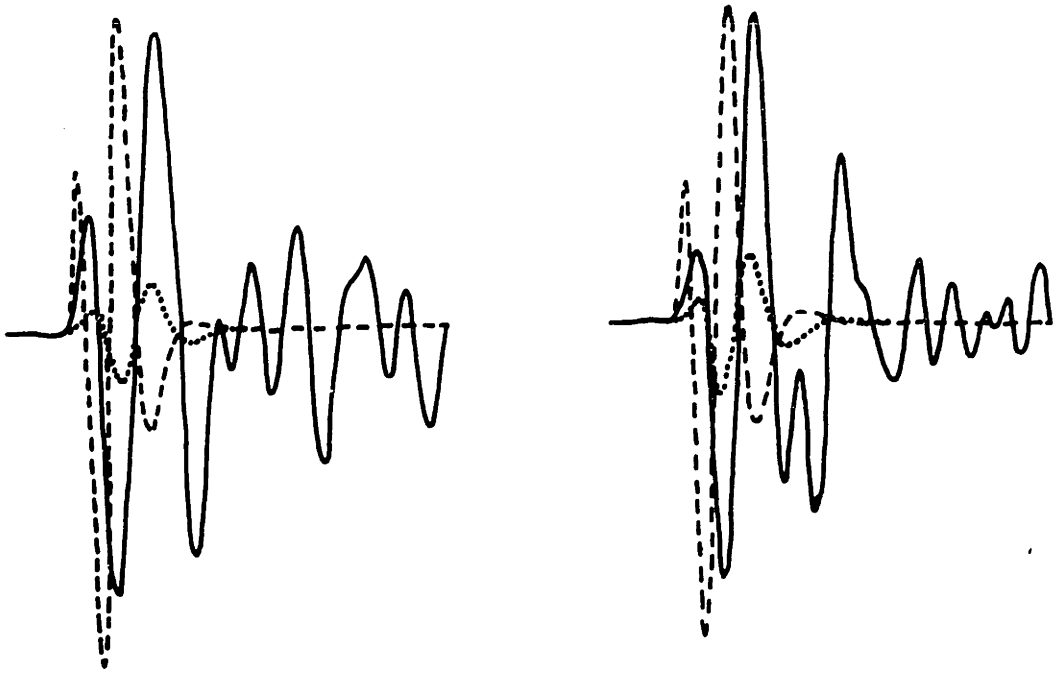

GRFO t*

----- 0.7

..... 0.2

KONO t*

------ 0.6

..... 0.2

Figure 5.5

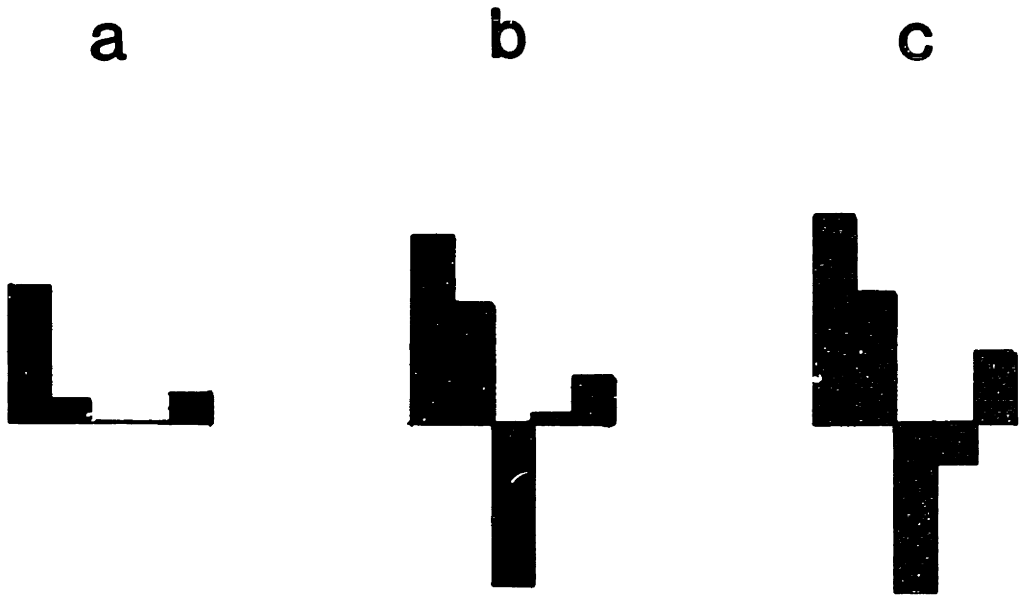

Figure 5.6

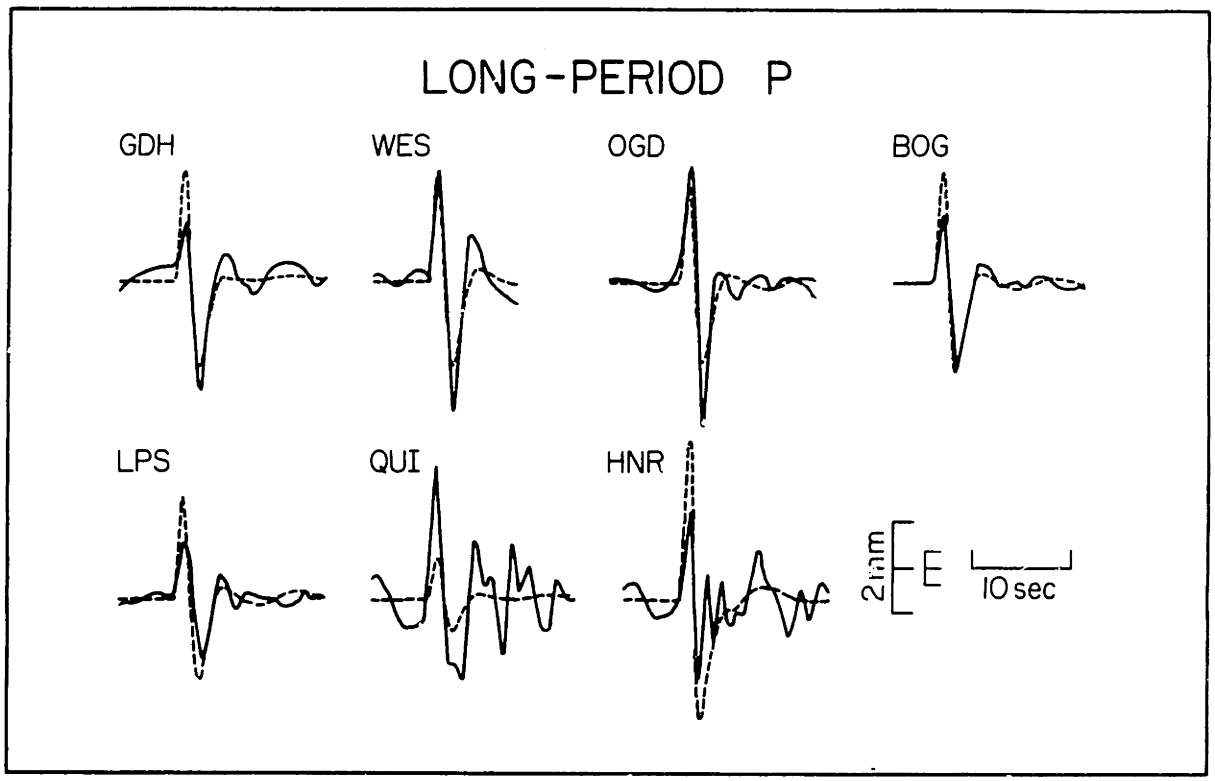

Figure 5.7a

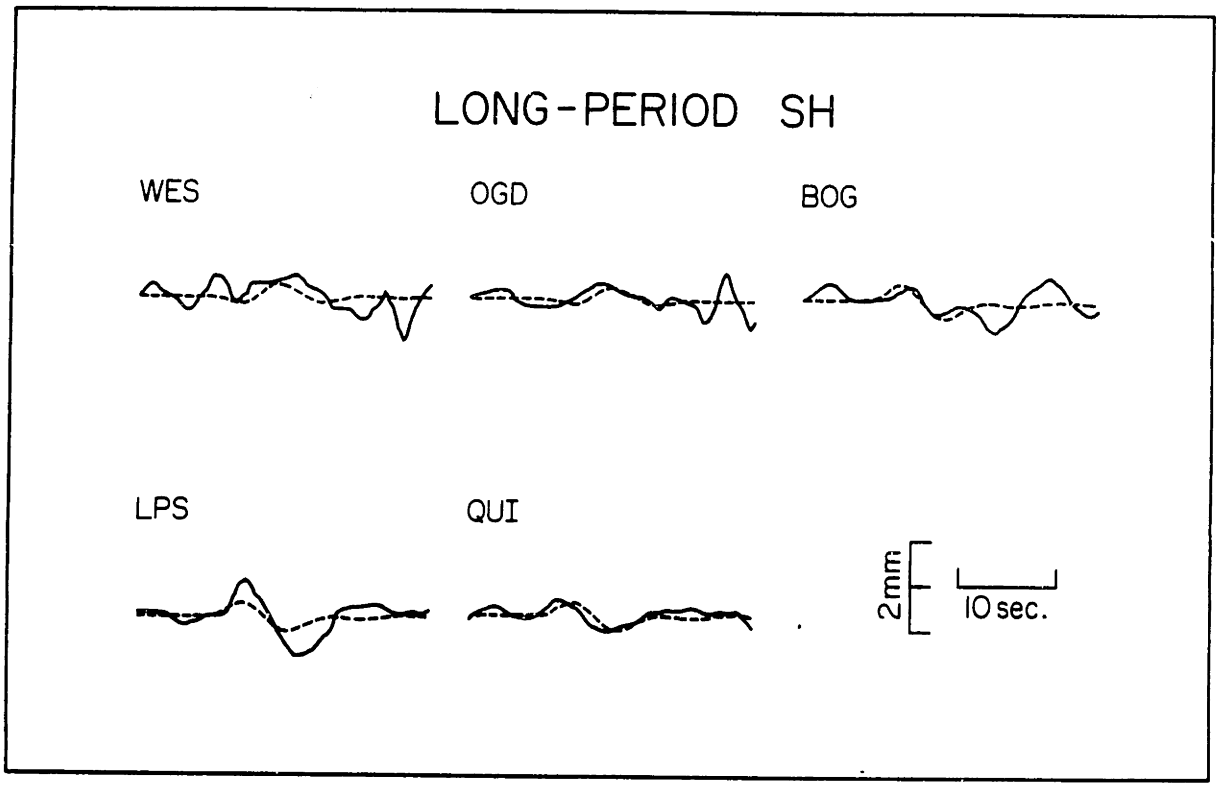

Figure 5.7b

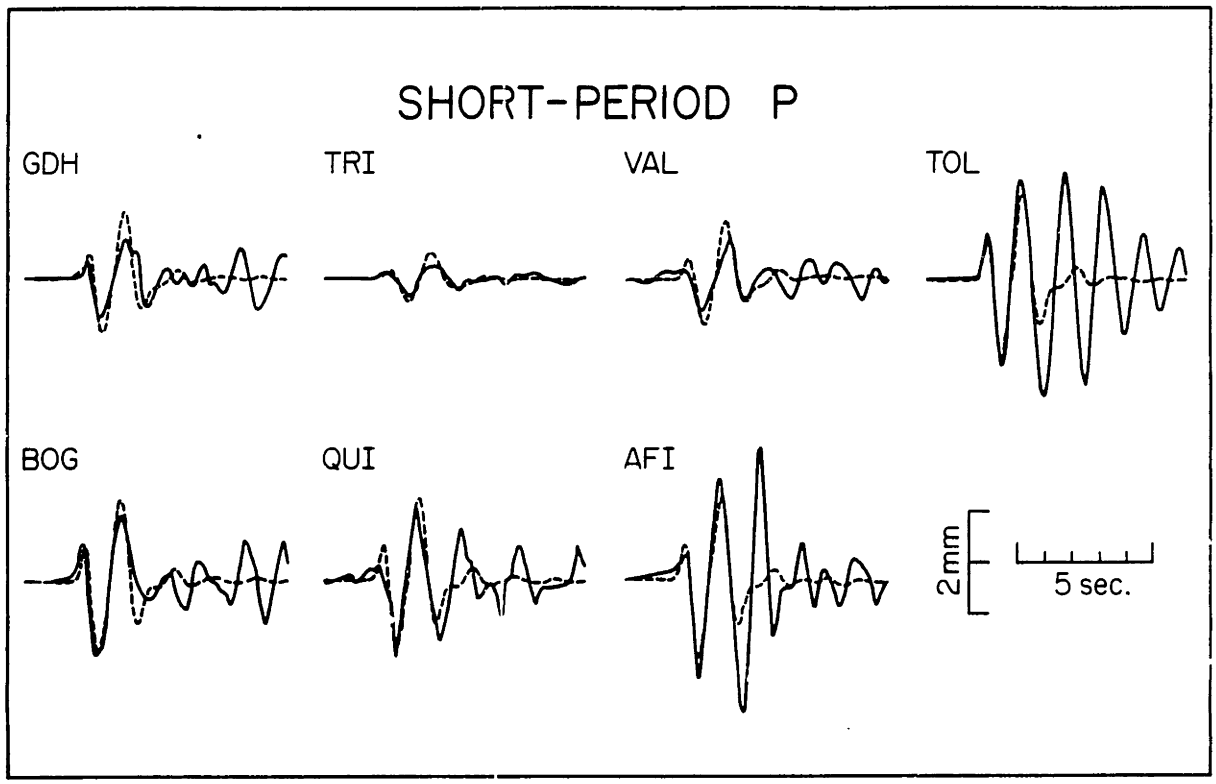

Figure 5.7c

CHAPTER VI

SUMMARY

In this study, various aspects of inversion of body wave data to obtain information on source parameters have been investigated. It was found that teleseismic body waves carry uncontaminated information about the earthquake source over wide frequency range. Under favorable conditions when an earthquake occurs in a region with no significant sediment cover, frequencies as short as 1 Hz appear to be usable. The body wave inversions for the purpose of determining the average, long-period, long-wavelength characteristics of the source are stable and appear to give precise parameter estimates. Due to steep take-off angles the teleseismic body waves provide good constraints on the source depth, an often elusive but geologically very important parameter.

A pre-requisite of stable point source inversion is that the dominant wavelengths of the data are longer than the fault dimensions. This prerequisite is usually met when studying events of magnitudes 6 to 7 using WWSSN or GDSN data (e.g., Lice earthquake). Usually the conditions are such that good estimates of all centroidal parameters can be obtained. Under favorable conditions, events with magnitudes of about 5-5.5 may be analyzed by applying the same techniques to the short period data (e.g., New Brunswick mainshock and aftershock).

Large shallow events (magnitude >7, e.g., El Asnam), however, are difficult to analyze. Due to long rupture durations, source time function effects dominate over depth effects and, especially for strike-slip events, large trade-offs between the source time function and source depth occur. In order to resolve the source depth and the M_{xz} and M_{yz} moment tensor components, data with wavelengths of the order of the source depth or

shorter are required. Because of the large horizontal extent of most large (magnitude > 7) events, the point source approximation usually breaks down for the wavelengths which are required to resolve the depth and M_{xz} and M_{yz}. In the analysis of large shallow events we must, therefore, choose between either using long-period, long-wavelength data and the point source approximation and thus sacrificing the resolution of certain basic source parameters, or introducing additional source parameters which account for the source finiteness.

Inversions of large events are also difficult because of the instrumental limitations of WWSSN and GDSN networks which seldom have sufficient bandwidth necessary for constraining all parameters. Filtering, instrument deconvolution, or any additional data handling introduce uncertainties into the analysis. In the future, the availability of broad-band data should greatly simplify the analysis of large events; the limitation imposed by the wave interactions with the earth's surface cannot, however, be removed. Even if only average parameters are desired, more sophisticated parameterizations than that of a simple point source will be required for the analysis of large shallow events. As we have seen by the example of the El Asnam earthquake, the determination of other than the average, centroidal parameters requires considerable care and may be impractical in routine applications.

At present, there is a wealth of geologically interesting data available to which the techniques discussed in this thesis can be directly applied on a routine basis. An example of such an application is the study of earthquakes in the Indian Ocean by Bergman, Nabelek and Solomon [1984].

REFERENCES

Aggarwal, Y. P., and L. R. Sykes, Earthquakes, faults and nuclear power plants in southern New York-northern New Jersey, Science, 200, 425-429, 1978.

Aki, K., Generation and propagation of G waves from the Niigata earthquake of June 16, 1964, Bull. Earthquake Res. Inst. Tokyo Univ., 44, 23-88, 1966.

Aki, K., Scaling law of seismic spectrum, J. Geophys. Res., 72, 1217-1231, 1967.

Aki, K., Signal to noise ratio in seismic measurements, in Volcanoes and Tectonosphere, eds. H. Aoki and S. Iizuka, Tokyo, Tokai University Press, 1976.

Aki, K., Evolution of quantitative models of earthquakes, SIAM-AMS Proceedings, 12, 43-57, 1979a.

Aki, K., Characterization of barriers on an earthquake fault, J. Geophys. Res., 84, 6140-6148, 1979b.

Aki, K., M. Bouchon, B. Chouet, and S. Das, Quantitative prediction of strong motion for a potential earthquake fault, Ann. Goephis., XXX, 341-368, 1977.

Aki, K., and P. G. Richards, Quantitative Seismology: Theory and Methods, W. H. Freeman, San Francisco, 1980.

Ambraseys, N. N., The El Asnam (Algeria) earthquake of 10 October: Conclusions drawn from a field study, Q. J. Eng. Geol., 14, 143-148, 1981.

Arpat, E., Lice Depremi, Yeryuvari ve Insan, 2, 15-27, Feb., 1977.

Arpat, E., and F. Sargolu, The East Anatolian fault system: Thoughts on its development, Bull. Miner. Res. Explor. Inst., Turk., 78, 33-3, 1972.

Bache, T. C., T. G. Barker, N. Rimer, and J. T. Cherry, The contribution of two-dimensional source effects to the far-field seismic signatures of underground nuclear explosions, SSS-R-80-4569, S-Cubed, La Jolla, California, 1980.

Backus, G. E., Interpreting the seismic glut moments of total degree two or less, Geophys. J. R. Astr. Soc., 51, 1-25, 1977a.

Backus, G. E., Seismic sources with observable glut moments of spacial degree two, Geophys. J. R. Astr. Soc., 51, 27-45, 1977b.

Backus, G., and M. Mulcahy, Moment tensors and other phenomenological descriptions of seismic sources, - I. Continuous displacements, Geophys. J. R. Astr. Soc., 46, 341-361, 1976a.

Backus, G., and M. Mulcahy, Moment tensors and other phenomenological descriptions of seismic sources - II. Discontinuous displacements, Geophys. J. R. Astr. Soc., 46, 341-361, 1976b.

Basham, P. W., D. H. Weichert, and M. J. Berry, Regional assessment of seismic risk in eastern Canada, Bull. Seis. Soc. Am., 69, 1567-1602, 1979.

Baysal, A. M., Lice depremi art sarsintilari, Thesis, Istanbul Teknik Univesitesi, 1977.

Ben-Menahem, A., Radiation of seismic surface waves from finite moving source, Bull. Seis. Soc. Am., 51, 401-435, 1961.

Bergman, E. A., J. L. Nabelek, and S. C. Solomon, An extensive region of off-ridge normal-faulting earthquakes in the southern Indian Ocean, J. Geophys. Res., in press, 1984.

Betti, E., Il Nuovo Cimento (Ser. 2), t. 7, 1872.

Boatwright, J., A spectral theory for circular seismic sources; simple estimates of source dimensions, dynamic stress drop, and radiated seismic energy, Bull. Seis. Soc. Am., 70, 1-27, 1980.

Bouchon, M., Teleseismic body wave radiation from a seismic source in a layered medium, Geophys. J. R. Astr. Soc., 47, 515-530, 1976.

Bouchon, M. A dynamic source model for the San Fernando earthquake, Bull. Seis. Soc. Am., 68, 1555-1576, 1978.

Bullen, K. E., An Introduction to the Theory of Seismology, Cambridge University Press, 1963.

Burdick, L. J., and G. R. Mellman, Inversion of the body waves from the Borrego Mountain earthquake to the source mechanism, Bull. Seis. Soc. Am., 66, 1485-1499, 1976.

Burdick, L. J., and D. V. Helmberger, The upper mantle P velocity structure of the western United States, J. Geophys. Res., 83, 1699-1712, 1978.

Burridge, R., and L. Knopoff, Body force equivalents for seismic dislocations, Bull. Seis. Soc. Am., 54, 1875-1888, 1964.

Burridge, R., and J. Willis, The self-similar problem of the expanding ellipti l crack in an anisotropic solid, Proc. Camb. Phil. Soc., 66, 443-468, 1969.

Buyukasikoglu, S., Eurasian-African plate boundary in southern Turkey and eastern Mediterranean, in Proceedings of the 7th World Conference on Earthquake Engineering, Geoscience Aspects, Part 1, vol. 1, 209-212, 1980.

Chapman, C. H., A new method of computing synthetic seismograms, Geophys. J.R. Astr. Soc., 51, 275-312, 1977.

Choy, G. J. Boatwright, J. W. Dewey, and S. A. Sipkin, A teleseismic analysis of the New Brunswick earthquake of January 9, 1982, J. Geophys. Res., 88, 2199-2212, 1983.

Cipar, J., Source process of the Haicheng, China earthquake from observations of P and S waves, Bull. Seis. Soc. Am., 69, 1903-1916, 1979.

Cipar, J., Broadband time domain modeling of earthquakes from Friuli, Italy, Bull. Seis. Soc. Am., 71, 1215-1231, 1981.

Cisternas, A., J. Dorel, and R. Gaulon, Models of the complex source of the El Asmam earthquake, Bull. Seis. Soc. Am., 72, 2245-2266, 1982.

Comer, R. P., Tsunami generation by earthquakes, Ph.D. Thesis, Mass. Inst. of Technol., Cambridge, 1982.

Cormier, V. F., The effect of attenuation on seismic body waves, Bull. Seis. Soc. Am., 72, S162-S200, 1982.

Cormier, V. F., and G. L. Choy, Theoretical body wave interactions with upper mantle structure, J. Geophys. Res., 86, 1673-1678, 1981.

Dahlen, F. A., On the ratio of P-wave to S-wave corner frequencies for shallow earthquake sources, Bull. Seis. Soc. Am., 64, 1159-1180, 1974.

as, S., and K. Aki, Fault plane with barriers: A versatile earthquake model, J. Geophys. Res., 82, 5658-5670, 1977.

Der, Z. A., T. W. McElfresh, and A. O'Donnell, An investigation of the regional variatons and frequency dependence of anelastic attenuation in the mantle under the United States in the 0.5-4 Hz band, Geophys. J. R. Astr. Soc., 69, 67-100, 1982.

Deschamps, A., Y. Gaudemer, and A. Cisternas, The El Asnam earthquake of October 10, 1980; multiple-source mechanism from long-period records, Bull. Seis. Soc. Am., 72, 1111-1128, 1982.

Doornbos, D. J., Seismic moment tensors, in Identification of Seismic Sources, eds. E. S. Husebye and S. Mykkeltveit, D. Reidel, Dordrecht, Holland, 207-232, 1981.

Doornbos, D.J., Seismic moment tensors and kinematic source parameters, Geophys. J. R. Astr. Soc., 69, 235-251, 1982.

Douglas, A., Seismic source identification: A review of past and present research efforts, in Identification of Seismic Sources, eds. E. S. Husebye and S. Mykkeltveit, D. Reidel, Dordrecht, Holland, 1-48, 1981

Dziewonski, A. M., and F. Gilbert, Temporal variation of the seismic moment and the evidence of precursive compression for two deep earthquakes, Nature, 247, 185-188, 1974.

Dziewonski, A. M., T. -A. Chou, and J. H. Woodhouse, Determination of earthquake source parameters from waveform data for studies of global and regional seismicity, J. Geophys. Res., 86, 2825-2852, 1981.

Dziewonski, A. M., and J. H. Woodhouse, An experiment in systematic study of global seismicity: Centroid-moment tensor solutions for 201 moderate and large earthquakes of 1981, J. Geophys. Res., 88, 3247-3271, 1983.

Ebel, J. E., and D. V. Helmberger, P-wave complexity and fault asperities; the Borrego Mountain, California, earthquake of 1968, Bull. Seis. Soc. Am., 72, 413-437, 1982.

Eshelby, J. D., The determination of the elastic field of an ellipsoidal inclusion, and related problems, Proc. Roy. Soc. Lon. A241, 376-396, 1957.

Evinson, F. F., Earthquakes and faults, Bull. Seis. Soc. Am., 53, 873-892, 1963.

Farrell, W. E., and J. L. Stevens, t^* estimates from deterministic discrimination applied to SRO body wave recordings from NTS and Kazakh explosions, S-Cubed Memorandum, July, 1982.

Fitch, T. J., D. W. McCowan, and M. W. Shields, Estimation of the seismic moment tensor from teleseismic body wave data with application to intraplate and mantle earthquakes, J. Geophys. Res., 85, 3817-3828, 1980.

Fletcher, J. B., A. G. Brady, and T. C. Hanks, Strong-motion accelerograms of the Oroville, California, aftershocks: Data processing and the aftershock fo 0350 August 6, 1975, Bull. Seis. Soc. Am., 70, 243-267, 1980.

Futterman, W. I., Dispersive body waves, J. Geophys. Res., 67, 5279-5291, 1962.

Gilbert, F., Excitation of the normal modes of the Earth by earthquake sources, Geophys. J.R. Astr. Soc., 22, 223-226, 1971.

Gilbert, F., Derivation of source parameters from low-frequency spectra, Phil. Trans. Roy. Soc. London, Ser. A., 274, 369-371, 1973.

Gilbert, F., and A. M. Dziewonski, An application of normal mode theory to the retrieval of structural parameters and source mechanisms from seismic spectra, Phil. Trans. Roy. Soc. London, Ser. A., 278, 187--269, 1975.

Gupta, I. N., Body wave radiation patterns from elementary sources within a half space, Bull. Seis. Soc. Am., 57, 657-675, 1967.

Hanks, T. C., The faulting mechanism of the San Fernando earthquake, J. Geophys. Res., 78, 1215-1229, 1974.

Hanks, T. C., Crustal earthquake stress drops, Proc. of Conference IX, Magnitude of Deviatoric Stress in Earth's Crust and Upper Mantle II, 491-518, 1975.

Hanks, T. C., b-values and seismic source models: Implications for tectonic stress variations along active crustal fault zones and the estimation of high-frequency strong ground motion, J. Geophys. Res., 84, 2235-2242, 1979.

Hanks, T. C., Crustal earthquake stress drops, Proc. of Conference IX, Magnitude of Deviatoric Stress in Earth's Crust and Upper Mantle II, 491-518, 1980.

Harkrider, D. G., Theoretical and observed acoustic-gravity waves from explosive sources in the atmosphere, J. Geophys. Res., 69, 5295-5321, 1964.

Hartzell, S., Faulting process of the May 17, 1976 Gazli, USSR, earthquake, Bull. Seis. Soc. Am., 70, 1715-1736, 1980.

Haskell, N. A., The dispersion of surface waves in multilayered media, Bull. Seis. Soc. Am., 43, 17-34, 1953.

Haskell, N. A., Total energy and energy spectral density of elastic wave radiation from propagating faults, Bull. Seis. Soc. Am., 54, 1811-1841, 1964.

Haskell, N. A., Analytic approximation for the elastic radiation from a contained underground explosion, J. Geophys. Res., 72, 2583-2587, 1967.

Helmberger, D. V., Generalized ray theory for shear dislocations, Bull. Seis. Soc. Am., 64, 45-64, 1974.

Helmberger, D. V., and D. M. Hadley, Seismic source functions and attenuation from local and teleseismic observations of the NTS events JORUM and HANDLEY, Bull. Seis. Soc. Am., 71, 51-67, 1981.

Herrin, E., Introduction to "1968 seismological tables for P phases," Bull. Seis. Soc. Am., 58, 1193-1241, 1968.

Herrmann, R. B., C. A. Langston, and J. E. Zollweg, The Sharpsburg, Kentucky earthquake of 27 July 1980, Bull. Seis. Soc. Am., 72, 1219-1239, 1982.

Honda, H., On the mechanism and the types of the seismograms of shallow earthquakes, Geophys. Mag., 5, 69-88, 1932.

Ida, Y., Cohesive force across the tip of a longitudinal shear crack and Griffith's specific surface energy, J. Geophys. Res., 77, 3796-3805, 1972.

Ishimoto, M., Study of Earthquakes (in Japanese), Kokin-Shoin, Tokyo, 1935.

Jackson, D. D., The use of a priori data to resolve non-uniqueness in linear inversion, Geophys. J. R. Astr. Soc., 57, 137-157, 1979.

Jackson, J., Errors in focal depth determination and the depth of seismicity in Iran and Turkey, Geophys. J. R. Astr. Soc., 61, 285-301, 1980.

Kafka, A. L., and D. J. Weidner, The focal mechanisms and depths of small earthquakes as determined from Rayleigh wave radiation patterns, Bull. Seis. Soc. Am., 69, 1379-1390, 1979.

Kanamori, H., Use of seismic radiation to infer source parameters, Proceedings of Conference III, Fault Mechanics and Its Relation to Earthquake Prediction, Geol. Surv. Open File Rep. U.S., 78-380, 283-318, 1978.

Kanamori, H., and D. L. Anderson, Theoretical basis of some empirical relations in seismology, Bull. Seis. Soc. Am., 65, 1073-1095, 1975.

Kanamori, H., and J. Given, Use of long period surface waves for rapid determination of earthquake-source parameters, Phys. Earth Planet. Int., 27, 8-31, 1981.

Kanamori, H., and J. Given, Use of long period surface waves for fast determination of earthquake source parameters, 2. Preliminary determination of source mechanism of large earthquakes (Ms > 6.5) in 1980, Phys. Earth Planet. Int., 30, 260-268, 1982.

Kanamori, H., and G. S. Stewart, Mode of strain release along the Gibbs fracture zone, mid-Atlantic ridge, Phys. Earth Planet. Int., 11, 312-332, 1976.

Kanamori, H., and G. S. Stewart, Seismological aspects of the Guatemala earthquake of February 4, 1976, J. Geophys. Res., 83, 3427-3434, 1978.

Kane, M. F., Correlation of major eastern U.S. earthquake centers with mafic/ultramafic masses, Eos Trans. AGU, 57, 963, 1976.

Keilis-Brook, V. I., On the estimation of the displacement in an earthquake source and of source dimensions, Ann. Geofis., 12, 205-214, 1959.

Kikuchi, M., and H. Kanamori, Inversion of complex body waves, Bull. Seis. Soc. Am., 72, 491-506, 1982.

King, G. C. P., and C. Vita-Finzi, Active folding in the Algerian earthquake of 10 October 1980, Nature, 292, 22-26, 1981.

King, G., and G. Yielding, The evolution of a fault-system: Process of rupture initiation, propagation and termination in the 1980 El Asnam (Algeria) earthquake, manuscript, 1984.

Knopoff, L., Energy release in earthquakes, Geophys. J. R. Astr. Soc., 1, 44-52, 1958.

Knopoff, L., and A. F. Gangi, Seismic reciprocity, Geophys., 24, 681-691, 1959.

Knopoff, L., and M. Randall, The compensated linear-vector dipole: A possible mechanism for deep earthquakes, J. Geophys. Res., 75, 4957-4963, 1970.

Kostrov, B. V., Unsteady propagation of longitudinal shear cracks, J. Appl. Math. Mech., 30, 1241-1248, 1966.

Kostrov, B. V., Mechanics of the source tectonic earthquakes, Nauka, Moscow, 1975.

Kroeger G. C., and R. J. Geller, An efficient method for synthesizing teleseismic body waves for sources in a vertically layered crust, manuscript, 1982.

Langston, C. A., The effect of planar dipping structure on source and receiver responses for constant ray parameter, Bull. Seis. Soc. Am., 4, 1029-1050, 1977.

Langston, C. A., Source inversion of seismic waveforms: The Koyna, India, earthquake of 13 September 1967, Bull. Seis. Soc. Am., 71, 1-24, 1981.

Langston, L. C., and R. Buttler, Focal mechanism of the August 1, 1975 Oroville earthquake, Bull. Seis. Soc. Am., 66, 1111-1120, 1976.

Langston, C. A., and D.V. Helmberger, A procedure for modeling shallow dislocation sources, Geophys. J. R. Astr. Soc., 42, 117-130, 1975.

Lawson, C. L., and R. J. Hanson, Solving Least Squares Problems, Prentice-Hall, Inc., Englewood Cliffs, New Jersey, 1974.

Liu, H. -P., D. L. Anderson, and H. Kanamori, Velocity dispersion due to anelasticity: Implications for seismology and mantle composition, Geophys. J. R. Astr. Soc., 47, 41-58, 1976.

Lundquist, G. M., and V. F. Cormier, Constraints on the absorption band model of Q, J. Geophys. Res., 85, 5244-5256, 1980.

Madariaga, R., Dynamics of an expanding circular fault, Bull. Seis. Soc. Am., 66, 639-666, 1976.

Madariaga, R., On the relation between seismic moment and stress drop in the presence of stress and strength heterogeneity, J. Geophys. Res., 84, 2243-2250, 1979.

Madariaga, R., Dynamics of seismic sources, in Identification of Seismic Sources, eds. E. S. Husebye and S. Mykkeltveit, D. Reidel, Dordrecht, Holland, 207-232, 1981.

McCaffrey, R., and J. Nabelek, The geometry of backarck thrusting along eastern Sunda arc, Indonesia: Constraints from earthquake and gravity data, submitted to J. Geophys. Res., 1984.

McKenzie, D., Active tectonics of the Mediterranean region, Geophys. J. R. Astr. Soc., 30, 109-185, 1972.

McKenzie, D., The East Anatolian fault; A major structure in eastern Turkey, Earth Planet. Sci. Lett., 29, 189-193, 1976.

McKeown, F. H., Hypothesis: Many earthquakes in the central and southeastern United States are causally related to mafic intrusive bodies, J. Res. U. S. Geol. Surv., 6, 41-50, 1978.

Minster, J. B., Transient and impulse responses of a one-dimensional linearly attenuating medium - I. Analytical results, Geophys. J. R. Astr. Soc., 52, 479-501, 1978.

Molnar, P., B. E. Tucker, and J. N. Brune, Corner frequencies of P and S waves and models of earthquake sources, Bull. Seis. Soc. Am., 63, 2091-2104, 1973.

Morse, P. M., and H. Feshbach, Methods of Theoretical Physics, McGraw-Hill, New York, 1953.

Nabelek, J., Teleseismic constraints on the 1979 Coyote Lake and the 1980 El Asnam Earthquakes, Workshop on the Dynamics of Earthquake Faulting as Inferred from Recordings of Strong Ground Motion, Lake Tahoe, California, October 20-23, 1981.

North, R. G., and T. J. Fitch, Moment-tensor inversion for very shallow sources, Seismic Discrimination, Semiannual Technical Summary, Lincoln Laboratory. M.I.T., Lexington, Massachusetts, March, 1980.

Ouyed, M., M. Meghraoui, A. Cisternas, A. Deshamps, J. Dorel, J. Freshet, R. Gaulon, D. Hatzfeld, and H. Philip, Seismotectonics of the El Asnam earthquake, Nature, 292, 26-31, 1981.

Ouyed, M., G. Yielding, D. Hatzfeld, and G. C. P. King, An aftershock study of the El Asnam (Algeria) earthquake of 1980, Geophys. J. R. Astr. Soc., in press, 1984.

Papageorgiou, A. S., and K. Aki, A specific barrier model for the quantitative description of inhomogeneous faulting and the prediction of strong ground motion. Part I. Descripton of the model, Bull. Seis. Soc. Am., 73, 693-722, 1983a.

Papageorgiou, A. S., and K. Aki, A specific barrier model for the quantitative description of inhomogeneous faulting and the prediction of strong ground motion. Part II. Applications of the model, Bull. Seis. Soc. Am., 73, 953-978, 1983b.

Patton, H., Reference point equalization method for determining source and path effects of surface waves, J. Geophys. Res., 85, 821-848, 1980.

Patton, H., and K. Aki, Bias in the estimate of seismic moment tensor by the linear inversion method, Geophys. J. R. Astr. Soc., 59, 479-495, 1979.

Perl, N., F. J. Thomas, J. Trulio, and L. Woodie, Effect of burial depth on seismic signals, PSR-815, Pacific Sierra Research, Santa Monica, California, 1979.

Philip, H., and M. Meghraoui, Structural analysis and interpretation of the surface deformations of the El Asnam earthquake of October 10, 1980, Tectonics, 1, 17-49, 1983.

Pulli, J. J., Seismicity, earthquake mechanisms, and seismic wave attenuation in the northeastern United States, Ph. D. Thesis, Mass. Inst. Technol., Cambridge, Massachusetts, June, 1983.

Pulli, J. J., and M. N. Toksoz, Fault plane solutions for northeastern United States earthquakes, Bull. Seis. Soc. Am., 71, 1875-1882, 1981.

Rial, J. A., The Caracas, Venezuela, earthquake of July, 1962: Multiple-source event, J. Geophys. Res., 83, 5405-5414, 1978.

Richards, P. G., The dynamic field of a growing plane elliptical shear crack, Int. J. Solids Struct., 9, 843-861, 1973.

Romanowicz, B., Depth resolution of earthquakes in central Asia by moment tensor inversion of long-period Rayleigh waves: Effects of phase velocity variations across Eurasia, J. Geophys. Res., 86, 5963-5984, 1981.

Romanowicz, B., and P. Guillemant, An experiment in the retrieval of depth and source mechanism of large earthquakes using long period Rayleigh wave data, submitted to Bull. Seis. Soc. Am., 1984.

Rotstein, Y., and A. L. Kafka, Seismotectonics of the southern boundary of Anatolia, eastern Mediterranean region: subduction, collision, and arc jumping, J. Geophys. Res., 87, 7694-7706, 1982.

Rudnicki, J. W., and H. Kanamori, Effects of fault interaction on moment, stress drop, and strain energy release, J. Geophys. Res., 86, 1785-1793, 1981.

Ruegg, J. C., M. Kasser, A. Tarantola, J. C. Lepine, and B. Chovikrat, Deformations associated with the El Asnam earthquake of 10 October 1980: Geodetic determination of vertical and horizontal movements, Bull. Seis. Soc. Am., 72, 2227-2244, 1982.

Saito, M., Excitation of free oscillations and surface waves by a point source in a vertically heterogeneous earth, J. Geophys. Res., 72, 3689-3699, 1967.

Sato, T., and T. Hirasawa, Body wave spectra from propagating shear cracks, J. Phys. Earth, 21, 415-431, 1973.

Savage, J. C., Radiation from a realistic model of faulting, Bull. Seis. Soc. Am., 56, 577-592, 1966.

Savage, J. C., Relation of corner frequency to fault dimensions, J. Geophys. Res., 27, 3788-3795, 1972.

Sbar, M. L., and L. R. Sykes, Contemporary compressive stress and seismicity in eastern North America: An example of intraplate tectonics, Geol. Soc. Am. Bull., 84, 1861-1882, 1973.

Sengor, A. M. C., The North Anatolian transform fault: Its age, offset and tectonic significance, J. Geol. Soc. Lodon, 136, 269-282, 1979.

Sholz, C. H., Scaling laws for large earthquakes: consequences for physical models, Bull. Seis. Soc. Am., 72, 1-14, 1982.

Silver, P., Retrieval of source-extent parameters and the interpretation of corner frequency, Bull. Seis. Soc. Am., 73, 1499-1511, 1983.

Silver, P. G., and T. H. Jordan, Total-moment spectra of fourteen large earthquakes, J. Geophys. Res., 88, 3273-3293, 1983.

Spencer, T., The method of generalized reflection and transmission coefficients, Geophys., 25, 625-641, 1960.

Starr, A. T., Slip in a crystal and rupture in a solid due to shear, Proc. Camb. Phil. Soc., 24, 489-500, 1928.

Stauder, W., M. Kramer, G. Fisher, S. Schaefer, and S. T. Morrissey, Seismic characteristics of southeast Missouri as indicated by a regional telemetered microearthquake array, Bull. Seis. Soc. Am., 66, 1953-1964, 1976.

Stewart, G. S., and D. V. Helmberger, The Bermuda earthquake of March 24, 1978: A significant oceanic intraplate event, J. Geophys. Res., 86, 7027-7036, 1981.

Stewart, G. S., and H. Kanamori, Compexity of rupture in large strike-slip earthquakes in Turkey, Phys. Earth Planet. Int., 28, 70-84, 1982.

Street, R. L., and F. T. Turcotte, A study of northeastern North American spectral moments, magnitudes, and intensities, Bull. Seis. Soc. Am., 67, 599-614, 1977.

Strelitz, R. A., Moment tensor inversions of source models, Geophys. J. R. Astr. Soc., 52, 359-364, 1978.

Stump, B. W., Higher-degree moment tensors - the importance of source finiteness and rupture propagation on seismograms, Geophys. J. R. Astr. Soc., 69, 721-743, 1982.

Stump, B. W., and L. R. Johnson, Determination of source properties by the linear inversion of seismograms, Bull. Seis. Soc. Am., 67, 1489-1502, 1977.

Suarez, G., Seismicity, tectonics, and surface wave propagation in the central Andes, Ph.D. Thesis, Mass. Inst. Technol., Cambridge, Massachusetts, December, 1982.

Sykes, L. R., Intraplate seismicity, reactivation of preexisting zones of weakness, alkaline magmatism, and other tectonism postdating continental fragmentation, Rev. Geophys. Space Phys., 16, 621-688, 1978.

Tarantola, A., and B. Valette, Generalized nonlinear inverse problems solved using the least squares criterion, Rev. Geophys. Space Phys., 20, 219-232, 1982.

Taylor, S. R., Three-dimensional crust and upper mantle structure at the Nevada test site, J. Geophys. Res., 88, 2220-2232, 1983.

Toksoz, M. N., and H. Kehrer, Tectonic strain release by underground nuclear explosions and its effect on seismic discrimination, Geophys. J. R. Astr. Soc., 31, 141-161, 1972.

Toksoz, M. N., A. F. Shakal, and A. J. Michael, Space-time migration of earthquakes along the North Anatolian Fault Zone and seismic gaps, Pageoph., 117, 1258-1270, 1979.

Trehu, A. M., J. L. Nabelek, and S. C. Solomon, Source characterization of two Reykjanes Ridge earthquakes: surface waves and moment tensors; P waveforms and nonorthogonal nodal planes, J. Geophys. Res., 86, 1701-1724, 1981.

Tsai, Y. B., and K. Aki, Simultaneous determination of the seismic moment and attenuation of seismic surface waves, Bull. Seis. Soc. Am., 59, 275-287, 1969.

Yanev, P. I., The Lice, Turkey, earthquake of September 6, 1975, Newsletter, Earthquake Engineering Research Institute, Ankara, Turkey, 9, 6, 1975.

Yang, J. P., and Y. P. Aggarwal, Seismotectonics of northeastern United States and adjacent Canada, J. Geophys. Res., 86, 4981-4998, 1981.

Yielding, G., J. A. Jackson, G. C. P. King, H. Sinvhal, C. Vita-Finzi, and R. M. Wood, Relation between surface deformation, fault geometry, seismicity and rupture characteristics during the El Asnam (Algeria) earthquake of 10 October 1980, Earth Planet. Sci. Lett., 56, 287-304, 1981.

Ward, S., Ringing P waves and submarine faulting, J. Geophys. Res., 84, 3057-3062, 1979.

Ward, S. N., Body wave calculation using moment tensor sources in spherically symmetric, inhomogeneous media, Geophys. J. R. Astr. Soc., 60, 53-66, 1980a.

Ward, S. N., Relationships of tsunami generation and an earthquake source, J. Phys. Earth, 28, 441-474, 1980b.

Ward, S. N., Body wave inversion: Moment tensors and depths of oceanic intraplate bending earthquakes, J. Geophys. Res., 88, 9315-9330, 1983.

Weidner, D. J., Rayleigh wave phase velocities in the Atlantic Ocean, Geophys. J. R. Astr. Soc., 36, 105-139, 1974.

Wetmiller, R. J., J. Adams, A. E. Stevens, H. S. Hasegawa, and J. Berube, Aftershock sequence for the New Brunswick earthquakes of January 9th and 11th, March 31st, and June 16th, 1982, Earthquake Notes, 53, 41, 1982.

White, J. E., Use of reciprocity theorem for computation of low-frequency radiation patterns, Geophys., XXV, 613-624, 1960.

Woolard, G. P., Tectonic activity in North America as indicated by earthquakes, in the Earth's crust and upper mantle, Geophys. Monogr. Ser., 13, ed. P. J. Hart, 125-133, AGU, Washington, DC, 1969.

Zoback, M. L., and M. Zoback, State of stress in the conterminous United States, J. Geophys. Res., 85, 6113-6156, 1980.

APPENDIX A

ELASTIC WAVES FROM A SOURCE IN VERTICALLY STRATIFIED MEDIUM

In a cartesian coordinate system, the displacement u_k at a point $\underline{x}$ and time t due to an arbitrary point moment tensor M_{ij} located at the origin can be expressed by

$$u_k(\underline{x},t) = g_{ki,j}(\underline{x},t;\underline{0},0)*M_{ij}(\underline{0},t) \tag{A1}$$

[Gilbert, 1971, 1973; Gilbert and Dziewonski, 1975; Stump and Johnson, 1977; Doornbos, 1982] where g_{ki} is the elastodynamic Green's function and a comma in the subscript indicates differentiation.

If all components of $M_{ij}(\underline{0},t)$ have the same time dependence S(t), the above expression may be written as

$$u_k(\underline{x},t) = [g_{ki,j}(\underline{x},t;\underline{0},0)*S(t)]M_{ij}. \tag{A2}$$

In the case of an axially-symmetric medium, the problem separates into P-SV and SH components and azimuth-dependent terms of the radiation pattern can be factored out. For the P-SV coupled waves, the displacement at time t, distance Δ and azimuth ϕ due to a source at depth h is

$$\begin{aligned}\underline{u}^{PSV}(\phi,\Delta,t) = \{&\underline{I}^{PSV2}(\Delta,h,t)\left[\tfrac{1}{2}(M_{yy}+M_{xx}) - \tfrac{1}{2}(M_{yy}-M_{xx})\cos 2\phi + M_{xy}\sin 2\phi\right] \\ &+ \underline{I}^{PSV1}(\Delta,h,t)\left[M_{yz}\sin\phi + M_{xz}\cos\phi\right] \\ &+ \underline{I}^{PSV0}(\Delta,h,t)M_{zz}\}*S(t).\end{aligned} \tag{A3}$$

Similarly, for the SH coupled waves

$$\underline{u}^{SH}(\phi,\Delta,t) = \{\underline{I}^{SH2}(\Delta,h,t)[\tfrac{1}{2}(M_{yy}-M_{xx})\sin 2\phi + M_{xy}\cos 2\phi] + \underline{I}^{SH1}(\Delta,h,t)[M_{yz}\cos\phi - M_{xz}\sin\phi]\}*S(t). \quad (A4)$$

[Ward, 1980a] (here, as in the rest of the text, we follow coordinate conventions of Aki and Richards [1980]).

The medium response functions $\underline{I}^0$, $\underline{I}^1$, and $\underline{I}^2$ are independent of azimuth. In terms of the Green's functions they are

$$I^0_\gamma = g_{\gamma z,z} \qquad I^1_\gamma = g_{\gamma r,z} + g_{\gamma z,r} \qquad I^2_\gamma = g_{\gamma r,r} \quad (A5)$$

where (r,ϕ,z) are cylindrical coordinates centered on the source and γ is the direction of the displacement at the receiver. Thus in order to determine the radiation due to an arbitrary moment tensor, we need only know the medium response to vertical and horizontal unit force impulses. By differentiation, we can then obtain the four couples comprising the three elementary seismograms $\underline{I}^0$ $\underline{I}^1$, and $\underline{I}^2$.

The above result applies to all waves generated by the source. The medium response to vertical and horizontal force impulses can be obtained by a variety of methods, depending on the type of wave studied (e.g. for teleseismic body waves, see Helmberger [1974], Langston and Helmberger [1975], Bouchon [1976], Ward [1980a]; for surface waves, see Harkrider [1964], Saito [1967]; for tsunamis, see Ward [1980b], Comer [1982]). Examples of $\underline{I}^0$, $\underline{I}^1$ and $\underline{I}^2$ for various wave types are shown in Figure 3.1.

At teleseismic distances the P and S waves arrive well separated in time from each other, as well as from other seismic phases, and therefore can be analyzed independently. The waves forming the packets of teleseismic P and S waves are characterized by essentially constant ray parameter and involve all direct, reflected and converted waves which

propagate through the earth's mantle along the path of minimum travel time as P or S waves, respectively. The Green's functions for these waves can be expressed in the the form:

$$\underline{g}(t) = \underline{C}^r(t) * M(t) * \underline{g}^s(t) \qquad (A6)$$

[Langson and Helmberger, 1975] where $\underline{g}^s(t)$, depending on the type of wave studied, is the displacement of the P, SV or SH waves emerging at the bottom of the crust in the source region in response to a force impulse, and M(t) and $\underline{C}^r(t)$ are the responses to these waves by the mantle and the crust at the receiver. In the distance range of about 30 to 90°, M(t) includes only the effects of anelastic attenuation, geometrical spreading and travel time [Burdick and Helmberger, 1978]. The response at the bottom of the crust in the source region can be derived using the first motion approximation [Helmberger, 1974; Langston and Helmberger, 1975] or, more simply, using the reciprocity theorem [Gupta, 1967; Bouchon, 1976].

The most variable and uncertain aspect of the body wave Green's functions is the total travel time through the earth. In modeling of actual data, one way to remove this uncertainty is to align the first motion of the Green's function with the first motion of the observed direct arrival (preferably determined from the short-period records). If the nucleation point and centroidal point of the source are significantly displaced from each other, the location of the "equivalent" point source relative to the location of the nucleation point must be specified.

Typically, the unknown source parameters are determined by trial-and-error or by some methodical iterative procedure which requires numerous calculations of the theoretical seismograms. The general

formulation presented above (eq. A3 and A4) is particularly useful when the depth of the event is known, because the three elementary seismograms $\underline{I}^0$, $\underline{I}^1$ and $\underline{I}^2$ need be computed only once. When source depth is also to be determined, other formulations may be computationally more efficient. For teleseismic body waves we employ a modification based on the approximation that the wave packets of these waves are composed of waves with a constant ray parameter. This approximation is valid for body waves in the distance range of 30-90° and implies that only four rays generated by the source (generalized rays, if they are inhomogeneous), the up- and down-going P and S, contribute to the subsequent generation of phases which comprise a given teleseismic P or S wave packet. This further implies that the $\underline{g}^s$'s (Green's functions at the bottom of the crust in the source region) can be decomposed into components expressing the response of the crust to these four up- and down-going rays. Thereby, after regrouping similar terms, we obtain a new set of four (two for SH waves) elementary seismograms which, as we shall see from the subsequent discussion, can be used more efficiently when repeated computations of seismograms are required for a source at different depths [Bouchon, 1976; Kroeger and Geller, 1982].

Starting with the decomposed $\underline{g}^s$'s, then after convolution using equation (A6) and differentiation using equation (A5), we obtain the following expressions for $\underline{I}^0$, $\underline{I}^1$ and $\underline{I}^2$:

$$
\begin{aligned}
\underline{I}^{PSV^0} &= \alpha_\ell^2 \eta_{\alpha_\ell}^2 \underline{\dot{I}}_\ell^{P\uparrow} + \alpha_\ell^2 \eta_{\alpha_\ell}^2 \underline{\dot{I}}_\ell^{P\downarrow} - \beta_\ell^2 p \eta_{\beta_\ell} \underline{\dot{I}}_\ell^{SV\uparrow} + \beta_\ell^2 p \eta_{\beta_\ell} \underline{\dot{I}}_\ell^{SV\downarrow} \\
\underline{I}^{PSV^1} &= -2\alpha_\ell^2 p \eta_{\alpha_\ell} \underline{\dot{I}}_\ell^{P\uparrow} + 2\alpha_\ell^2 p \eta_{\alpha_\ell} \underline{\dot{I}}_\ell^{P\downarrow} + \beta_\ell^2 (\eta_{\beta_\ell}^2 - p^2) \underline{\dot{I}}_\ell^{SV\uparrow} - \beta_\ell^2 (\eta_{\beta_\ell}^2 - p^2) \underline{\dot{I}}_\ell^{SV\downarrow} \\
\underline{I}^{PSV^2} &= \alpha_\ell^2 p^2 \underline{\dot{I}}_\ell^{P\uparrow} + \alpha_\ell^2 p^2 \underline{\dot{I}}_\ell^{P\downarrow} + \beta_\ell^2 p \eta_{\beta_\ell} \underline{\dot{I}}_\ell^{SV\uparrow} + \beta_\ell^2 p \eta_{\beta_\ell} \underline{\dot{I}}_\ell^{SV\downarrow}
\end{aligned}
\tag{A7}
$$

$$\underline{I}^{SH1} = \beta_\ell p \dot{\underline{I}}_\ell^{SH\uparrow} + \beta_\ell p \dot{\underline{I}}_\ell^{SH\downarrow}$$

$$\underline{I}^{SH2} = -\beta_\ell \eta_{\beta_\ell} \dot{\underline{I}}_\ell^{SH\uparrow} + \beta_\ell \eta_{\beta_\ell} \dot{\underline{I}}_\ell^{SH\downarrow}.$$

η_{v_ℓ} is $[(1/v_\ell^2)-p^2]^{1/2}$, where v_ℓ is either the compressional velocity (α) or shear velocity (β) in layer ℓ, and p is the appropriate ray parameter ($p = \frac{1}{r_h}\frac{dT}{d\Delta}$, where r_h is the distance of the earthquake hypocenter from the center of the Earth, and T, depending on the wave studied, is the total travel time from the source to the receiver of either the direct P or direct S wave). The new elementary seismograms, $\dot{\underline{I}}_\ell^{P\uparrow}$ and $\dot{\underline{I}}_\ell^{P\downarrow}$, are the time derivatives of the response of the medium (in a time window appropriate for either the teleseismic P or SV wave) to the up- and down-going P waves generated by a unit impulse point P-wave source located within the layer ℓ. Similarly, $\dot{\underline{I}}_\ell^{SV\uparrow}$, $\dot{\underline{I}}_\ell^{SV\downarrow}$, $\dot{\underline{I}}_\ell^{SH\uparrow}$ and $\dot{\underline{I}}_\ell^{SH\downarrow}$ are the corresponding time derivatives of the responses to S waves from a point SV and SH source (for definition of the point sources and their properties see Aki and Richards [1980]). The terms multiplying the new elementary seismograms are the vertical radiation patterns associated with the three groups of the moment tensor components (eq. A3 and A4). In this study the responses are computed using propagator matrixes as in Bouchon [1976] or Trehu _et al._ [1981]. After rearranging, the teleseismic P wave displacement due to a point moment tensor located within a crustal layer ℓ at a depth d, recorded by a station at azimuth ϕ and an epicentral distance corresponding to the ray parameter p is:

$$\underline{u}^P(\phi,p,t) = M_n[\underline{I}_\ell^{P\uparrow}(t-\eta_{\alpha_\ell}d,p)r_\ell^{P\uparrow}(p) + \underline{I}_\ell^{P\downarrow}(t+\eta_{\alpha_\ell}d,p)r_\ell^{P\downarrow}(p)$$
$$+ \underline{I}_\ell^{SV\uparrow}(t-\eta_{\beta_\ell}d,p)r_\ell^{SV\uparrow}(p) + \underline{I}_\ell^{SV\downarrow}(t+\eta_{\beta_\ell}d,p)r_\ell^{SV\downarrow}(p)]* \dot{S}(t). \quad (A8)$$

The expression for the teleseismic SV wave displacement has an identical form, but with different ray parameter, and the response functions $\underline{I}_\ell^{P\uparrow}$, $\underline{I}_\ell^{P\downarrow}$, $\underline{I}_\ell^{SV\uparrow}$ and $\underline{I}_\ell^{SV\downarrow}$ include rays which contribute to the SV wave packet. The SH wave displacement is:

$$\underline{u}^{SH}(\phi,p,t) = M_n[\underline{I}_\ell^{SH\uparrow}(t-\eta_{\beta_\ell}d,p)r_\ell^{SH\uparrow}(p) + \underline{I}_\ell^{SH\downarrow}(t+\eta_{\beta_\ell}d,p)r_\ell^{SH\downarrow}(p)]* \dot{S}(t). \quad \text{(A9)}$$

In the above expressions, r_ℓ's are the source radiation patterns for the corresponding up- and down-going rays:

$$\begin{aligned}
r_\ell^{P\uparrow} &= \alpha_\ell^2 [a_1 p^2 + a_2 \eta_{\alpha_\ell}^2 - 2a_3 p\eta_{\alpha_\ell}] \\
r_\ell^{P\downarrow} &= \alpha_\ell^2 [a_1 p^2 + a_2 \eta_{\alpha_\ell}^2 + 2a_3 p\eta_{\alpha_\ell}] \\
r_\ell^{SV\uparrow} &= \beta_\ell^2 [a_3(p^2-\eta_{\beta_\ell}^2) - (a_2-a_1)p\eta_{\beta_\ell}] \\
r_\ell^{SV\downarrow} &= \beta_\ell^2 [a_3(p^2-\eta_{\beta_\ell}^2) + (a_2-a_1)p\eta_{\beta_\ell}] \\
r_\ell^{SH\uparrow} &= \beta_\ell [a_4 p - a_5 \eta_{\beta_\ell}] \\
r_\ell^{SH\downarrow} &= \beta_\ell [a_4 p + a_5 \eta_{\beta_\ell}]
\end{aligned} \quad \text{(A10)}$$

with

$$\begin{aligned}
a_1 &= \hat{M}_{xx}\cos^2\phi + \hat{M}_{xy}\sin 2\phi + \hat{M}_{yy}\sin^2\phi \\
a_2 &= \hat{M}_{zz} \\
a_3 &= \hat{M}_{xz}\cos\phi + \hat{M}_{yz}\sin\phi \\
a_4 &= \frac{1}{2}(\hat{M}_{yy}-\hat{M}_{xx})\sin 2\phi + \hat{M}_{xy}\cos 2\phi \\
a_5 &= -\hat{M}_{xz}\sin\phi + \hat{M}_{yz}\cos\phi
\end{aligned} \quad \text{(A11)}$$

M_n is the norm of the moment tensor ($M_n \equiv \|\underline{M}\|$) and $\hat{M}_{ij}$ are normalized moment-tensor components defining the source mechanism ($\hat{M}_{ij} = M_{ij}/M_n$). The individual response functions are calculated for a source located at an infinitesimal distance below the upper boundary of the layer ℓ. The response functions for a source at depth d below this boundary are found by delaying or advancing the original responses by an appropriate amount. (Here we assumed that the waves in the layer containing the source are homogeneous, i.e. $\eta_{\nu\ell}$'s are real.)

For a double-couple mechanism, it is customary to describe the source strength in terms of the scalar seismic moment M_o [Aki, 1966] and the source orientation in terms of its strike θ, dip δ, and rake λ. Using equation 1, Box 4.4 of Aki and Richards [1980] we obtain

$$\begin{aligned}
a_1 &= [\sin\delta\cos\lambda\sin 2(\phi-\theta) - \sin 2\delta\sin\lambda\sin^2(\phi-\theta)]/\sqrt{2} \\
a_2 &= [\sin 2\delta\sin\lambda]/\sqrt{2} \\
a_3 &= [-\cos\delta\cos\lambda\cos(\phi-\theta) + \cos 2\delta\sin\lambda\sin(\phi-\theta)]/\sqrt{2} \\
a_4 &= [\sin\delta\cos\lambda\cos 2(\phi-\theta) - \tfrac{1}{2}\sin 2\delta\sin\lambda\sin 2(\phi-\theta)]/\sqrt{2} \\
a_5 &= [\cos\delta\cos\lambda\sin(\phi-\theta) + \cos 2\delta\sin\lambda\cos(\phi-\theta)]/\sqrt{2} \\
M_n &= \sqrt{2}M_o
\end{aligned} \tag{A12}$$

For stress drop seismic sources such as earthquakes or underground explosions, the source time function of an equivalent point source is step-like; the far-field source time function

$$\Omega(t) = \dot{S}(t) \tag{A13}$$

is pulse-like.

In this study, $\Omega(t)$ is parameterized by a series of overlapping triangle functions with adjustable relative amplitudes (Figure 2.6):

$$\Omega(t) = \sum_{k=1}^{n} w_k T_{\Delta\tau}(t-\tau_k) \tag{A14}$$

where $T_{\Delta\tau}(t)$ is an isosceles triangle function of duration $2\Delta\tau$ and w_k is the amplitude. The time delay of each triangle function is $\tau_k = (k-1)\Delta\tau$. Because the sum of two adjacent triangles is always a trapezoid, this parameterization is equivalent to an approximation by the trapezoidal rule. The individual amplitudes are normalized by the total area under the time function. The appropriate value for $\Delta\tau$ depends on the frequency content of the data, which varies with the recording instrument and wave type. The number of individual elements n is then determined by the source duration, which is easily found by a few trials. The parameterization of the source time function in terms of the triangle functions insures f^{-2} amplitude decay at high frequencies that is commonly observed for earthquakes [Aki, 1967; Hanks, 1979; Aki and Richards, 1980].

Using this form for the source time function, we can rewrite expressions (A8) and (A9) in a computationally more useful form. Including the effect of the seismometer response R(t), the expression for the theoretical teleseismic body wave seismogram becomes

$$s(t) = M_n \sum_{k=1}^{n} \sum_{i=1}^{m} w_k H_i[t-\tau_k-(\eta_i-\eta_1)d+\bar{\eta}_1\zeta+p\rho\cos(\phi-\psi)]r_i \tag{A15}$$

where

$$H_i(t) = I_i(t-t_c)*T_{\Delta\tau}(t)*R(t) \tag{A16}$$

with

$$\underline{I} = (I_\ell^{P\downarrow}, I_\ell^{P\uparrow}, I_\ell^{SV\downarrow}, I_\ell^{SV\uparrow})$$

$$\underline{\eta} = (-\eta_{\alpha_\ell}, \eta_{\alpha_\ell}, -\eta_{\beta_\ell}, \eta_{\beta_\ell})$$

$$\underline{r} = (r_\ell^{P\downarrow}, r_\ell^{P\uparrow}, r_\ell^{SV\downarrow}, r_\ell^{SV\uparrow})$$

$$m = 4$$

for P and SV waves, and (A17)

$$\underline{I} = (I_\ell^{SH\downarrow}, I_\ell^{SH\uparrow})$$

$$\underline{\eta} = (-\eta_{\beta_\ell}, \eta_{\beta_\ell})$$

$$\underline{r} = (r_\ell^{SH\downarrow}, r_\ell^{SH\uparrow})$$

$$m = 2$$

for SH waves. The response functions $\underline{I}$ are for the component of displacement recorded by the seismometer. t_o is the travel time of the direct phase from the source nucleation point to the receiver. (ρ,ψ,ζ) are the coordinates of the source centroid in a cylindrical coordinate system centered on the nucleation point and give a first order estimate for the direction of rupture. (Note, unless the nucleation point coincides with the centroidal point of the source, the "equivalent" point source seismogram will not begin at t=0.) $\bar{\eta}_l$ is the average η_α (for the P-SV case) or η_β (for the SH case) over the vertical distance ζ. With this formulation, a synthetic seismogram is constructed simply by time shifts of the four (two for SH) elementary seismograms $H_i(t)$, weighted by the radiation pattern term r_i and the source time function amplitude term w_k. The time shift is dependent on the source location (centroid depth and epicenter) and the time delay of a time function element. The response

functions $H_i(t)$ need only be computed once for sources within a given crustal layer. This is particulary useful when the seismograms are repeatedly updated, as in an iterative inversion procedure, because they are generally the most costly component of the seismogram to compute.

In studies utilizing short-period data or involving large events, the effects of source finiteness may become significant. For a source characterized by a large component of unilateral rupture, a line source may be a sufficient approximation. The effect of a propagating line source is easily introduced into our formulation by replacing the triangular constant duration time function elements of the point source by trapezoidal elements,

$$T_{\Delta\tau_i}(t) = B_{\Delta\tau_i}(t) * B_{\Delta\tau^R}(t) \qquad \text{(A18)}$$

$$\tau_k = (k-1)\Delta\tau_i$$

formed by the convolution of two box functions, one of variable duration $\Delta\tau_i$ and the other of duration $\Delta\tau^R$, representing the rise time (Figure 2.7). The rise time is expected to be at least as long as the travel time of the rupture front over a half of the fault width [Savage, 1972]. In general $\Delta\tau_i$ will be different for each $H_i(t)$, and will depend on the station azimuth and ray parameter [Ben Menahem, 1961; Haskell, 1964; Aki and Richards, 1980]:

$$\Delta\tau_i = \Delta\tau^L\{1 - v^\theta p\cos(\phi-\theta) - v^\delta[-\eta_i\sin\delta + p\cos\delta\sin(\phi-\theta)]\} \qquad \text{(A19)}$$

where

v^θ is the rupture velocity along the strike of the fault

v^δ is the rupture velocity along the dip of the fault (down is positive)

$\Delta\tau^L$ is analogous to the point source $\Delta\tau$ and is specified using the same criteria. It can be interpreted as the time it takes for the rupture to propagate along a fault segment ΔL ($\Delta\tau^L=\Delta L/|(v^\theta,v^\delta)|$). w_k, the weight of each trapezoid, represents the relative moment of each fault segment.

This source model is a generalization of the Haskell model. The v^θ term may dominate for large shallow events, where faulting is usually confined to a narrow zone within the brittle layers of the upper crust. In this case $\Delta\tau_i$ simplifies to:

$$\Delta\tau_i = \Delta\tau' = \Delta\tau^L[1 - v^\theta p\cos(\phi-\theta)]. \qquad (A20)$$

The effect of the horizontal component of rupture is very easy to incorporate in the synthetic seismogram, because its effect on all up- and down-going waves is the same. Note also that if the rupture velocity is zero, and we set $\Delta\tau^L = \Delta\tau^R = \Delta\tau$, we obtain the triangular function $T_{\Delta\tau}$ which was used as a time function element for the point source.

When dealing with a large complex source, a single set of the parameters described above may not be sufficient for its characterization. A subdivision into smaller subevents of different depths and mechanisms may be required. Displacement due to a multiple source with n_e subevents is given by

$$s(t) = \sum_{e=1}^{n_e} s_e(t-\Delta t_e) \qquad (A21)$$

where $s_e(t)$, the displacement due to a subevent e, is calculated by the procedures outlined in this appendix; Δt_e is the time delay of the subevent relative to the origin time of the first event.

APPENDIX B

MAXIMUM LIKELIHOOD INVERSION OF WAVEFORMS

In Appendix A I described a procedure for calculating waveforms of teleseismic body waves due to a source in a layered medium. In the usual application, the goal is to recover information about the source contained in the observed waveforms by matching them with the synthetics. The presence of noise, uncertainty in the properties of the medium and various approximations of the source preclude a perfect match. A compromise solution to this problem can be obtained by minimization of some objective function which describes the mismatch between the observed and the synthetic seismograms. A reasonable function for this purpose is the sum of squares of residuals. Because the synthetics are a nonlinear function of the source parameters, the minimization is usually achieved iteratively, with adjustments at each step based on a linearized model. In practice, it is natural to give less weight to data contaminated by noise, and similarly, to allow only small changes in model parameters about which we have some *a priori* knowledge, while allowing larger changes in poorly known parameters. Such weighting and constraints should result in a more stable and more meaningful estimate of the source model parameters.

Ideally, both data and model parameters can be treated as statistical variables, with some expected value and associated uncertainty expressed by the covariance. If the data $\underline{d}$ (an array of all digitized seismogram amplitudes) and the model parameters $\underline{p}$ (an array of the source parameters) follow a normal distribution, the joint likelihood of the data $\underline{d}$ being matched by the model $\underline{m}(\underline{p})$ (an array of all synthetic seismogram amplitudes) and of observing the *a priori* model parameter estimates $\underline{p}_o$ is

$$L_p(\underline{d},\underline{p}_o) \sim e^{-1/2\chi^2} \tag{B1}$$

where the exponent is given by

$$\chi^2 = [\underline{d} - \underline{m}(\underline{p})]^T \underline{C}_{d_o}^{-1} [\underline{d} - \underline{m}(\underline{p})] + [\underline{p}_o - \underline{p}]^T \underline{C}_{p_o}^{-1} [\underline{p}_o - \underline{p}]$$

and $\underline{C}_{d_o}$ and $\underline{C}_{p_o}$ are the *a priori* estimates of the covariance of the data and parameters, respectively. The uncertainties in $\underline{d}$ and $\underline{p}_o$ are assumed to be independent.

The best *a posteriori* estimate of the parameters ($\hat{\underline{p}}$) is the one for which the likelihood is maximum, or equivalently, for which χ^2 is minimum. At the minimum

$$\frac{\delta \chi^2}{\delta p_i} = 0 \tag{B2}$$

and consequently,

$$[\underline{d} - \underline{m}(\hat{\underline{p}})]^T \underline{C}_{d_o}^{-1} \underline{J}(\hat{\underline{p}}) + [\underline{p}_o - \hat{\underline{p}}]^T \underline{C}_{p_o}^{-1} = 0 \tag{B3}$$

where $\underline{J}$ is a matrix of partial derivatives $J_{ij} = \partial m_i / \partial p_j$. Because $\underline{m}(\hat{\underline{p}})$ is nonlinear, we solve this equation for $\hat{\underline{p}}$ iteratively using a linear approximation ($\underline{m}(\hat{\underline{p}}) = \underline{m}(\underline{p}) + \underline{J}^T(\hat{\underline{p}} - \underline{p}) + \ldots$). The improvement to $\hat{\underline{p}}$ from the k'th to k+1'th iteration is given by

$$\hat{\underline{p}}_{k+1} = \underline{p}_k + (\underline{J}_k^T \underline{C}_{d_o}^{-1} \underline{J}_k + \underline{C}_{p_o}^{-1})^{-1} \{\underline{J}_k^T \underline{C}_{d_o}^{-1} [\underline{d} - \underline{m}(\underline{p}_k)] + \underline{C}_{p_o}^{-1} (\underline{p}_o - \underline{p}_k)\} \tag{B4}$$

Various forms of this relation have been presented in the geophysical literature, e.g. Jackson [1979], Aki and Richards [1980], and Tarantola and Valette [1982].

If the problem is not strongly nonlinear, the *a posteriori* parameter covariance is given by [Jackson, 1979]

$$\underline{C}_p = (\underline{J}^T \underline{C}_{d_o}^{-1} \underline{J} + \underline{C}_{p_o}^{-1})^{-1} \tag{B5}$$

When we have no a priori knowledge about the parameter variance, we have to assume $\underline{C}_{p_o} = \sigma_p^2 \underline{I}$, where $\sigma_p^2 \to \infty$. For an overdetermined problem equation (B4) then reduces to:

$$\hat{\underline{p}}_{k+1} = \underline{p}_k + (\underline{J}_k^T \underline{C}_{d_o}^{-1} \underline{J}_k)^{-1} \underline{J}_k^T \underline{C}_{d_o}^{-1} [\underline{d} - \underline{m}(\underline{p}_k)] \tag{B6}$$

which is the classical nonlinear maximum likelihood solution. The a posteriori parameter covariance is then expressed as

$$\underline{C}_p = (\underline{J}^T \underline{C}_{d_o}^{-1} \underline{J})^{-1}. \tag{B7}$$

If the a priori data variances $\underline{C}_{d_o}$ are relative, rather than absolute, the a posteriori estimate of data variance can be obtained from

$$\underline{C}_d = \sigma_d^2 \underline{C}_{d_o}$$

with (B8)

$$\sigma_d^2 = [\underline{d} - \underline{m}(\hat{\underline{p}})]^T \underline{C}_{d_o}^{-1} [\underline{d} - \underline{m}(\hat{\underline{p}})]/(n_d - n_p)$$

where n_d is the number of data points and n_p the number of free model parameters. Then

$$\underline{C}_p = (\underline{J}^T \underline{C}_d^{-1} \underline{J})^{-1} = \sigma_d^2 (\underline{J}^T \underline{C}_{d_o}^{-1} \underline{J})^{-1}. \tag{B9}$$

From equations B4-B7 we see that the size of each iteration step is controlled by the a posteriori variance of each parameter at a given step. In order to avoid wild iteration steps, in practice, it is useful to introduce additional damping factor $\varepsilon \underline{D}_{p_o}$ in which ε is gradually reduced to zero upon approaching convergence to the solution, i.e.

$$\hat{\underline{p}}_{k+1} = \underline{p}_k + (\underline{J}_k^T \underline{C}_{d_o}^{-1} \underline{J}_k + \underline{C}_{p_o}^{-1} + \varepsilon \underline{D}_{p_o})^{-1} \{\underline{J}_k^T \underline{C}_{d_o}^{-1} [\underline{d} - \underline{m}(\underline{p}_k)] + \underline{C}_{p_o}^{-1} (\underline{p}_o - \underline{p}_k)\} \tag{B10}$$

Such damping is usually necessary when the a priori variance of the model parameters is large.

In this study, the unknown source parameters are the mechanism ($\hat{M}_{ij}$ or strike, dip, and rake), moment-tensor norm or scalar seismic moment, depth, relative weights of the triangle functions comprising the source time function and coordinates of the source centroid relative to the nucleation point. In the case of a multiple event, in addition to this set of parameters for each subevent, we also need to determine their time separation. The partial derivatives of the synthetic seismograms with respect to the source parameters comprising the matrix $\underline{\underline{J}}$ are obtained by differentiation of the equations (A15) and (A21) of Appendix A.

For a source in a given crustal layer, the partial derivatives with respect to the components of the source mechanism Θ are:

$$\frac{\partial s}{\partial \Theta} = M_n \sum_{k=1}^{n} \sum_{i=1}^{m} w_k \, H_i[t-\tau_k-(\eta_i-\eta_1)d+\bar{\eta}_1\zeta+p\rho\cos(\phi-\psi)] \, \frac{\partial r_i}{\partial \Theta} \qquad \text{(B11)}$$

$$\Theta = \hat{M}_{ab} \quad \text{or} \quad \theta, \delta, \lambda,$$

with respect to the weight of an element j of the source time function:

$$\frac{\partial s}{\partial w_j} = M_n \sum_{i=1}^{m} H_i[t-\tau_j-(\eta_i-\eta_1)d+\bar{\eta}_1\zeta+p\rho\cos(\phi-\psi)] \, r_i, \qquad \text{(B12)}$$

with respect to the depth:

$$\frac{\partial s}{\partial d} = M_n \sum_{k=1}^{n} \sum_{i=2}^{m} (\eta_1-\eta_i) w_k \, \frac{\partial H_i[t-\tau_k-(\eta_i-\eta_1)d+\bar{\eta}_1\zeta+p\rho\cos(\phi-\psi)]}{\partial t} \, r_i \qquad \text{(B13)}$$

and with respect to the relative centroid location coordinates:

$$\frac{\partial s}{\partial \rho/\rho} = p\rho\cos(\phi-\psi)\,\frac{\partial s}{\partial t}\,, \tag{B14}$$

$$\frac{\partial s}{\partial \psi} = p\rho\sin(\phi-\psi)\,\frac{\partial s}{\partial t}\,, \tag{B15}$$

$$\frac{\partial s}{\partial \zeta} = \eta_1\,\frac{\partial s}{\partial t}\,. \tag{B16}$$

For a multiple source we also need partial derivatives, with respect to the time delay of a subevent e:

$$\frac{\partial s}{\partial \Delta t_e} = -\frac{\partial s_e}{\partial t}. \tag{B17}$$

All these partial derivatives are determined analytically except for the time derivatives, which are obtained by finite differences (e.g. $\partial H_i(t)/\partial t = [H_i(t+\Delta t)-H_i(t-\Delta t)]/2\Delta t$, Δt being the digitizing interval). Note that all the partial derivatives are simple functions of the elementary seismograms H_i. The moment-tensor norm or scalar moment need not be explicitly included in the inversion, since it provides only a linear scaling for the seismograms which can be absorbed in the source time function or $\hat{M}_{ij}$ and recovered when the time function or $\hat{M}_{ij}$ are renormalized.

APPENDIX C

DETERMINATION OF TELESEISMIC BODY WAVE RADIATION USING RECIPROCITY

For a bounded medium with homogeneous boundary conditions and elastic properties obeying Hooke's Law, the reciprocity theorem can be stated as follows [White, 1960]:

> "If a transient force F(t) applied in some particular direction α at some point P creates at a second point Q a transient displacement whose component in some direction β is u(t), then the application of the same force F(t) at point Q in the direction β will cause a displacement at point P whose component in the direction α is u(t)" (i.e., $g_{ij}(P,Q) = g_{ji}(Q,P)$).

This useful theorem, as stated here, is a special case of Betti's theorem [Betti, 1872] and was introduced to seismology by Knopoff and Gangi [1959].

theorem not only saves us from double work if the solution to the reciprocal problem is known, but in many cases it can lead to a much simpler derivation of the solution; although the direct and reciprocal solutions are equivalent, the reciprocal problem can be easier to solve, and this possibility should be always investigated.

The determination of body wave radiation from a shallow source to a point deep in a halfspace is a nice example of when the reciprocal problem is almost trivial compared to the direct problem. Formulated in this fashion, the solution for a source in a homogeneous halfspace was obtained by Gupta [1967] and for a source in a layered crust by Bouchon [1976].

Our goal is to determine the displacement at a point Q deep in the homogeneous halfspace (mantle) in the time windows of the P and S wave arrival generated by horizontal and vertical unit point force impulse

acting at a point P in a crustal or upper mantle layer (Figure C.1). We are interested in the high frequency solution.

In the direct approach, from all energy generated by the source, we would have to identify and extract that portion which contributes significantly to the body wave signal in the halfspace and determine the effect of the interaction of the curved wavefronts with the horizontal crustal layers. After such analysis, we would conclude that the teleseismic body wave seismogram can be constructed simply by using geometrical ray theory (assuming all waves are homogeneous), but that the plane wave reflection and transmission coefficients must be multiplied by the ratio of apparent vertical slownesses of the parent and daughter waves, in order to account for the discontinuous geometrical spreading of the curved wavefronts at each crustal interface [Spencer, 1960; Langston and Helmberger, 1975].

The reciprocal configuration of this problem is to consider a unit impulse point force acting at point Q deep in the halfspace and to observe the horizontal and vertical displacements at the position of the true source (point P), within the crust (Figure C.1). For reciprocity to hold, the point force in the halfspace must act in the direction of the desired response, i.e., in the radial direction for P waves and in the appropriate transverse direction for SV and SH waves. For a force deep in the halfspace, the wave incident at the bottom of the crust is essentially a plane wave with an angle of incidence θ ($\theta = \sin^{-1} pv$, where v is α or β depending on whether P or S waves are being studied). For the radial force, the incident wave is a P wave with amplitude $\frac{1}{4\pi\rho\alpha^2 r}$, while for transverse force, the incident wave is an S wave of amplitude $\frac{1}{4\pi\rho\beta^2 r}$. Displacement within a stack of layers in response to an incident plane wave

can be easily obtained either by geometrical ray theory or propagator. Notice no correction for curved wavefronts is required, nor must we go through a whole series of approximations and risk an error in order to derive the solution. The only assumption made was that the reciprocal source is far enough from the crustal interface that the incident waves can be treated as plane waves.

The question naturally arises of why the direct approach requires a correction to the plane wave transmission and reflection coefficients whereas the reciprocal approach does not. Since both solutions are correct, where is this factor hiding in the reciprocal solution? Obviously, it must be hidden in the reflection and transmission coefficients which are reciprocal to those in the direct problem. For example, if in the direct problem a ray undergoes an S to P conversion upon reflection at some interface, in the reciprocal problem the equivalent ray undergoes P to S conversion at the same interface; the ratio between these two reflection coefficients contains the missing geometrical spreading correction factor.

To illustrate the reciprocal approach, we look at the problem of P waves from a horizontal point force in a homogeneous halfspace. The direct wave from the reciprocal source will arrive at point P with the delay r/α, and the horizontal component of its displacement will be $\frac{\sin\theta}{4\pi\rho\alpha^2 r}$. The P and SV reflections from the free surface will arrive at the same point with additional delay of $2h\eta_\alpha$ and $h(\eta_\alpha+\eta_\beta)$, and the horizontal component of their displacement will be $\frac{\sin\theta}{4\pi\rho\alpha^2 r}\Pi^{PP}$ and $\frac{\cos\theta'}{4\pi\rho\alpha^2 r}\Pi^{PS}$, respectively. The complete Green's function is therefore

$$\frac{1}{4\pi\rho\alpha^2 r}\left[\sin\theta\,\delta(t-r/\alpha) + \sin\theta\,\Pi^{PP}\delta(t-2h\eta_\alpha-r/\alpha) + \cos\theta'\,\Pi^{PS}\delta(t-h(\eta_\alpha+\eta_\beta)-r/\alpha)\right].$$

This is identical to:

$$\frac{1}{4\pi\rho\alpha^2 r}\left[\sin\theta\,\delta(t-r/\alpha) + \sin\theta\,\Pi^{PP}\delta(t-2h\eta_\alpha-r/\alpha) + \cos\theta'\frac{\alpha^2}{\beta^2}\frac{\eta_\alpha}{\eta_\beta}\Pi^{SP}\delta(t-h(\eta_\alpha+\eta_\beta)-r/\alpha)\right]$$

that one would obtain after a rather lengthy analysis using the direct approach [Langston and Helmberger, 1975].

FIGURE CAPTION

Figure C.1 Problem configuration related to Appendix C (adopted from Bouchon [1976]).

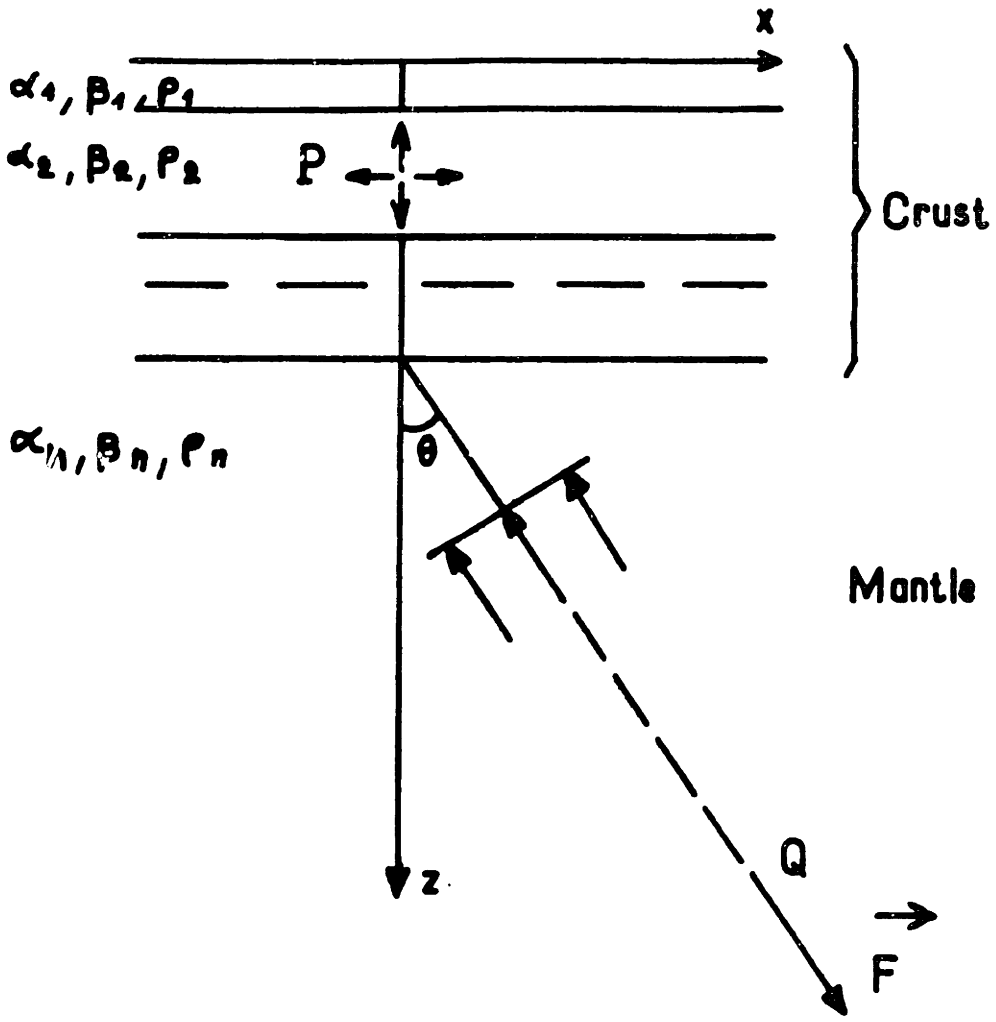
x
$\alpha_1, \beta_1, \rho_1$
$\alpha_2, \beta_2, \rho_2$
P
Crust
$\alpha_n, \beta_n, \rho_n$
θ
Mantle
z
Q
F

Figure C.1

APPENDIX D

COMPUTATION OF THE BODY WAVE GREEN'S FUNCTION USING PROPAGATOR MATRICES

In this thesis the Green's functions are calculated in the frequency domain using propagator matrices and the reciprocity theorem as outlined by Bouchon [1976] (Appendix C). The incident P-wave potential at the bottom of the crustal layers from a radial force impulse in the half-space is $\frac{-i}{4\pi\rho_n\alpha_n\omega r}$; similarly, the SV-wave potential from a transverse force impulse is $\frac{i}{4\pi\rho_n\beta_n\omega r}$, where ρ_n, α_n, and β_n are the density and compressional and shear velocity in the half-space and r is the distance to the source. The compressional and shear potentials in a layer ℓ of the crust excited by these waves are

$$\begin{aligned}\phi(x,d,\omega) &= [A(\omega)\exp(-i\eta_\alpha\omega d) + B(\omega)\exp(i\eta_\alpha\omega d)]\exp[i\omega(t+px)]\\ \psi(x,d,\omega) &= [C(\omega)\exp(-i\eta_\beta\omega d) + D(\omega)\exp(i\eta_\beta\omega d)]\exp[i\omega(t+px)]\end{aligned} \tag{D.1}$$

where d is the depth of the receiver measured from the interface above, η's are the vertical slownesses and p is the horizontal slowness (ray parameter) of the waves. A, B, C, and D are obtained by standard propagator matrix procedures [Haskell, 1953]. The horizontal and vertical displacements, u and w, are given by

$$\begin{aligned}u &= \phi_{,x} - \psi_{,z}\\ w &= \phi_{,z} + \psi_{,x}\end{aligned} \tag{D.2}$$

The $g_{ik} = g_{ik}^{P\downarrow} + g_{ik}^{P\uparrow} + g_{ik}^{S\downarrow} + g_{ik}^{S\uparrow}$ for the direct problem with a source at d=0 and x=0 is therefore determined by the following expressions

$$
\begin{aligned}
g_{i1}^{P\downarrow}(\omega) &= i\omega p A(\omega) & g_{i1}^{P\uparrow}(\omega) &= i\omega p B(\omega) \\
g_{i1}^{S\downarrow}(\omega) &= i\eta_\beta \omega C(\omega) & g_{i1}^{S\uparrow}(\omega) &= -i\eta_\beta \omega D(\omega) \\
g_{i3}^{P\downarrow}(\omega) &= -i\omega \eta_\alpha A(\omega) & g_{i3}^{P\uparrow}(\omega) &= i\omega \eta_\alpha B(\omega) \\
g_{i3}^{S\downarrow}(\omega) &= i\omega p C(\omega) & g_{i3}^{S\uparrow}(\omega) &= i\omega p D(\omega)
\end{aligned}
\tag{D.3}
$$

It is useful to define

$$
\begin{aligned}
h^{P\downarrow}(\omega) &= i\omega A(\omega) & h^{P\uparrow}(\omega) &= i\omega B(\omega) \\
h^{SV\downarrow}(\omega) &= i\omega C(\omega) & h^{SV\uparrow}(\omega) &= i\omega D(\omega)
\end{aligned}
\tag{D.4}
$$

which are recognized as the responses of the layered crust to a pure point P and a pure point SV source located just below the upper boundary of the source layer. A set of these functions for each crustal layer is found simultaneously in the Thomson-Haskell procedure and stored. They are the principal part of the elementary seismograms $H_1(t)$ defined in Appendix A. The expressions for the SH waves are obtained in an analogous fashion. Note, the function g_{ki} here is the same as g_{ki}^{s} in Appendix A. Similarly, $I_1(\omega) = h_1(\omega)C^R(\omega)M(\omega)$, where $\underline{h} = (h^{P\downarrow}, h^{P\uparrow}, h^{SV\downarrow}, h^{SV\uparrow})$.

APPENDIX E

COORDINATE CONVENTIONS

Coordinate conventions of Aki and Richards [1980] are used throughout this thesis. The conventions are illustrated in the following figures.

Figure E.1 The fault-plane parameter convensions. The slip-direction is defined by the motion of the hanging wall of the fault.

Figure E.2 Various equivalent notations.

Figure E.3 The centroid location in terms of two coordinate systems.

Figure E.4 The crustal layer convention and the reference points from which the source depth is measured.

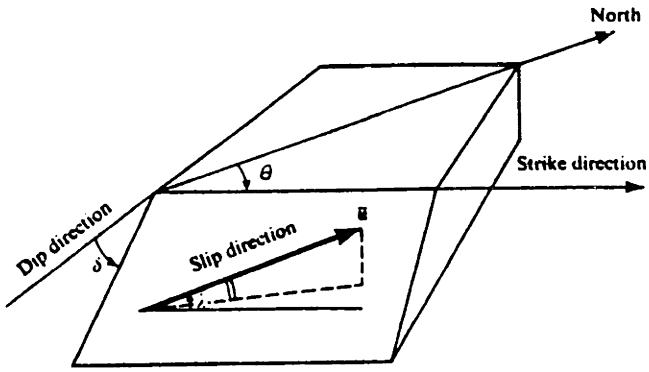

Definition of the fault-orientation parameters (strike θ, dip δ), and slip-direction. θ is measured clockwise round from north, with the fault dipping down to the right of the strike direction: $0 \leq \theta < 2\pi$. δ is measured down from the horizontal: $0 \leq \delta \leq \pi/2$.

Figure E.1

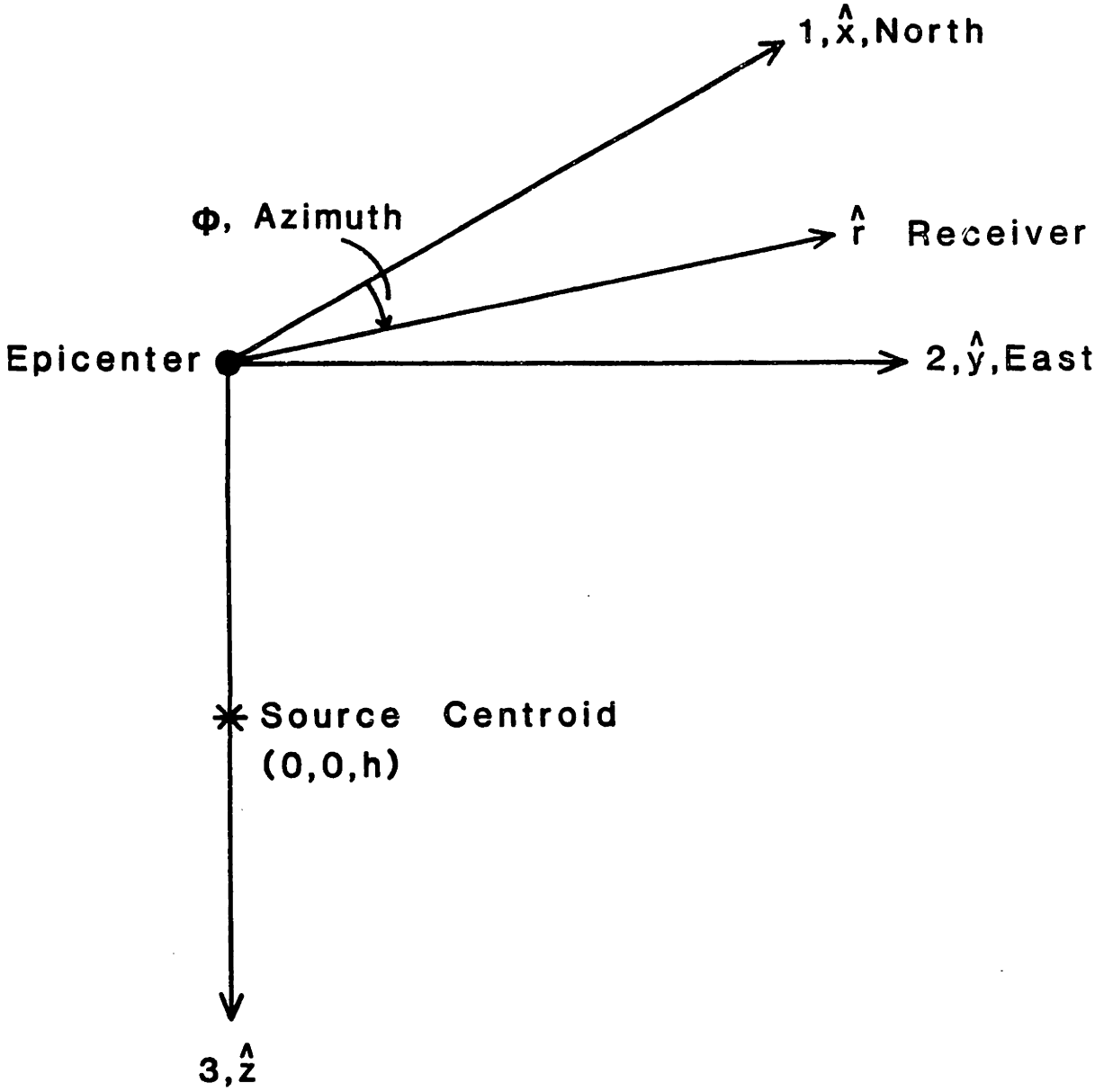
1, x̂, North
Φ, Azimuth
r̂ Receiver
Epicenter
2, ŷ, East
Source Centroid
(0,0,h)
3, ẑ

Figure E.2

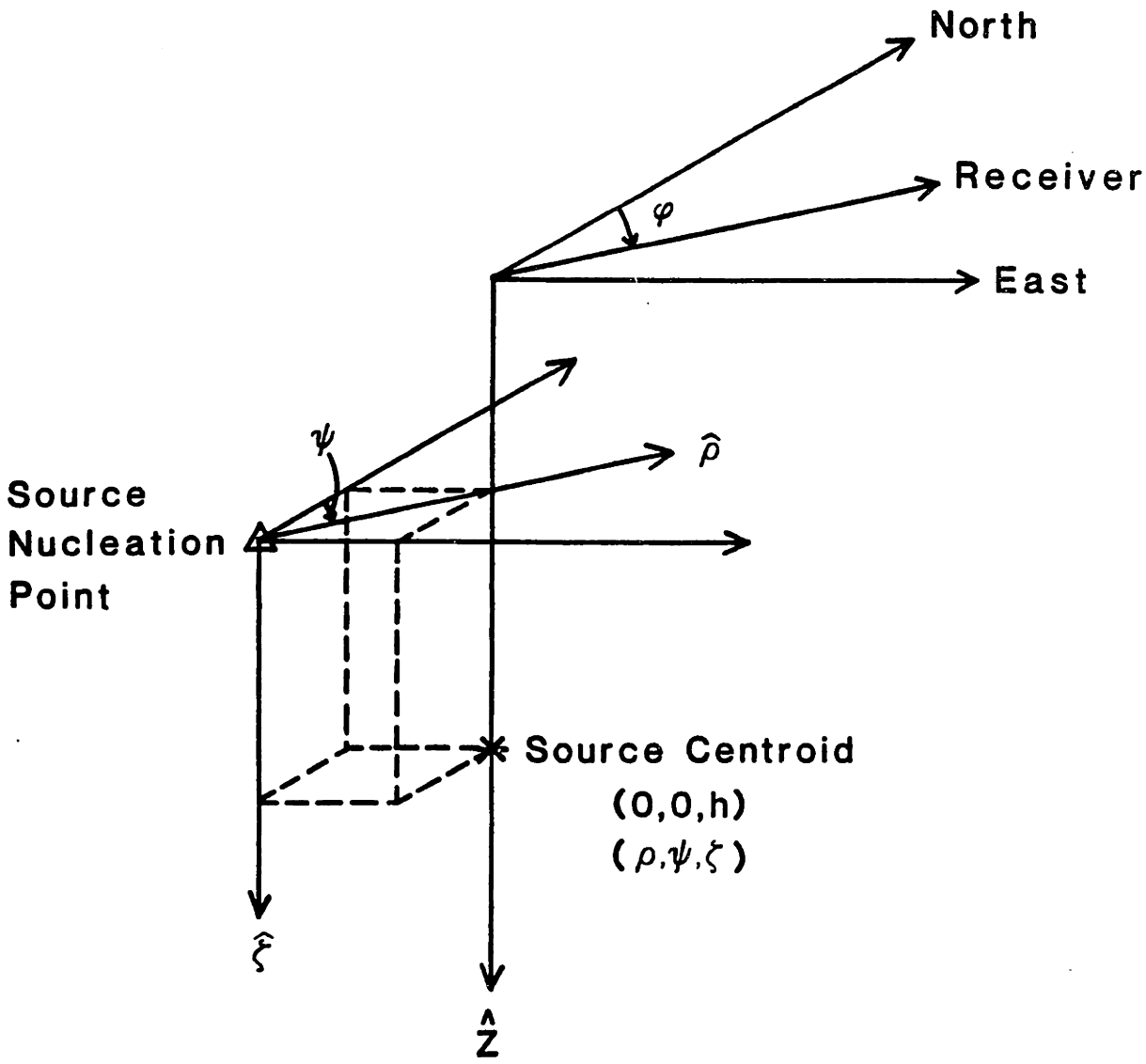
North
Receiver
East
φ
ψ
ρ̂
Source
Nucleation
Point
Source Centroid
(0,0,h)
(ρ,ψ,ζ)
ζ̂
Ẑ

Figure E.3

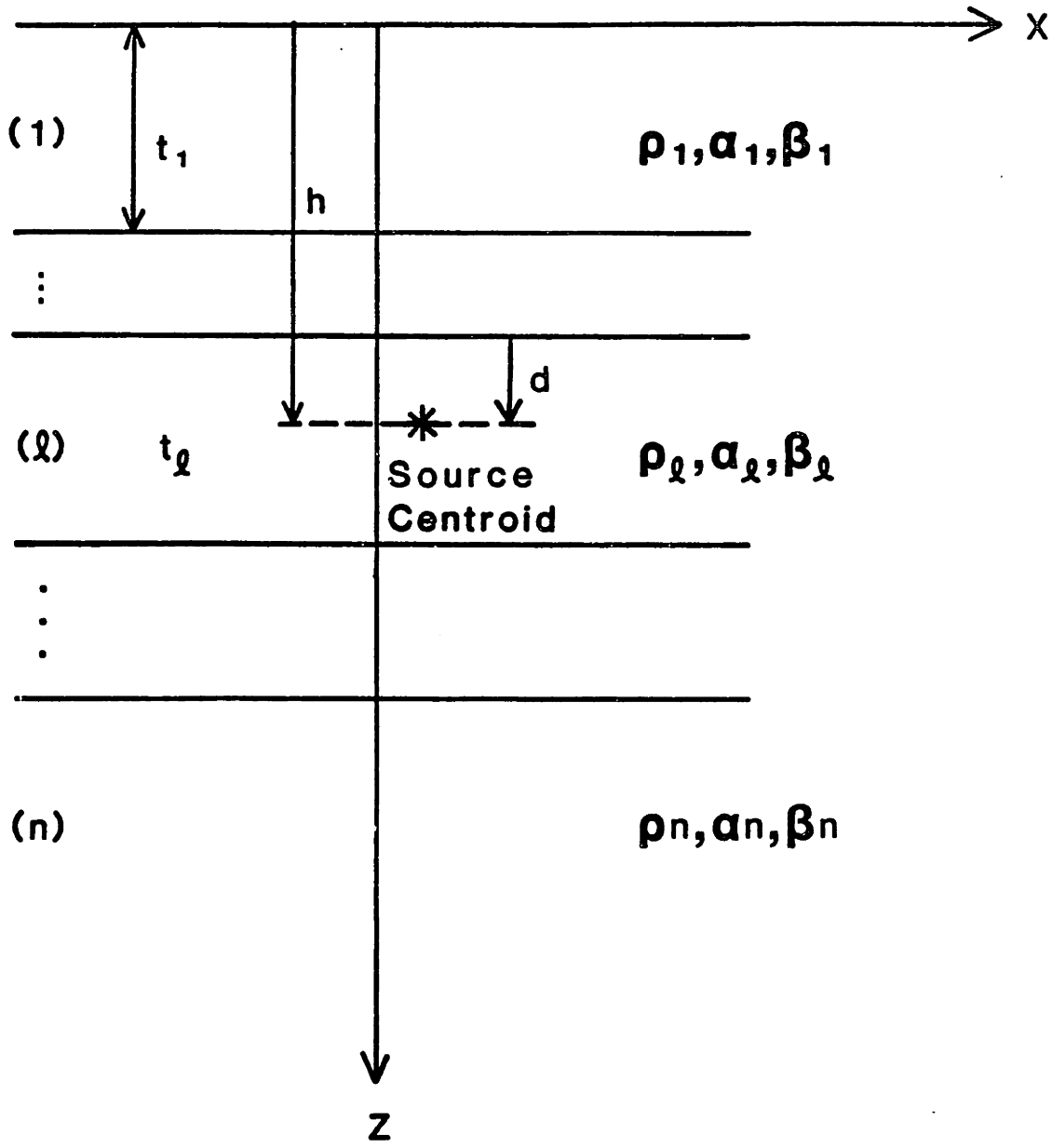
X
(1)
t_1
h
ρ_1,α_1,β_1
d
(ℓ)
t_ℓ
Source
Centroid
$\rho_\ell,\alpha_\ell,\beta_\ell$
(n)
ρ_n,α_n,β_n
Z

Figure E.4

APPENDIX F

THE GEOMETRY OF BACKARC THRUSTING ALONG THE EASTERN SUNDA ARC, INDONESIA: CONSTRAINTS FROM EARTHQUAKE AND GRAVITY DATA†

Abstract. The Flores earthquake of December 23, 1978 represents the first seismological evidence for active backarc thrusting behind the eastern Sunda Arc. This m_b=5.8 earthquake occurred north of Flores Island where seismic reflection profiling has revealed backarc thrusting - apparently a reaction to compression of the arc following collision with the Australian continent. We investigate the source mechanism and depth of the Flores earthquake by inversion of long period P waveforms and relocate the earthquake's epicenter incorporating arrival time data from local stations. We find that this event occurred about 20 - 30 km south of the thrust zone north of Flores at a depth of 11 km (7 km below the sea floor). The best fit fault plane solution is consistent with active southward thrusting of the floor of the Flores Basin beneath the volcanic arc along a shallow 30° dipping fault plane. The morphology of the thrust zone and the free-air gravity profile over the Flores Basin in the epicentral region resembles those of oceanic trenches suggesting that thrusting is confined to a single plane. The observed gravity gradient indicates that the crust of the Flores Basin dips smoothly below the small accreted wedge at an angle of about 3°. The position of the earthquake hypocenter relative to the Flores Thrust and the fault plane solution suggest that the 1978 earthquake is analogous to subduction zone thrust events representing slip within basement between the subducting and overriding plates. The Flores Thrust is thus the surface expression of a deep seated thrust zone, probably

---

† by Robert McCaffrey and John Nabelek, submitted to J. Geophys. Res.

representing the initial stage of polarity reversal of the eastern Sunda Arc.

INTRODUCTION

One of the consequences of plate motions is the eventual involvement of continents and other non-subductable terrains in convergence zones. A few areas of the world are thought to derive their structural complexity from the attempted subduction of continental crust but the details of the process are far from obvious. Involvement of non-subductable terrains in a convergent boundary may not always result in a large scale deformation as in the continent-continent collision between India and Asia, but is nevertheless likely to trigger changes in the subduction regime.

McKenzie [1969] suggested that attempted subduction of continental lithosphere beneath an oceanic island arc would result in reversal of subduction polarity because of the buoyancy of the continental crust. A likely place for this to have happened in the past is northern New Guinea during the Tertiary [Dewey and Bird, 1970; Johnson and Molnar, 1972; Hamilton, 1979] although reversal is not a necessary interpretation [Johnson and Molnar, 1972; Johnson and Jaques, 1980]. Reversal may also be underway behind the Sangihe arc in the northern Molucca Sea [Silver and Moore, 1978; Stewart and Cohn, 1979; Moore and Silver, 1982] following collision between island arcs. Arc polarity reversal is undoubtedly difficult to identify in the geologic record and thus it is important to study any modern example of where it may possibly be occurring.

Probably the best area to study the incipient subduction of continental material and backarc thrusting is the eastern Sunda Arc where Australia is presently impinging on the subduction zone. South of Timor and around the great bend in the Banda Arc to the north, continental crust

of Australia is found seaward of the Timor Trough (Figure 1) and extends arcward to beneath the trough itself [Jacobson et al., 1978]. Reflection profiles crossing the Australian shelf and the Timor Trough show typical subduction zone morphology and clearly indicate thrusting of Australia beneath the deformed outer arc ridge (which includes Timor) south of the volcanic islands [Jacobson et al., 1978; von der Borch, 1979; Hamilton, 1979; Bowin et al., 1980]. West of Sumba, oceanic lithosphere of the Indian Ocean plate is being consumed at the Java Trench. In the transition zone between the Java Trench and the Timor Trough, the presence of the Scott Plateau, possibly a subsided part of the Australian shelf, and Sumba, possibly a continental fragment caught within the forearc, adds a great deal of complexity to the convergent margin.

Because of the young age of Australia's collision with the eastern Sunda Arc, it has thus far caused only small morphological changes in the subduction system. The available evidence, however, indicates that backarc thrusting has been initiated [Silver et al., 1983; Usna et al., 1979; Hamilton 1979] which, if continued, may result in either reversal of the subduction polarity, thus removing the backarc basin from the surface of the earth, or in crustal thickening by thrusting thereby producing a belt of ophiolites. The present mode of deformation appears to favor the former scenario.

North of the Sunda island arc from western Sumbawa to east of Wetar (Figure 1) (except for a small stretch between east Flores and Alor), seismic reflection profiling has revealed thrusting at the base of the slope of the volcanic pile [Silver et al., 1983; Usna et al., 1979; Hamilton, 1979]. The sense of thrusting is such that oceanic crust of the Flores Basin is being overridden by the volcanic islands. Silver et al.

[1983] estimate the amount of convergence between the Flores Basin and the island arc in the Flores region at 30 - 60 km based on the volume of material accreted to the toe of the volcanic arc. This length is consistent with the amount of northward indentation of this portion of the arc with respect to those portions behind which thrusting is not observed. There is, however, no evidence that this thrust zone is associated with a south dipping zone of intermediate depth earthquakes [Cardwell and Isacks, 1978].

In this paper we describe an m_b = 5.8 earthquake from the thrust zone north of Flores whose fault plane solution constitutes the first seismological evidence to support interpretations that active backarc thrusting occurs behind the Banda Arc. Also, a simple model for the backarc thrust zone is presented based on free-air and Bouguer gravity values and published seismic refraction and reflection profiles. These data suggest that the crust (probably oceanic) of the Flores Basin dips beneath the small backarc accretionary prism at an angle of about 3°. The presence of a large negative (-110 mGal) free-air anomaly over the accreted wedge 30 km south of the thrust zone signifies that the Flores Basin crust is out of isostatic equilibrium and suggests flexure of the underthrusting plate as in more developed subduction zones. The position of the earthquake hypocenter relative to the Flores Thrust and the fault-plane solution indicate that the 1978 earthquake was due to slip between the Flores Basin crust and the overriding island arc.

THE EARTHQUAKE OF DECEMBER 23, 1978

Location

The earthquake of December 23, 1978 together with one foreshock and seven aftershocks were relocated using arrival time data from the regional network of Indonesia and southeast Asia [Hodgson, 1980], from a local network operating on Sulawesi [McCaffrey and Sutardjo, 1982], and from ISC Bulletins. We repicked arrival times for all regional and many of the WWSSN stations. The main shock was located at latitude 8.33°S, longitude 121.34°E (Figure 1) and origin time $05^h10^m50^s$. This epicenter is only 8 km southwest of the ISC reported epicenter. Depth was fixed at 11 km as determined from the body wave analysis discussed below.

The location of the event of December 23 based on arrival time data is about 30 km south of the Flores Thrust near its eastern end (Figure 1). Since the regional structure is oriented east-west, uncertainty in the location due to lateral variations in the velocity structure is probably greater in the north-south direction. Clear P arrivals at stations in central Sumba, western Timor, and southern Sulawesi, however, give strong control on the epicenter. The absence of reported damage on Flores and the presence of strong water reverberations in the P wave seismograms indicate that the earthquake occurred beneath the sea and not beneath Flores Island. Furthermore, the period of the water reverberations requires a water depth of about 4.5 km which implies that the epicenter may have been a few kilometers to the north of that determined from the arrival time data (Figure 1).

The foreshock and aftershocks were relocated relative to the main shock by the method of joint hypocenter determination [Dewey, 1971]. The depths of these events were fixed at 15 km for lack of independent depth

information, but the choice of any depth above 50 km for these events has little effect on the epicentral location. The foreshock and aftershocks appear to have been concentrated to the northeast of the main shock, closer to the eastern termination of the Flores Thrust (Figure 1) as mapped by reflection profiling [Silver et al., 1983]. The apparent northeast trend of the epicenters may be ficticious since the 95% confidence ellipses for most of the relocations are aligned in that direction.

P-wave Analysis

Long-period P waves from the vertical component of ten WWSSN stations were inverted simultaneously for orientation of the double-couple source, depth and source time function. The source time function was parameterized by a series of box-car elements, each 2.0 s in duration (this parameterization is identical to that by Langston [1981]). Data were inverted with two choices for the error function which was minimized in a least squares sense: 1) $o_i - s_i$ and 2) $o_i/(\Sigma o_j^2)^{1/2} - s_i/(\Sigma s_j^2)^{1/2}$, where o_i are the amplitudes of the digitized observed waveforms and s_i are the corresponding synthetic seismogram amplitudes. The summations are carried over the number of data points at a given station. The first error function uses information contained in the amplitude variation between the stations, while the second is sensitive only to the shape of the seismograms at the individual stations. When the second error function is used, seismic moment is determined by matching the original unscaled data in the least squares sense with the source parameters determined during the final iteration. Details of these procedures are described in Nabelek [1984] and are similar to those used by Langston [1981] and Ward [1980], the main difference being that the source depth is also determined in our inversion procedure.

Observed seismograms were digitized at half second intervals and filtered with a highpass filter with cutoff at 0.017 Hz in order to remove the low frequency drift which was observed at some stations. The first 60 points (30 s) from the onset of the direct P wave were used for the analysis. The onset of the P arrival was determined from the short-period seismograms but was allowed to vary by up to 1.5 s if improved cross-correlation between the observed and synthetic waveforms could be found. Because the inversion using a full moment tensor source yielded an almost pure double couple mechanism, the double couple constraint was subsequently applied. The solutions using the moment tensor or constrained double couple source, and both choices of the error function are essentially identical. The solutions are summarized in Table 1. The estimated parameters for the source centroid are: depth 10 - 12 km, strike 105 - 120°, dip 28 - 32°, and rake 105 - 120°. The largest contribution to the total seismic moment comes from the first four elements of the source time function; the rupture duration was therefore about 8 seconds. The seismic moment is 1.5 - 2.2 X 10^{25} dyne-cm, the exact value being mainly sensitive to the estimate of the source depth. Estimates of the uncertainties above are based on formal variances for a given model and on variations in solutions using different error functions and different acceptable crustal models, and are therefore larger than the formal uncertainties given in Table 1. The north dipping nodal plane is clearly the better resolved of the two.

Observed and synthetic seismograms for the best-fit solution are shown in Figure 2. The seismograms are plotted at true amplitude and have been corrected to equal distance (40°) and instrument magnification (×3000).

Also shown are first motion polarities for P waves which were read for many more stations and the uncertainties in the P, T, and B axes. The synthetic seismograms were generated using the source crustal structure shown in Table 2. This structure is based on the seismic refraction profile MSN-13 (Figure 1) of Curray et al. [1977]. The water depth was chosen to fit the period of the reverberations which show up on most of the seismograms. A t* of 1 s was used to account for the anelastic attenuation.

Although the synthetics for the northern stations appear to satisfy the dilatational first motions observed on the short-period instruments (a dilatational direct P is clearly visible on the short-period record at MAT in Figure 3), the synthetic direct P arrivals at these stations are in fact compressional. The first discernable pulse in the long-period records at these stations corresponds to a strong dilatational pP (P wave reflection from the sea floor) which, because of the shallow focus of this event, obscures the direct P arrival. The discrepancy between the short-period first motion data and our model is probably real. The source orientation obtained from the long-period waveforms represents the average over the whole fault area while the first motions (at short periods) represent only the orientation at the nucleation point of the rupture. Some variability in the source orientation is to be expected considering the long duration of rupture (8 s), hence a fault length of at least 20 km. The change in the direction of slip is probably also responsible for the small oscillation observed in the first few seconds of the long-period waveform at KBL (Figure 2) which cannot be accounted for with our point source model.

The complexity of the latter part of the waveforms is mainly due to reverberations within the water column. The period of these reverberations

provides strong constraint on the depth of the water above the hypocenter. For example, if our estimate of the water depth were off by 0.5 km, after one bounce the mismatch in phase between the observed waveforms and the synthetics would be a mere 1.5 s, insignificant in the long period data. After five bounces, however, the phase mismatch would be 7.5 s, which is clearly observable even on the long period records.

The lithospheric slab which dips to the north beneath the epicentral region does not appear to have a strong influence on the observed seismograms, because the matches between the data and the synthetics are generally good. Some of the secondary waveform complexities which are observed in the data but not in the synthetics, however, may be due to structural complexity of the source region. For example, the small oscillation in the initial part of the waveform at KBL, which we discussed above, may be alternatively explained by multipath ray propagation through the high velocity slab of the subducting Indian Ocean plate because the paths of the rays arriving at this station parallel the strike of the slab. Finally, an attempt was made to identify the actual fault plane from the waveform distortion which would be expected from rupture propagating along a finite fault plane, but the results were inconclusive.

STRUCTURE IN THE EPICENTRAL REGION

The Flores earthquake of December 23, 1978, occurred in the region north of Flores where there are large negative free-air gravity anomalies over a small but distinct trench with an associated deformed accretionary prism. The strong correlation between the presence of the backarc trench and free-air gravity lows behind the Sunda Arc suggests that the lows result from depression of the crust of the Flores Basin in the process of underthrusting below the arc [Silver et al., 1983]. The gravity lows are

most strongly developed north of western Flores over the epicentral region of the earthquake described in this paper. Here, free-air gravity values reach below -110 mGal with the minimum centered over the accretionary prism south of the trench rather than over the bathymetric low of the backarc trench. In this section we explore crustal structure in the vicinity of the December 23 earthquake by generating a simple model satisfying seismic refraction data (profile MSN-13 of Curray et al. [1977]), seismic reflection, bathymetric, and free-air gravity data north of Flores [Silver et al., 1983], and Bouguer gravity data on Flores [Geological Research and Development Centre, Indonesia, Annual Report, 1983, in prep.]. Our simplest and preferred model is shown in Figure 4 along with a line drawing interpretation of a seismic reflection profile across the thrust (from Silver et al. [1983]).

In computing the gravity effect of our 2 dimensional model, densities were estimated from seismic velocities obtained from refraction profile MSN-13 and the compressional velocity-density relations of Nafe and Drake [1963] for the sediment layer and of Christensen and Salisbury [1975] for oceanic rocks. The velocity of the lowest layer from profile MSN-13 (7.7 km/s at 14 km depth) falls between the majority of lower crust and upper mantle observations for oceanic basins making it difficult to determine if this velocity represents lower crust or upper mantle. Because the density for oceanic crustal rocks of that velocity is close to our value for the upper mantle [Christensen and Salisbury, 1975] such a distinction need not be made for the purposes of the density model.

The starting model was an isostatically balanced section across the Flores Basin as shown by dash-dotted lines in Figure 4c. The crustal and sediment thicknesses beneath the central Flores Basin were taken from

refraction profile MSN-13 at about km 50 of the profile. The thickness of the oceanic crust was considered constant beneath the basin and assumed to thicken towards the north and south reaching 34 km beneath the coastlines at both edges of the profile. Seafloor topography shows up strongly as short wavelength gravity anomalies suggesting a lack of local compensation. The match in amplitudes between observed and calculated short wavelength anomalies validates our choice of sediment density. In our model we included the effect of the subducted Indian Ocean plate which likely has a long wavelength positive contribution to the gravity field across the profile. The slab geometry we assumed (Figure 4e) is based on seismic zone contours from Cardwell and Isacks [1978] and the density contrast of 0.05 g/cm^3 between the slab and asthenosphere is based on thermal and petrologic considerations by Grow and Bowin [1975]. The computed gravity effect of the subducted Indian Ocean plate is 54 mGal over Flores Island and decreases to 38 mGal over the northern end of the profile, a gradient of only 0.1 mGal/km. By including the slab, the model fits the observed gravity values better over the islands at the ends of the profile than does the isostatically balanced crustal model alone.

Relative to the isostatically balanced model with the effect of the subducted Indain Ocean plate included, there is a low of approximately 70 mGal over the Flores Basin (Figure 4a). The low is centered over the accretionary wedge and suggests that the crust of the Flores Basin dips below the deformed sediments. If the crust of the Flores Basin is of fairly constant thickness, we can compute the dip angle θ from the observed gravity gradient by noting that the gravity gradient is approximately equal to $2\pi G(\rho_m-\rho_s)\tan\theta$ where ρ_m is the mantle density, ρ_s is the density of the sediments overlying the crust, and G is the universal gravitational

constant. This simple relation is better than 4% accurate for $\theta < 5°$. The gradient of the residuals over the northern Flores Basin is approximately 2.0 mGal/km. For a mantle density of 3.3 ±0.1 g/cm^3 and sediment density of 2.3 ±0.1 g/cm^3, the dip angle θ is approximately 3.0 ±0.5°.

It is interesting that the dip angle determined here is similar to that of many subducting plates at trenches in the western Pacific [Watts and Talwani, 1974]. We suggest that the Flores Basin lithosphere behaves as an elastic plate while thrusting beneath the island arc and that the large gravity anomalies are due to bending of the plate in response to vertical forces applied to the underthrust portion of the plate. Because the free-air gravity values are negative almost as far south as the north coast of Flores, the vertical load of the crustal material between Flores Island and the Flores Thrust cannot by itself account for the deflection of the Flores Basin lithosphere. Therefore either underthrusting extends as far south as Flores (approximately 50 km) or the plate's own gravitational instability aids to pull it into the asthenosphere.

A model which produces acceptable fit to the observed data is shown in Figure 4c. In this model, the crust of the Flores Basin beneath the site of refraction profile MSN-13 agrees in general with those results and from this point dips to the south at about 3° reaching a maximum depth of 9.5 km beneath the minimum in the gravity field. This simple structure deviates significantly from the isostatic model only in the dip of the Flores Basin crust and in the geometry of the Moho beneath the north coast of Flores. Both of these changes act to decrease the total mass beneath the south margin of the Flores Sea.

DISCUSSION

The Flores earthquake represents the first seismological evidence that active thrusting occurs behind the Sunda Arc north of Flores. Based on the following evidence, we suggest that the south dipping nodal plane corresponding to the fault plane and that the 1978 event reflects subduction of the Flores Basin under the island arc: (1) the strike of this plane agrees better with the local strike of the Flores Thrust than does the strike of the steeper plane, (2) planar sediments of the Flores Basin are observed to dip southward below the deformed accreted wedge (Figure 4d), and (3) gravity evidence suggests that the Flores Basin crust dips toward and under the deformed sediments south of the thrust zone and therefore implies a southside-up sense of relative motion.

The south dipping nodal plane dips to the SSW at about 30°. This angle is significantly steeper than the 3° dip of the Flores Basin crust beneath the accreted wedge determined from gravity data or the 6° dip of planar sediments into the thrust zone observed in the reflection profile of Figure 4d. Similarly, along the Philippine Trench, Cardwell et al. [1980] found the dip of the seismic zone defined by earthquake hypocenters and fault planes from shallow thrust events to be 24 ± 10° in the north to 45 ± 15° in the south although the events examined occurred only 50-100 km landward of the trench. The Philippine Trench is associated with a seismic zone extending to only 150 km depth and is not associated with active volcanism; it is therefore thought to be quite young [Cardwell et al., 1980].

In Figure 5 we present three alternative models of the Flores backarc thrust zone. The first (Figure 5a) is the subduction model which is the most consistent with all available evidence. In this model the Flores

Basin lithosphere thrusts smoothly beneath northern Flores and the Flores earthquake represents slip between the two rigid plates. Sediments are detached from the downgoing plate along a shallow dipping decollement which crops out at the Flores Thrust. About 40 km of shortening is represented in Figure 5a. The projections of the Philippine and the New Hebrides seismic zones [Cardwell et al., 1980] are shown for comparison and indicate that the slip angle and position of the Flores earthquake with respect to the trench are consistent with the subduction interpretation within the limits imposed by observations in other parts of the world.

Figure 5b shows an imbricate thrust model in which shortening is taken up along a series of south dipping faults in basement. These faults may be shallow dipping within basement as suggested by the Flores earthquake and steepen within the sedimentary section to produce the nearly vertical faults observed in the reflection profile (Figure 4d). Contrary to the previous case, closure of the Flores Basin in this fashion would leave its mark in the geologic record as an ophiolite belt sandwiched between two volcanic belts (Flores and Sulawesi). An argument against this model is the presence of a gravity low over the deformed ridge south of the Flores Thrust. If crustal thrust sheets were part of the accreted material and causing flexure of the Flores Basin crust, they would be associated with a gravity high, being dynamically supported by the plate's flexural strength.

The final and least likely model (Figure 5c) is based on the assumption that the north dipping P wave nodal plane is the fault plane. This implies that Flores thrusts beneath the Flores Basin along steeply dipping reverse faults. We consider this possibility highly unlikely because buoyancy forces at the contact between the different crustal types

would tend to push the less dense island arc crust out over the oceanic crust when external horizontal compressive forces are applied. Also, the seismic reflection profile in Figure 4d clearly shows planar sediments from the north side dipping below the accreted wedge.

Silver et al. [1983] discuss the relative importance of possible driving mechanisms and present arguments in favor of continent collision as the primary driving force in the development of backarc thrusting behind the eastern Sunda Arc. The slip vector for the December 23 earthquake (Figure 2) also suggests that collision may be a major driving force as it is essentially the same as the direction of relative plate motion between Australia and Southeast Asia (azimuth 0°) determined by Cardwell et al. [1981] for the region east of western Java.

The Australian continent has not, however, impinged on the subduction zone south of Flores. The region is complicated by the presence of the Scott Plateau (a continental block) south of the trench and the (possibly continental) Sumba block in the forearc. Although it lies on strike with the deformed outer arc ridge, Sumba remains undeformed, having undergone only uplift. The northward indentation of the Sunda Arc north of Sumba and its strong correlation with the extent of backarc thrusting is an indication that Sumba plays a key role in the mechanism of the collision. Sumba is probably underlain by thick crust which may act as a stress guide between the subducting Indian Ocean plate and the island arc.

Another possibility is that the subducted part of the Indian Ocean lithosphere is at present detaching from the surface plate at the Java Trench south of Sumba. This section of the Java Trench experiences an unusually large number of normal faulting earthquakes, including the 1977 (M_s=7.9) event. Detachment of the slab would remove a potentially large

vertical pull on the surface plate allowing it to thrust at a shallower angle thereby increasing the coupling between the upper and lower plates.

Although it is not possible at present to say with much confidence whether the observed incipient thrusting is or will eventually become a self-sustaining subduction system in the sense that the negative buoyancy of the lithospheric mantle overtakes forces resisting subduction (i.e. buoyancy of the crust, friction on the thrust surface, and resistance to bending), we suggest that the conditions behind the eastern Sunda Arc are favorable for this to occur. Because the arc is still volcanically active, the lithosphere is probably fairly warm and weak, offering diminished frictional resistance to thrusting. In addition, volcanic activity causes high sedimentation rates behind the arc and plate deflection will be infilled by sediments (see Figure 4). Infilling with the higher density sediments rather than water decreases the restoring force when the plate is bent by about a factor of about 2. Although little oceanic crust exists north of Flores to feed the newly developing subduction system, further east the Banda Sea contains several hundred kilometers of oceanic crust which may be subducted southward beneath the Banda Arc constituting a true arc polarity reversal.

Acknowledgements. We thank E.A. Silver and M. Untung for allowing us to use their gravity data. We also thank Anne Trehu and Eli Silver for valuable comments and criticisms. This work was supported by N.S.F. Grant EAR-8115909 and by the Advanced Research Projects Agency of the Department of Defense, monitored by the Air Force Office of Scientific Research under grant F 49620-82-K-0004.

REFERENCES

Bowin, C.O., G.M. Purdy, C. Johnston, G.G. Shor, L. Lawver, H.M.S. Hartono, and P. Jezek, Arc-continent collision in the Banda Sea region, Am. Assoc. of Petroleum Geol. Bull., 64, 868-915, 1980.

Cardwell, R.K. and B.L. Isacks, Geometry of subducted lithosphere beneath the Banda Sea in eastern Indonesia from seismicity and fault plane solutions, J. Geophys. Res., 83, 2825-2838, 1978.

Cardwell, R.K., B.L. Isacks and D.E. Karig, The spatial distribution of earthquakes, focal mechanism solutions and plate boundaries in the Philippine and northeastern Indonesian Islands, In: The Tectonic and Geologic Evolution of Southeast Asian Sea and Islands, Geophys. Monogr., vol. 23, (D.E. Hayes, ed.), 1-36, AGU, Washington, D.C., 1980.

Cardwell, R.K., E.S. Kappel, M.S. Lawrence and B.L Isacks, Plate convergence along the Indonesian arc (abstract), EOS, 62, 404, 1981.

Christensen, N.I. and M.H. Salisbury, Structure and constitution of the lower oceanic crust, Rev. Geophys. Space Phys., 13, 57-86, 1975.

Curray, J.R., G.G. Shor, R.W. Raitt and M. Henry, Seismic refraction and reflection studies of crustal structure of the eastern Sunda and western Banda arcs, J. Geophys. Res., 82, 2479-2489, 1977.

Dewey, J.F. and J.M. Bird, Mountain belts and the new global tectonics, J. Geophys. Res., 75, 2625-2647, 1970.

Dewey, J.W., Seismicity studies with the method of joint hypocenter determination, Ph.D. Thesis, U.C. Berkeley, 124 pp., 1971.

Grow, J.A. and C.O. Bowin, Evidence for high-density crust and mantle beneath the Chile Trench due to descending lithosphere, J. Geophys. Res., 80, 1449-1458, 1975.

Hamilton, W., Tectonics of the Indonesian region, U.S. Geol. Surv. Prof. Paper 1078, 345 pp., 1979.

Hodgson, J.H., A short-period seismograph network in southeast Asia, Bull. Seismol. Soc. Am., 70, 385-392, 1980.

Jacobson, R.S., G.G. Shor, R.M. Kieckhefer and G.M. Purdy, Seismic refraction and reflection studies in the Timor-Aru trough system and Australian continental shelf, AAPG Memoir 29, 209-222, 1979.

Johnson, R.W. and A.L. Jaques, Continent-arc collision and reversal of arc polarity: New interpretation from a critical area, Tectonophysics, 63, 111, 1980.

Johnson, T., and P. Molnar, Focal mechanisms and plate tectonics of the southwest Pacific, J. Geophys. Res., 77, 5000-5032, 1972.

Langston, C.A., Source inversion of seismic waveforms: The Koyna, India, earthquakes of 13 September 1967, Bull. Seismol. Soc. Am., 71, 1-24, 1981.

McCaffrey, R. and R. Sutardjo, Reconnaissance microearthquake survey of Sulawesi, Indonesia, Geophys. Res. Lett., 9, 793-796, 1982.

McKenzie, D.P., Speculations on the consequences and causes of plate motion, Geophys. J. R. Astron. Soc., 18, 1-18, 1969.

Moore, G.F., and E.A. Silver, Collision processes in the northern Molucca Sea, in The Tectonic and Geologic Evolution of Southeast Asian Seas and Islands, Part II, Geophys. Monogr., 23, (D.E. Hayes, ed.), 360-372, AGU, Washington, D.C., 1983.

Nabelek, J. L., Determination of earthquake source parameters from inversion of body waves, Ph. D. thesis, Mass. Inst. of Technol., Cambridge, MA, 1983.

Nafe, J.E. and C.L. Drake, Physical properties of marine sediments, in The Sea, 3, (M.N. Hill, ed.), John Wiley, New York, 794-815, 1963.

Silver, E.A. and J.C. Moore, The Molucca Sea collision zone, Indonesia, J. Geophys. Res., 83, 1681-1691, 1978.

Silver, E.A., D.R. Reed, R. McCaffrey and Y. Joyodiwiryo, Backarc thrusting in the eastern Sunda Arc, Indonesia: A consequence of arc-continent collision, J. Geophys. Res., in press, 1983.

Stewart, G.S. and S.N. Cohn, The 1976 August 16, Mindanao, Philippine earthquake (M_s=7.8) -evidence for a subduction zone south of Mindanao, Geophys. J. R. Astron. Soc., 57, 51-65, 1979.

Usna, I., S. Tjokrosapoetro and S. Wiryosujono, Geological interpretation of a seismic reflection profile across the Banda Sea between Wetar and Buru Islands, Bull. Geol. Res. Dev. Centre, 1, 7-15, 1979.

von der Borch, C.C., Continent-island arc collision in the Banda arc, Tectonophysics, 54, 169, 1979.

Ward, S.N., A technique for the recovery of the seismic moment tensor applied to the Oaxaca, Mexico, earthquake of November 1978, Bull. Seismol. Soc. Am., 70, 717-734, 1980.

Watts, A.B. and M. Talwani, Gravity anomalies seaward of deep-sea trenches and their tectonic implications, Geophys. J. R. Astron. Soc., 36, 57-90, 1974.

Table 1.

Source Parameters Determined From the Inversion of P waves
Using Different Source Parameterizations
and Choices for the Error Function*

MOMENT TENSOR

Error Function 1

Depth = 11.1 ±0.3† km

Normalized moment-tensor components:

M_{xx} = -0.51 ±0.03		M_{xy} = -0.11 ±0.07	
M_{yy} = -0.10 ±0.03		M_{xz} = -0.40 ±0.02	
M_{zz} = 0.61 ±0.01		M_{yz} = 0.09 ±0.02	

Moment-tensor norm = 2.61 ±0.30 $\times 10^{25}$ dyne-cm

Principal axes:

	Eigenvalue	Azimuth	Plunge
P	-0.65 ±0.04	9 ±7°	17 ±1°
T	0.75 ±0.02	156 ±5°	70 ±1°
B	-0.10 ±0.04	276 ±6°	10 ±4°

Decomposition:‡ Double couple = 87% Linear vector dipole = 13%

Best Double couple:
Scalar moment = 1.83 $\times 10^{25}$ dyne-cm
Strike = 114° Dip = 29° Rake = 111°

Amplitudes of the source time function elements:§
0.23 ±0.01, 0.37 ±0.33, 0.29 ±0.02, 0.13 ±0.01, -0.02 ±0.02

CONSTRAINED DOUBLE-COUPLE

	Error Function 1	Error Function 2
Depth (km)	11.4 ±0.4	10.1 ±0.3
Scalar moment (10^{25}dyne-cm)	1.83 ±0.08	1.69 ±0.10
Strike (deg)	114 ±9	117 ±6
Dip (deg)	30 ±2	32 ±1
Rake (deg)	114 ±6	115 ±3
Amplitudes of the source time function elements		
	0.24 ±0.02	0.34 ±0.02
	0.40 ±0.02	0.48 ±0.02
	0.26 ±0.02	0.19 ±0.02
	0.14 ±0.02	0.06 ±0.02
	-0.04 ±0.02	-0.07 ±0.02

* The two choices for the error function are discussed in the text.
† All quoted uncertainties represent one standard deviation.
‡ The moment tensor is constrained to be purely deviatoric.
§ The duration of each source time function element is 2.0 s.

Table 2.

Crustal Structure Used in the Calculation of the Synthetic Seismograms

	Thickness (km)	V_p (km/s)	V_s (km/s)	Density (g/cm^3)
Source Region:				
	4.5	1.51	0.00	1.03
	2.0	3.20	1.31	2.30
	half-space	6.10	3.10	2.90
Receiver Region:				
	half-space	6.00	3.46	2.80

FIGURE CAPTIONS

Figure 1. Location map (insert) and detailed map of the Flores region. Thrust faults are indicated by solid lines with barbs on the overriding plate and bathymetric contours are in kilometers (from Silver et al., [1983]). The dashed line in the inset shows the inferred northwestern limit of Australian continental crust (and the Scott Plateau) beneath the outer arc ridge (from Hamilton, [1979]). The large hexagonal symbol shows the epicenter of the 1978 earthquake. Also shown is the position of the profile A-A' of Figure 4.

Figure 2. Observed (solid lines) and synthetic (dashed lines) long-period P waves and the best fit fault plane solution for the 1978 Flores earthquake. The bars on the time scale represent the source function in 2.0 second intervals. The amplitude scale for the seismograms is in millimeters at a magnification of 3000 and epicentral distance of 40°. Also shown is a lower hemisphere plot of first motion polarities. Filled circles represent compressional first motions and unfilled circles are dilatations. The dotted lines enclose the possible orientations of the P, T, and B axes as labeled. The arrow shows the horizontal projection of the slip vector.

Figure 3. Tracing of the short period vertical seismogram from station MAT. The first motion is clearly dilatational.

Figure 4. Crustal model across the thrust zone (line A-A' of Figure 1) satisfying gravity and refraction data. Filled circles in (b) are free-air gravity anomalies and the dotted line over Flores is the Bouguer gravity field. The dashed curves show the residuals in (a) and calculated gravity in (b) for the isostatically balanced crustal model (dashed line in c) based on an average density of 2.8 g/cm^3 to a depth of 34 km. Solid curves

show the residuals, calculated gravity and crustal model for the dipping crust model. Densities (indicated by values within each layer) and bathymetry are the same for both models. (d) is a line drawing interpretation of a reflection profile from Silver et al. [1983] across the Flores Thrust along the northern segment of the line A-A'. The bottom figure (e) shows the assumed deep structure and its computed contribution to the gravity field over the region of the Flores Basin (shaded box). The effect of the deep structure was included in the isostatically balanced model.

Figure 5. Alternative models of the Flores Basin thrust zone and role of the Flores earthquake. Discussion is given in the text. All models are drawn at the same scale and without vertical exaggeration. Model (a) is the most consistent with available evidence.

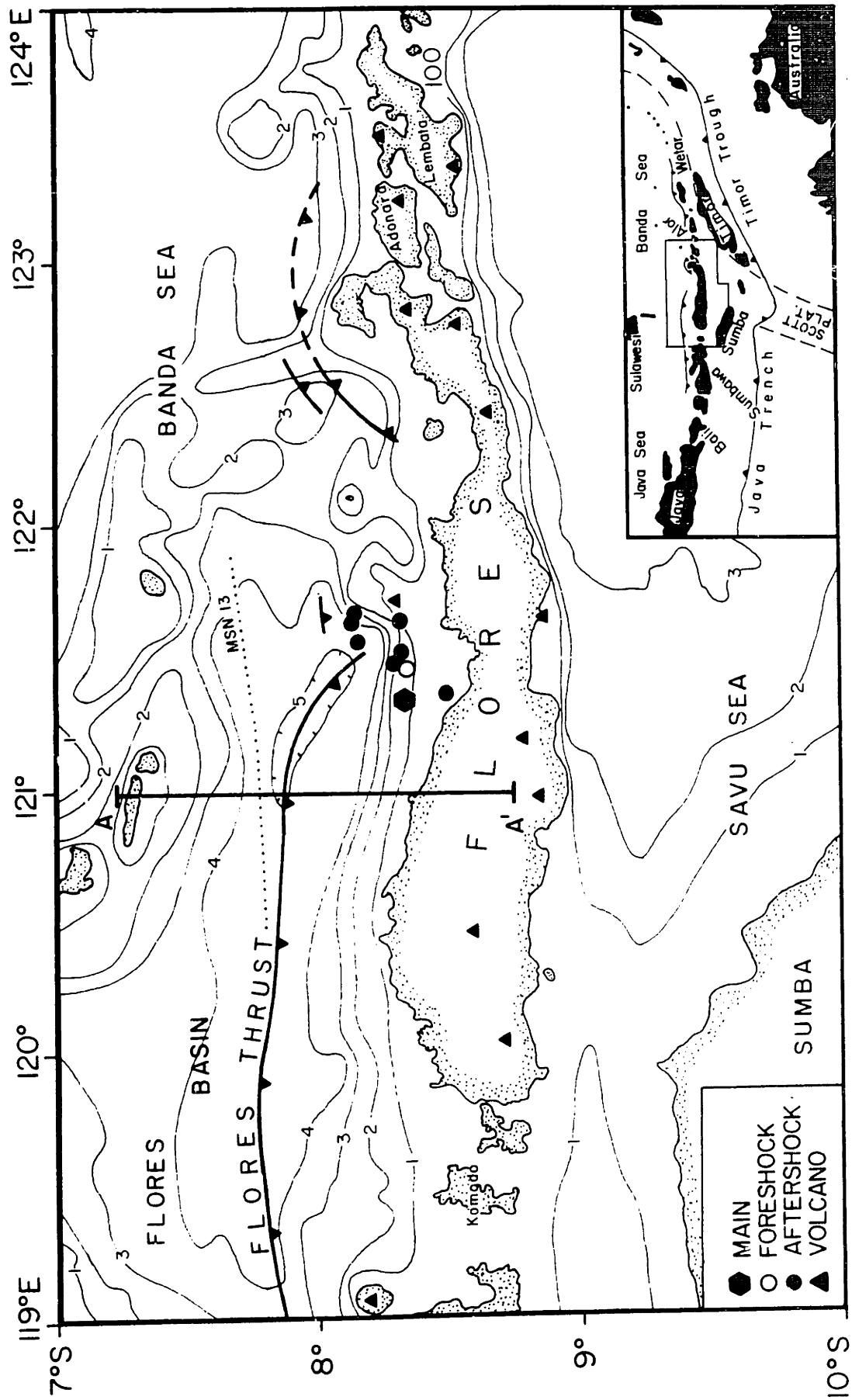
124°E
123°
122°
121°
120°
119°E
7°S
8°
9°
10°S
BANDA SEA
FLORES BASIN
FLORES THRUST
FLORES
SAVU SEA
SUMBA
Komodo
Adonara
Lembata
MSN 13
A
A'
MAIN
FORESHOCK
AFTERSHOCK
VOLCANO
Java Sea
Sulawesi
Banda Sea
Java
Bali
Sumbawa
Sumba
Timor
Java Trench
Timor Trough
Scott Plateau
Australia

Figure 1

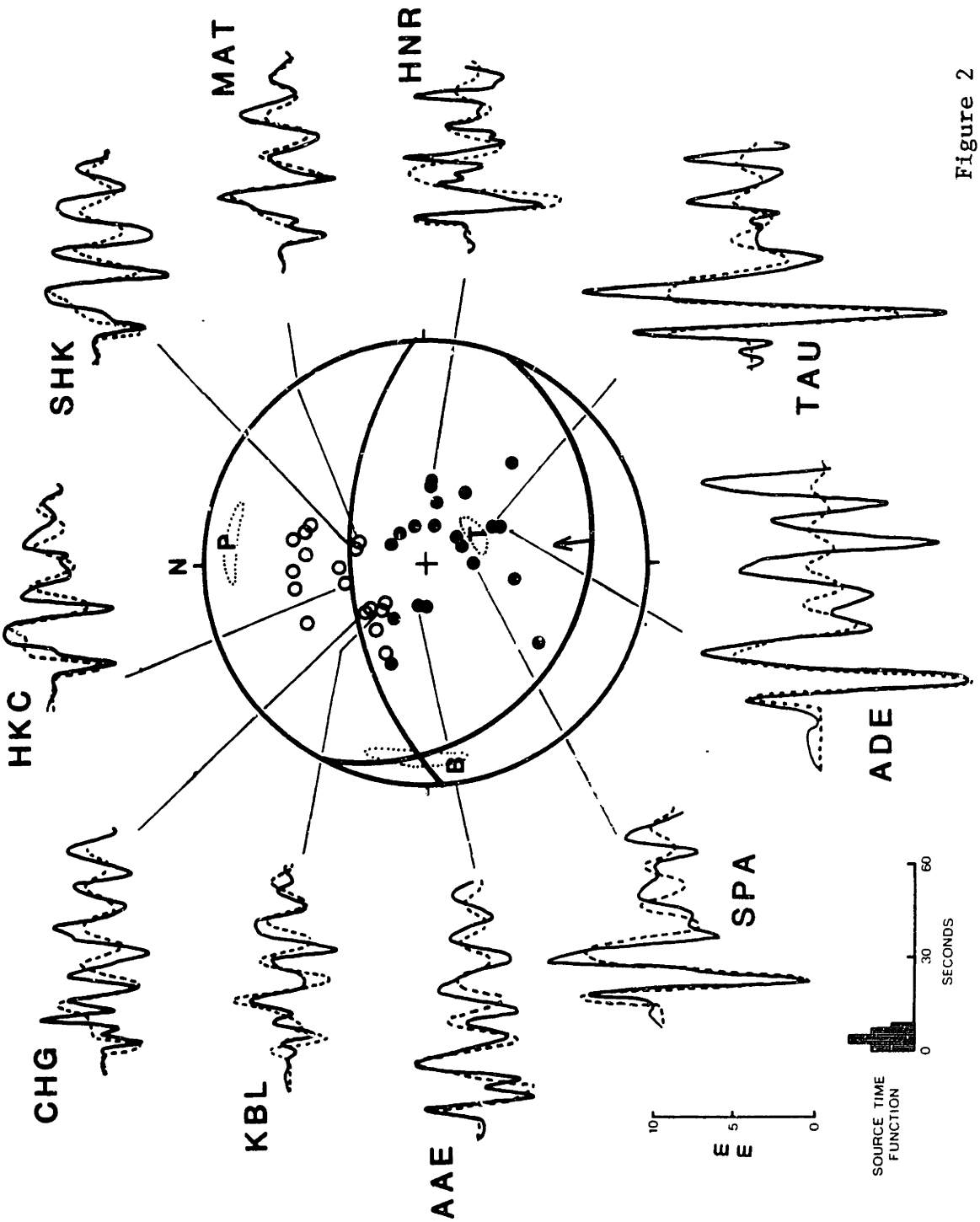
HKC
SHK
MAT
HNR
CHG
KBL
AAE
SPA
TAU
ADE
N
P
T
B
10
5
0
E
E
SOURCE TIME FUNCTION
0
30
60
SECONDS

Figure 2

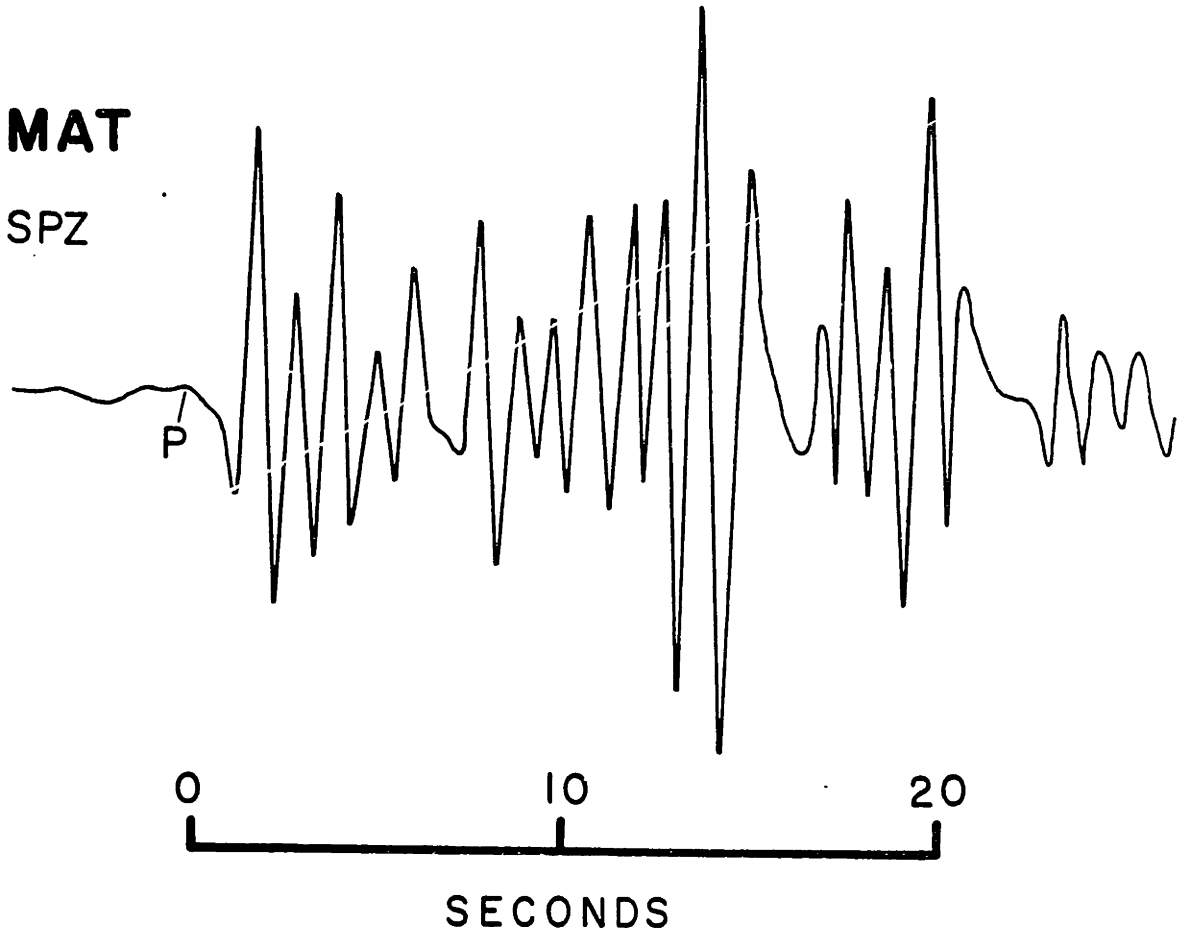

Figure 3

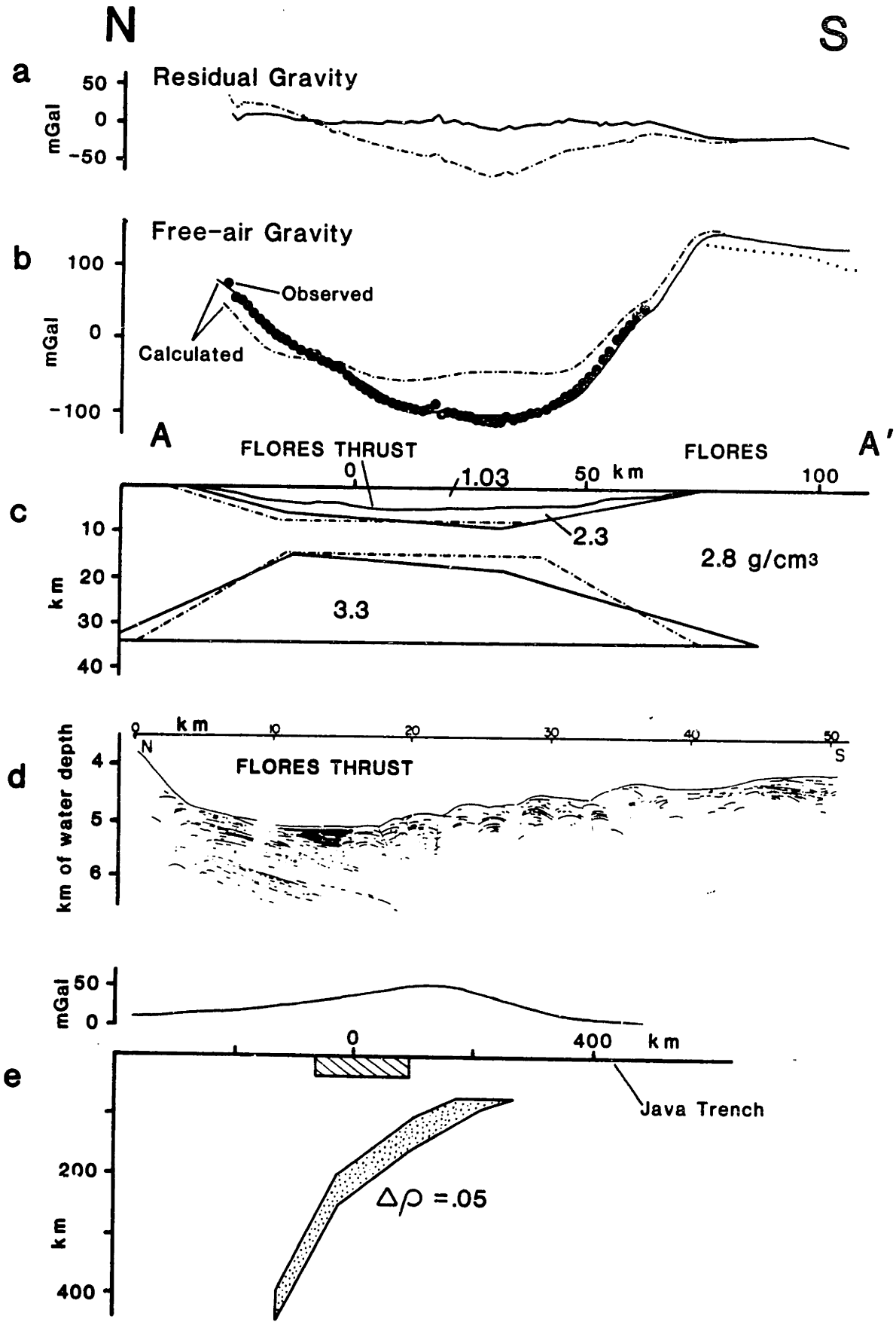
N
S
a
Residual Gravity
50
0
-50
mGal
b
Free-air Gravity
100
0
-100
mGal
Observed
Calculated
A
A'
c
FLORES THRUST
FLORES
0
1.03
50 km
100
10
20
30
40
km
2.3
2.8 g/cm3
3.3
d
0 km
10
20
30
40
50
N
S
FLORES THRUST
km of water depth
4
5
6
e
mGal
50
0
0
400 km
Java Trench
200
400
km
Δρ =.05

Figure 4

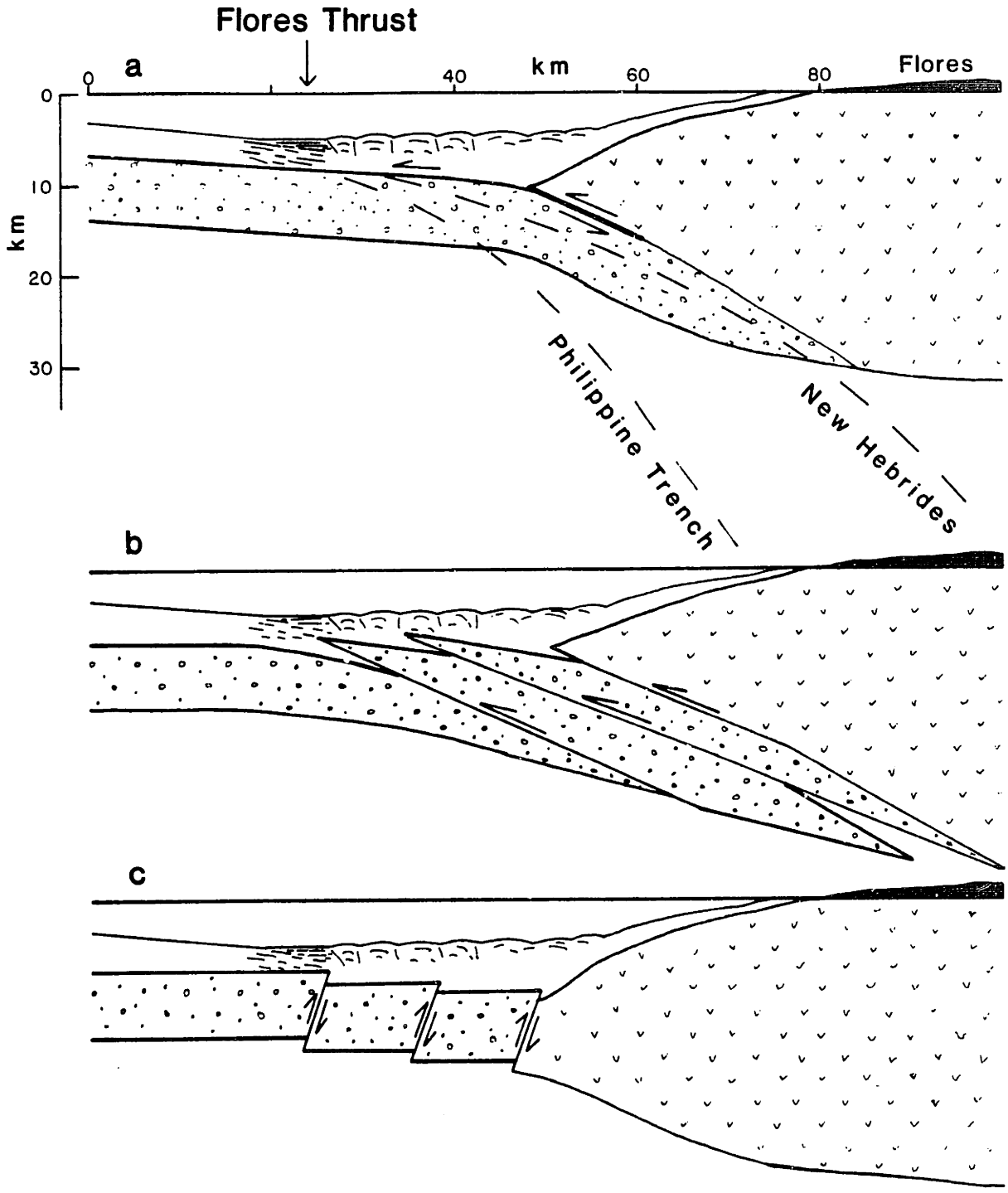
Flores Thrust
a
0
40
km
60
80
Flores
0
10
20
30
km
Philippine Trench
New Hebrides
b
c

Figure 5

JOURNAL OF GEOPHYSICAL RESEARCH, VOL. 86, NO. B3, PAGES 1701-1724, MARCH 10, 1981

Source Characterization of Two Reykjanes Ridge Earthquakes: Surface Waves and Moment Tensors; *P* Waveforms and Nonorthogonal Nodal Planes

ANNE M. TRÉHU

MIT/WHOI Joint Program in Oceanography, Massachusetts Institute of Technology, Cambridge, Massachusetts 02139

JOHN L. NÁBĚLEK AND SEAN C. SOLOMON

Department of Earth and Planetary Sciences, Massachusetts Institute of Technology, Cambridge, Massachusetts 02139

Well-constrained fault plane solutions from *P* wave first motions for mid-ocean ridge normal faulting earthquakes usually require nonorthogonal nodal planes. Local structural effects and/or departures from a double-couple source mechanism have been invoked to explain this phenomenon. In order to obtain an independent determination of the source mechanisms for the April 24, 1970, and April 3, 1972, events on the southern Reykjanes Ridge, we invert the Rayleigh wave radiation pattern to obtain the source moment tensor. The moment tensor formulation should be particularly well suited to this problem because it is not restricted a priori to a double-couple source mechanism. A potential drawback of the technique, however, is the requirement that phase velocities along the earthquake-station paths be known very accurately in order to obtain the source phase from the observed phase, and an objective of this study was to determine whether a regionalized phase velocity model compiled from published dispersion curves is adequate. The results of the moment tensor inversion for both events indicate shallow normal faulting with the tension axis approximately horizontal and perpendicular to the local strike of the ridge. Apparent departures from a pure double-couple source seem to result from errors in the data and the poor resolution of the M_{xz} and M_{yz} components of the moment tensor for shallow sources. After performing the inversion under a series of increasingly more stringent constraints we conclude that the data for both events are compatible with pure double-couple sources with moments of 4.8 and 7.5 $\times 10^{24}$ dyn cm, respectively. We then show that interference between *P*, *pP*, and *sP* due to shallowness of the source can account for the observed nonorthogonality and match the observed *P* waveforms for the April 3, 1972, event with theoretical seismograms calculated for a shear fault whose orientation is consistent with the surface wave solution. The best fit to the data is obtained for a long, narrow fault (13 km by 3 km), with rupture initiating near the seafloor. The moment indicated by the *P* waves is 7.5 $\times$ 10^{24} dyn cm. These source parameters give an average displacement of about 60 cm and a stress drop of 30–60 bars, taking into account various uncertainties. Although we might expect attentuation to be high in the mid-ocean ridge environment, the average attenuation required to fit the teleseismic data is not higher than normal ($t^* = 1$ s). The *P* waves from the April 24, 1970, earthquake were too small to be suitable for quantitative modeling by synthetic seismograms but are qualitatively consistent with a shallow fault model similar to that for the larger event. We conclude that the faulting process described by these two earthquake mechanisms is directly related to the formation of rift valley topography.

INTRODUCTION

Fault plane solutions of ridge crest earthquakes regularly indicate nonorthogonal nodal planes for normal faulting events [*Sykes*, 1967, 1970; *Solomon and Julian*, 1974]. Because orthogonal nodal planes are implicitly required by the double-couple faulting mechanism from which the fault plane solution is derived, either a process must be found whereby the true body wave radiation pattern is distorted to yield an apparent nonorthogonality, or an alternative faulting mechanism must be found. Several explanations for this phenomenon have been proposed. *Solomon and Julian* [1974] demonstrated that a low-velocity wedge below the ridge, the existence of which is predicted by thermal models and confirmed by surface wave and refraction studies, can focus rays from a source on the ridge, thus collapsing the apparent dilatational quadrant. Other explanations include (1) an explosive volcanic component superimposed upon the double couple [*Solomon and Julian*, 1974], (2) a mechanism of extensional failure in a porous, fluid-saturated medium [*Robson et al.*, 1968], and (3) interference between *P*, *pP*, and *sP* resulting from the shallowness of the source [*Hart*, 1978].

Focusing of rays below the source and interference at the surface are explanations invoking structural effects which would distort the apparent body wave radiation pattern of a double-couple fault but which should not strongly affect the surface wave radiation pattern. A true source mechanism of an explosion or of tensional cracking, on the other hand, should be manifested in the surface waves as well as in the body waves. An independent source mechanism determination obtained from the surface waves should therefore help to distinguish the cause of the nonorthogonality. The recently developed technique of inverting surface wave data to obtain the source moment tensor should be especially suited to this problem, since the moment tensor is not restricted a priori to correspond to a double couple. The surface wave solution can then provide a base from which the body wave problem can be reexamined.

The frequency of teleseismically observable events combined with a fortuitous location with respect to azimuthal coverage by the World-Wide Standard Seismograph Network (WWSSN) makes the southern Reykjanes Ridge an excellent laboratory for studying the mechanism of faulting on a slowly

Paper number 80B1369.
0148-0227/81/080B-1369$01.00

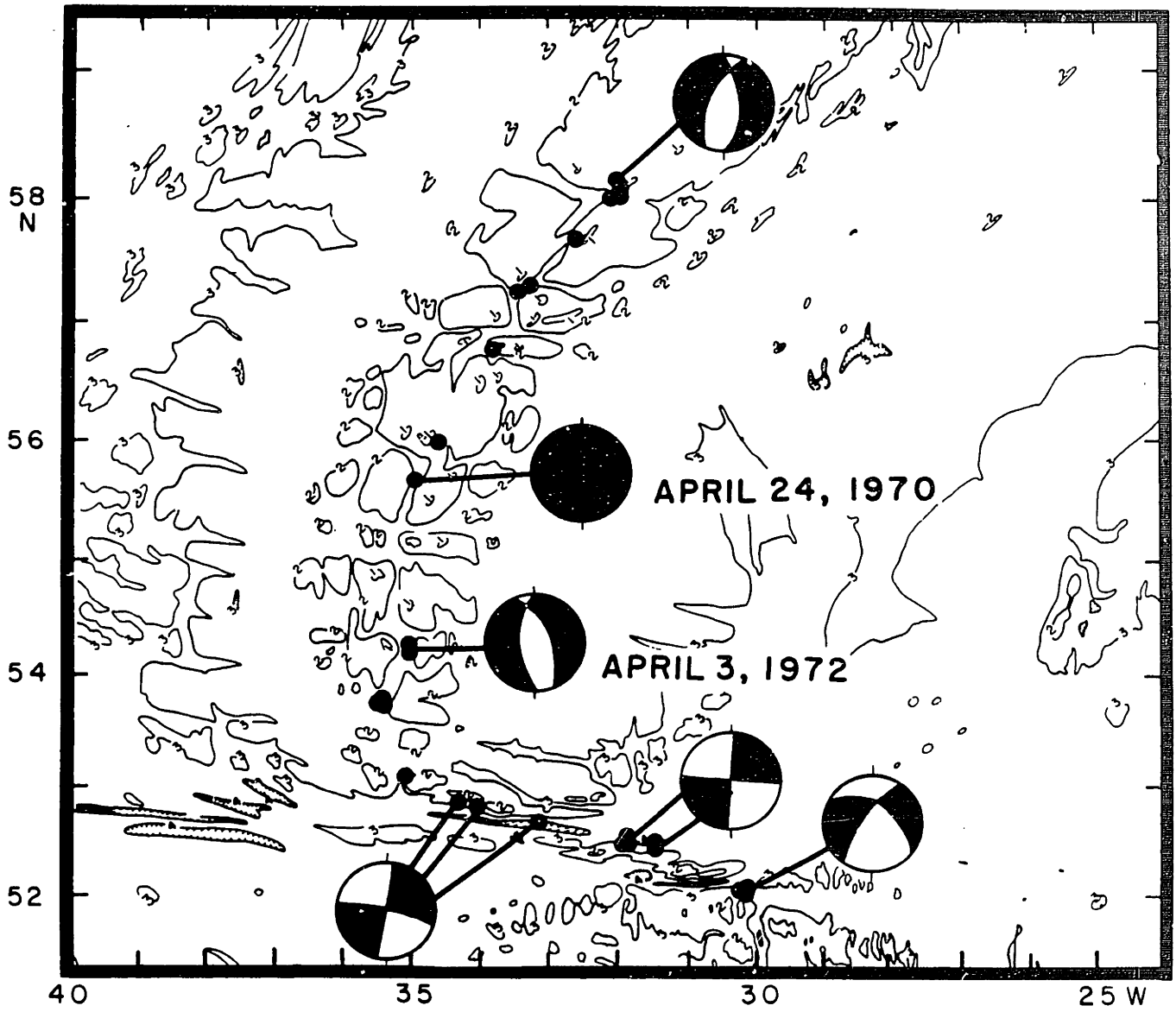

Fig. 1. Bathymetric map of the southern Reykjanes Ridge and Gibbs Fracture Zone. Contours are at 1-km intervals. Earthquakes of m_b greater than 5.0 recorded by the WWSSN from 1962 to 1978 are shown by dots. Fault plane solutions are from *Einarsson* [1979]. Bathymetry from NAVOCEANO World Relief Map, NA-4, May 1977.

spreading ridge and the phenomenon of nonorthogonal nodal planes. Although one could argue that the area might be anomalous owing to proximity to the Iceland hot spot, topographically and geochemically, the ridge south of about 59°N appears to be beyond the hot spot's direct influence [*Vogt and Johnson*, 1975]. Spreading direction is approximately perpendicular to the ridge, and the axis is broken by an axial valley characteristic of its spreading rate. This contrasts with the obliquely spreading, smooth, shallow ridge to the north. The seismicity south of 59°N is also much more characteristic of that of the 'average' Mid-Atlantic Ridge [*Francis*, 1973]. North of 59°N the Reykjanes Ridge is nearly aseismic, resembling in this respect a fast spreading rise. The southern Reykjanes Ridge, on the other hand, has experienced several earthquakes with body wave magnitude m_b up to 5.5 since the inception of the WWSSN. Detailed bathymetric studies show that the transition between the two regimes is marked by a several-fold increase in offset across the fault scarps which border the axial constructional volcanic pile [*Laughton et al.*, 1979].

Figure 1 is a topographic map of the area showing earthquakes with m_b greater than 5 which were recorded between 1962 and 1978. Most of the ridge earthquakes display the pronounced distortion of the body wave radiation pattern characteristic of mid-ocean ridge events. Note, however, that for the April 24, 1970, earthquake at 56°N, compressional first arrivals appear nearly to cover the focal sphere. This mechanism, determined by *Einarsson* [1979], originally inspired our interest in the area. Einarsson suggested that this event might be an extreme manifestation of the nonorthogonality. An analysis of the surface wave radiation pattern was undertaken to determine whether this event might perhaps be an explosion.

In this paper the Rayleigh wave displacement spectra from the April 24, 1970, Reykjanes Ridge earthquake are inverted to obtain the source moment tensor. A moment tensor solution was also obtained for the April 3, 1972, event (Figure 1),

TABLE 1. Locations of Reykjanes Ridge Earthquakes Studied in This Paper (From the International Seismological Centre)

Date	Time, UT	Location, deg	Magnitude* m_b	Magnitude* M_S†
April 24, 1970	0123:17	55.64°N, 35.03°W	5.3	5.4
April 3, 1972‡	2036:20	54.33°N, 35.20°W	5.1	5.5

*Although the 1970 event is assigned a larger m_b by the ISC, an examination of seismograms recorded at the same station for the two events indicates that these values are erroneous, as P wave as well as surface wave arrivals are consistently of larger amplitude for the 1972 event.

†From USCGS and NEIC.

‡This event was the second of a pair of events at the same location and of approximately the same magnitude which were separated in time by 1 hour, 43 min. Seismograms for the two events are remarkably similar. The second event was chosen for study because clear P wave arrivals were observable for a greater range of azimuths and distances. These two events were not accompanied by any smaller teleseismically recorded events, unlike the 1970 earthquake, which was the largest event of a swarm sequence.

which yielded a well-constrained fault plane solution from P wave first motions requiring nodal planes separated by approximately 60°. The locations of these events are given in Table 1. The moment tensor solutions for both events indicate shallow normal faulting with the tension axis perpendicular to the strike of the spreading center.

We then show that the apparent nonorthogonality of the body wave solution for the April 3, 1972, event may be attributed to the interference effects between direct P, pP, and sP and that the body waveforms can be reconciled with the source mechanism obtained from the surface waves. We conclude that the April 24, 1970, event was too small to yield a reliable fault plane solution if the amplitude of the background noise and expected amplitude of the first arrival are considered. The observed body waves from the slightly larger April 3, 1972, event, however, are matched with synthetic seismograms calculated for a finite fault with an orientation corresponding to the moment tensor solution and suggest a narrow, long, shallow fault plane which reached the seafloor. This mechanism may correspond to faulting which breaks through the thin axial crust and contributes to the topography of rift valley and mountains.

SOURCE MECHANISM FROM SURFACE WAVES

Background

Surface waves are especially useful for studying oceanic earthquakes because such events are often too small to yield reliable fault plane solutions [*Kafka and Weidner*, 1979]; those fault plane solutions which have been obtained for spreading center events raise questions concerning the basic assumptions about the source mechanism. The radiation pattern of surface waves can be used to obtain an independent determination of the source mechanism. Moreover, because the surface waves used for this determination have a longer wavelength than the body waves used for the fault plane solution, they are less affected by structural anomalies immediately below the ridge axis.

The representation of the far-field displacement in terms of the moment tensor was first presented by *Gilbert* [1970] and *Gilbert and Dziewonski* [1975] for free oscillations and was extended to surface waves by *McCowan* [1976] and *Mendiguren* [1977] and to body waves by *Stump* [1976] and *McCowan* [1977]. Seismic waves radiated from a source at a given depth can be expressed as a linear combination of the moment tensor components. For surface waves, the inversion to obtain the moment tensor is much more rapid than the traditional trial and error method of calculating theoretical spectra for all possible combinations of strike, dip, and slip of a double-couple fault and matching the observed amplitude and phase spectra independently [e.g., *Ben-Menahem and Toksöz*, 1962, 1963; *Mitchell*, 1973; *Patton*, 1976]. Another advantage of the moment tensor representation is that it is not restricted to a double-couple source mechanism and should therefore provide insights into possible departures from this generally assumed faulting model. Other possible mechanisms contain isotropic and/or compensated linear vector dipole components [*Knopoff and Randall*, 1970]. For example, a tensional crack corresponds to the superposition of an explosion and a compensated linear vector dipole.

The formulation of the problem of retrieving the moment tensor from the vertical component of the Rayleigh wave is given in Appendix A. In summary, the moment tensor components can be retrieved from the real and imaginary parts of the observed source spectrum [*Mendiguren*, 1977; *Patton and Aki*, 1979]:

$$\text{real} = A_{ij}\cos\phi_{ij} = M_{zz}G_2(h, f_i) + (M_{xx} + M_{yy})G_1(h, f_i) \cdots (M_{yy} - M_{xx})G_1(h, f_i)\cos 2\theta_j + 2M_{xy}G_1(h, f_i)\sin 2\theta_j + E_{ij}^R \quad (1a)$$

$$\text{imaginary} = A_{ij}\sin\phi_{ij} = M_{xz}G_3(h, f_i)\cos\theta_j + M_{yz}G_3(h, f_i)\sin\theta_j + E_{ij}^I \quad (1b)$$

In (1), A_{ij} and ϕ_{ij} are the amplitude and phase delay observed at station j and frequency f_i after having been corrected for the effects of propagation and the source time function, θ_j is the azimuth of station j with respect to the earthquake, and the E_{ij}^R and E_{ij}^I are error terms. The G_k are real functions of depth and frequency and are calculated for the appropriate source velocity and density structure using *Saito*'s [1967] al-

TABLE 2. Velocity Model for the Mid-Atlantic Ridge, From *Weidner* [1974]

Thickness, km	ρ, g/cm^3	α, km/s	β, km/s
3	1.03	1.52	0.0
6	3.05	6.40	3.70
11	3.40	8.10	4.60
10	3.40	8.10	4.33
10	3.38	8.00	4.33
20	3.38	7.92	4.33
20	3.38	7.68	4.33
20	3.36	7.65	4.33
20	3.36	7.76	4.00
20	3.36	7.82	4.00
20	3.36	8.10	4.00
100	3.36	8.15	4.00
20	3.37	8.15	4.00
20	3.38	8.15	4.00
20	3.39	8.15	4.00
20	3.40	8.15	4.44
20	3.41	8.22	4.51
20	3.45	8.27	4.55
20	3.50	8.32	4.58
300	3.68	8.70	4.80

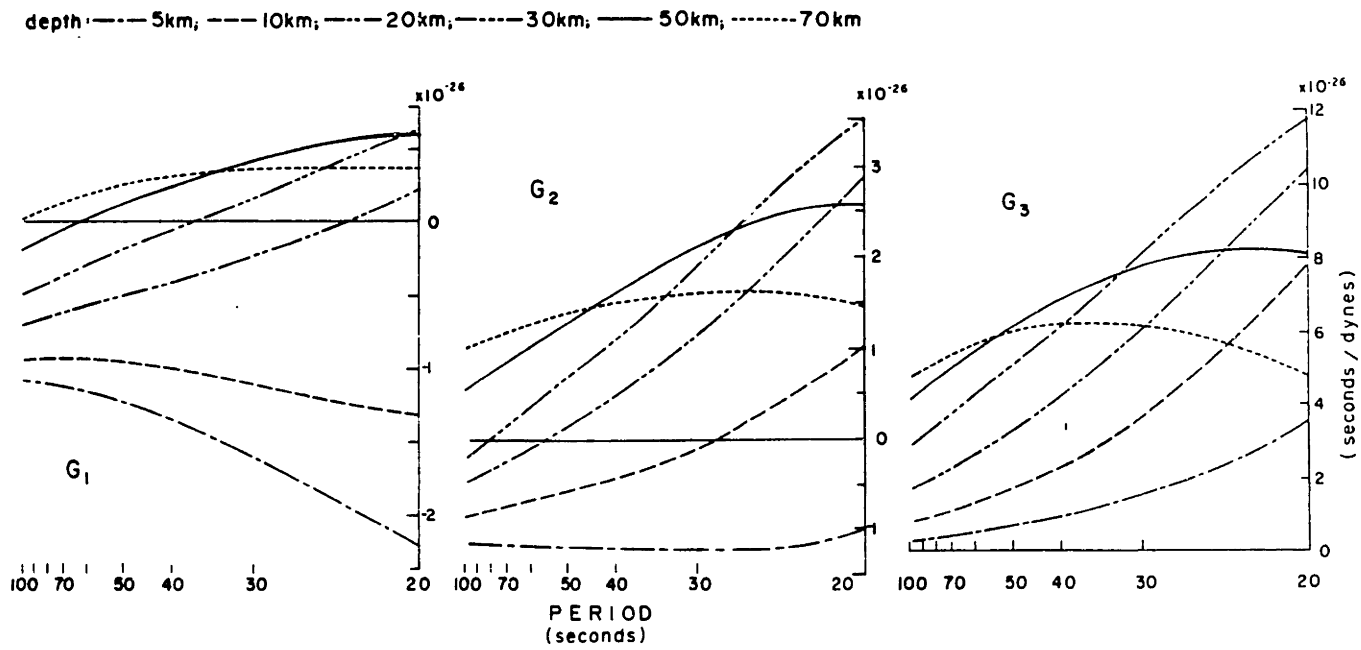

Fig. 2. Response curves calculated at different depths for the oceanic model of Table 2: $G_1 = AkY_3(h, \omega)/2$; $G_2 = A[-Y_2(h, \omega) - \lambda(h)kY_3(h, \omega)]/[\lambda(h) + 2\mu(h)]$; $G_3 = AY_4(h, \omega)/\mu h)$; $A = [Y_1(0, \omega)/4U\omega^2 I](2k/\pi r)^{1/2}$, where r is the data equalization distance of 4000 km. For definition of other terms, see Appendix A.

gorithm; G_k calculated for an oceanic model (Table 2) are displayed in Figure 2. For a given depth, the moment tensor components can be obtained from a one-step inversion of the real and imaginary parts of the spectrum. Depth can be determined by inverting for the moment tensor at a series of depths and choosing that depth which minimizes the residual $E^2 = \sum_{ij}\{(E_{ij}^R)^2 + (E_{ij}^I)^2\}$.

The resolving power of the inversion is determined by the behavior of the functions G_k over the period range of the data. We see from (1*a*) that with data from only a single frequency we cannot independently determine $(M_{xx} + M_{yy})$ and M_{zz}; even with data from a range of frequencies, G_1 and G_2 have too similar a frequency dependence over the frequency range of long-period surface wave data to permit independent resolution of the diagonal components for most source depths [*Mendiguren*, 1977]. The constraint $\sum_{i=1}^{3} M_{ii} = 0$, equivalent to no volume change, can be analytically imposed without destroying the linearity of the problem. Under this constraint, however, an explosive component in the source will masquerade as a vertically oriented compensated linear vector dipole. This effect will be examined further in the discussion of the surface wave results. We can also see that G_3 approaches zero as depth decreases because it is proportional to one of the stress eigenfunctions (Appendix A). This results in poor resolution of the M_{xz} and M_{yz} components for very shallow sources, and we may be forced to impose an additional constraint. If we have evidence indicating that the principal stress axes are approximately horizontal and vertical, we can assume that the imaginary part of the spectrum is due to noise in the data and solve for M_{xx}, M_{yy}, M_{zz}, and M_{xy} with M_{xz} and M_{yz} identically equal to zero. This constrains the corresponding double couple fault mechanism to be either dip slip with a dip of 45° or vertical strike slip.

A drawback of the moment tensor inversion method is the requirement that the phase velocity along the earthquake-station path be known very accurately [*Aki and Patton*, 1978] in order to correct the observed phase back to the source. In the moment tensor formulation, amplitude and phase cannot be decoupled without destroying the linearity of the problem (for an example of a nonlinear inversion using amplitude data alone, see *Kafka and Weidner* [1979]).

The relationship between the observed phase and the ϕ_{ij} of (1), in units of cycles, is

$$\phi_{ij} = \phi_{ij}^{\text{observed}} - \phi_{ij}^{\text{instr}} + [T_j - D_j/C_{ij}]f_i + 0.125 \pm n \quad (2)$$

where ϕ_{ij}^{instr} is the instrument phase response, T_j is the time between the origin time and the beginning of the digitized record, D_j is epicentral distance in kilometers, C_{ij} is the phase velocity, the constant 0.125 includes the effects of the source time function (assumed to be a step) and the asymptotic expansion of the Hankel function for the notation of equations (A5) and (1), and n is a constant which arises from the periodicity of the phase and is determined by C_{ij}. If we assume that T_j and D_j are known exactly, the error in ϕ_{ij} due to an error ΔC_{ij} in C_{ij} is $\Delta\phi_{ij} \simeq (f_i D_j \Delta C_{ij})/C_{ij}$. Numerical experiments [*Patton and Aki*, 1979] indicate that random errors on the phase of up to ±0.125 cycles lead to the introduction of an apparent non-double-couple component of 0 to 10%; an error of up to 0.25 cycles can lead to 36% non-double couple. The orientation of the principal axes of the moment tensor, however, remains very stable. For values typical of our data set, an epicentral distance of 2500 km and a velocity of 4 km/s, the phase change for a 50-s wave resulting from 0.25% error in the phase velocity is 0.13 cycles. For a given error in C, the error increases with increasing epicentral distance and decreasing period.

In his application of the method to a family of earthquakes in central Asia, *Patton* [1980] began by calculating phase velocities for the station-source paths by the method of *Weidner and Aki* [1973] using two neighboring earthquakes with different known source mechanisms to separate the path and source

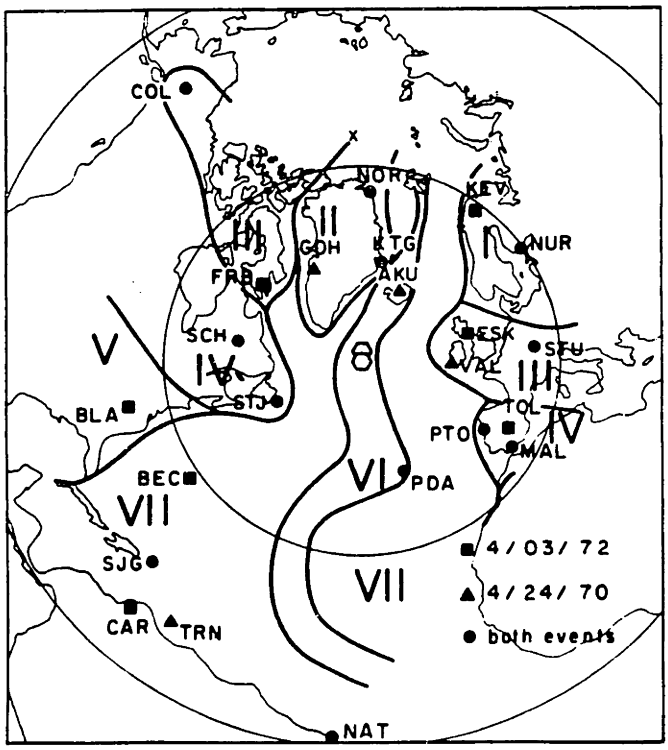

Fig. 3. Stations and regionalization used for the surface wave analysis plotted on an azimuthal equidistant projection centered on the April 3, 1972, event. Regions are labeled with Roman numerals, and the corresponding phase velocity dispersion curves are displayed in Figure 4. Circles mark distances of 30° and 60° from the epicenter of the 1972 event.

effects. The moment tensors of other earthquakes in the region were then calculated using these path parameters. An iterative scheme was adopted whereby once the mechanism of an earthquake had been determined, its 'known' mechanism was used to refine the values of the path parameters. A motivation for conducting the moment tensor inversions for the Reykjanes Ridge earthquakes was to see if reasonable results could be obtained simply by using a regionalized velocity model to correct for propagation and thus obtain a source mechanism solution for a single isolated event. An excellent azimuthal distribution of stations with short, structurally simple earthquake-station paths coupled with the availability of Rayleigh wave phase velocity studies in the North Atlantic Ocean and adjacent continental regions suggested that such an approach might be fruitful.

Data

For the April 24, 1970, event, vertical component Rayleigh waves from 23 stations of the WWSSN and Canadian network were digitized at an interval of 2 s. Each digitized time series was then Fourier-analyzed and corrected for instrument response, geometrical spreading, and attenuation. The Q model of *Tsai and Aki* [1969] was used. Amplitude spectra were equalized to a common distance of 4000 km. To decrease the effect of amplitude fluctuations due to multipathing, the amplitude spectra were smoothed by averaging over a frequency window of 0.04 Hz centered at each frequency.

The phase spectra were corrected for propagation effects using the regionalized phase velocity model of Figures 3 and 4. Regional boundaries were determined from geologic and bathymetric considerations. The oceanic domain was divided into young and old lithosphere roughly by the 20-m.y. isochron, and the continental margin was defined by the 4000-m isobath. For several necessary continental provinces, phase velocity dispersion curves were not available in the literature for the entire period range from 20 to 100 s, and an appropriate curve was extrapolated from curves published for geologically similar regions. The estimated errors on the phase velocities given by the authors of the regional studies range from about 0.2% (oceanic regions and recent studies of continental regions) to 1.0% (older continental studies). Table 3*a* shows the percentage of each earthquake-station path within a given region. These percentages were used to calculate an appropriate phase velocity for each period at each station.

The corrected source spectra were then sampled at 2-s intervals in period. Examples of seismograms and corrected source spectra are shown in Figure 5*a*. Only data for periods between 30 and 60 s were used in the inversion. The earthquake was too small to excite waves at periods much greater than 60 s, and data at periods shorter than 30 s were considered unreliable because of the effects of structural heterogeneities along the path and of phase velocity errors on the phase correction. The source spectra were then examined visually to see if phases were coherent. A few stations were dropped from the calculations at this stage, leaving 16 stations (256 data) for the final inversion. The rejected stations usually corresponded to long paths with sections parallel to structural discontinuities, and the incoherency of the phase was probably due to the interference effects of multipathing. Spurious phases or amplitudes at certain periods for otherwise coherent spectra were also noted and assigned zero weight (e.g., 52-s period at station VAL; see Figure 5*a*).

The vertical component of the Rayleigh wave for the April 3, 1972, event was treated similarly to that for the 1970 event except that amplitude spectra were not smoothed. The stations used for the analysis of this event are shown in Figure 3, the regionalization of the paths is given in Table 3*b*, and a

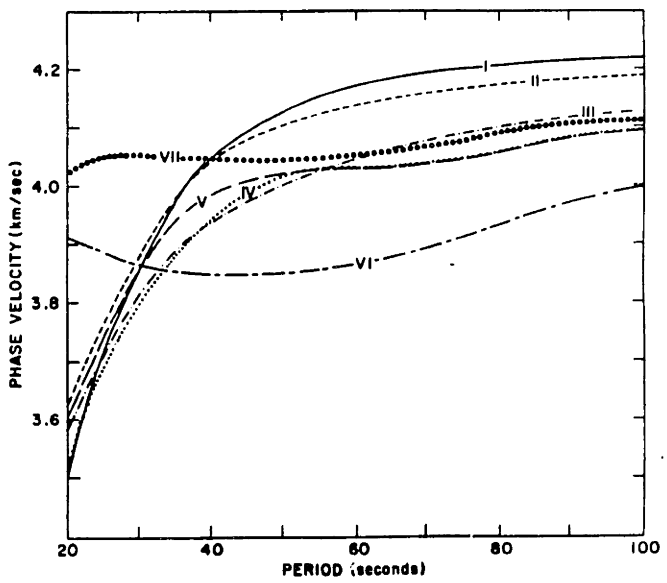

Fig. 4. Phase velocity dispersion curves for the regions shown in Figure 3. References are I, *Naponen* [1966] and *Calgagnile and Panza* [1978]; II, *Gregersen* [1971]; III and IV, *Wickens* [1971]; V, *Oliver et al.* [1961]; VI, *Forsyth* [1975] (5–10 m.y. normalized to water depth of 3.2 km); VII, *Weidner* [1974] (normal ocean basin).

TABLE 3*a*. Regionalization of Surface Wave Paths for the April 24, 1970, Event

Station	Distance, deg	Azimuth, deg	Fraction of Path by Region						
			I	II	III	IV	V	VI	VII
AKU	13.0	32.4	...	...	...		...	1.0	...
COL	49.2	328.8	...	0.20	0.66	...	...	0.03	0.11
GDH	16.0	335.8	...	0.56	...	...	...	0.16	0.28
KTG	15.9	16.1	...	0.20	...	...	...	0.48	0.32
MAL	28.0	119.5	...	...	...	0.25	...	0.15	0.60
NAT	60.6	180.0	...	...	...	...	...	0.44	0.56
NOR	26.6	5.9	...	0.60	...	...	...	0.20	0.20
NUR	30.9	56.1	0.36	...	...	...	...	0.18	0.46
PDA	19.0	156.6	...	...	...	...	...	1.0	...
PTO	22.6	118.9	...	...	...	0.08	...	0.18	0.74
SCH	18.0	280.6	...	...	...	0.30	...	0.06	0.64
SJG	44.3	224.8	...	...	...	...	...	0.09	0.91
STJ	13.6	241.0	...	...	...	0.22	...	0.16	0.62
STU	27.5	85.7	...	...	0.60	...	...	0.09	0.31
TRN	49.5	215.1	...	...	...	...	...	0.11	0.89
VAL	15.0	93.9	...	...	0.21	...	...	0.17	0.62

sample of the data is shown in Figure 5*b*. Periods from 32 to 78 s at 19 stations were used for a total of 456 data.

The data for the 1972 earthquake were filtered using the time variable filter technique of *Landisman et al.* [1969] to avoid potential interference from higher modes and multipathing. This time-variable filtering did not significantly change the source spectrum at most stations. Erratic phase values were not eliminated by the filtering, although they were sometimes shifted by up to ±4 s in period (Figure 5*b*). For one station, BLA, the analysis did suggest interference from a mode clearly separated in time from the fundamental mode. In this case, the filtering smoothed the source spectra significantly (Figure 5*b*), suggesting that the technique will be useful for treating the data from events less auspiciously located with respect to the WWSSN than those along the southern Reykjanes Ridge. Using filtered data did not improve the resolution of the inversion, and in the rest of this study, only results obtained from the unfiltered data will be presented.

Results

The inversions were performed under a series of increasingly more stringent constraints. With all six moment tensor components unconstrained (constraint 1 in Table 4) the diagonal components were poorly resolved. The no-volume-change constraint was therefore imposed (constraint 2). It then became apparent that the sources were very shallow and that large, poorly determined M_{xz} and M_{yz} components were dominating the solutions. As normal faulting with the tension axis approximately horizontal was indicated, the constraint that the imaginary part of the spectrum be zero was then imposed, both without and with the no-volume-change constraint (constraints 3 and 4, respectively).

The residuals of the inversions, normalized to the number of data minus the degrees of freedom, are plotted against depth in Figure 6. The behavior of the residuals with depth is similar for the two events. For the inversion of the real part,

TABLE 3*b*. Regionalization of Surface Wave Paths for the April 3, 1972, Event

Station	Distance, deg	Azimuth, deg	Fraction of Path by Region						
			I	II	III	IV	V	VI	VII
BEC	30.3	235.7	...	...	...	0.12	...	0.12	0.76
BLA	35.1	259.7	...	...	...	0.39	.32	0.08	0.21
CAR	50.5	222.2	...	...	...	...	...	0.09	0.91
COL	50.3	329.3	...	0.22	0.63	...	...	0.08	0.07
ESK	18.3	73.8	...	...	0.36	...	...	0.17	0.47
FRB	19.3	312.4	...	0.20	...	0.15	...	0.16	0.49
KEV	31.2	36.4	0.12	...	...	...	...	0.53	0.35
KTG	17.2	15.1	...	0.19	...	...	...	0.53	0.28
MAL	27.5	117.1	...	...	...	0.25	...	0.13	0.62
NAT	59.3	179.8	...	...	...	...	...	0.35	0.65
NOR	27.9	5.7	...	0.56	...	...	...	0.24	0.20
NUR	31.7	54.2	0.37	...	...	...	...	0.11	0.52
PDA	17.8	154.6	...	...	...	...	...	1.0	...
PTO	22.0	115.8	...	...	...	0.06	...	0.15	0.79
SCH	18.2	284.5	...	...	...	0.26	...	0.15	0.59
SJG	43.3	225.6	...	...	...	...	...	0.10	0.90
STJ	12.9	245.6	...	...	...	0.19	...	0.25	0.56
STU	27.7	83.0	...	...	0.59	...	...	0.11	0.30
TOL	25.4	111.8	...	...	...	0.23	...	0.13	0.64

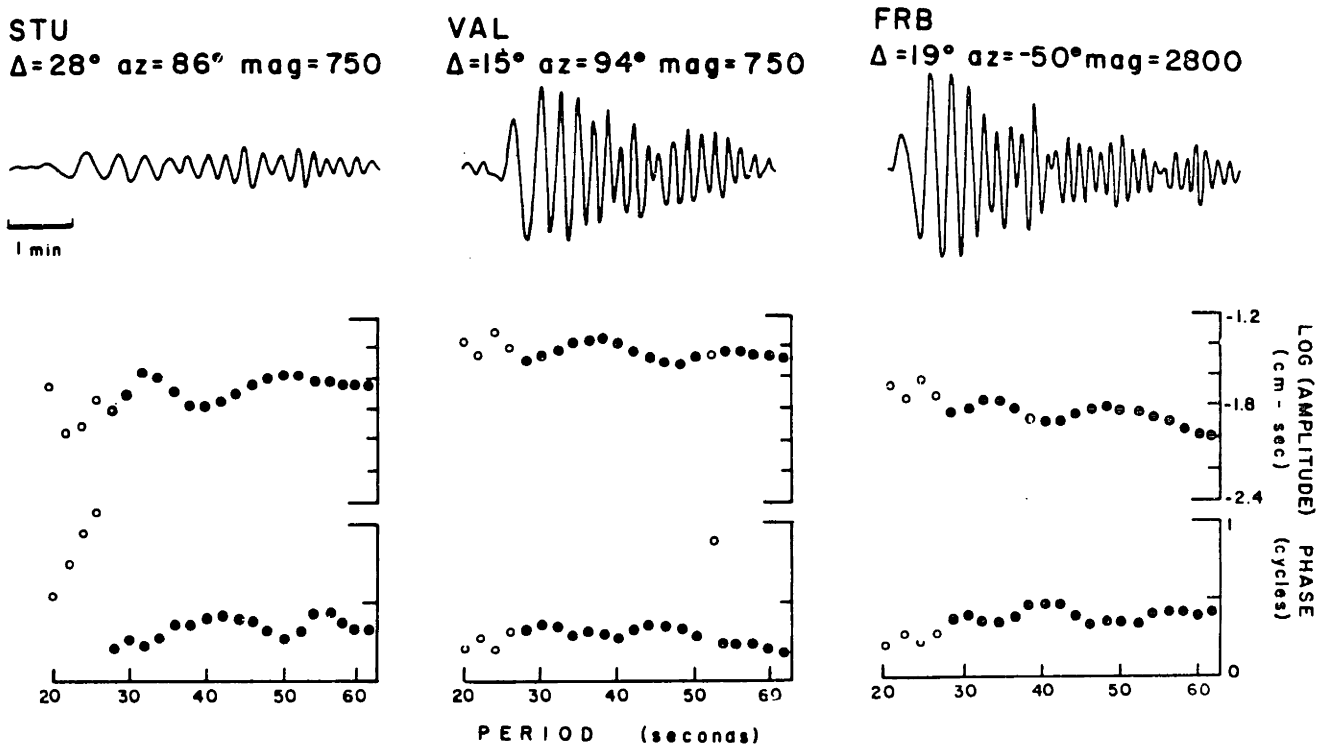

Fig. 5a. Examples of seismograms and corrected source spectra for the April 24, 1970, event. Displayed seismograms were traced directly from WWSSN records and are not equalized to a common epicentral distance and station magnification. Open circles in the source spectra indicate points which were eliminated from the data set for the inversion during the visual inspection of the data; Δ is epicentral distance in degrees, az is station azimuth in degrees from north, and mag is station magnification.

we observe minima for both shallow (4–10 km, or 1–7 km below seafloor) and deep (80–90 km) depths, regardless of the constraint imposed. This ambiguity is to be expected because over the period range of the data the behavior of G_1 and G_2 is similar for both shallow and deep events. The minima are more sharply defined when the constraint $\sum_{i=1}^{3} M_{ii} = 0$ is imposed. The inversion of the imaginary part provides no constraint on the depth. Imposing the constraint that the imaginary part of the spectrum is zero and that the observed amplitude reflects the real part decreases the residuals. Since one would expect to obtain larger residuals for the more highly constrained case, this behavior implies that by recasting the amplitude and phase spectra in terms of real and imaginary components, we are actually adding noise to the real part. This question will be discussed further when the results of the inversion under the various constraints are compared to the observations.

The results of the inversion for depths corresponding to minima in the residuals are given in Tables 4a and 4b. The errors for the eigenvalues and eigenvectors represent the first-order perturbation resulting from errors in the moment tensor components [*Mathews and Walker*, 1964; *Strelitz*, 1980]. First, note that although the calculated errors on the diagonal components are so large as to render the solution meaningless when the trace is not constrained to be zero (solutions for a depth of 4 km below seafloor, constraints 1 and 3), the orientation of the principal axes and the percentage of double-couple mechanism in the solution are similar to those for the corresponding solutions with the trace constrained (constraints 2 and 4, respectively). By imposing the no-volume-change constraint we are not suppressing any information which could otherwise be extracted from the data.

Next, let us discuss the results of the inversion under constraint 2. For shallow depths the solutions indicate normal faulting with tension approximately perpendicular to the spreading center. They do, however, contain important strike slip components and suggest significant departures from a pure double-couple source mechanism. We can also observe a marked rotation of the axes as depth increases from 1 to 7 km below the seafloor. Examination of the individual moment tensor components reveals that as depth decreases, the solution becomes increasingly dominated by the M_{xz} and M_{yz} components. The reason for the instability of the inversion of the imaginary part for shallow sources has been discussed above.

In order to avoid problems due to the poor resolution of M_{xz} and M_{yz} we tried performing the inversion under constraint 4, assuming a normal faulting mechanism ($\phi_{ij} = 0.5$ cycles for all i and j). For both events, the solution for a depth of 1 to 7 km below seafloor is very stable: double-couple normal faulting along a strike parallel to that of the spreading center. The moments increase regularly with depth; for a depth of 7 km (4 km below seafloor) the moments are 4.8 and 7.5 $\times$ 10^{24} dyn cm for the 1970 and 1972 events, respectively.

The solutions at 80 km under constraints 2 and 4 indicate primarily non-double-couple source mechanisms and do not bear any apparent relationship to the local geologic setting. The interchanging of the compression and tension axes relative to the shallow solutions (constraint 4) indicates that the ambiguity in determination of depth from the minimum in

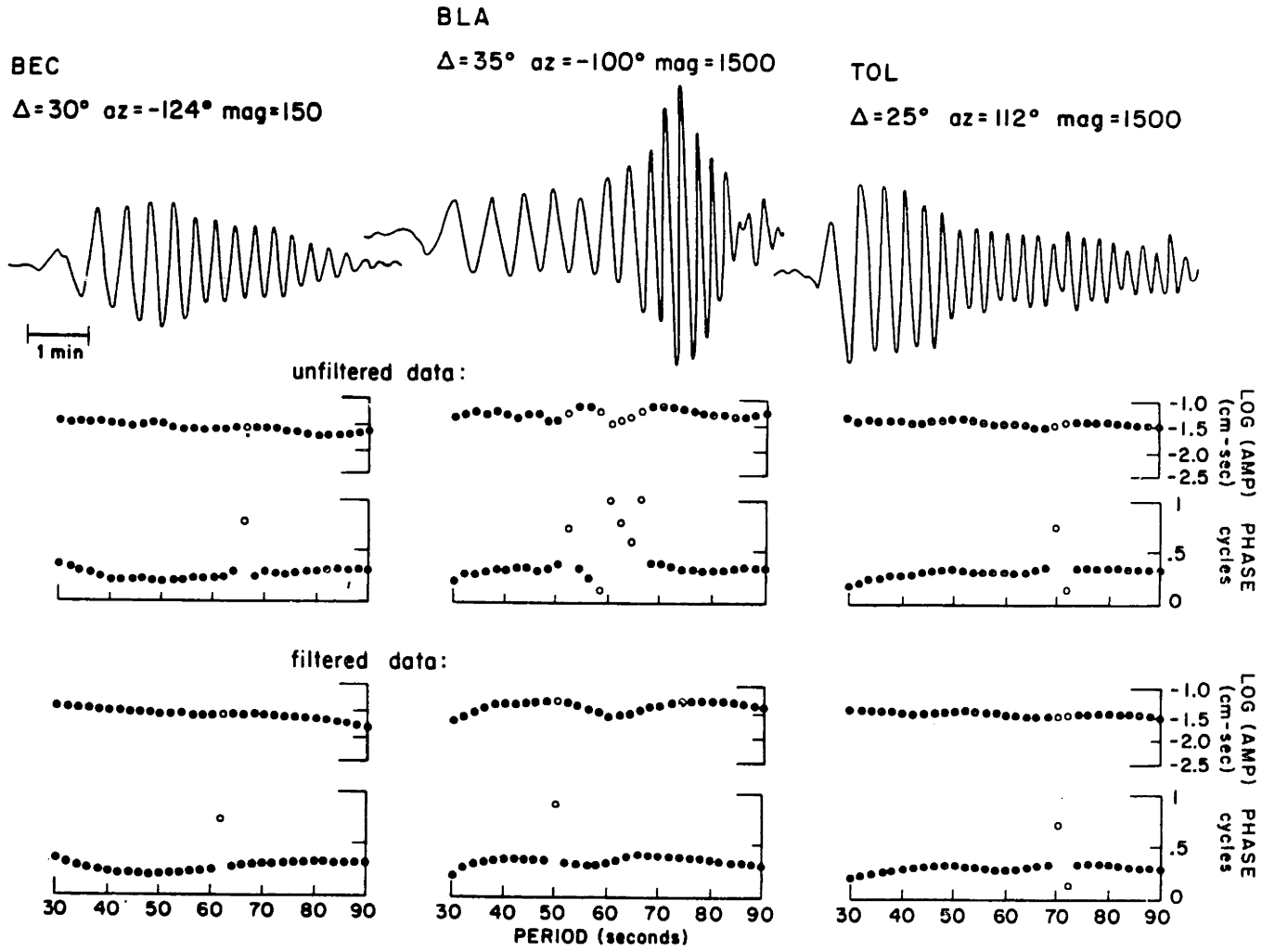

Fig. 5b. Examples of seismograms and corrected source spectra for the April 3, 1972, event. Source spectra obtained from filtered records are also shown.

the residuals of the surface wave inversion is a direct result of the similar behavior, with opposite sign, of G_1 and G_2 for both shallow and deep sources. In the next section we will see that the body waves are not compatible with a deep source and the solutions at 80 km will not be considered further.

Discussion

The fault plane solutions corresponding to the moment tensors obtained under constraints 2 and 4 for a depth of 7 km are superimposed on the observed *P* wave fault plane solutions in Figures 7*a* and 7*b*. We can see that the *P* wave first-motion pattern for the 1972 event displays the nonorthogonal nodal planes characteristic of mid-ocean ridge normal faulting events (Figure 7*b*). For the 1970 event, the data coverage is less complete, and the observed nodal planes are poorly constrained but are consistent with a normal faulting solution requiring nonorthogonal nodal planes. The large strike slip component in both moment tensor solutions under constraint 2 implies a pronounced asymmetry in the *P* wave radiation pattern which is not observed. Except for the observed nonorthogonality, the *P* wave first-motion patterns are consistent with the results of the surface wave inversion under constraint 4.

It has been noted that the residuals of the inversion are smaller under constraints 3 and 4 than under 1 and 2, implying that by separating the observed spectrum into its real and imaginary parts one is actually adding noise to the real part. An examination of the fit of the solution to the data, expressed both as real and imaginary part and as amplitude and phase, provides insights into this behavior. For the 1970 event (Figure 8), the observed value of the imaginary part is generally greater than that of the model (Figure 8*a*), and the phase is about 0.1 cycle less (Figure 8*b*). From (2) an origin time error of 5 s can result in a 0.1-cycle underestimation of the initial phase delay for a 50-s wave. If the true initial phase delay is 0 or 0.5 cycles, the result of such an error in the real part is to underestimate the amplitude and consequently the moment. That this is indeed happening is clear in Figure 8*b*, where the amplitude data are compared to the solutions calculated under constraints 2 and 4.

By comparing Figures 8*a* and 9*a* to Figures 8*b* and 9*b*, we see that the variation in the imaginary part of the spectrum with azimuth leading to large M_{xz} and M_{yz} components is primarily controlled by the variation in phase and that stations in the Caribbean (215° to 230° azimuth) are particularly important in defining this pattern. These stations have long earthquake-station paths relative to most of the other data used in this study and therefore have a greater potential error

TABLE 4*a*. Results of the Moment Tensor Inversion for the April 24, 1970, Event

	Depth Below Seafloor (Constraint)									
	4 km (4)	4 km (3)	4 km (2)	4 km (1)	1 km (4)	1 km (2)	7 km (4)	7 km (2)	77 km (4)	77 km (2)
					Moment Tensor Components, 10^{24} dyn cm					
M_{xx}	4.83 ± 0.10	4.94 ± 5.11	3.88 ± 0.17	4.74 ± 8.68	3.86 ± 0.08	3.14 ± 0.14	5.71 ± 0.12	4.58 ± 0.20	−13.9 ±0.4	−12.1 ±0.7
M_{xy}	−1.03 ± 0.09	−1.03 ± 0.09	−0.46 ± 0.15	−0.46 ± 0.16	−0.87 ± 0.08	−0.39 ± 0.13	−1.22 ± 0.11	−0.55 ± 0.19	4.2 ± 0.4	1.9 ± 0.7
M_{yy}	0.47 ± 0.10	0.58 ± 5.13	−0.54 ± 0.17	0.33 ± 8.73	0.20 ± 0.08	−0.58 ± 0.14	0.45 ± 0.12	−0.70 ± 0.20	4.2 ± 0.4	6.1 ± 0.7
M_{xz}	...	...	2.67 ± 0.65	2.67 ± 0.65	...	10.3 ± 2.50	...	2.53 ± 0.61	...	0.7 ± 0.2
M_{yz}	...	...	−4.47 ± 0.66	−4.47 ± 0.66	...	−17.3 ± 2.56	...	−4.24 ± 0.62	...	−1.1 ± 0.2
M_{zz}	−5.30 ± 0.09	−4.81 ± 23.8	−3.34 ± 0.15	0.67 ± 40.40	−4.05 ± 0.07	−2.56 ± 0.12	−6.16 ± 0.10	−3.88 ± 0.18	9.6 ± 0.2	6.1 ± 0.3
					Eigenvalues, 10^{24} dyn cm					
Tension	5.06 ± 0.10	5.17 ± 4.87	5.53 ± 0.53	7.21 ± 14.11	4.05 ± 0.09	19.39 ± 2.53	5.98 ± 0.12	5.83 ± 0.46	9.6 ± 0.2	7.3 ± 0.4
Intermediate	0.24 ± 0.10	0.34 ± 4.89	1.43 ± 0.49	2.78 ± 8.35	0.00 ± 0.09	1.79 ± 0.48	0.18 ± 0.12	1.27 ± 0.51	5.2 ± 0.4	5.1 ± 0.4
Compression	−5.30 ± 0.09	−4.81 ± 23.80	−6.96 ± 0.63	−4.25 ± 20.95	−4.05 ± 0.07	−21.18 ± 2.54	−6.16 ± 0.10	−7.9 ± 0.59	−14.8 ± 0.4	−12.1 ± 0.7
					Eigenvectors (Strike°/Dip°)					
Tension	−77± 1/0	−77 ± 19/0	−64 ± 6/26 ± 2	−59 ± 218/35 ± 26	−77 ± 1/0	37 ± 8/42 ± 4	−78 ± 1/0	−70 ± 5/21 ± 1	0/90	4 ± 5/43 ± 8
Intermediate	13 ± 1/0	13 ± 19/0	37 ± 3/22 ± 6	49 ± 251/24 ± 82	13 ± 1/0	58 ± 3/5 ± 6	12 ± 1/0	30 ± 3/25 ± 5	12 ±1/0	−171 ± 2/48 ± 8
Compression	0/90	0/90	162 ± 2/54 ±4	165 ± 156/45 ± 81	0/90	154 ± 3/47 ± 5	0/90	164 ± 2/56 ± 4	−78 ± 1/0	96 ± 2/2 ± 2
					Percent					
Double couple	91	91	59	53	100	83	94	64	30	18
CLVD	9	4	41	21	0	17	6	36	70	82
Explosion	–	5	–	26	–	–	–	–	–	–
Double-couple scalar moment, 10^{24} dyn cm	4.8	4.7	4.1	3.8	4.1	17.6	5.8	4.5	4.4	2.2

TABLE 4*b*. Results of the Moment Tensor Inversion for the April 3, 1972, Event

	Depth Below Seafloor (Constraint)									
	4 km (4)	4 km (3)	4 km (2)	4 km (1)	1 km (4)	1 km (2)	7 km (4)	7 km (2)	77 km (4)	77 km (2)
					Moment Tensor Components, 10^{24} dyn cm					
M_{xx}	7.84 ± 0.16	7.99 ± 7.73	7.32 ± 0.18	7.12 ± 8.90	6.43 ± 0.14	6.08 ± 0.16	9.04 ± 0.19	8.46 ± 0.21	−23.3 ± 0.7	−24.3 ± 0.8
M_{xy}	−0.71 ± 0.12	−0.71 ± 0.12	−1.60 ± 0.14	−1.60 ± 0.14	−0.61 ± 0.11	−1.37 ± 0.12	−0.83 ± 0.15	−1.67 ± 0.17	3.1 ± 0.6	6.9 ± 0.6
M_{yy}	0.49 ± 0.16	0.64 ± 0.12	−1.28 ± 0.18	−1.48 ± 9.35	0.21 ± 0.14	−1.27 ± 0.16	0.35 ± 0.19	−1.64 ± 0.21	8.0 ± 0.7	12.7 ± 0.8
M_{xz}	...	...	−8.85 ± 0.81	−8.85 ± 0.61	...	−34.3 ± 3.15	...	−8.35 ± 0.76	...	−2.0 ± 0.2
M_{yz}	...	...	−5.96 ± 0.99	−5.96 ± 0.99	...	−23.2 ± 3.87	...	−5.59 ± 0.81	...	−1.3 ± 0.2
M_{zz}	−8.33 ± 0.13	−7.69 ± 33.6	−6.04 ± 0.15	−6.90 ± 38.6	−6.64 ± 0.11	−4.80 ± 0.13	−9.39 ± 0.15	−6.82 ± 0.17	15.4 ± 0.3	11.6 ± 0.3
					Eigenvalues, 10^{24} dyn cm					
Tension	7.91 ± 0.16	8.06 ± 7.66	11.86 ± 0.69	11.52 ± 10.67	6.49 ± 0.14	40.64 ± 3.31	9.12 ± 0.19	12.16 ± 0.60	15.4 ± 0.3	14.7 ± 0.6
Intermediate	0.42 ± 0.16	0.57 ± 8.05	1.60 ± 0.66	1.33 ± 8.85	0.15 ± 0.14	2.24 ± 0.71	0.27 ± 0.19	1.26 ± 0.61	8.3 ± 0.7	10.9 ± 0.3
Compression	−8.33 ± 0.13	−7.69 ± 33.60	−13.47 ± 0.88	−14.10 ± 26.01	−6.64 ± 0.11	−42.88 ± 3.44	−9.39 ± 0.15	−13.42 ± 0.75	−23.7 ± 0.7	−25.6 ± 0.8
					Eigenvectors (Strike°/Dip°)					
Tension	95 ± 1/0	95 ± 8/0	83 ± 3/28 ± 1	83 ± 67/27 ± 12	96 ± 1/0	62 ± 5/42 ± 2	95 ± 1/0	87 ± 3/24 ± 1	0/90	12 ± 1/27 ± 1
Intermediate	5 ± 1/0	5 ± 8/0	−18 ± 3/21 ± 3	−17 ± 45/20 ± 37	6 ± 1/0	−33 ± 3/5 ± 4	5 ± 1/0	−14 ± 3/23 ± 2	6 ± 1/0	−175 ± 1/62 ± 3
Compression	0/90	0/90	−140 ± 3/54 ± 3	−139 ± 89/55 ± 44	0/90	−129 ± 4/47 ± 3	0/90	−141 ± 3/55 ± 2	96 ± 1/0	−80 ± 2/3 ± 3
					Percent					
Double couple	90	90	76	75	95	90	94	81	30	15
CLVD	10	6	24	22	5	10	6	19	70	85
Explosion	–	4	–	3	–	–	–	–	–	–
Double-couple scalar moment, 10^{24} dyn cm	7.5	7.3	10.2	10.6	6.3	38.6	8.8	10.9	7.1	3.8

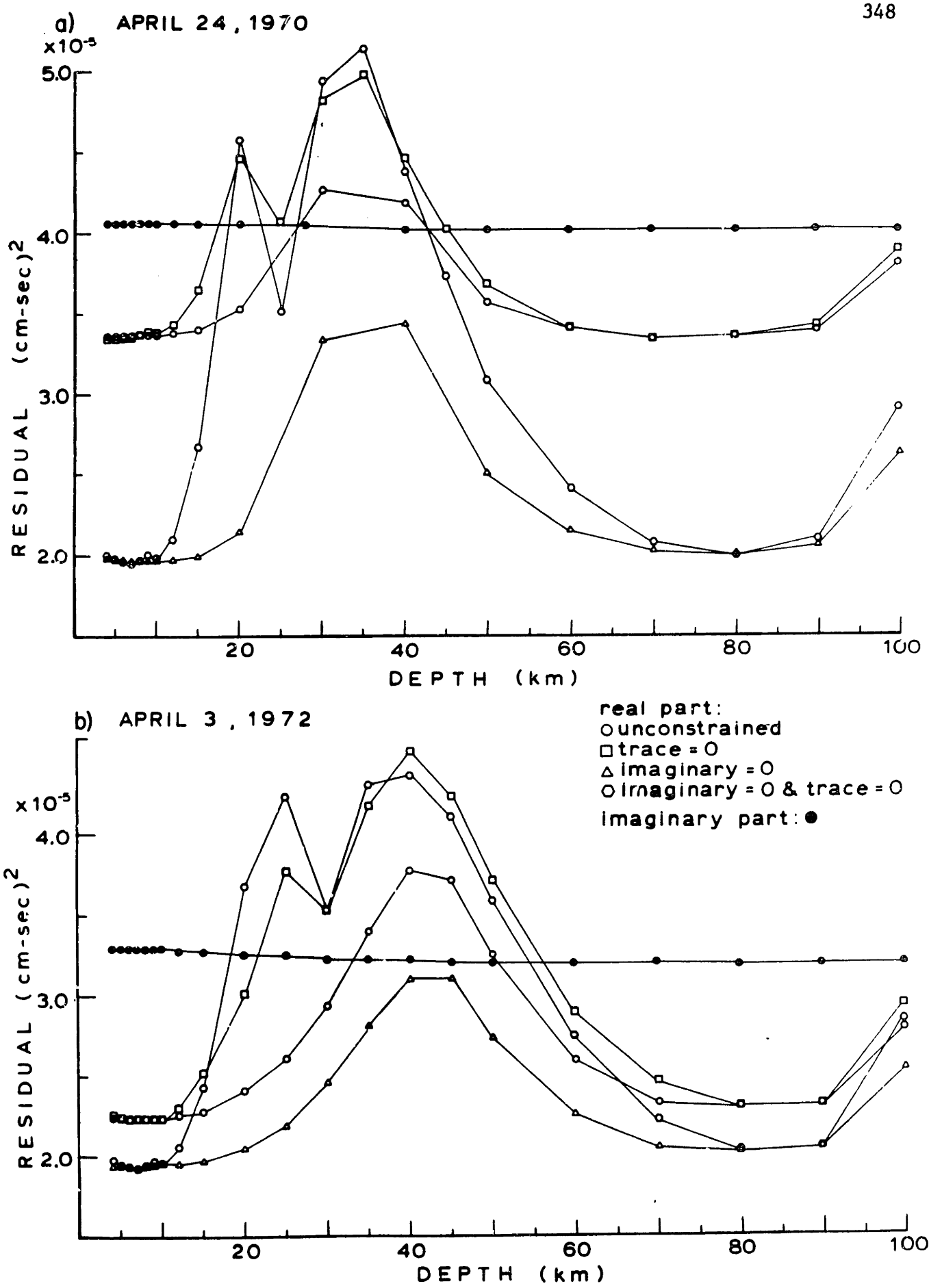

Fig. 6. (*a*) Residuals versus focal depth for the inversion of the Rayleigh wave radiation pattern to obtain the moment tensor for the April 24, 1970, event. (*b*) Residuals versus focal depth for the April 3, 1972, event.

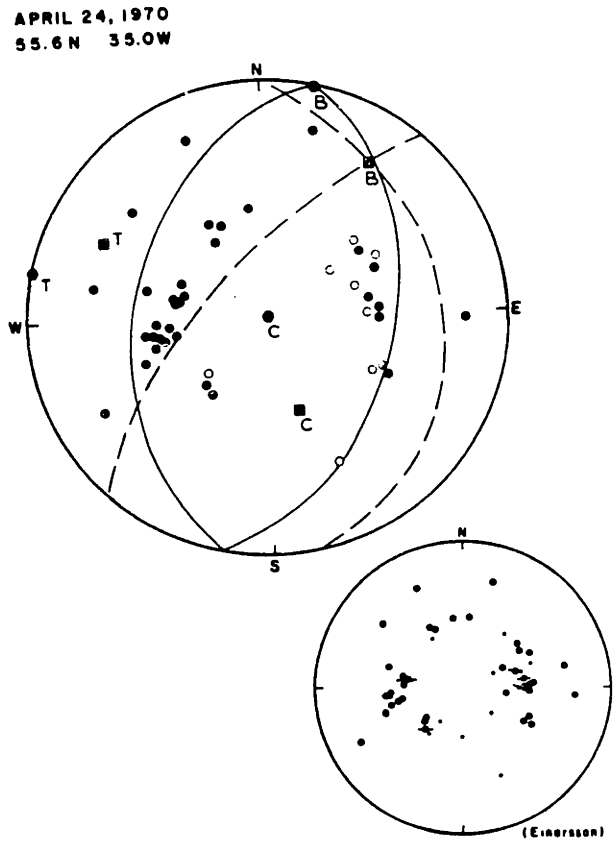

Fig. 7*a*. Fault plane solution for the April 24, 1970, event. Superimposed are the axes and double-couple fault plane solutions corresponding to the results of the moment tensor inversion under constraints 2 and 4 for a focal depth of 4 km below the seafloor. Dashed line and solid square, constraint 2; solid line and hexagon, constraint 4. T is tension; B is intermediate; C is compression. Closed circles indicate compressional first motion of the *P* wave. Open circles indicate stations for which the first motion was originally thought to be compressional but for which this interpretation was subsequently modified when considering the moment tensor solution and the expected amplitude of the first motion as predicted by synthetic seismograms. In the lower right-hand corner is the fault plane solution presented by *Einarsson* [1979]. Large dots signify clear arrivals, whereas small dots indicate less reliable picks. Arrows indicate *S* wave polarization angles.

due to phase velocity errors. Moreover, the phase velocity over the Caribbean portion of the path is poorly known. *Weidner* [1974] found anomalous phase velocities for paths to stations in the Caribbean from earthquakes along the Mid-Atlantic Ridge at 35°N and 15°N and attributed this to anomalously thick sediment cover. Inclusion of his model into the regionalization further decreases the initial phase at station CAR by about 0.23 cycles at 40 s, where the effect is maximum, and by 0.05 cycles at 80 s. Another possible source of error in the initial phase is epicentral mislocation; a mislocation of 12 km will impart a sinusoidal variation to the corrected initial phase with a maximum amplitude of about 0.1 cycles at 30 s and 0.04 cycles at 80 s.

If the true initial phase were close to 0.5 cycles at all azimuths, these errors would dominate the behavior of the imaginary part and induce additional noise on the real part. That the residuals decrease when the inversion is performed under constraints 3 and 4 suggests that this is indeed happening to some degree for the events studied in this paper. Although the sources for the two events studied may indeed contain minor M_{xz} and M_{yz} components, the values obtained from the inversion of the imaginary part seem to be overestimated, and we are unable to resolve their magnitude from our data.

Before proceeding to the body wave analysis, we should examine the effect on the inversion of the no-volume-change constraint when the source actually contains a volume change component, because this constraint must usually be imposed to resolve the diagonal components of the moment tensor. For a shallow explosive source with moment tensor

$$M_0 \begin{bmatrix} 1 & 0 & 0 \\ 0 & 1 & 0 \\ 0 & 0 & 1 \end{bmatrix}$$

the inversion should yield a solution of

$$b \cdot M_0 \begin{bmatrix} \frac{1}{2} & 0 & 0 \\ 0 & \frac{1}{2} & 0 \\ 0 & 0 & -1 \end{bmatrix}$$

which corresponds to a compensated linear vector dipole (CLVD) with compression along the z axis and tension along

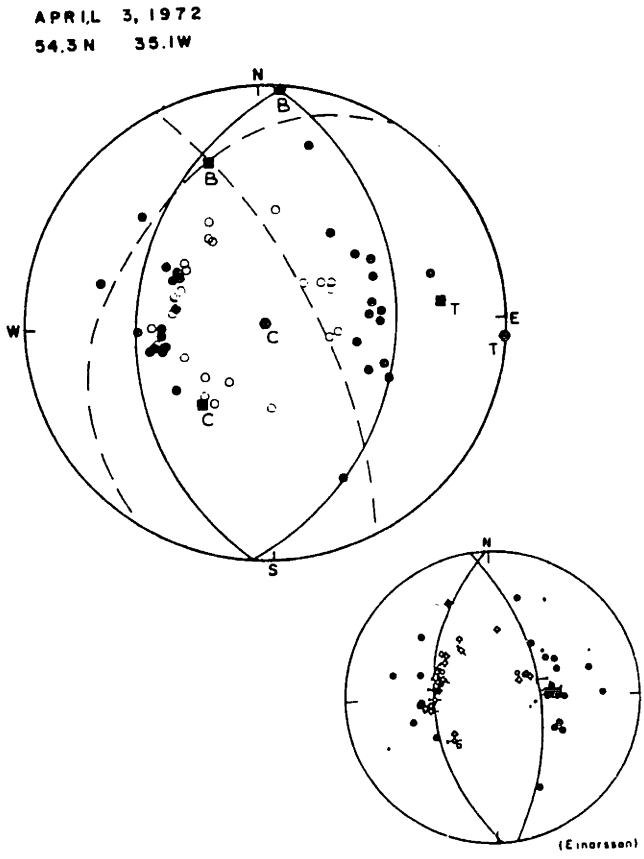

Fig. 7*b*. Fault plane solution for the April 3, 1972, event. Superimposed are the axes and nodal planes corresponding to the results of the moment tensor inversion for a focal depth of 4 km below the seafloor. Solid circles indicate compressional first motion of the *P* wave; open circles indicate dilatational first motion. Apparent nodal planes separated by approximately 60° are constrained by the data. In the lower right-hand corner is the fault plane solution presented by *Einarsson* [1979]: solid circles are compression; open circles are dilatation; crosses are nodal.

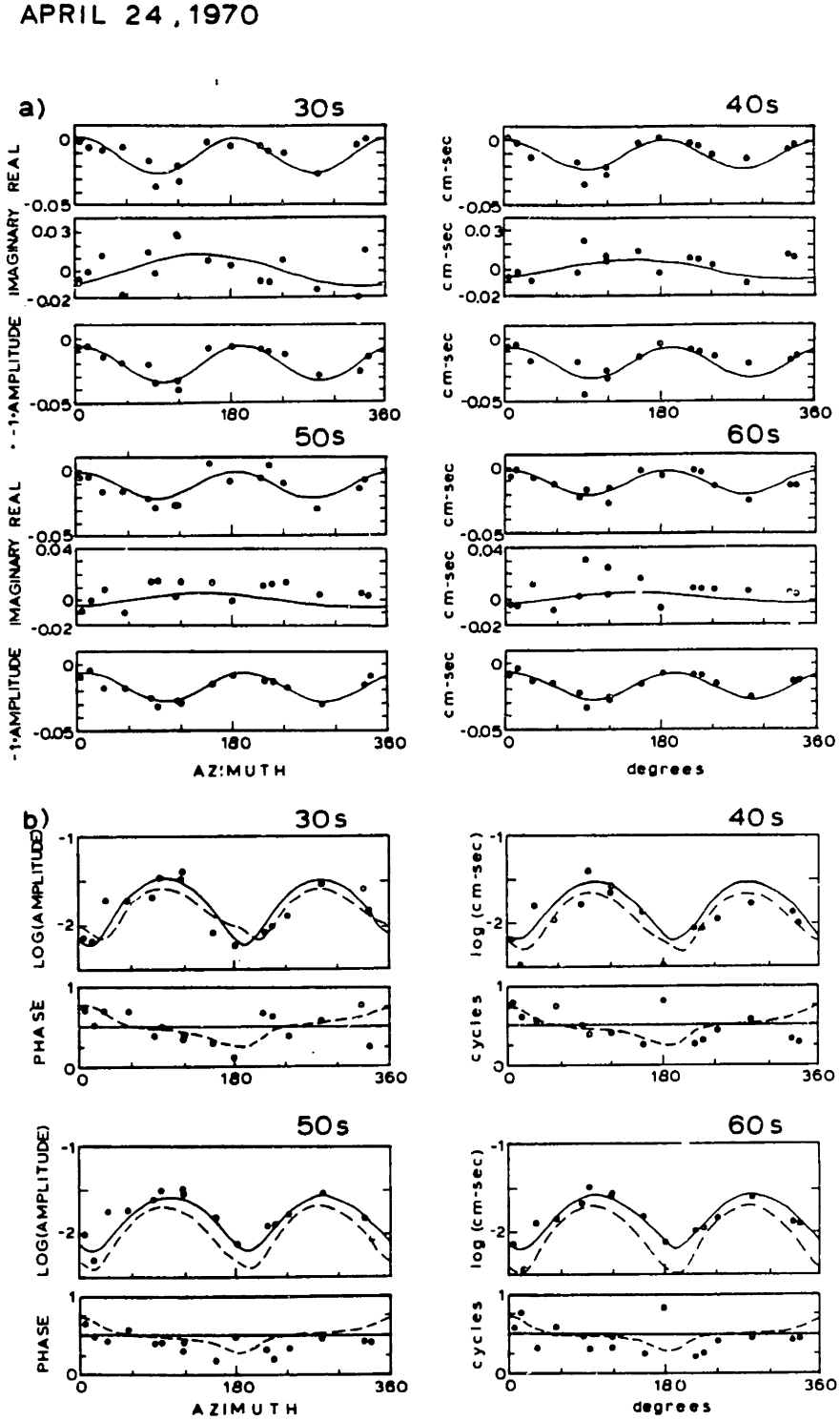

Fig. 8. (*a*) Examples at several periods of the fit of the moment tensor solution to the observed data for the April 24, 1970, event for a depth of 4 km below seafloor. Plots of the real and imaginary parts versus azimuth illustrate the fit when the inversion is performed under constraint 2; plots of negative amplitude versus azimuth show the result under constraint 4 (real part = amplitude, imaginary part = 0). Open circles indicate data that were weighted by zero during the visual inspection of the spectra. (*b*) Fit of the model to the data recast into the form of amplitude and phase: the solution under constraint 2 is given by dashed lines, the solution under constraint 4 is given by solid lines.

x and y. The factor b depends on depth and is close to 1 for a shallow source [*Patton*, 1978]. An explosion should be clearly distinguishable from a double-couple both with and without the no-volume-change constraint. A vertical tension crack in the y-z plane corresponds to the sum of a CLVD, with tension along x and compression along y and z, and an explosion. Under the $\sum_{i=1}^{3} M_{ii} = 0$ constraint, the explosive component will masquerade as a CLVD with compression along z; the sum of the two CLVD, assuming $b = 1$ and $\lambda = \mu$, is

$$M_0 \begin{bmatrix} 13/6 & 0 & 0 \\ 0 & 1/6 & 0 \\ 0 & 0 & -14/6 \end{bmatrix}$$

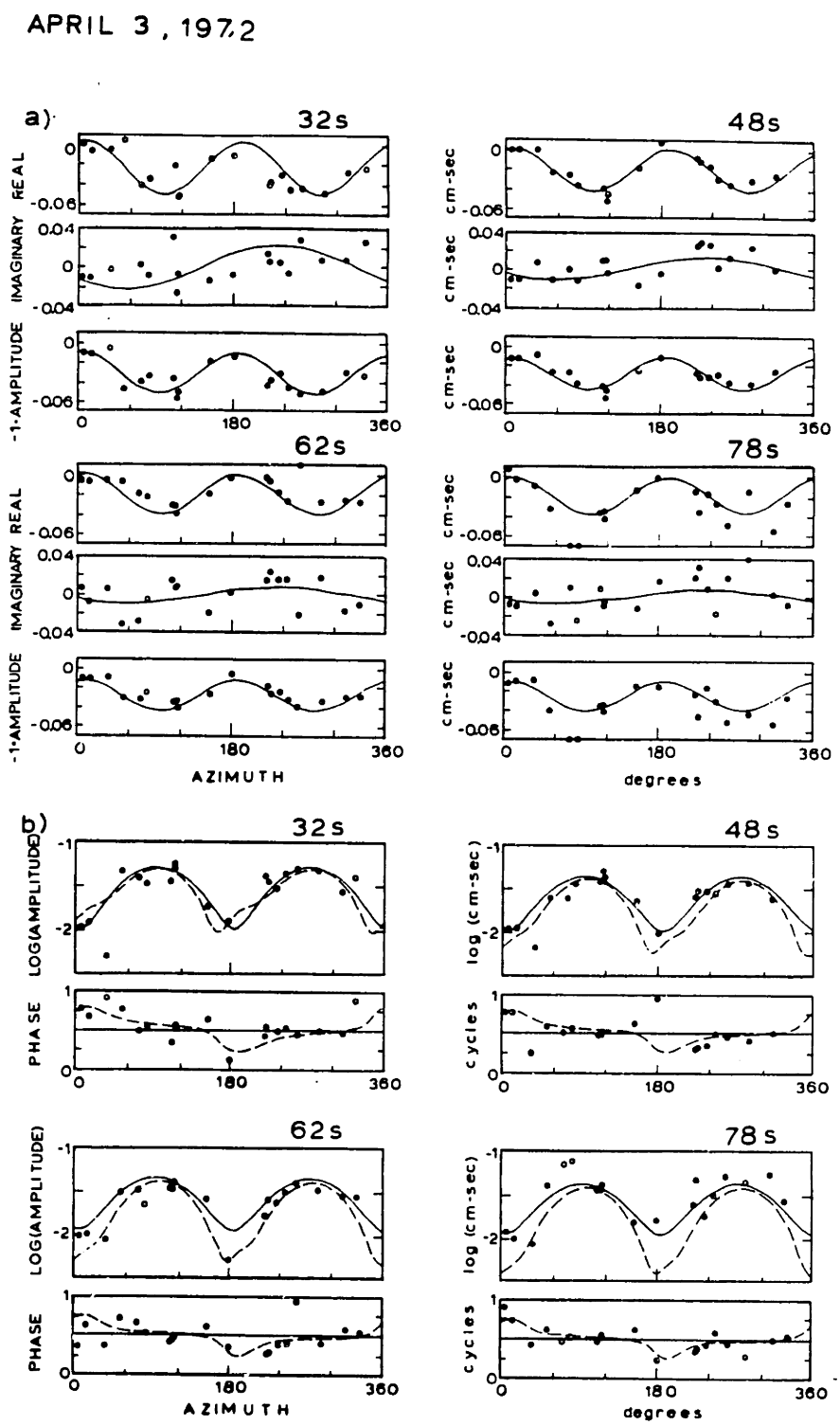

Fig. 9. Examples of the fit to the data of the moment tensor solution for the April 3, 1972, event for a depth of 4 km below seafloor (see caption to Figure 8).

resembling a source with 86% double-couple mechanism. For the events studied in this paper, the double-couple component of the source remains stable when the no-volume-change constraint is removed, and the CLVD component distributes itself between the new CLVD and the explosive components; moreover, the double-couple component increases as the residuals decrease. This suggests that the sources were primarily double couple and that noise in the data is appearing as apparent non-double-couple components.

In summary, the inversion of the surface waves to obtain the source moment tensor for two events on the Reykjanes Ridge indicates double-couple source mechanisms corresponding to normal faulting along planes with a dip of about 45° and strike parallel to the local strike of the spreading center. Both events appear to have been very shallow (1–7 km below seafloor). This study has demonstrated the difficulty in resolving M_{xz} and M_{yz} components of the moment tensor for very shallow events using data that are less than perfect. Be-

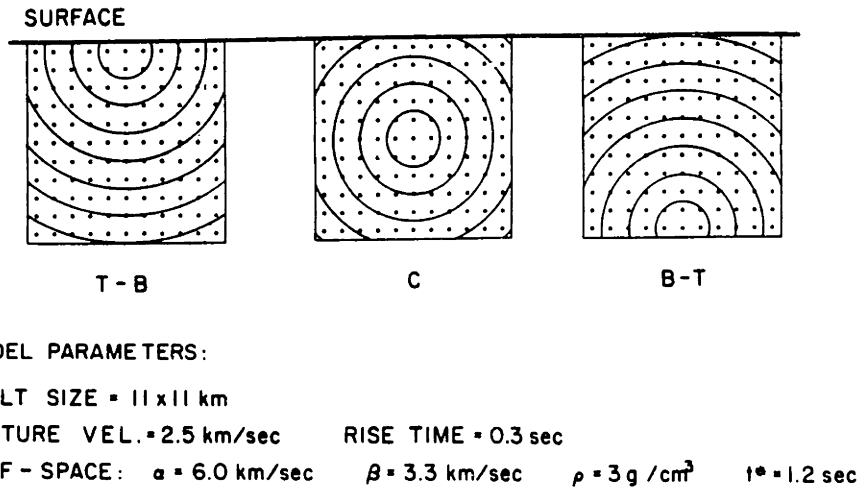

Fig. 10. Model parameters and fault geometry used in the example of *P* wave synthesis for a shallow, finite earthquake source. Circles are successive rupture fronts. Rupture propagates from top to bottom (T-B), from the center (C), and from bottom to top (B-T) in the three cases shown.

cause errors in the corrected initial phase due to mislocation and origin time errors alone are large enough to severely affect the determination of M_{xz} and M_{yz}, the corrected source phase obtained using a regionalized phase velocity model is not sufficiently accurate to resolve these two components of the moment tensor. We have not determined whether the regionalized model is adequate for slightly deeper events for which the inversion is not inherently plagued by this problem.

Body Wave Analysis

Background

A striking feature discerned in the surface wave analysis of the two mid-ocean ridge events is the exceptionally shallow focal depth. This result suggests that interference between the direct and reflected body wave phases, as proposed by *Hart* [1978], might be responsible for the apparently nonorthogonal nodal planes. For a dip slip fault, arrivals reflected from the surface at the epicenter can have much larger amplitudes than and opposite polarities to the direct arrivals. If the source is shallow, the temporal separation of the arrivals is less than the pulse width of the impulse resonse of the long-period WWSSN seismometer convolved with the attenuation operator. The arrivals interfere destructively and the apparent nodal planes can be shifted well into the dilatational quadrant. *Langston* [1976] used such interference to constrain the depth of the 1967 Koyna, India, earthquake and cautioned that the interference could lead to errors when determining fault plane solutions from first-motion polarities for earthquakes with shallow focal depths.

We first present a simple hypothetical case of a shallow dip slip fault in a homogeneous half space and show that the interaction of surface reflections with the direct arrivals can indeed cause an apparent reversal of the first-motion polarity at certain take-off angles. We then demonstrate that the surface wave and the body wave observations can be reconciled for the April 3, 1972, earthquake if the event originated near the ocean floor. Although the April 24, 1970, event was too small to be suitable for quantitative modeling by synthetic seismograms, a qualitative inspection of the observed *P* waves suggests that interference could be reponsible for the apparent reversal of first-motion polarity.

The method used to calculate the synthetic seismograms is an extension of the point-source formulation of *Bouchon* [1976] to a finite fault. Seismograms are calculated by numerical integration of point sources distributed on a rectangular grid approximating the fault area. Rupture propagation is simulated by progressively firing individual point sources in a circular pattern radiating from the rupture origin with an appropriate rupture velocity. In order to approximate a smooth rupture, the grid spacing must be such that the firing intervals are smaller than the shortest period important to the problem. As attenuation and the response of the long-period WWSSN instrument effectively filter out periods shorter than 4s, a grid spacing of 1 km is appropriate for a rupture velocity between 2 and 3 km/s. The method incorporates the propagator matrix formulation [*Haskell*, 1953] for computation of the crustal response at the source and receiver and is particularly well

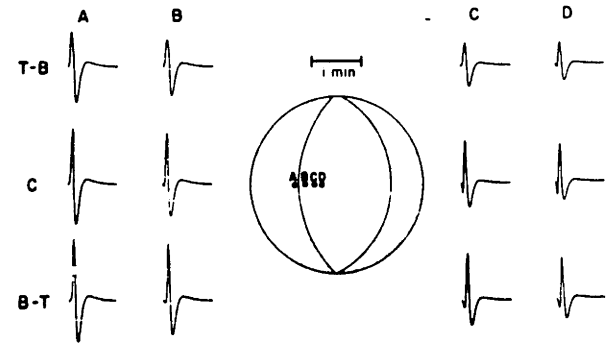

Fig. 11. Theoretical seismograms for models described in Figure 10. The dip of the fault is 55°. Also shown is the theoretical fault plane solution; points A, B, C, and D represent projections of ray paths for which seismograms were calculated. T-B, C, and B-T signify rupture propagation radiating from top-to-bottom, from the center, and from bottom-to-top, respectively.

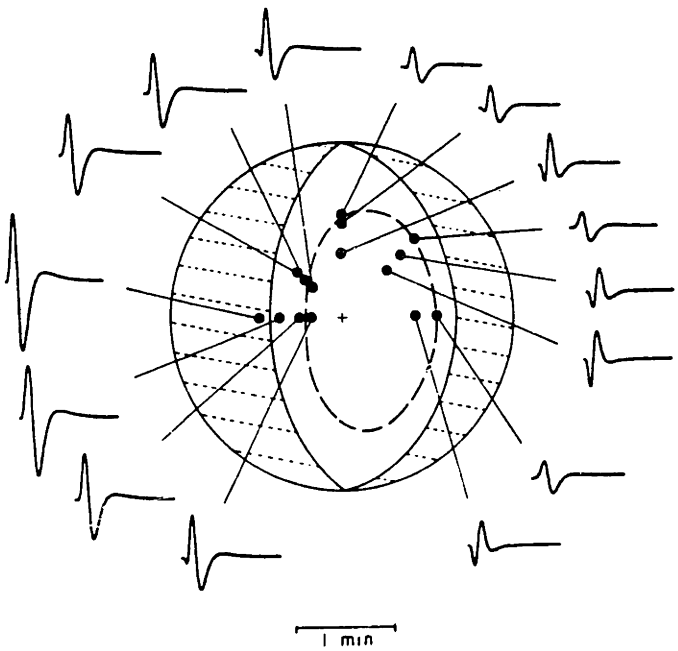

Fig. 12. Theoretical seismograms for case T-B in Figure 10 illustrating the apparent distortion of the fault plane solution due to interference between the direct and reflected phases. Solid line is the true fault plane solution, whereas dashed line delimits the apparent dilatational quadrant. The dip of the fault is 55°.

suited for crustal structures which cause extensive reverberation (e.g., structures with a water layer). A more detailed description of the method is presented in Appendix B.

The fault geometry and the medium parameters used in the example are shown in Figure 10. The fault is an 11 by 11 km rectangle which is located in a homogeneous half space and whose top edge reaches the surface. The rupture velocity is 2.5 km/s (0.8 times the shear velocity of the medium). Each point source has a rise time of 0.3 s. We have investigated three possible situations (Figure 10): rupture initiation (1) at the top, (2) in the center, and (3) at the bottom of the fault. Figure 11 shows synthetic *P* wave seismograms calculated for the three models depicted in Figure 10. Also shown are the theoretical nodal planes and the projections of the ray paths onto the focal sphere. The dip of the fault is 55°. In all figures the calculated seismograms begin at the time of the first expected arrival. No motion will be observed at that time if interference is canceling the first motion. In the examples, the seismograms are equalized to a common radius on the focal sphere, and the vertical-horizontal scale ratio is kept constant; the relative variations in amplitude for different ray paths are as shown.

Points B, C, and D lie within the theoretical dilatational quadrant, and we would therefore expect to observe downgoing first pulses. This is indeed what we observe when the rupture initiates at the center or at the bottom of the fault. An important aspect of the finite source model which influences the relative amplitude of the direct and reflected arrivals is vertical directivity; downward rupture propagation increases the amplitudes and shortens the effective time functions of the direct arrivals and decreases the amplitudes and lengthens the effective time functions of the reflected arrivals whereas upward propagation has the opposite effect. Because of directivity, the first motion has a larger amplitude if the rupture initiates at the center than at the bottom. Although directivity enhances direct arrivals most when rupture propagates from top to bottom, it plays a secondary role if the hypocenter is very shallow. In this case, destructive interference between the direct arrivals and surface reflections effectively masks the direct arrivals for certain take-off angles. First arrivals along ray paths B and C appear to be compressional, although they lie well within the theoretical dilatational quadrant. The nodal plane appears to be shifted into the dilatational quadrant by approximately 15°. Figure 12 illustrates the distortion of the fault plane solution for 55° dipping fault with rupture initiating near the free surface. If noise were superimposed on the signal, the observable dilatational quadrant would be further reduced.

The fault geometry and medium parameters affect the degree to which interference influences the waveform. For large faults, the finiteness and directivity strongly influence the radiation pattern. Because the vertical directivity for a rupture propagating from top to bottom increases the amplitude of the direct arrivals, decreasing the width of the fault will diminish this effect and increase the amount of observed nonorthogonality. Effects which increase the effective rise time will also cause an emergent direct *P* arrival and may further contribute to the distortion of the apparent dilatational quadrant (e.g., higher attenuation, lower rupture velocity, and longer rise time).

To apply the results for a normal fault to thrust faulting, only the polarity of the seismograms must be changed. These results can also be generalized to include earthquakes originating beneath low-velocity layers such as water or sediment, the base of which provides sufficient impedance contrast to produce large reflections. The predicted distortion of the apparent first motions, however, applies only to normal and thrust faults. For strike slip faults, the direct *P* and *sP* have the same polarity and, while *pP* has opposite polarity, its amplitude is too small to entirely cancel the direct arrival.

Data

The *P* wave fault plane solution based on long-period observations from the earthquake of April 3, 1972, is shown in

TABLE 5. Stations Used for the Body Wave Analysis of April 3, 1972, Earthquake

Station	Azimuth, deg	Distance, deg	Magnification
	WWSSN Network		
ATU	87.5	42.6	1500
BKS	−67.6	58.6	3000
CAR	−137.8	50.5	3000
COL	−30.7	50.3	1500
DUG	−71.9	51.8	3000
IST	80.2	43.6	1500
JER	84.5	53.6	3000
KBL	58.1	70.1	6000
NUR	54.2	31.7	1500
OXF	−95.1	42.2	3000
QUE	62.4	72.5	6000
QUI	−130.7	65.0	3000
SCP	−97.8	31.2	1500
TRI	85.1	32.0	3000
TUC	−80.2	56.2	1500
	Canadian Network		
EDM	−57.9	43.8	4500
FFC	−61.5	37.0	4200
FSJ	−51.3	48.3	3400

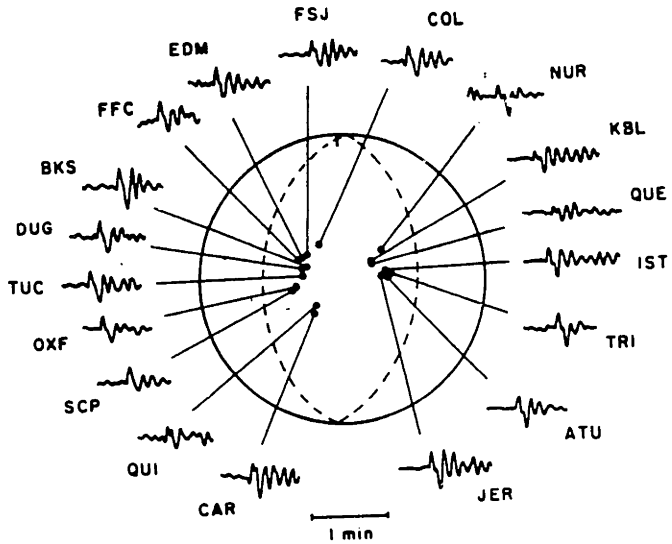

Fig. 13. Examples of long-period *P* wave seismograms (vertical component) observed for the April 3, 1972, event. Seismograms were equalized by correcting for geometrical spreading and for differences in the seismometer magnifications. Dots indicate projections of ray paths to the given stations. Also shown is the preferred fault plane solution.

Figure 7*b* and exhibits characteristically nonorthogonal nodal planes. Examples of the *P* waveforms used in the body wave analysis (Table 5) are shown in Figure 13. Several seconds of background noise preceding each *P* arrival are shown in order to illustrate the signal-to-noise ratio. This event is among the largest recorded on the Mid-Atlantic ridge and provides the best possible data from this tectonic region. In order to avoid complications due either to core or upper mantle structure, only stations at epicentral distances between 30° and 80° were used [*Burdick and Helmberger*, 1978]. Seismograms were equalized by correcting for differences in instrument magnification and for geometrical spreading. The correction for geometrical spreading was calculated using the formula of *Carpenter* [1966] and the *P* wave travel times of *Herrin* [1968]. The similarity in shape and amplitude of seismograms from neighboring stations indicates that background noise and crustal structure below the receivers do not significantly affect the observations. One nodal plane appears to pass through stations OXF and FFC; first motions at stations TUC, DUG, and EDM begin to show a dilatational character, whereas BKS, CAR, and COL are clearly dilatational. The other apparent nodal plane passes between stations KBL and JER. The monochromatic oscillations in the later portion of the seismogram are due to reverberation within the water layer.

Results

The synthesized seismograms are compared to the observations in Figure 14. The best overall match was obtained with a source mechanism compatible with that obtained from the surface wave inversion under constraint 4. The model parameters used in the synthesis are shown in Figure 15. The data do not enable us to determine which of the two nodal planes corresponds to the actual fault plane, and the westward dipping plane was arbitrarily chosen.

The match between the synthetic and observed waveforms is quite good. The fact that the observations tend to show a larger amplitude for the water reverberations than the theoretical seismograms indicates that the fault broke the seafloor. In the calculation of theoretical seismograms, the fault stops just below the surface of the seafloor; a finite displacement of the seafloor would enhance the amplitude of water arrivals. The period of the water reverberations constrains the water depth to be 2.8 km, in good agreement with the bathymetric data (Figure 1). The best overall match was obtained for a fault length of 13 km and a width of 3 km with rupture initiating near the seafloor and propagating bilaterally. We assumed a rupture velocity of 2.6 km/s (0.8 of the shear wave velocity). If the rupture propagation were not perfectly bilateral, the fault could be somewhat shorter. Unilateral rupture propagation, however, does not fit the observations, as it would require a noticeable directivity effect for stations with northern and southern azimuths. The width of the fault is constrained by the observed nonorthogonality. Keeping the other parameters unchanged, the width can be increased to 4 km without significant deterioration of the overall match. Lowering the rupture velocity may further slightly increase the maximum acceptable width and decrease the length. For a 44° dip this bound on width implies that the fault is confined to the upper 3 km or less of the crust.

Figure 16*a* illustrates the sensitivity of the solution to the fault geometry. For the 13 × 3 km fault, the effect of vertical directivity is negligible, and interference between the direct and reflected phases determines the apparent nonorthogonality. For a 6-km-wide fault with rupture propagation from top to bottom, however, the downward directivity enhances the amplitude of the direct arrival, so that it can be observed at take-off angles corresponding to the examples in Figure 16*a*. For bottom-to-top propagation, the direct and reflected arrivals from a 6-km-wide fault are sufficiently separated in time for the direct arrival to be observed. (Although top-to-bottom rupture propagation matches the observed seismograms better than bottom-to-top propagation for a 3 km wide fault, we do not ascribe any tectonic significance to this observation).

In Figure 16*a* we can also see that a model of a point source below the seafloor at a depth of 0.35 km matches the observed data as well as the 13 × 3 km finite fault model. This is not surprising, since for such a narrow fault the effect of vertical directivity is negligible. Although one might argue that extension of the point source model to a finite fault is therefore not justified, for this event we are able to constrain the fault geometry by using a finite fault model, and we feel that this added information is useful for understanding the tectonic processes involved.

The seismograms in Figure 16*b* were calculated for the moment tensor obtained from the surface wave inversion under constraint 2 for a depth of 4 km below seafloor (Table 4*b*). The overall match is worse than that for the solution under constraint 4, supporting the conclusion that the magnitude of the M_{xz} and M_{yz} components of the moment tensor is indeed an artifact of their poor resolution for shallow sources.

The average moment from the body wave analysis is 7.5×10^{24} dyn cm, the same as that obtained from the surface waves. This moment corresponds to about 60 cm of average displacement on the fault. The body wave moment was calculated by normalizing the amplitude of the synthetic seismograms to the first upgoing pulse of the observed *P* waves. The variation in the moment obtained from individual stations (Figure 14) indicates that the average value may be in error by as much as 50%.

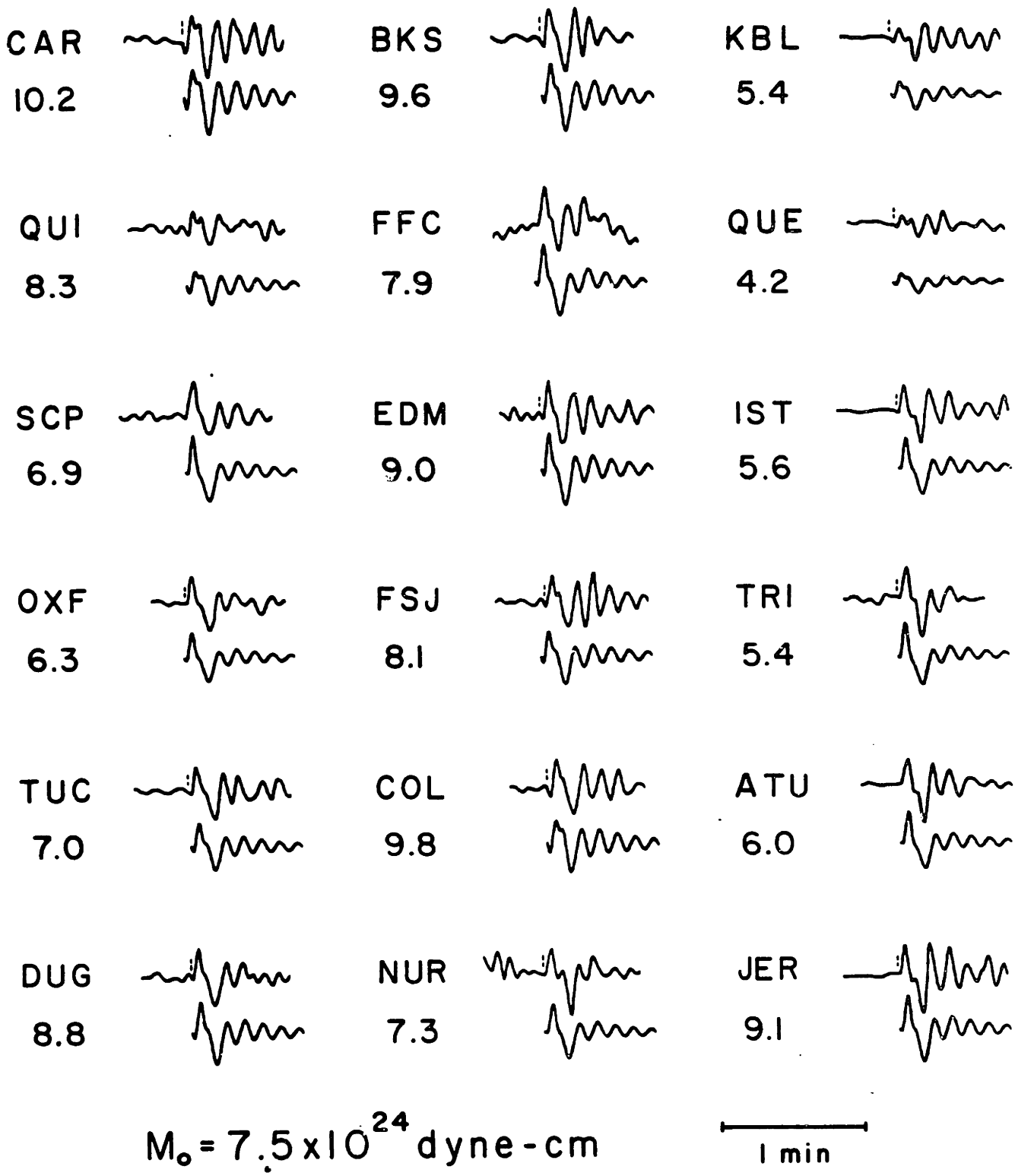

Fig. 14. Theoretical seismograms (vertical component) compared to observed *P* wave data for the April 3, 1972, event. Upper trace is observed; lower trace is calculated. Seismograms were equalized to a seismometer magnification of 3000. Numbers below the station names corresponded to moment (in units of 10^{24} dyn cm) at the given station, and M_0 is the average moment. Dotted lines on the observed seismograms indicate the time of the first motion observed on the short-period vertical component.

For a dip slip fault the stress drop can be expressed as

$$\Delta\sigma = \frac{4(\lambda + \mu)M_0}{\pi(\lambda + 2\mu)LW^2} \quad (3)$$

where λ and μ are the Lame's constants, M_0 is the scalar seismic moment of the double couple, and L and W are the length and width of the fault [*Knopoff*, 1958]. Allowing for the uncertainties discussed above, the stress drop is between 30 and 60 bars. This stress drop is similar to that found for other interplate events [*Kanamori and Anderson*, 1975].

The attenuation correction was applied by keeping a constant value of $t^* = T/Q$, where T is the travel time and Q is

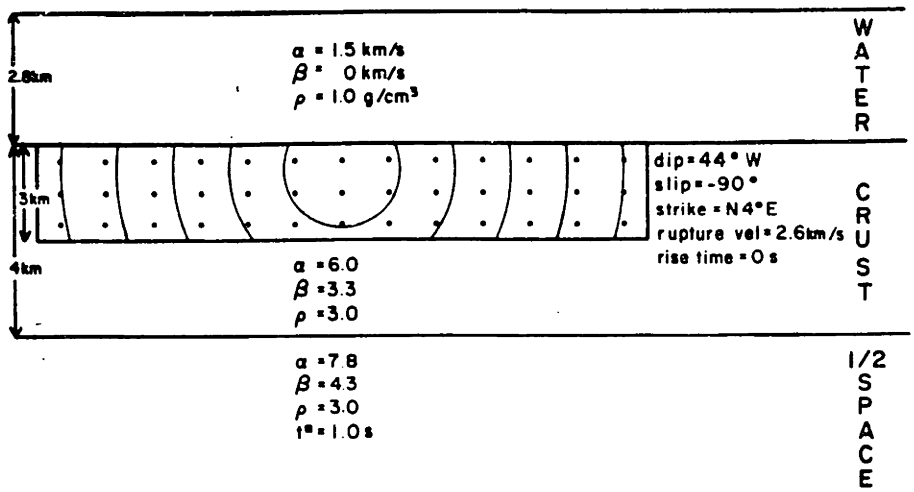

Fig. 15. Model parameters used for the calculation of the theoretical seismograms shown in Figure 14. The indicated fault width is measured downdip and the fault is projected onto a vertical plane parallel to the strike of the fault. Dots represent individual point sources. Fault length is 13 km. The medium structure below the receivers is a homogeneous halfspace with $\alpha = 6$ km/s, $\beta = 3.46$ km/s, and $\rho = 3$ g/cm^3.

the average quality factor along the path. A t^* of 1 s yielded a satisfactory match to the observed data, whereas a value larger than this produced overly smooth synthetic waveforms.

We have also examined the short-period seismograms. At most stations, a low-energy first arrival followed about 1.5 s later by a much stronger arrival was observed (Figure 17). The short-period first-motion arrival time corresponds well to the expected first-motion time indicated by the synthetic long-period records (Figure 14). In order to determine whether the larger arrival could be a depth phase, we calculated seismograms using the instrument response of the WWSSN short-period seismometer but were not able to match the observations by either a simple point source or a smoothly rupturing fault. A match could be obtained only if we assumed a discontinuous rupture process. Because of the large degree of nonuniqueness involved in modeling short-period seismograms, we did not pursue this analysis further.

A poor signal-to-noise ratio for the *P* waves from the April 24, 1970, earthquake made them unusable for quantitative waveform modeling. However, because of the similarity of the source mechanisms deduced from the source moment tensor inversions, we used the synthetic waveforms calculated for the April 3, 1972, event for a qualitative comparison. Examples of seismograms corresponding in distance and azimuth to those used to model the April 3, 1972, event are shown in Figure 18. If the amplitude of the background noise and expected ampli-

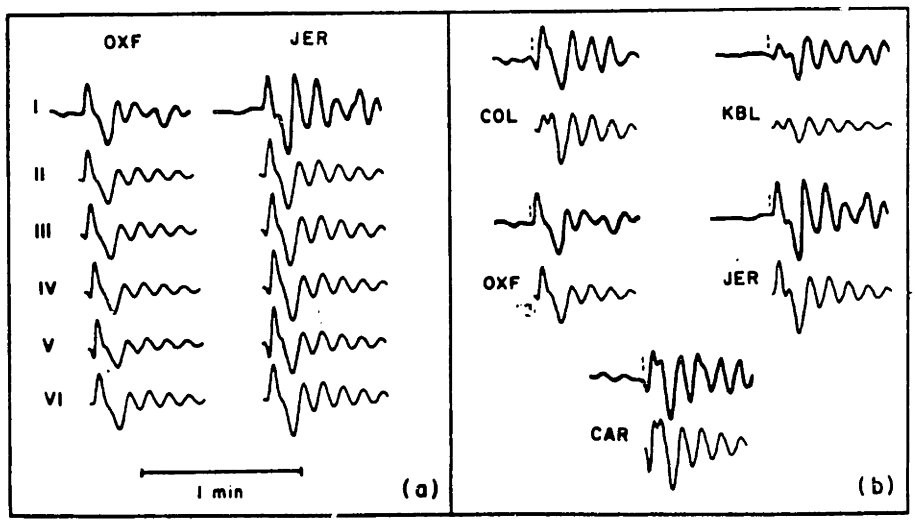

Fig. 16. (*a*) Theoretical *P* wave seismograms calculated for several fault geometries compared to the observed data (seismogram I). Fault dimensions are 13-km length by 3-km width for seismograms II and III and 7-km length by 6-km width for IV and V. Seismograms II and IV were calculated for rupture initiating at the top of the fault, whereas III and V were calculated for rupture initiating at the bottom. Other parameters are the same as in Figure 15. Seismogram VI was calculated for a point source at a depth of 0.35 km below seafloor and a triangular time function with a 0.8-s rise and 1.8-s roll-off. (*b*) Theoretical *P* wave seismograms (lower trace) calculated for the moment tensor obtained from the Rayleigh wave inversion under constraint 2 (Table 4*b*, 4 km below sea floor) compared to the observed data at several representative stations (upper trace). The seismograms were calculated for a point source with the same depth and time function as in Figure 16*a*. The fit is worse than that for constraint 4 (Figure 14). For example, constraint 2 requires that station CAR be further within the dilatational quadrant than is indicated by the data and that KBL have the wrong first-motion polarity.

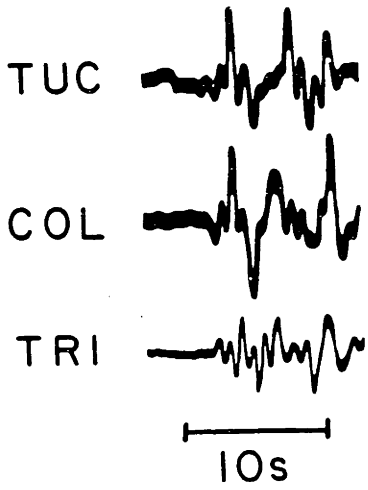

Fig. 17. Examples of short-period *P* wave seismograms (vertical component) for the April 3, 1972, event. Seismograms are direct copies of observed records.

tude of the first arrival are considered, it is not surprising that all the first motions were originally picked to be compressional. First motion polarity determinations at several stations were later revised to be 'possible' dilatations (e.g., KBL, TAB; Figure 18). The observed waveforms can qualitatively be explained by a shallow fault, similar to that deduced for the April 3, 1972 event.

Discussion

In summary, the body waveforms for the April 3, 1972, Mid-Atlantic ridge earthquake can be matched without invoking anomalous ray propagation if the source is confined to the upper 3 km or less of the crust. The nonorthogonality of the *P* wave fault plane solution can be entirely explained in terms of interference between the direct and reflected phases. Because of the trial-and-error technique used in the *P* wave analysis we must, however, admit the possibility of nonuniqueness in the solution.

The moment tensor inversion from the surface waves show that the source was consistent with a pure double-couple mechanism. Because of the long periods used in the surface wave inversion, however, one might argue that a small precursor with an explosive or tensile mechanism could cause the nonorthogonality of the *P* wave nodal planes and not be observable by the surface waves. Although this is a valid argument, it is not easy to prove because precursors of any mechanism would cause an emergent *P* wave which, especially for a shallow source, would be very difficult to pick. The agreement between the arrival time measured on the short-period records and that predicted by the synthetic seismograms argues against this explanation.

Thermal models of mid-ocean ridges and observed attenuation of teleseismic *S* waves passing under the southern Reykjanes Ridge [*Solomon*, 1973] suggest that we might also expect high attenuation of teleseismic *P* waves. The *P* wave attenuation ($t^* = 1$ s), however, does not appear to be larger than average. The results for *P* and *S* waves are not necessarily contradictory. If the low *Q* zone in the vicinity of the ridge crest is caused by partial melting, the compressional waves should be less affected than shear waves.

Our results do not exclude the possibility of a small amount of focusing contributing to the nonorthogonality. This would allow a slightly wider fault than that indicated by our analysis. We prefer that shallowness of the source be the explanation for the anomalous *P* wave fault plane solutions because of the simplicity of such a mechanism and because of the agreement between the results of the body wave synthesis and surface wave inversion.

CONCLUSIONS

The major conclusions of this study are the following:

1. The source moment tensor can be retrieved from the Rayleigh wave radiation pattern for a single isolated event. This method of obtaining the source mechanism is useful for small events for which the body wave fault plane solutions may be inconclusive and/or perplexing. For very shallow sources, however, the M_{xz} and M_{yz} components become poorly resolved and very sensitive to errors in the data; moreover, the three diagonal components cannot be independently determined. By comparing the results of the inversion performed under a series of increasingly more stringent constraints, we are able to qualitatively evaluate the validity of imposing constraints which lead to a stable solution.

2. The final moment tensor solutions for two events along the southern Reykjanes Ridge indicate double-couple, normal faulting mechanisms with the tension axis approximately horizontal and oriented perpendicular to the spreading center. For both events, the surface waves indicate a focal depth of 1–7 km below the seafloor.

3. The nonorthogonality of the nodal planes frequently observed in the body wave fault plane solutions for mid-ocean ridge normal faulting events can be attributed to extreme shallowness of the source which results in interference between the direct and reflected phases and effectively masks the first-motion recorded on long-period seismograms.

4. Comparison of observed *P* waveforms from the April 3, 1972, Reykjanes Ridge event to those calculated for a fault with an orientation obtained from the surface wave analysis indicates that the source was a long, narrow fault which broke the seafloor.

The faulting process implied by these results provides additional constraints on models of spreading center tectonics and thermal structure. The double-couple nature of the solutions relates these earthquakes to tectonic rather than volcanic processes and supports the evidence from seismicity and topography which associates teleseismically observable ridge-crest activity with rift valley formation. An important question about mid-ocean ridges concerns the depth of hydrothermal circulation and its effect on the thermal structure of the crust. The close agreement between observed ridge crest topography and that calculated for the simple model of a con-

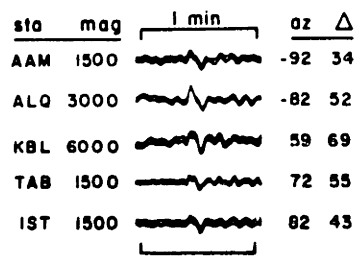

Fig. 18. Examples of long-period *P* wave seismograms recorded for the April 24, 1970, earthquake. Seismograms are direct copies of observed vertical component records. Mag is station magnification, az is station azimuth, and Δ is epicentral distance.

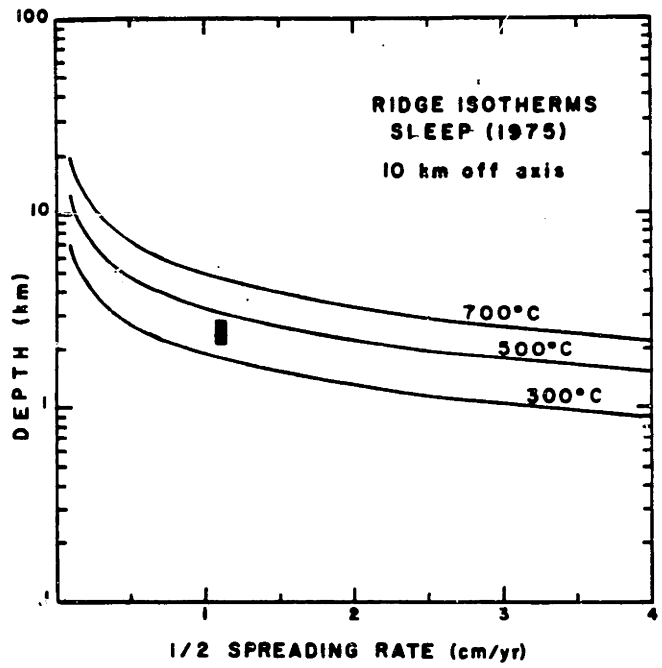

Fig. 19. Depth to various isotherms at a distance of 10 km from the ridge axis versus spreading rate, calculated for the thermal model of *Sleep* [1975]. Also indicated is the depth of faulting, 2.1–2.8 km, corresponding to the 3- to 4-km-wide fault obtained for the April 3, 1972, event. Figure modified from *Solomon and Burr* [1979].

ductively cooling slab suggests that extensive hydrothermal circulation is restricted to the top few kilometers of the crust [*Fehn and Cathles*, 1979]. On the other hand, deep (5–8 km) hydrothermal circulation has been invoked in order to depress the isotherms enough to produce a cold brittle layer of sufficient thickness to support faults with the dimensions implied by the moments of the largest spreading center events if it is assumed that length-width ratios and stress drops are similar to those observed for other plate boundary earthquakes [*Solomon*, 1979]. The long, narrow fault plane suggested by an analysis of the body waves from the earthquake on the Reykjanes Ridge, however, can be entirely accommodated within the brittle crust determined from the purely conductive model of *Sleep* [1975] if it is assumed that the earthquake occurred 10 km from the axis, along the rift valley walls (Figure 19). An as yet unanswered question is whether the length-width ratio will increase with increasing moment; the largest earthquake studied from this region had a moment of 2×10^{25} dyn cm [*Hart*, 1978], approximately twice that of the larger event studied here. Further studies of fault dimensions, stress drops, and recurrence intervals for ridge earthquakes in regions spanning a range of spreading rates should permit the incorporation of time-dependent faulting and stress release in models which simulate the spreading process and are used to explain the relationship between spreading rate, topography, and magma supply [e.g., *Sleep and Rosendahl*, 1979].

APPENDIX A: MOMENT TENSOR SOURCE REPRESENTATION AND SURFACE WAVE RADIATION

The displacement at y at time ζ in the direction $\hat{k}$ due to a seismic source at time t can be represented as

$$u_k(\mathbf{y}, \zeta) = \int_{-\infty}^{\infty} dt \left\{ \int_V dV_x G_{kj}(\mathbf{y}, \zeta; \mathbf{x}, t) \gamma_j'(\mathbf{x}, t) + \int_S dS_x G_{kj}(\mathbf{y}, \zeta; \mathbf{x}, t) \gamma_j'(\mathbf{x}, t) \right\} \quad \text{(A1)}$$

where V is the source volume, S is the surface of the source volume, γ_j' and γ_j' are the equivalent volume and surface forces corresponding to a physical mechanism, $G_{kj}(\mathbf{y}, \zeta; \mathbf{x}, t)$ is the impulse response or Green's function of the medium, and repeated indices imply summation [*Aki and Richards*, 1980]. If the 'moment density tensor' $\mathbf{m}$ is defined to be a symmetric tensor such that $m_{ij,j} = -\gamma_j'$ in V and $n_i m_{ij} = \gamma_j'$ on S ($\mathbf{n}$ being the unit normal to the surface), we can regroup the expression for displacement into one term using Gauss's theorem [*Backus and Mulcahy*, 1976]:

$$\begin{aligned} u_k(\mathbf{y}, \zeta) &= \int_{-\infty}^{\infty} \left\{ -\int_V dV_x G_{kj} m_{ij,j} + \int_S dS_x G_{kj} n_i m_{ij} \right\} dt \\ &= \int_{-\infty}^{\infty} \left\{ -\int_V dV_x G_{kj} m_{ij,j} + \int_V dV_x (G_{kj} m_{ij})_{,i} \right\} dt \\ &= \int_{-\infty}^{\infty} dt \int_V dV_x m_{ij} G_{kj,i} = \int_{-\infty}^{\infty} dt\, M_{ij} G_{kj,i} \end{aligned} \quad \text{(A2)}$$

For an effective point source, the 'moment tensor' $\mathbf{M}$ can be defined as the integral of the moment density tensor over the source volume and surface and can be retrieved from the far-field displacement radiation pattern (for free oscillations, see *Gilbert* [1970] and *Gilbert and Dziewonski* [1975]; for surface waves, see *McCowan* [1976] and *Mendiguren* [1977]; for body waves, see *McCowan* [1977] and *Strelitz* [1978]). The advantage of this representation is that the inversion of far-field displacements to obtain the moment tensor is linear and is not dependent on a presupposed source mechanism.

We can then relate observed moment tensors derived from data to phenomenological source models through the equivalent body forces. Although the total equivalent force is uniquely determined from the resulting motion, the interpretation in terms of a phenomenological source model, however, is not unique, as a given moment tensor can result from several different linear combinations of moment tensors. This ambiguity is inherent in any determination of source mechanism from the displacement field [*Aki and Richards*, 1980].

If we assume that the principal stress axes of the various components are coincident, the diagonalized moment tensor can be uniquely decomposed into isotropic, double-couple, and compensated linear vector dipole components. We first remove the isotropic part:

$$\begin{aligned} \mathbf{M}' &= \mathbf{M} - \tfrac{1}{3}(\text{trace } \mathbf{M})\mathbf{I} \\ &= M_0 \begin{bmatrix} 1 & 0 & 0 \\ 0 & f-1 & 0 \\ 0 & 0 & -f \end{bmatrix} \qquad 0 \le f \le \tfrac{1}{2} \end{aligned} \quad \text{(A3)}$$

where $\mathbf{I}$ is the identity matrix. We may then separate the double couple and compensated linear vector dipole components [*Knopoff and Randall*, 1970]:

$$M' = M_0 \left\{ (1-2f) \begin{bmatrix} 1 & 0 & 0 \\ 0 & -1 & 0 \\ 0 & 0 & 0 \end{bmatrix} + 2f \begin{bmatrix} 1 & 0 & 0 \\ 0 & -\frac{1}{2} & 0 \\ 0 & 0 & -\frac{1}{2} \end{bmatrix} \right\} \quad \text{(A4)}$$

The double-couple scalar moment M_{DC} is $(1-2f)M_0$, and the corresponding fault plane solution can be obtained from the principal axes of the moment tensor. M_{DC} can be related to the dimensions of a shear fault: $M_{DC} = \mu\bar{u}A$, where μ is the shear modulus, $\bar{u}$ is average displacement, and A is fault area [*Aki*, 1966].

In this study, the moment tensor is derived from the surface wave radiation pattern. For a vertically heterogeneous earth, the Fourier spectrum of the vertical component of the fundamental Rayleigh wave due to a point source with a step function source time function is

$$u(r, \theta, \omega) = Ae^{i\phi} = \frac{Y_1(0, \omega)}{4CUI\omega} [2/(\pi kr)]^{1/2} \exp [-i(\omega r/C - \pi/4)]$$

$$\cdot \left\{ (M_{xx} + M_{yy}) \frac{kY_3(h, \omega)}{2} + M_{zz} \frac{-Y_2(h, \omega) - \lambda(h)kY_3(h, \omega)}{\lambda(h) + 2\mu(h)} \right.$$

$$- (M_{yy} - M_{xx}) \frac{kY_3(h, \omega) \cos 2\theta}{2} + M_{xy} kY_3(h, \omega) \sin 2\theta$$

$$\left. -i \left[M_{xz} \frac{Y_4(h, \omega) \cos \theta}{\mu(h)} + M_{yz} \frac{Y_4(h, \omega) \sin \theta}{\mu(h)} \right] \right\} \quad \text{(A5)}$$

where A and ϕ are the observed amplitude and phase at the angular frequency ω and the M_{ij} are the moment tensor components in Cartesian coordinates with the x, y, and z axes pointed east, north, and up [*Mendiguren*, 1977]. The position of the receiver is expressed in polar coordinates, where r is distance and θ is azimuth measured counterclockwise from east. The $Y_i(h, \omega)$ are the eigenfunctions derived by *Saito* [1967] for the surface wave excitation problem and are functions of angular frequency and depth h; $\lambda(h)$ and $\mu(h)$ are the Lamé coefficients; $\omega^2 I$, k, C, and U are the kinetic energy, wave number, phase velocity, and group velocity. The moment tensor components can be retrieved through a linear inversion of the real and imaginary parts of the observed radiation pattern if a good azimuthal distribution of stations is available.

Appendix B: Method of *P* Wave Synthesis for Finite Sources

A fundamental assumption in calculations of teleseismic body waves from shallow sources is that only the free surface and the crustal and uppermost mantle structure at the source and receiver have a significant effect on the shape of the seismograms. Gradients within the mantle are considered to be too small to cause converted or reflected phases and travel time caustics, and the effect of the mantle portion of the propagation path is restricted to geometrical spreading and attenuation. For epicentral distances between 30° and 80° these assumptions are well justified [*Burdick and Helmberger*, 1978]. The synthetic seismogram is obtained by convolution of the response of the source $U(t)$ with the responses of the receiver $I(t)$, the crust below the receiver $R(t)$, attenuation $A(t)$, and geometrical spreading G.

Our technique for calculating source response is an extension of the formulation of *Bouchon* [1976] for a double-couple point source to a finite fault with circular rupture propagation. Contributions from point sources distributed along the fault surface on an equally spaced grid are numerically integrated. Rupture propagation is simulated by progressively firing individual point sources in a circular pattern radiating from the origin with a constant rupture velocity. In order to approximate a smooth rupture, the grid spacing must be such that the firing intervals are smaller than the shortest period important to the problem. The integration is performed in the frequency domain and then transformed back into the time domain. This enables efficient use of the propagator matrix algorithm of *Haskell* [1953] to obtain the response of the medium. This approach is particularly useful for the case examined in this paper because of the prolonged ringing of the P wave in the water layer. The ray-theoretical approach [e.g., *Langston and Helmberger*, 1974] is less efficient for such a large number of rays. Although we integrate in the frequency domain, we can separate individual phases by setting appropriate potentials to zero.

The problem configuration is the same as in the work of *Bouchon* [1976]. We assume that the dislocation has the same time dependence at any point on the fault surface and can be written in the form

$$D(\xi, t) = F(\xi)E(t - |\xi - \xi_0|/c) \quad \text{(B1)}$$

Its Fourier transform is

$$\hat{D}(\xi, \omega) = F(\xi)\hat{E}(\omega) \exp (-i\omega|\xi - \xi_0|/c) \quad \text{(B2)}$$

where $\xi = (\xi_1, \xi_2)$ is a point on the fault surface, ξ_0 is the point of origin of the rupture, c is the rupture velocity, and ω is the angular frequency. The fault is a rectangle of length $L = N\Delta\xi$, parallel to the surface, and of width $W = M\Delta\xi$, dipping at an arbitrary angle; $\Delta\xi$ is the grid spacing; and N and M are integers. The far-field P wave displacement spectrum due to this source can be expressed as

$$\hat{U}(\omega) = \Delta\xi^2 \sum_{n=1}^{N} \sum_{m=1}^{M} \mu_j \hat{D}(\xi, \omega)$$

$$\cdot \exp [ik(\xi_1 \cos \phi - \xi_2 \cos d \cdot \sin \phi)]$$

$$\cdot \sum_{i=1}^{4} g_{ij}(\omega) \exp [i\Delta_{ij}(z_0 + \xi_1 \sin d)] \quad \text{(B3)}$$

with

$$\xi_1 = (n - \tfrac{1}{2})\Delta\xi \qquad \xi_2 = (m - \tfrac{1}{2})\Delta\xi$$

where z_0 is the depth to the top of the fault; k is the horizontal wave number, which is determined by the take-off angle; ϕ and d are azimuth and dip of the fault; and μ_j is the shear modulus. The subscript j refers to the layer within the crustal model in which the point source is located. The terms g_{ij} and Δ_{ij} are as defined by *Bouchon* [1976] and are related to the upgoing and downgoing P and S waves excited by a source located within the layer j.

Following the same notation, the response of the crustal layers below the receiver to an incident P wave can be written in the form

$$\hat{R}(\omega) = [(A_{21} - A_{11})\nu_1 - (B_{11} + B_{21})k]\alpha_n/\omega \quad \text{(B4)}$$

where A_{ij} and B_{ij} represent upgoing and downgoing compres-

sional and rotational potentials in the layer immediately below the receiver; ν_1 is the corresponding vertical compressional wave number; and α_n is the compressional velocity of the medium below the crustal layers.

When calculated seismograms are to be compared to observed data, a correction must be made for geometrical spreading. This is a frequency-independent term which can be expressed in the form [*Carpenter*, 1966]

$$G = \frac{\alpha_S}{r_S r_R}\left(\frac{\rho_S \alpha_S}{\rho_R \alpha_R}\frac{1}{\sin\Delta\cos i_S \cos i_R}\frac{dT}{d\Delta}\left|\frac{d^2T}{d\Delta^2}\right|\right)^{1/2} \quad \text{(B5)}$$

with

$$\sin i_S = \frac{\alpha_S}{r_S}\frac{dT}{d\Delta} \qquad \sin i_R = \frac{\alpha_R}{r_R}\frac{dT}{d\Delta}$$

where α_S, ρ_S, α_R, and ρ_R are the velocity and density of the material below the crustal layers at the source and receiver, respectively, i_S is the angle the ray makes with the vertical at the base of the crust below the source and i_R is the corresponding angle below the receiver, r_S and r_R denote the distance from the base of the crust at the source and receiver to the center of the earth, T is the P wave travel time, and Δ is the angular distance between the source and receiver.

The effect of attenuation in the mantle is introduced by the causal Q operator of *Futterman* [1962]. In the frequency domain the operator is given by

$$A(\omega) = \exp\left[-\tfrac{1}{2}t^*\left(\frac{\omega}{1+\frac{1}{\pi}\ln\frac{\omega}{\omega_0}}\right)\right]$$

$$\cdot \exp\left[it^*\omega Q\left(\frac{1}{1+\frac{\pi}{Q}\ln\frac{\omega_1}{\omega_0}} - \frac{1}{1+\frac{\pi}{Q}\ln\frac{\omega}{\omega_0}}\right)\right] \quad \text{(B6)}$$

for the angular frequency ω in the range $\omega_0 \le \omega \le \omega_1$, ω_1 and ω_0 being the highest and lowest frequencies resolved in the data. The quantity t^* is defined as T/Q, where Q is the average quality factor along the path.

Finally, the seismogram must be convolved with the appropriate instrument response; for long-period WWSSN stations we use the formula by *Hagiwara* [1958].

Acknowledgments. We thank Pall Einarsson for first drawing our attention to the unusual earthquake of April 24, 1970, and for an early preprint of his paper. We also thank Kei Aki, Doug McCowan, Howard Patton, and Gerardo Suarez for assistance with the moment tensor analysis, and Michel Bouchon for advice on body wave synthesis. This research was supported by the Division of Earth Sciences, National Science Foundation, under NSF grant EAR77-09965; by the Advanced Research Projects Agency under contract F44620-75-C-0064 administered by the Air Force Office of Scientific Research; and by fellowships from the National Science Foundation (A.M.T.) and the Alfred P. Sloan Foundation (S.C.S.).

REFERENCES

Aki, K., Generation and propagation of G waves from the Niigata earthquake of June 16, 1964, *Bull. Earthquake Res. Inst. Tokyo Univ.*, *44*, 23–88, 1966.

Aki, K., and H. Patton, Determination of seismic moment tensor using surface waves, *Tectonophysics*, *43*, 213–222, 1978.

Aki, K., and P. Richards, *Methods of Quantitative Seismology*, vol. 1, W. H. Freeman, San Francisco, Calif., 1980.

Backus, G., and M. Mulcahy, Moment tensors and other phenomenological descriptions of seismic sources, I, Continuous displacements, *Geophys. J. R. Astron. Soc.*, *46*, 341–361, 1976.

Ben-Menahem, A., and M. N. Toksöz, Source mechanism from spectra of long-period seismic surface waves, 1, Mongolian earthquake of December 4, 1957, *J. Geophys. Res.*, *67*, 1943–1955, 1962.

Ben-Menahem, A., and M. N. Toksöz, Source mechanism from spectra of long period seismic surface waves, 3, The Alaska earthquake of July 10, 1958, *Bull. Seismol. Soc. Am.*, *53*, 905–919, 1963.

Bouchon, M., Teleseismic body wave radiation from a seismic source in a layered medium, *Geophys. J. R. Astron. Soc.*, *47*, 515–530, 1976.

Burdick, L. J., and D. V. Helmberger, The upper mantle *P* velocity structure of the western United States, *J. Geophys. Res.*, *83*, 1699–1712, 1978.

Calganile, G., and G. F. Panza, Crust and upper mantle structure under the Baltic shield and Barents Sea from dispersion of surface waves, *Tectonophysics*, *47*, 59–71, 1978.

Carpenter, E. W., A qualitative evaluation of teleseismic explosion record, *Proc. R. Soc., Ser. A*, *290*, 396–407, 1966.

Einarsson, P., Seismicity and earthquake focal mechanisms along the mid-Atlantic plate boundary between Iceland and the Azores, *Tectonophysics*, *55*, 127–153, 1979.

Fehn, U., and L. M. Cathles, Hydrothermal convection at slow-spreading mid-ocean ridges, *Tectonophysics*, *55*, 239–260, 1979.

Forsyth, D. W., The early structural evolution and anisotropy of the oceanic upper mantle, *Geophys. J. R. Astron. Soc.*, *43*, 102–162, 1975.

Francis, T. J. G., The seismicity of the Reykjanes Ridge, *Earth Planet. Sci. Lett.*, *18*, 119–124, 1973.

Futterman, W. I., Dispersive body waves, *J. Geophys. Res.*, *67*, 5279–5291, 1962.

Gilbert, F., Excitation of the normal modes of the earth by earthquake sources, *Geophys. J. R. Astron. Soc.*, *22*, 223–226, 1970.

Gilbert, F., and A. M. Dziewonski, An application of normal mode theory to the retrieval of structural parameters and source mechanism from seismic spectra, *Phil. Trans. R. Soc. London, Ser. A*, *278*, 187–269, 1975.

Gregersen, S., Surface wave dispersion and crust structure in Greenland, *Geophys. J. R. Astron. Soc.*, *22*, 29–39, 1971.

Hagiwara, T., A note on the theory of the electromagnetic seismograph, *Bull. Earthquake Res. Inst. Tokyo Univ.*, *36*, 139–164, 1958.

Hart, R., Body wave studies of the September, 1969, North Atlantic Ridge earthquake (abstract), *Eos Trans. AGU*, *59*, 1135, 1978.

Haskell, N. A., The dispersion of surface waves in multilayered media, *Bull. Seismol. Soc. Am.*, *43*, 17–34, 1953.

Herrin, E., Introduction to '1968 Seismological tables for *P* phases,' *Bull. Seismol. Soc. Am.*, *58*, 1193–1241, 1968.

Kafka, A. L., and D. J. Weidner, The focal mechanisms and depths of small earthquakes as determined from Rayleigh wave radiation patterns, *Bull. Seismol. Soc. Am.*, *69*, 1379–1390, 1979.

Kanamori, H., and D. L. Anderson, Theoretical basis of some empirical relations in seismology, *Bull. Seismol. Soc. Am.*, *65*, 1073–1096, 1975.

Knopoff, L., Energy release in earthquakes, *Geophys. J. R. Astron. Soc.*, *1*, 44–52, 1958.

Knopoff, L., and J. Randall, The compensated linear vector dipole—A possible mechanism for deep earthquakes, *J. Geophys. Res.*, *75*, 4957–4963, 1970.

Landisman, M., A. Dziewonski, and Y. Sato, Recent improvements in the analysis of surface wave observations, *Geophys. J. R. Astron. Soc.*, *17*, 359–403, 1969.

Langston, C. A., Body wave inversion of the Koyna, India, earthquake of December 10, 1967, and some implications for body wave focal mechanisms, *J. Geophys. Res.*, *81*, 2571–2572, 1976.

Langston, C. A., and D. V. Helmberger, A procedure for modeling shallow dislocation sources, *Geophys. J. R. Astron. Soc.*, *42*, 117–130, 1975.

Laughton, A. S., R. C. Searle, and D. G. Roberts, The Reykjanes Ridge crest and the transition between its rifted and non-rifted regions, *Tectonophysics*, *55*, 173–177, 1979.

Mathews, J., and R. Walker, *Mathematical Methods of Physics*, pp. 273–275, W. A. Benjamin, New York, 1964.

McCowan, D. W., Moment tensor representation of surface wave sources, *Geophys. J. R. Astron. Soc.*, *44*, 595–599, 1976.

McCowan, D. W., A moment tensor representation of body-wave displacement vectors on the focal sphere, semi-annual technical summary, pp. 9–11, Lincoln Lab., Mass. Inst. of Technol., Cambridge, March 1977.

Mendiguren, J. A., Inversion of surface wave data in source mechanism studies, *J. Geophys. Res., 82,* 889–894, 1977.
Mitchell, B. J., Radiation and attenuation of Rayleigh waves from the southeastern Missouri earthquake of October 21, 1965, *J. Geophys. Res., 78,* 886–899, 1973.
Naponen, I., Surface wave phase velocities of Finland, *Bull. Seismol. Soc. Am., 56,* 1093–1104, 1966.
Oliver, J., R. Kovach, and J. Dorman, Crustal structure of the New York–Pennsylvania area, *J. Geophys. Res., 66,* 215–225, 1961.
Patton, H., A note on the source mechanism of the southeastern Missouri earthquake of October 21, 1965, *J. Geophys. Res., 81,* 1483–1486, 1976.
Patton, H. J., Source and propagation effects of Rayleigh waves from central Asian earthquakes, Ph.D. thesis, 342 pp., Mass. Inst. of Technol., Cambridge, 1978.
Patton, H., Reference point method for determining the source and path effects of surface waves, *J. Geophys. Res., 85,* 821–848, 1980.
Patton, H., and K. Aki, Bias in the estimate of seismic moment tensor by the linear inversion method, *Geophys. J. R. Astron. Soc., 59,* 479–495, 1979.
Robson, G. R., K. G. Barr, and L. C. Luna, Extension failure: An earthquake mechanism, *Nature, 218,* 28–32, 1968.
Saito, M., Excitation of free oscillations and surface waves by a point source in a vertically heterogeneous earth, *J. Geophys. Res., 72,* 3689–3699, 1967.
Sleep, N. H., Formation of oceanic crust: Some thermal constraints, *J. Geophys. Res., 80,* 4037–4042, 1975.
Sleep, N. H., and B. R. Rosendahl, Topography and tectonics of mid-ocean ridge axes, *J. Geophys. Res., 84,* 6831–6839, 1979.
Solomon, S. C., Shear wave attenuation and melting beneath the Mid-Atlantic Ridge, *J. Geophys. Res., 78,* 6044–6059, 1973.
Solomon, S. C., Earthquake source parameters, median valley faulting, and the depth of hydrothermal circulation for slow spreading ridges (abstract), *Eos Trans. AGU, 60,* 376, 1979.
Solomon, S. C., and N. C. Burr, The relationship of source parameters of ridge-crest and transform earthquakes to the thermal structure of oceanic lithosphere, *Tectonophysics, 55,* 107–126, 1979.
Solomon, S. C., and B. R. Julian, Seismic constraints on ocean-ridge mantle structure: Anomalous fault phane solutions from first motions, *Geophys. J. Roy, Astron. Soc., 38,* 265–285, 1974.
Strelitz, R. A., Moment tensor inversions and source models, *Geophys. J. R. Astron. Soc., 52,* 359–364, 1978.
Strelitz, R. A., The fate of the downgoing slab: A study of the moment tensors from body waves of complex deep focus earthquakes, *Phys. Earth Planet. Int., 21,* 83–96, 1980.
Stump, B. W., The determination of source mechanism by linear inversion of seismograms (abstract), *Eos Trans. AGU, 57,* 953, 1976.
Sykes, L. R., Mechanism of earthquakes and nature of faulting on the mid-ocean ridge, *J. Geophys. Res., 72,* 2131–2153, 1967.
Sykes, L. R., Focal mechanism solutions for earthquakes along the world rift system, *Bull. Seismol. Soc. Am., 60,* 1749–1752, 1970.
Tsai, Y. B., and K. Aki, Simultaneous determination of the seismic moment and attenuation of seismic surface waves, *Bull. Seismol. Soc. Am., 59,* 275–287, 1969.
Vogt, P. R., and G. L. Johnson, Transform faults and longitudinal flow below the mid-oceanic ridge, *J. Geophys. Res., 80,* 1399–1428, 1975.
Weidner, D. J., Rayleigh wave phase velocities in the Atlantic Ocean, *Geophys. J. R. Astron. Soc., 36,* 105–139, 1974.
Weidner, D. J., and K. Aki, Focal depth and mechanism of mid-ocean ridge earthquakes, *J. Geophys. Res., 78,* 1818–1831, 1973.
Wickens, A. J., Variations in lithospheric thickness in Canada, *Can. J. Earth Sci., 8,* 1154–1162, 1971.

(Received November 13, 1979;
revised September 9, 1980;
accepted September 23, 1980.)